



Using Ultrasound to Enhance Targeted Radiotherapy

Jonathan Vince

St. Catherine's College

Supervisors

Professor Eleanor Stride

Professor Andrew Lewis

A thesis submitted to the Department of Engineering Science

towards the degree of Doctor of Philosophy

September 2021

Statement of Originality

I hereby declare that this submission is my own work and, to the best of my knowledge, it contains no materials previously published or written by another person, or substantial proportions of material which have been accepted for the award of any other degree or diploma at the University of Oxford or any other educational institution, except where due acknowledgement is made in the thesis.

Any contribution made to the research by others, with whom I have worked at the University of Oxford or elsewhere, is explicitly acknowledged in the thesis.

I also declare that the intellectual content of this thesis is the product of my own work, except to the extent that assistance from others in the project's design and conception or in style, presentation and linguistic expression is acknowledged.



Jonathan Vince

September 2021

Acknowledgements

Years ago, the prospect of reaching higher education appeared almost impossible to me. To now be concluding my graduate studies at Oxford University, feels incredibly surreal to both my family and myself. There are numerous people to thank for my experience at Oxford and whom without, this thesis would not have been possible.

Firstly, I would like to thank Professor Andrew Lewis for his mentorship, support and guidance over the past few years. For nurturing both my professional and academic careers, encouraging me to pursue further education and the opportunities it presents thereafter. I definitely owe you more than a beer, or two.

I am forever grateful to Eleanor Stride, for her continued support and assistance in my research. For making me feel a welcome and valued part of the BUBBL group; despite my initial hesitations and concerns about joining such a prestigious group and university. Imparting me with the self-belief that I was capable to complete my studies, despite the numerous obstacles that I encountered throughout it. I hope we'll continue to stay in touch however you may now need to find a new penguin, to do all your heavy lifting.

I would like to express my sincerest gratitude to the Royal Commission of 1851 for awarding me my industrial fellowship and sponsorship of this research. In particular, I would like to thank Amahl Smith for being so accommodating of my situation post redundancy and enabling me to complete my studies despite the withdrawal of my industrial sponsor. The charity and support given to me, has comforted me on countless sleepless nights.

I acknowledge the generous support of the Kennedy Trust for Rheumatology Research for the microscopy facilities used in this research. Honourable mentions to Emma Carter-Biggs for her aid in facilitating my return to the Kennedy during the relaxation of the pandemic restrictions.

I would like to thank Mr Puneet Plaha, associate professor and consultant neurooncology surgeon of the John Radcliffe Hospital Oxford, for his collaboration in this research and the unique opportunity to witness a surgical resection in person; an experience I will treasure and never forget.

All of this would not have been possible without the staff of St.Catherine's college, Oxford University and Oxford University Innovation; particularly the help of Dinalia de Silva in helping us navigate the complex and sometimes convoluted structure of patent language and aiding in our successful patent submission.

My work would have been impossible without the incredible facilities and staff of the Institute of Biomedical Engineering. My sincerest thanks to Dr. Michael Gray, for his knowledge and teachings on transducer characterisation; and to Jim Fisk of the IBME workshop, for his constructive criticism and fabrication of my engineering schematics.

I owe a great deal to Dr. Catherine Paverd, Dr. Bernard Shieh and Cameron Smith for their help in pursuit of this DPhil. All of whom have been incredibly patient with me and taken it upon themselves to educate me on numerous areas of acoustics of which I am incredibly grateful. To Alex Martin, Tamsyn Clarke and Dr. Laura Spiers for their comradery, moral support and uplifting spirits during the long nights into the early hours. Friends I won't soon forget. I wish them all the best of luck in their new careers moving forward.

Abstract

The use of radiation as a selective modality for the treatment of cancer and various other diseases is a fundamental principle in modern medicine. However, despite decades of research and development, selective internal radiation therapy (SIRT), the arterial delivery of radioactive particles for the treatment of hepatic tumours, remains a poorly utilised technology outside of the liver. A major challenge for SIRT is the current lack of control over the distribution of particles in the affected tissue. Achieving a uniform distribution throughout the tumour mass is critical for ensuring a therapeutically relevant dose of radiation and hence successful treatment. Cavitation of microbubbles has been successfully employed to facilitate the extravasation of various nanoparticles and therapeutic agents in tissue. It is hypothesised that ultrasound induced cavitation has the potential to move larger micron sized particles used within SIRT, to increase the distribution of the therapeutic microspheres. The primary goal of this doctoral thesis is to investigate the potential use of ultrasound-induced cavitation to enhance SIRT by facilitating transport of radioactive microspheres in tissue.

A secondary goal of the thesis is to explore its use in the treatment of other types of cancer, in particular Glioblastoma Multiforme; a particularly grave cancer of high incidence. First, a tissue phantom and experimental protocol are designed to enable observation of the transport of microspheres induced by ultrasound exposure using high resolution X-ray computed tomography (μCT) imaging. Proof of concept results are obtained to confirm the feasibility of the approach. An analysis framework and image processing software are then employed to enable quantification of microsphere transport in three dimensions and the corresponding radiation exposure that could be achieved. A detailed investigation of the parameter space is then made using a statistical Design-of-Experiments methodology to identify the conditions under which a suitable microsphere distribution can be achieved; peak negative pressure

correlated non-linearly with post focal projection depth and could be used to make predictions with 88.4% confidence for 95% of the observations used in the model. Finally, ultra-high speed imaging (0.1-2Mfps) is used to explore the mechanisms by which cavitation promotes microsphere transport; producing novel brightfield images of microbubble cloud activity and mass transport of dense glass microspheres. Overall, the results presented in the thesis demonstrate the feasibility of using ultrasound induced cavitation to enhance SIRT within target tissues not readily treated by an arterial route. Further work to understand the impact of tissue heterogeneity and the design of a bespoke ultrasound transducer will be required to enable clinical translation.

Contents

1. Introduction and Literature Review 16

1.1. Glioblastoma Multiforme 16

1.1.1. Adjuvant Chemotherapy 17

1.1.2. Adjuvant Whole Brain Radiotherapy 18

1.1.3. Effects of radiation on tumour cells 19

1.2. TheraSphere® and SIRT 20

1.2.1. Microsphere Distribution and Relative Density 22

1.2.2. TheraSphere® Procedure 23

1.3. Limitations of SIRT 26

1.4. Ultrasound 27

1.4.1. Thermal Ablation 27

1.4.2. Mechanical Effects 28

1.4.3. Acoustic Cavitation 29

1.5. Cavitation Nuclei 30

1.5.1. Microbubbles and Nanobubbles 30

1.5.2. Nanocups 31

1.5.3. Nanodroplets 34

1.6. Cavitation Enhanced Extravasation of Particles 34

1.6.1. Microjetting 35

1.6.2. Microstreaming 36

1.6.3. Microbubble Tunnelling 36

1.6.4. Microbubble Cloud Formation 37

1.7. Novelty and Thesis Objectives 40

2. In Vitro Extravasation of Glass Microspheres in Hydrogel Cavities 55

Summary 55

2.1. Introduction 55

2.1.1. Ultrasonic Aspiration for Tumour Resection 56

2.1.2. Ultrasound Induced Cavitation as a Treatment Modality for Glioblastoma Multiforme 57

2.2. Methods 58
2.2.1. Phantom Development 58
2.2.1. Malignancies of the Brain and Ex Vivo Surrogates 58
2.2.4. Tissue Phantom Mould 64
2.2.5. Fabrication of Bespoke Ultrasound Tank and Movement Stages 65
2.2.6. Ultrasound Transducer Setup and Calibration 66
2.2.7. Ultrasound Transducer Alignment 70
2.3. Experimental Procedure and Analysis Techniques 71
2.3.1. Micro Computed Tomography (µCT) 72
2.3.2. µCT Image Analysis 73
2.4. Characterisation of Microsphere Extravasation 74
2.4.1. Phantom Well 75
2.4.2. Microsphere Projection 75
2.4.3. Projection Channels 76
2.4.4. Projection Bulbs 77
2.5. Discussion 78
2.6. Conclusion 79
2.6.1. Limitations 80

3. In Silico Analysis and Interpretation of Cavitation Induced Projections of Glass Microspheres 87
3.1. Introduction 87
3.2. Methods 88
3.2.1. Minimum-volume enclosed ellipsoid (MVEE) 89
3.3. Single Well Elimination Microsphere Projection Interpretation 89
3.3.1. Predicting ^{90}Yttrium β Radiation Emission from Glass Microspheres 94
3.3.2. Factorial Design – Response Surface 95
3.3.3. Parameters Investigated 97
3.3.4. Post Focal Projection Depth Surface Design 99
3.4. Results 105
3.4.1. 0.5 MHz Non-linear Regression 105
3.5. Discussion 109
3.5.1. Experimental Order 109
3.5.2. Primary Factor Responses Using Linear Regression 110
3.5.3. Factor Interaction Responses Using Linear Regression 113

3.5.4. Comparison of Predictive Outputs for Regression Models 114
3.6. Conclusion 115
3.6.1. Limitations 117
3.6.2. Future Work 118

4. High-speed Imaging of Cavitation Enhanced Projection Events 123
4.1. Introduction 123
4.2. Methods 123
4.2.1. Mould Design 123
4.2.2. Ultrasound Tank and Movement Stages 125
4.2.3. Shimadzu Hypervision HPV-X2 High-speed Camera 127
4.2.4. High Speed Camera Triggering 128
4.2.5. Ultrasound Exposure Conditions to Facilitate High-speed Imaging 130
4.3. Results 131
4.3.1. Extravasation of Glass Microspheres through Agar Phantoms 131
4.3.2. Microsphere Bolus Speed Measurements 135
4.3.3. Rippling of the Edge of the Well 137
4.3.4. Observations of Bubble Cloud and Microsphere Interactions 139
4.3.5. Microsphere Bolus Movement 151
4.4. Discussion 156
4.4.1. Order of Events Leading to Microsphere Extravasation 156
4.4.2. Microsphere Imaging Capability and Clarity 157
4.4.3. Microbubble Cloud Erosion of the Agar Medium 159
4.4.4. Microsphere Projection Wake Banding 161
4.5. Conclusion 164
4.5.1. Limitations 167
4.5.2. Future Work 168

5. Conclusions 174
5.1. Publications 177
5.2. Limitations 177
5.3. Future Projects 178
5.3.1. Tumour Inhomogeneity 179
5.3.2. Prototype Optimisation 182

Appendices

1. Khachiyan Algorithm - Minimum Volume Enclosed Ellipse Code 188

2. Single Well Elimination Microsphere Projection Interpretation Code 190

3. Interaction Plot for Post Focal Projection Depth (mm) 197

4. HPV-X2 Image Calibration and Objective Limitations 198

5. HPV-X2 External Trigger Methods 201

5.1. Manual Gated Timing 201

5.2. Light Responsive Trigger Method 205

6. Microsphere Banding within Projection Channels 210

7. Design and Fabrication of a Novel Ultrasound Horn for Intraoperative adjuvant use in Glioblastoma Multiforme Resections 215

7.1. Proof of Principle 215

7.2. Methods 217

7.2.1. Design Parameters 217

7.2.2. Horn Prototypes x1c & x3c 218

7.3. Results 220

7.3.1. Acoustic Field (x1c) 220

7.3.2. Pressure Output (x1c) 224

7.3.3. Acoustic Field (x3c) 225

7.3.4. Pressure Output (x3c) 227

7.3.5. LDV Measurements x3c 228

7.3.6. Initial In Vitro Phantom Testing 230

7.4. Discussion 231

7.4.1. Variable Impedance of the x1c and x3c Horn Prototypes 231

7.4.2. Design Improvements 232

7.5. Conclusion 233

Acronyms and Abbreviations

µCT	Micro Computed Tomography
5-ALA	5-aminolevulinic dye
ARF	Acoustic Radiation Force
BBB	Blood Brain Barrier
BTIC	Brain Tumour Initiating Cells
CBD	Cannabinoids
CSF	Cerebrospinal Fluid
CT	Computer Tomography
CTE	Chronic Traumatic Encephalopathy
DICOM	Digital Imaging and Communications in Medicine
DoE	Design of Experiment
DSB	Double strand breaks
Duty Cycle	DC
EBRT	external Beam Radiotherapy
EOR	Extent of Resection
FOV	Field of View
GBM	Glioblastoma Multiforme
HA	Hyaluronic acid
HCC	Hepatocellular Carcinoma
HeNe	Helium Neon
HIFU	High Intensity Focussed Ultrasound
HPS	Hepatopulmonary Shunting
IBME	Institute of Biomedical Engineering
IORT	intraoperative radiation therapy
kVp	Peak Kilovoltage
LED	Light Emitting Diode
LRT	localised radiotherapy
LS	Lung Shunting
MB	Microbubble
MGMT	O6-methylguanine-DNA-methyltransferase
MIP	Maximum Intensity Projections
MRI	Magnetic Resonance Imaging
MTIC	3-methyl-(triazen-1-yl)imidazole-4-carboxamide

MVEE	Minimum-volume Enclosed Ellipsoid
Mw	Molecular Weight
NO	Nitric Oxide
OV	Oncolytic Viruses
PET	Photon Emission Tomography
PMMA	Polymethyl Methacrylate
PNP	Peak Negative Pressure
PRF	Pulse Repetition Frequency
PVA	Polyvinyl alcohol
RBC	Red Blood Cell
ROBs	Radiopaque Beads
ROS	Reactive Oxygen Species
SIRT	Selective Internal radiotherapy
SPECT	Single Photon Emission Computed Tomography
SRT	Stereotactic Radiation Therapies
SSB	Single Strand Breaks
SWL	Shockwave Lithotripsy
TAE	Trans arterial embolisation
TBI	Traumatic Brain Injuries
Tc^{99m}-MAA	$Technetium^{99}$ labelled Macro Aggregated Albumin
TMZ	Temozolomide
VGEF	Vascular Endothelial Growth Factor
WBRT	Whole Brain Radiotherapy
YAS	Yttrium-Aluminium-Silicon

CHAPTER 1

Introduction

1. Introduction and Literature Review

1.1. Glioblastoma Multiforme

Glioblastoma Multiforme (Glioblastoma, GBM) is the second most frequently reported brain tumour, after meningioma, and the most common malignant tumour. Glioblastoma accounts for 15.4% of all primary brain tumours and 45.6% of primary malignant brain tumours in the United States[3] alone. Life-expectancies from meningiomas in contrast are significantly better; with 57.2% surviving ten or more years[3].

The brain is an incredibly complex organ, it is no surprise therefore that cancers of the brain are also equally intricate and inherently difficult to study. GBM is exceptionally heterogenous, with differing cell types, lines and histologies within a single patient, further compounded by increasing variation between patient genders, populations and disease staging's[185-188].

Unlike Medulloblastoma, GBM does not appear to produce any desmoplasia or reinforcement of the GBM capsule[194]. GBM however does exhibit a particular sub-set of brain tumour initiating cells (BTIC) which are thought to be a large contributing factor in the invasion of cancerous cells into the otherwise healthy periphery beyond the central tumour mass[185,186,189]. These BTICs have stem cell like properties, producing a variety of different cells types, which work in tandem with non-BTIC within the tumour bulk to promote tumour growth[185,187,190]. However, BTIC tumorigenesis alone fails to account for the varied functional behaviours of different BTIC populations[191], with recent studies demonstrating significant difference in molecular signatures between men and woman, for tumorigenic behaviour [188,189,191].

GBM is one of the most aggressive and frequently reported brain tumours in the western world[4–6]. Due to the aggressive infiltration of tumour cells outside that of the central tumour mass, patients with GBM have a mean survival of 1 year with only 5% of individuals living for 5 or more years, with no prevention strategy or standardised second-line treatment available.

These distressing figures are reflective of the limited treatments available, with most procedures failing to prevent reoccurrence and disease progression occurring within 10 to 30 weeks[7]. Current approaches for the treatment of glioblastoma combine surgical resection with adjuvant radiotherapy and chemotherapy; a particularly aggressive and demanding protocol particularly considering incidence of the disease is highest in patients aged 75 years and above[3,7]; with patients rarely reaching the 2 year survival period[4].

1.1.1.Adjuvant Chemotherapy

Treatment with chemotherapeutic drugs has limited efficacy and a high risk of side-effects, most drugs being non-selective and having limited access to the brain due to the blood brain barrier (BBB). Temozolomide (TMZ) is a prodrug with some limited selectivity, having 100% oral bioavailability and is capable of crossing the blood brain barrier. TMZ is metabolised in the gut, into 3-methyl-(triazen-1-yl)imidazole-4-carboxamide (MTIC); MTIC and its subsequent derivatives are thought to be primarily responsible for its effect though the methylation of DNA base nucleotides at the N-7 or O-6 positions[8]. During replication this methylation causes mutation which can induce intrinsic apoptosis[9–11]. However, the effects of methylation can be repaired by the cancerous cells, despite TMZs ubiquitous bioavailability.

As a result TMZ's efficacy in GBM is significantly better than other dacarbazine derivatives, offering improvements in 6- month progression free and overall survival for brain cancers[12]. Efforts continue investigating a combination of chemotherapy agents and therapies, to bolster the effects of TMZ in this indication[5,13–15].

Carmustine mustard gas is an alternative, non-selective agent used in chemotherapy. Infused into biodegradable wafers and implanted into resection cavities, it has shown some limited efficacy in increasing time to progression for patients who have already received a 'complete' resection and remain suitable for further surgical intervention[16,17]. However the use of

carmustine wafers has declined due to the threat of potential secondary infections and the need for costly repeated surgical intervention[18–20].

1.1.2. Adjuvant Whole Brain Radiotherapy

Glioblastomas are particularly aggressive in nature, with patients frequently having recurrence at the surgical site or development of new lesion(s) elsewhere in the brain[21]. Whole brain radiation therapy (WBRT) is an invaluable tool for slowing the reoccurrence of gliomas, and is a proven method for localised tumour control. Necrosis of tissue surrounding the surgical wound, however, prolongs the healing process[22].

A common approach for adjuvant WBRT consists of a total of 37.5Gy of radiation in 15 fractions or 30 Gy in 10 fractions over six weeks, to treat one or multiple locations of intracranial lesions; with the optimal timing for postoperative radiotherapy being at least one week after surgical invention[21,23]. This is to allow for sufficient time for immediate recovery from the invasive surgery, minimising the likelihood of post-operative complications.

Compared to chemotherapy treatment WBRT offers better prevention against progression of GBM when used as adjunctive therapy, particularly in the formation of new lesions elsewhere in the brain. Successive treatments of WBRT, however, are not possible due to memory loss, leukoencephalopathy and subsequent neurocognitive decline[21,12]. Combining WBRT with other more selective radiotherapies also increase the risk of developing leukoencephalopathy[12]. Whilst the brain remains fairly resilient to non-selective external beam radiation, repeated dosing as with any organ leads to a swift decline in patient health; there is a finite number of times a patient can be beneficially exposed to radiation[6,23–25].

Improvements in patient welfare have arisen more recently[16] as a result of from moving away from WBRT and towards localised radiotherapy (LRT) such as stereotactic radiation therapies

(SRT) or intraoperative radiation therapy (IORT) for cancerous lesions[21]. Improving local control can enhance procedural outcomes and in some cases overall survival of patients compared to WBRT for patients with a limited number of lesions or metastases [26,16]. Using this approach, not only is the damage to nearby critical structures reduced, but subsequent retreatments of secondary malignancies are possible; depending on previous dose exposure and proximity to the original lesion [17,16]. Using SRT as initial adjuvant radiotherapy, reserves the use of WBRT for further disease reoccurrences and as terminal treatment for palliative care[21].

As the majority of gliomas relapse adjacent to previously treated areas, localised reirradiation of the initial tumour volume either via external beam or stereotactic radiotherapy is an attractive approach for adjuvant therapy[27]. Intercranial brachytherapy has been investigated with the use of low dose rate ^{125}Iodine crystals, however efficacy of the stereotactic brachytherapy is dependent upon the number of large iodine crystals deposited[28] and the subsequent volume of tissue irradiated.

1.1.3.Effects of radiation on tumour cells

Ionizing radiation can be an incredibly powerful tool in treatment of cancerous lesions, inducing single (SSB) and double strand breaks (DSB) and base damage of cellular DNA. DSB, whilst the most toxic, occur less frequently than SSB which are produced in far higher yields. DSB or several SSB occurring within close proximity to one another, are resistant to repair and impair or completely inhibit, the cell replication via mitosis[29,30,31]. Radiation induced SSB breaks and base DNA damage lead to DSB upon subsequent DNA replication[31] therefore cancerous cells which undergo increased rates of replication, have less opportunity for repair and are more susceptible to apoptosis. Radiotherapy of cancerous lesions is therefore more selective of malignant cells, than that of healthy tissue[29–32] but may still result in undesired mutations in surviving healthy tissue[30].

1.2. TheraSphere® and SIRT

Selective internal radiotherapy (SIRT) is a modern evolution of surgical brachytherapy. Current approaches to SIRT, use isotopes of far higher purity and of known grade to localise radiation using non-biodegradable biocompatible microspheres, with calculated emission energies and treatment durations for specific indications.

As with brachytherapy, SIRT allows for precise, controlled radiotherapy to radiosensitive organs and tissues, which otherwise would not tolerate a large dose of unfocused, diffuse radiation. Treatment is minimally invasive, via femoral or radial access to the arterial supply, enabling delivery through out-patient care and making it an attractive alternative to external beam radiotherapy (EBRT). Despite the initial concept of treatment being developed in the 1950's, adoption and practice of SIRT as a palliative technique did not become widespread until the approval of current SIRT products in the 2000's[33]. SIRT remains a non-curative treatment, recommended by several health agencies across the globe for the treatment of hepatocellular carcinoma and colorectal metastasis in the liver.

TheraSphere® is a radioembolic glass microsphere, produced by BTG plc (recently acquired by Boston Scientific Corp.) and recommended by the European Society for Medical Oncology for SIRT in the treatment of colorectal liver metastasis and inoperable hepatic cholangiocarcinoma[34,35,36]. The spheres are a combination of three high purity metal oxides, yttrium, aluminium and silicon which are blended and melted together at extreme temperatures to produce a solid (YAS) glass. The glass is shattered, powdered and spherodised over a naked flame to form the YAS microspheres[37,38]. The exact composition of the YAS glass is key to the melting characteristics of the glass and obtaining a spherical radioembolic product.

Once sieved to generate a size range of 25-35 μm, the microspheres are subjected to neutron bombardment in a nuclear reactor, producing Yttrium 90 as the sole radioactive component. Other isotopes formed, as the result of the neutron bombardment, of silicon or aluminium are deemed stable or insignificant by composition[38,39]. The enriched ^{90}Y isotope undergoes β^- decay to ^{90}Zr with a half-life of 64.1h[40] and a mean decay energy of 0.93 MeV. Emissions of electrons from the unstable ^{90}Y atoms are decelerated by neighbouring atoms electrostatic repulsions; this deceleration and loss of kinetic energy is emitted as 'braking' gamma radiation to the surrounding cells (Bremsstrahlung or Cerenkov radiation) and can be detected externally for imaging[41,42,43]. The energy emitted into neighbouring cells causes DNA DSB, with downstream signalling of this DNA damage inducing cellular necrosis.

The depth of irradiation is dependent upon the permeability of the material and hence its density, atomic arrangement and the energy of the electrons emitted; all of which contribute to the frequency of the secondary irradiation produced[43]. The maximum observed depth of penetration for patients undergoing TheraSphere® treatment in a clinical environment is 2.5mm mean tissue penetration[43]. Variance in necrosis surrounding the radioembolic microsphere is associated with inter-sphere clustering. Where YAS spheres are closely packed, the gradient of energy release is larger, resulting in a slightly larger penetration distance[45]. TheraSphere®'s energy per microsphere is significantly higher than that of other competitor microspheres[46,47], resulting in a product that delivers a significantly larger radiation dose (205.7 ±19.7 vs. 128.9 ± 10.6 Gy, for TheraSphere *versus* SIR-Sphere®, $p<0.001$)[46] to the tumour. Deposition of a high activity based microsphere like TheraSphere leads to excessive irradiation of the surrounding tissue, which varies based upon the cellular heterogeneity, perfusion and volume of the tumour treated[182]. Despite its higher activity per sphere and the deposition of surplus radiation, the use of TheraSphere is deemed safe and approved for use in radioembolisation.

Despite being classed as a radioembolic, TheraSphere®'s primary mode of action is irradiation and not an embolic effect[48]. As it is incompressible *in vivo* and with a relative density of 3.6 gml^{-1}, its terminal placement is in the fine vasculature adjacent to the capillary beds supporting organ parenchyma. TheraSphere® is unable to pass through the capillary beds (5-10µm) due to its size and incompressibility, preventing it from passing into the venous system[45]. TheraSphere® is not currently promoted as a direct micro-embolic primarily because of the near-stasis flow surrounding the capillary beds, where any reduction of flow is negligible in necrotic tissue. Secondly, as the area of necrosis exceeds that of any micro-embolic effect, it is challenging to distinguish the physiological properties of TheraSphere® from its radiological ones[49]; of which the depth of radiation penetration predominates for individual microspheres.

In contrast, a resin based radioembolic product SIR-sphere® by SIRTex Medical Ltd., is significantly larger (20-60µm), less dense ($1.1gml^{-1}$) and has a higher embolic effect. The spheres become embedded within the arterioles feeding the tumour, more distal from the tumour than its smaller glass counterpart[7] reducing blood flow to a larger volume of tissue. It has been suggested however that in instances of accumulation in larger tumour feeding arteries TheraSphere® may also have a larger embolic effect[49].

1.2.1.Microsphere Distribution and Relative Density

The distribution of the β radiation and hence successful treatment of the intended malignancy, is largely governed by the terminal placement of the radioembolic microsphere. Treatment of larger surface areas or lobes of the liver, requires either a larger number of microspheres or a greater distribution of the same number of spheres; with a decreased intensity of radiation. Delivering the spheres from an arterial branch more distal from the tumour site, offers less control over targeted or super-selective delivery, an approach frequently used for lobectomy or segmentectomy in treatment of HCC[50].

Caine *et al*. simulated the effect of relative density, fluid viscosity, injection velocity, injection solution viscosity and injection flow rate on microsphere distribution; concluding that relative microsphere density had minimal influence on distribution, even in reduced flow conditions[33]. Flow behaviour is instead dominated by the fluid viscosity, flow rate and vascular geometry. The density of the microsphere does however play a more important role in controlling sedimentation of the radioembolic as the flow rate approaches stasis[33].

The distribution of the microspheres is ultimately limited by the placement of the catheter delivering them. In hypoxic solid tumours large areas of the tumour may remain untreated due to the vasculature of the cancer primarily being present on the periphery of the solid lesion, its poor vascular density preventing delivery of radioactive microspheres to the centre of the solid mass; in addition to any interstitial tumour pressure. Thus the energy of irradiation and its subsequent depth of irradiation, are vital to the viability of the procedure. If the depth of penetration of the radiation were to be extended, to enable treatment of a greater proportion of the tumour, it is expected that patient prognosis would also improve.

1.2.2.TheraSphere® Procedure

Once a patient has been assessed as eligible for TheraSphere® SIRT, the extent of the disease will be mapped and staged, in accordance with the Barcelona Clinic Liver Cancer (BCLC) staging crietria[183]. Mapping of the region of interest enables the pre-planning and visceral angiography, using radiopaque contrast agent to enhance the resolution of the arterial vasculature feeding the lesion and its periphery[51]. Once the route of administration has been determined (via the radial or femoral artery), the physician will perform a lung shunting assessment using Technetium[99] labelled macro aggregated albumin (Tc^{99m}-MAA)[51]. This colloidal suspension of protein encapsulated radioactive metal isotope tracer, with greater than 90% of the particles between 10-90 μm, is used to assess the percentage of material

delivered off-target either as extrahepatic shunting within the abdomen, hepatopulmonary shunting (HPS) more commonly known as lung shunting (LS), or reflux towards the gastrointestinal region[51]. If the percentage of off-target delivery is deemed hazardous, a preliminary trans arterial embolisation (TAE) procedure or coil placement may be performed. TAE procedures are used in two distinct cases, either for reducing the off-target delivery of microspheres outside the target region (preventing extra-hepatic leakage) or to minimise any observed hepatic vein shunting, where beads ultimately reside in the vasculature of the heart and lungs, a toxicity concern[39].

^{99m} Technetium is a meta stable gamma emitting isotope, with a short half-life of 6.00 hours and energy of 140keV[40]. The visualisation of the isotope and its distribution, is achieved via single photon emission computed tomography (SPECT). This is due to the photon emission having a much shorter (gamma) wavelength to that of conventional diagnostic x-ray equipment[40]. With such a brief radioactive period, 93.7% of the isotope is completely stable (as ^{99}Tc) within 24 hours, thus reducing potential side effects of radiation during the metabolism and excretion of the macro aggregated albumin[41].

The combination of the angiography data, mapping of the peripheral vasculature and administration route, scintigraphy and the particle distribution assessment data, culminates in a more consistently accurate prediction of the required radiation dose, for the treatment in relation to the grade of the disease[38,52].

Delivery of the glass YAS spheres is performed with sterile 0.9% saline, flushing the spheres out of their v-glass vial residing within a secondary acrylic holder, into the arterial vasculature via microcatheter. The placement of the tip and the internal diameter of the microcatheter is determined by the operator, availability and territory preferences. Completion of the irradiation treatment occurs within 2 weeks, with patient follow-up occurring after 6 weeks; consisting of further imaging of the parenchyma and necrotic tissue, potentially with further

histology to assess procedural performance[44,48,3]. The increased dose rate, total radiation dose in combination with a smaller seed size and larger volume of irradiation compared to iodine-125 crystals, places SIRT as a potentially effective adjuvant for stereotactic radiotherapy of glioblastoma and other gliomas.



Figure 1: Fig. 2.3 reproduced from Image-Guided Interventions in Oncology, pp 15-27 Physics and Physiology of 90Y Radioembolization for Liver Tumors40, with permission from Springer Nature. Copyright © 2020, Springer Nature Switzerland AG. (a) The TheraSphere administration box. The dose vial within the lead pig is positioned within the box, and the needle assembly has been snapped in place. Saline flushed through the "B" line suspends the microspheres which then flow from the dose vial into the exit tubing and microcatheter. (b) Close up image of the TheraSphere administration box shows the radiation dosimeter near the dose vial. The reading should drop to zero during administration. The overflow vial is seen below "A". This serves to limit the rate of injection. If there is excess pressure during administration, excess saline will flow into this vial rather than over-pressurize the needle assembly. (c) The SIR-Spheres administration box. Dextrose solution injected in line and needle "D" agitates and suspends the microspheres, which then exit the vial through the outlet needle toward the three-way stopcock mounted on the interior of the box, connected to the external black knob. The distal outlet line "A" is connected to the microcatheter, and can be cleared by turning the black knob toward "Flush/Contrast" and injecting into line "B". The external stopcock attached to line "B" allows injection of contrast medium to perform interval angiography between aliquots of microspheres to assess arterial flow for stasis. A radiation dosimeter has been placed inside the administration box to monitor completeness of administration (not recommended by manufacturer). (d) Interior of the SIR-Spheres administration box showing the administration needles positioned within the v-bottom dose vial. The inlet needle is positioned just above the microsphere pellet and is used to suspend the particles, and the outlet needle is positioned near the top of the meniscus where dilute suspended microspheres exit the proximal outlet line toward the three-way stopcock mounted on the interior of the box. The stopcock can be turned remotely by the external knob and allows alternating between microsphere aliquot administration and distal outlet line flushing or contrast medium injection.

1.3. Limitations of SIRT

SIRT remains an underutilised technology because of the restrictions imposed by the current intra-arterial catheter delivery method. Tumour vasculature is substantially different from that of healthy tissue, with vessels having a chaotic structure with blind ends, shunts and a tendency to collapse[53] . This is primarily due to the unchecked, rapid growth of vessels generated by increased expression levels of the vascular endothelial growth factor (VEGF) signalling protein at the periphery of solid tumours. The vessels themselves are also typically more porous or "leaky" than in healthy tissue vasculature[54]. The irregular distribution of vessels leads to oxygen levels (O_2%) being as low as 0.3 – 4.2% in some areas of solid tumours, compared with normal tissue oxygen levels 'normoxia' being 20-21%. The sparse and/or chaotic vessel structure reduces the number of radioactive microspheres that can be distributed in the tumour region. It also introduces high variability into the mean distance between microspheres which prevents a uniform dose of radiation from being delivered. For SIRT to be used effectively, a means of improving the distribution of microspheres is required

so that a uniform and sufficient dose of radiation can be delivered to the malignant tissue. This thesis explores the use of ultrasound induced cavitation in this context.

1.4. Ultrasound

Ultrasound is broadly defined as pressure perturbations having a frequency above the audible range of humans (20 kHz). The medical applications of ultrasound as a diagnostic imaging modality (sonography) are well established[55]. Medical sonography uses very low intensities, resulting in a safe and non-invasive methodology suitable for imaging sensitive tissues and organs[56]. At higher intensities, ultrasound can produce significant and destructive effects in tissue which can be exploited in therapeutic applications.

1.4.1.Thermal Ablation

High intensity focussed ultrasound (HIFU) is primarily used for non-invasive thermal ablation in current clinical practice. Absorption of the energy from the HIFU, can produce significant local elevation in temperature (hyperthermia) within the target tissue [57]. The heating or 'ablation' of the tissue is achieved either via continuous wave application over several seconds or repetitive pulses of HIFU over several minutes. Tissue coagulation, the combination of protein denaturation and permanent cell damage, is induced from 39°C with the relationship between temperature and permanent cellular damage standardised in minutes at 43°C *in vivo* [58, 59, 60], denoted as the thermal isoeffect dose (TID). TIDs allow for comparisons between treatment regimens independent of the exact parameters and time domains used, according to CEM°43 thermal does thresholding[184].

Pre-focal tissue, despite receiving ultrasound of lower intensity compared to the focal region, does experience pre-focal energy deposition and heating[61]. Pre-focal heating is an important concern for *in vivo* therapies involving the use of HIFU, where undesired collateral damage can

cause thermal ablation prior to the focal point, resulting in skin burns due to the pre-focal tissue being continuously exposed to converging HIFU wavefronts[61]. The problem is particularly acute in the brain which has a very low thermotolerance and where different regions have different thresholds for damage[62].

1.4.2.Mechanical Effects

Ultrasound can also produce a range of mechanical effects that can be exploited therapeutically [58,63,64]. For example, very high pressure acoustic waves can be used to break apart large solid masses, frequently used in shockwave lithotripsy (SWL) for minimally invasive treatment of small kidney stones[65]. Mechanical effects can enhance drug delivery and apoptosis[66,67], with the most extreme (high intensity histotripsy) leading to complete disintegration or homogenisation of tissue[68],[63],[64]. There are three key phenomena underpinning the mechanical effects of ultrasound:

1.4.2.1. *Acoustic Radiation Force*

As a result of focusing the ultrasound wave into a small focal region, a significant pressure gradient is produced compared to that of outside the focal region. When a particle is subject to this pressure field it experiences a force, the primary Bjerknes or primary acoustic radiation force (ARF)[69–71] .

$$\mathrm{F} = -\left(V_t \Delta P_{r,t}\right).$$

Equation 1: Time averaged acoustic radiation force on an object. Volume (V) Pressure gradient (ΔP)[72].

1.4.2.2. *Acoustic Streaming*

Eckart or 'bulk' streaming occurs in fluids as the result of momentum transfer from the propagating wave to the surrounding medium[73,74] which creates a velocity gradient and consequently net flow within the bulk fluid[75]. The timescales associated with bulk streaming are far larger than those produced by the primary acoustic radiation force.

When the flow of fluid is not in free space and is bound, a velocity gradient is established adjacent to the boundary interface. This creates a thin layer of fluid with increased streaming as a result of the no slip condition. The thickness of this boundary layer is given by:

$$d = \sqrt{\frac{\mu}{\rho\omega}}$$

Equation 2: Thickness of boundary layer driven streaming (d), frequency (ω), pressure (ρ) and dynamic viscosity (μ)76.

1.4.3.Acoustic Cavitation

Cavitation, the formation of gas bubbles, can occur when a liquid is exposed to ultrasound. To produce a bubble from within a completely pure liquid, the energy absorbed from the ultrasound wave must overcome the intermolecular bonding present, to allow for the collection of gas molecules as a bubble[77].

In practice lysis of the intermolecular bonds in a bulk fluid is not accomplished, as the energies required are very significant and even purified liquids contain pre-existing discontinuities which trap gases that act as nucleation sites for bubble formation[78–80]. When ultrasound is applied, these pre-existing pockets of gas are supplied with enough energy to overcome the liquid's surface tension and grow in size, producing a bubble. Free non-stabilised bubbles are swiftly eliminated from the bulk fluid by their buoyancy or will rapidly dissolve into the bulk medium if it is not super saturated with gas[79].

In liquids the use of surfactants can bring about fluctuations in the intermolecular bonding which produces discontinuities of lower surface tension[81–84] which promote the entrapment and coalescence of gases. Gas can also be entrapped within crevices and voids in the surface of the liquid container or on solid particles suspended within the bulk liquid, reducing the external pressure on the gas bubble and promoting their stability[85,85–87]. Exploiting the presence of cavitation nucleation sites can be beneficial in therapeutic[67,85,92,93] ultrasound.

1.5. Cavitation Nuclei

Cavitation nuclei can be described as any particle that under exposure to ultrasound, produces an expanding bubble of gas and/or vapour [54,85,94–98]. They may be endogenous (i.e. naturally occurring in tissue) as described above, or exogenous (i.e. deliberately added to promote cavitation). Unless otherwise specified the use of the term cavitation nuclei hereafter relates to exogenous nuclei.

1.5.1.Microbubbles and Nanobubbles

Microbubbles (MB) have been confirmed as occurring naturally *in vivo,* in swine kidneys and porcine liver[99,100] and the incidence of MBs is linearly proportional to the concentration of human red blood cells (RBC) *in vitro*[101].

When exposed to an external ultrasound field, gas-filled MBs will expand and contract with an amplitude dependent upon the amplitude and frequency of the field[102]. At low amplitudes the oscillations of bubbles are largely linear but as the amplitude increases the behaviour of the bubble is increasingly non-linear, whereby the ratio of radial expansion and contraction may vary significantly with the maximum volume of the MB dependent upon the wave pressure[103]. As the inertia of the surrounding liquid, primarily associated with temperature and pressure,

overcomes the internal pressure of the MB, the bubble collapses[102] with the loss of the periodic oscillation denoted as inertial, unstable or transient cavitation[104]. The onset of inertial cavitation can be denoted as the bubble expanding beyond a certain limit, the interior temperature exceeding a certain value or by the rate of collapse exceeding the speed of sound in the liquid. This unstable cavitation event can also produce new smaller MBs which have different critical excitation pressures and resonance frequencies.

Synthetic MBs primarily consist of a gas core, often perfluorocarbon, stabilised by a lipid or protein shell[98,105–108] to prevent the dissolution of gas from larger bubbles (>1µm) into the surrounding solution; with stabilised bubbles less than 1µm termed 'Nanobubbles'[95,110] . The core-shell chemistry can influence the stability and cavitation threshold of the MB population, often with substrates of interest (cytotoxins, metal particles, proteins, viruses) bound to the surface[67,93,110–114]. Excipients may be used with MB formulations to alter the surface tension and induce effects such as cell permeability, sonoporation, reduction of oscillation amplitude and increases in resonance frequency[115,66,116].

Synthetic MBs have been used *in vivo* as a contrast agent and a delivery vector for various applications including cytotoxic drugs for the treatment of solid tumours[117], ultrasound-accelerated fibrinolysis[118], magnetic nanoparticles for MRI imaging[67] and siRNA for gene therapy[67].

1.5.2.Nanocups

The presence of cavitation nuclei in combination with focused ultrasound can promote effects such as the transport of cytotoxic drugs or particles; e.g. improving oncolytic viruses (OV) delivery by up to fifty times compared to passive diffusion alone[119]. One of the largest drawbacks of MBs is their inability to cross tissue membranes; they are also cleared quickly *in vivo* due to their relative size (>1 µm) compared to that of: cellular endothelial pores (100-

800nm) and eukaryotic cells typically being in the range of 5-10 µm[56, 85]. In addition to this, under ultrasound exposure MBs are rapidly destroyed and so the concentration of nuclei within the circulation and associated cavitation activity cannot be sustained over long periods of time (1-2 minutes)[119].

As an alternative, sub-micrometre hollow polymer spheres can be prepared *via* seeded thermally initiated emulsion polymerisation. As the organic monomers react together, a polymer shell or lens is produced on the surface of the suspended droplets. Due to the osmotic pressure on the unsupported polymer film, the surface shell collapses inwards, producing a polymer disc or 'nanocup'. Changing the monomer composition changes the film viscosity generated on the particle during polymerisation and the subsequent size of the cavity produced within the nanocup[120].

The small cavity of the concave polymer nanocup, can entrap gases as nucleation sites for cavitation events[85]. Under exposure to ultrasound the associated gas nanobubble will expand radially and outside of the cavity in which it is situated. As the nanobubble grows in size, it will fill the cavity of the cup and at a critical size, where the contact angle between the bubble and the nanocup approaches its maxima, the bubble will dissociate itself from the nanocup; allowing the MBs to continue to expand in size[85] . The maximum radius the detached MB reaches, is independent of the size of the nanocup cavity or acoustic pressure but is directly related to frequency of the focused ultrasound wave[85]. Kwan et al. reported a fourfold increase in the duration of sustained cavitation when using nanocups (2 minutes) over commercial MBs (<30 seconds), a phenomena which produced a subsequent increase in extravasation of drugs, in an agarose hydrogel phantom[54].

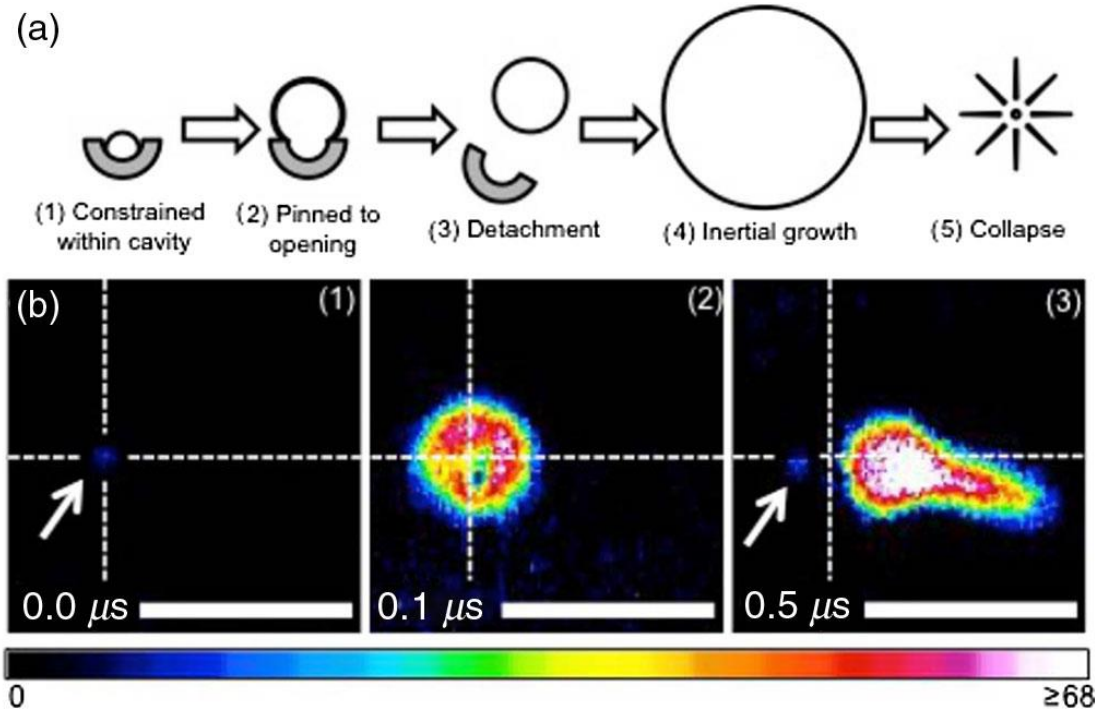


Figure 2: Reprinted Figure with permission from the American Physical Society. Copyright 2016 by the American Physical Society. https://doi.org/10.1103/PhysRevApplied.6.044004 .FIG. 3. Ultrahigh-Speed Dynamics of Micrometer-Scale Inertial Cavitation from Nanoparticles85. Comparison of hypothesized mechanism and experimental observation. (a) An illustration of a surface-trapped nanobubble undergoing inertial collapse. (b) Evidence for a (1) nanocup likely with a trapped nanobubble, (2) nucleation, and (3) detachment from a single large nanocup is shown. Dashed lines indicate the initial position of the nanocup. Scale bars represent 100 μm. The arrow points to the 600-nm-diameter nanocup. The time stamps on the images are based on the onset of cavitation. The color bar is the difference in pixel intensity (of arbitrary units) in each frame of the video compared to the same frame number of the no-ultrasound control video.

Nanocups can be fabricated in a variety of size distributions (174 ± 2, 425 ± 6, and 609 ± 8 nm) their relative size compared to perfluorocarbon MBs and endothelial pores allows nanocups to passively extravasate through tissue and out of the circulatory system after initial intravenous injection. The entrapped nanobubble grows under ultrasound exposure, becomes detached and is subsequently depleted whereas the polymer nanocup is not destroyed and has the potential to continue to nucleate cavitation activity despite their increased nuclei concentration[54,85,97].

1.5.3.Nanodroplets

Unlike MBs which have a stabilised gas core, nanodroplets have a liquid (e.g. perfluoropentane, perfluorohexane) perfluorocabon core which is stabilised by similar lipid or phospholipid molecules on the surface. Nanodroplets offer advantages over both MBs and nanocups. Unlike cups they can directly encapsulate drugs and at a much higher dose per unit volume due to their liquid core compared to the surface of MBs, requiring a much smaller dose to be injected. Secondly, nanodroplets have increased stability, particularly in circulation *in vivo*[121,122], compared to that of their microscale gas counterparts. Upon exposure to ultrasound, the highly volatile liquid is vaporised into a gas, breaking the shell coating and releasing the contents into its surrounding; a property frequently utilised for drug delivery applications[123–125]. The energy required for this phase transformation however is far higher compared to that of gas core cavitation agents, but still remains a viable option even for sensitive therapeutic delivery applications e.g. DNA, RNA, virus transfection[124].

1.6. Cavitation Enhanced Extravasation of Particles

Molecular delivery of therapeutic drugs can be enhanced by ultrasound, normally by the action of a cavitation agent. This in turn has led to the intentional design of MBs and other cavitation nuclei containing various therapeutic agents (chemotherapeutics[123,126,127,128], antibodies[129], metal complexes[124,130,131]) within them for simultaneous collapse of the cavitation agent and delivery of the therapeutic payload.

The majority of work within the field of ultrasound enhanced delivery focuses on molecular or nanometre sized objects [103,114,132,133](siRNA[124], viruses[119,134] etc.) . Producing extravasation of micro or larger scale particles has not been intensively investigated[135–137]. Moreover, to date MBs are only marketed as contrast agents, and not for enhancing the delivery of therapeutics, with or without ultrasound[61,81,112,138,139].

The inertial collapse of bubbles can produce a range of effects in addition to shock waves, light emission and bubble fragmentation that help to enhance the transport of therapeutic material out of the vasculature into surrounding tissues[54,109,140,141]. These effects are discussed below.

1.6.1.Microjetting

Non-spherical oscillations occur when bubbles are in close proximity with one another or when a single bubble approaches a boundary. The presence of the nearby surface causes a non-symmetrical pressure field around the bubble resulting in non-spherical motion and secondary (Bjerknes) radiation forces that can amplify the effect by drawing the bubble closer to the surface [116,142,143]. If a bubble is oscillating with sufficient amplitude then during its collapse the asymmetry can cause it to adopt a concave disc shape and eventually fully involute so that a jet of liquid pierces its centre[143]. The subsequent impact of this microjet on the proximal surface can be sufficient to erode metal surfaces[144] and theorised to be the possible mechanism for contrecoup damage in traumatic brain injuries (TBI) resulting from high explosive shock waves[145]. It has been demonstrated *in vitro* that this phenomenon can puncture cell membranes, hypothesised to be a mechanism of sonoporation and the cause of the increased uptake of drugs or nanoparticles[146, 126]; experiments *in vivo* however are less definitive due to the relatively soft boundary layers provided by tissues or tissue mimics which vary in architecture and stiffness[147–150]. The microjet impact could permanently damage cells and surrounding tissue which is not currently observed; it is more likely therefore that the non-inertial cavitation phenomena, including microstreaming, temporarily disrupt the cell membrane particularly when the pressure amplitude is low[116].

1.6.2.Microstreaming

As above, absorption of momentum from a propagating acoustic wave can generate a velocity gradient in the surrounding fluid that results in its motion, i.e. streaming[96,116,151,152].

Oscillating MBs can produce streaming on a far smaller scale, termed microstreaming, and hence shear stresses on nearby boundaries. If the boundary is the membrane of a biological cell, the microstreaming may aid in the transport of drugs and nanoparticles through both convection and membrane permeabilisation[74, 153, 151]. If the amplitudes of oscillation are too large however, cellular disruption can occur, resulting in internal haemorrhaging if the cells are endothelial cells lining a blood vessel [154, 155].

1.6.3.Microbubble Tunnelling

Oscillating MBs confined within a small channel or capillary[156] can "tunnel" into the surrounding medium, leaving an approximately cylindrical void in their wake. During the positive pressure phase of each ultrasound cycle, the bubble shrinks dramatically, becoming invisible under high speed light microscopy[157], enabling it to travel through the pores of the adjacent medium, in the direction of the propagating wave. When the MB undergoes expansion, during the negative pressure phase, the bubble remerges at a distance from its origin, producing a tunnel equivalent in diameter to the maximum diameter at peak expansion of the oscillating MBs[157]. Extended tunnels can hence be generated by long ultrasonic pulses as an accumulation of several individual MB tunnelling events. It should be noted that tunnelling is most likely produced by a combination of effects, including direct impingement due to the bubble oscillation, microjetting and ARF. For example, Caskey *et al.* demonstrated that increasing the ultrasound frequency increased the tunnel width. For pulses having equivalent time-averaged acoustic intensity, decreasing the pulse duration increased the pressure amplitude required to disrupt gel mediums[157]. Consideration should be made therefore of MB

concentration, centre frequency, acoustic pressure, and pulse duration when analysing the mechanisms of tunnel formation *in vitro* or *in vivo.*

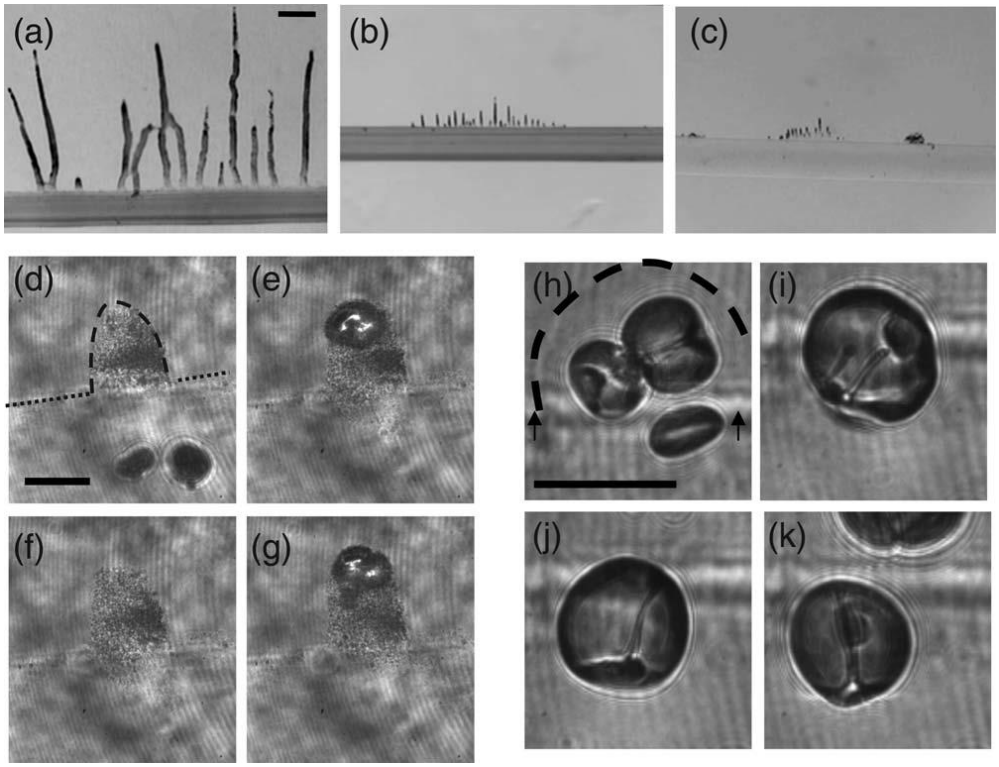


Figure 3: This figure is reproduced from The Journal of the Acoustic Society of America 125, EL183 (2009);https://doi.org/10.1121/1.3097679. Copyright 2009 by AIP Publishing LLC. Fig. 1. Tunnel images and high-speed microscopy157. Optical evidence of tunnel formation using a microbubble concentration of ~2.5 x 107 bubbles/ml and pulse duration of 10 ms. Tunnels created from insonation at (a) 1-MHz, (b) 2.25-MHz, and (c) 5-MHz ultrasonic pulses at matched MI of 1.5. Scale bar indicates 250 µm. Sequential high-speed images (d)–(g)show a microbubble oscillating during a 1-MHz pulse creating a 45µm-diameter tunnel. The frame rate is 10 kHz and the first image is acquired at 0.1 ms after the onset of insonation. Subsequent images were selected to show compressional and rarefactional half-cycles. The microbubble forms in (d) from the fusion of multiple microbubble fragments and then oscillates asymmetrically as it moves through the gel. Scale bar indicates 50 µm. High-speed images (h)-(k) show multi-bubble interactions and fluid jets during the formation of a 50µm tunnel. The frame rate is 10 kHz and the images are selected for clear jet visualization. Scale bar indicates 50 µm'. 0.75% (w/v) OmniPur agarose gel.

1.6.4.Microbubble Cloud Formation

When the concentration of cavitation nuclei and the peak negative pressure is high enough, the formation of MB clouds can be observed (Figures 3-7). These clouds exhibit behaviour similar to that of a bubble having a volume equivalent to the sum of the individual bubble

volumes. They can continue to oscillate for far longer than a single bubble[158], and induce significantly different effects on the surroundings.

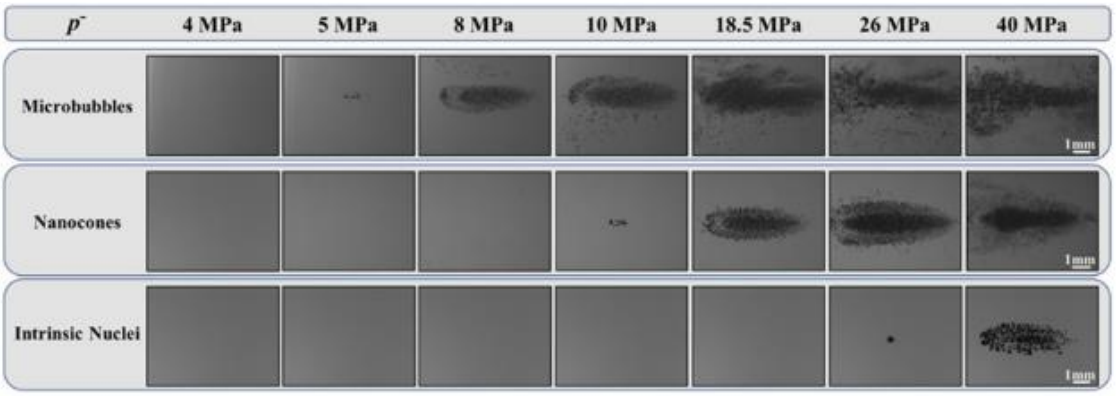


Figure 4: This figure is reproduced from Fig. 5. Bubble Cloud Behavior and Ablation Capacity for Histotripsy Generated from Intrinsic or Artificial Cavitation Nuclei 159 https://doi.org/10.1016/j.ultrasmedbio.2020.10.020. https://creativecommons.org/licenses/by-nc-nd/4.0. Histotripsy bubble cloud images. Optical images of cavitation bubble clouds generated inside agarose phantoms containing microbubbles, nanocones, or intrinsic nuclei captured by a high-speed camera. Ultrasound propagating left to right.. Peak negative Pressure (p-)bubble clouds generated at p- ranging from 0.15 to 45 MPa at a 0.5 Hz PRF inside agarose tissue phantoms containing gas-filled decafluorobutane-microbubbles or fluid-filled perfluorocarbon hexane-nanocones, or control phantoms without artificial nuclei. Ultrasound 0.5 MHz, 0.5 Hz PR. Tissue phantom contains 1% (w/v) agarose.

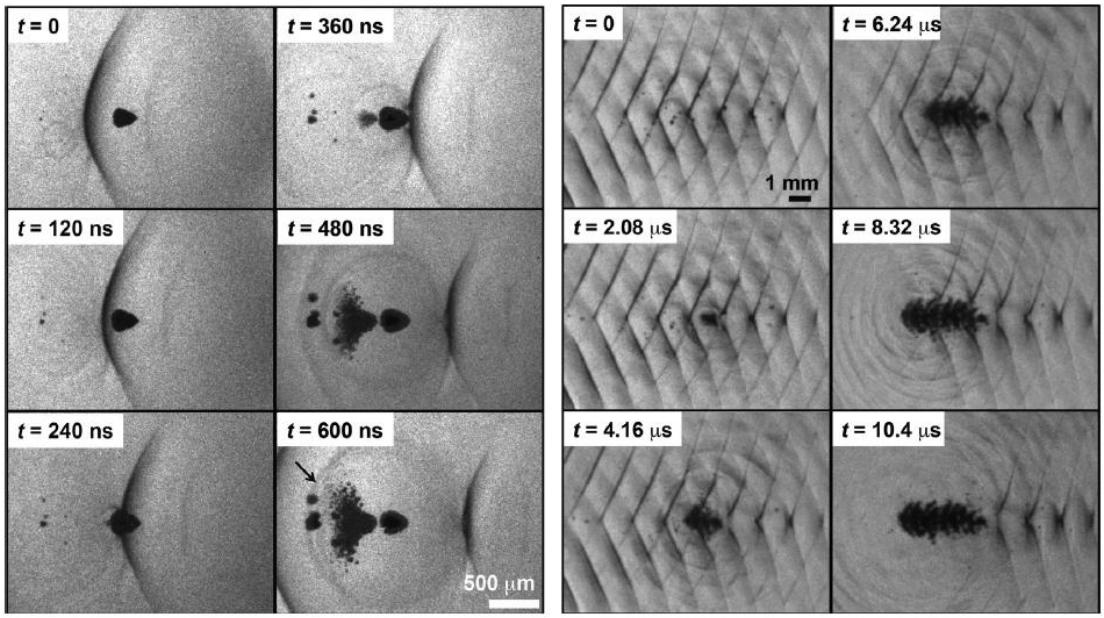


Figure 5: This figure is reproduced from Fig. 7. For Whom the Bubble Grows: Physical Principles of Bubble Nucleation and Dynamics in Histotripsy Ultrasound Therapy77. https://doi.org/10.1016/j.ultrasmedbio.2018.10.035. https://creativecommons.org/licenses/by-nc-nd/4.0/. Left: Initiation of a bubble cloud via shock scattering captured by shadowography. Ultrasound propagation is from left to right. The scattering bubble (dark cone, t = 0 frame) has been distorted because of the asymmetric incident shock wave (dark line). The large size of the scattering bubble

compared with the shock thickness and the flattened surface allow strong scattering of the incident shock wave. Furthermore, the pressure release boundary condition of the bubble/ gel interface inverts the shock. The scattered, inverted wave nucleates cavitation proximal to the bubble. Right: A shadowgraph sequence revealing formation of a bubble cloud over a 15-cycle pulse. The acoustic propagation is from left to right, but cloud growth forms in the opposite direction during passage of the pulse. 0.5 MHz fundamental frequency. 1% Agar tissue phantom.

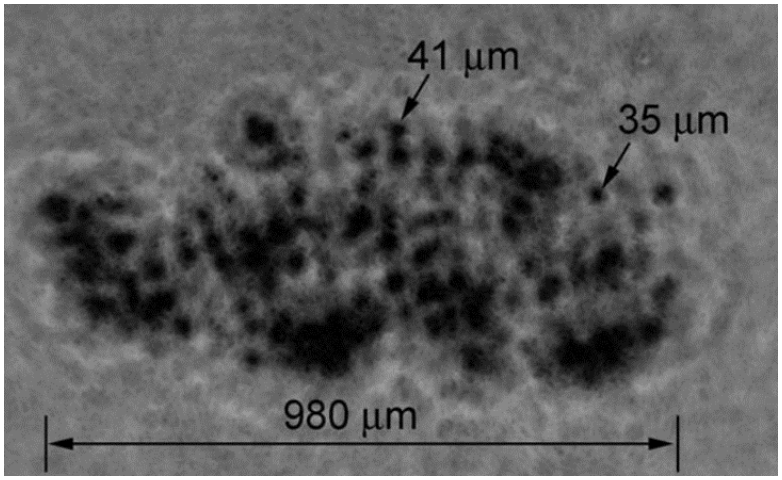


Figure 6: This figure is reproduced from Phys. Rev. Applied 15, 034033. Copyright 2021 by the American Physical Society. https://doi.org/10.1103/PhysRevApplied.15.034033. FIG. 5. Dynamics of cavitation clouds within a high-intensity focused ultrasonic beam160. A close-up view of the inner structure of a bubble cloud; pf = 1.44 MPa. This picture is generated by collapsing a series of reconstructed holograms from different depths onto a single plane.' 500kHz fundamental frequency, 1 million cycles per pulse. Single burst in quiescent water with particles ~10µm in diameter.

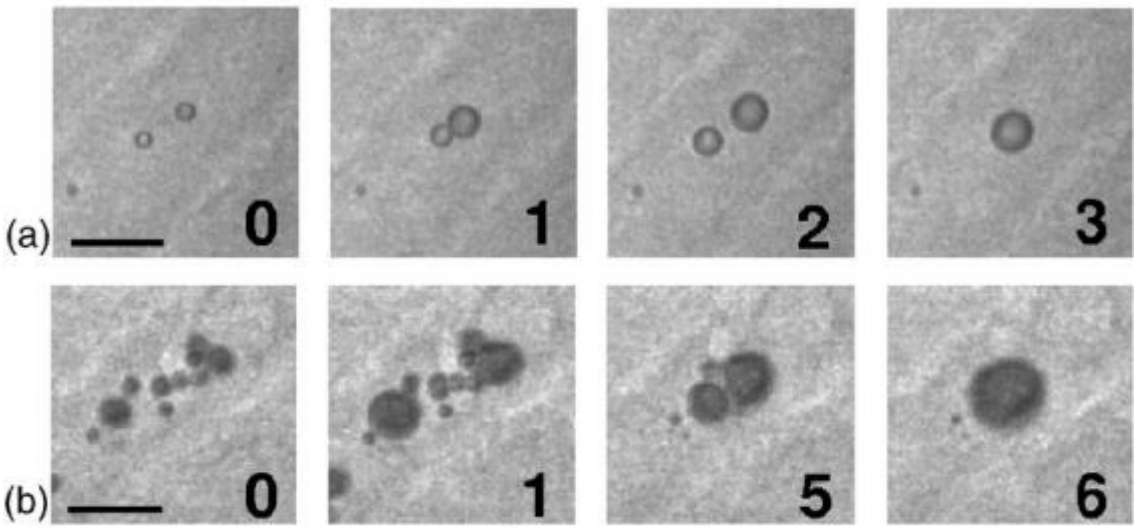


Figure 7:' This figure is reproduced from The Journal of the Acoustic Society of America 122, 1191 (2007); https://doi.org/10.1121/1.2747204. Copyright 2007 by AIP Publishing LLC. FIG. 5. Microbubble fusion. Two sequences of images indexed according to description in Fig. 2 obtained with a transmission center frequency of 1 MHz and peak rarefactional pressure of 0.8 MPa as multiple microbubbles approach and fuse. The vessel diameter in both sequences is approximately 12 µm. Scale bar indicates 10 µm.'. 2 Cycle wave burst. 161

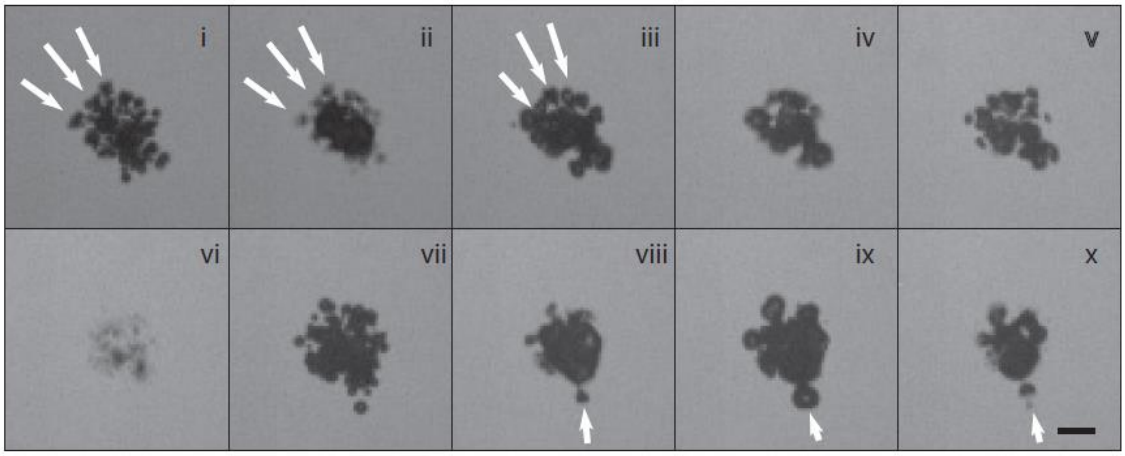


Figure 8: This figure is reproduced from Fig. 5 Bifurcation of ensemble oscillations and acoustic emissions from early stage cavitation clouds in focused ultrasound162. doi:10.1088/1367-2630/15/3/033044.https://creativecommons.org/licenses/by-nc-nd/4.0/. Sequential frames extracted from 80μs after the nucleation event, in HIFU of PNP = 1.29MPa, rich in jetting activity from bubbles peripheral to the cloud (examples arrowed white). Scale bar bottom right: 50μm. Acoustic cavitation is nucleated via a 6–8 ns 532nm laser-pulse. A total of 160 HIFU acoustic cycles are generated, with the laser-pulse incident after 80μs, to allow for transducer 'ring-up' to the required pressure amplitude. High-speed camera operation is triggered to capture a few frames prior to nucleation of cavitation activity, such that cloud development is observed from inception through ~50 HIFU cycles.' Fundamental frequency 0.521 MHz.

1.7. Novelty and Thesis Objectives

SIRT as a technology and as an extension of historical brachytherapy, is currently limited to indications within the liver[44,46,170–172,48,163–169]. Whilst research into other diseases in other organs continues, including the brain[173], colon[46,174] and pancreas[175], to date no individual or group has published any work on improving the delivery of radioactive microscale particles in either animal models or humans. The majority of parallel research in the field is aimed not at improving the efficacy of the therapy itself, but at improving the planning and diagnostic capabilities[45,47,176]. Investigations into the immune-stimulatory potential of SIRT[177–180] compared to EBRT are also underway but with limited results having been published to date. The propulsion of nanometre sized objects using ultrasound with or without cavitation[119,128,133,141] is well established and has been achieved in various models. With the exception of blood clot dissolution[118,181], no attempts have been made to extravasate micrometre-sized particles with or without radioactive isotopes.

GBM remains an unsolved challenging indication because of the lack of access to the central tumour and the cellular infiltration beyond it. Defining the extent of the disease infiltration by existing diagnostic methods (MRI, CT) does not provide sufficient information to improve existing external beam radiotherapies, whilst existing chemotherapeutic agents have proven insufficient for extending patient overall survival. Localised therapies continuously fail because of the extent of the 'invisible disease', the cellular infiltration of the cancerous cells beyond the central tumour mass, frequently referred to as GBM 'tendrils'. Whilst less precise than gamma knife surgery, it is hoped that using high activity radioactive microspheres to irradiate the margins surrounding the tumour mass will be selective towards the cancerous cells, reducing the collateral damage to the surrounding healthy tissue. As in the case of resection, the use of high-dose stereotactic radiotherapy is not used in the pursuit of a cure for the disease but focussed on improving the palliative care and quality of life for those who are already undergoing resection surgery. Improving upon the current standard of care for the disease and hopefully the dire 2-year survival statistic.

In order to improve the current standard of care for GBM patients eligible for resection, TheraSphere® is proposed as a hypothetical solution for the stereotactic radiotherapy of the surrounding tumour margins, during current resection procedures. To be successful, the biocompatible glass microspheres must be deposited and then propelled into the surrounding soft tissue of the resection cavity. This propulsion is intended to be achieved by intraoperative ultrasound induced inertial cavitation (Figure 9).

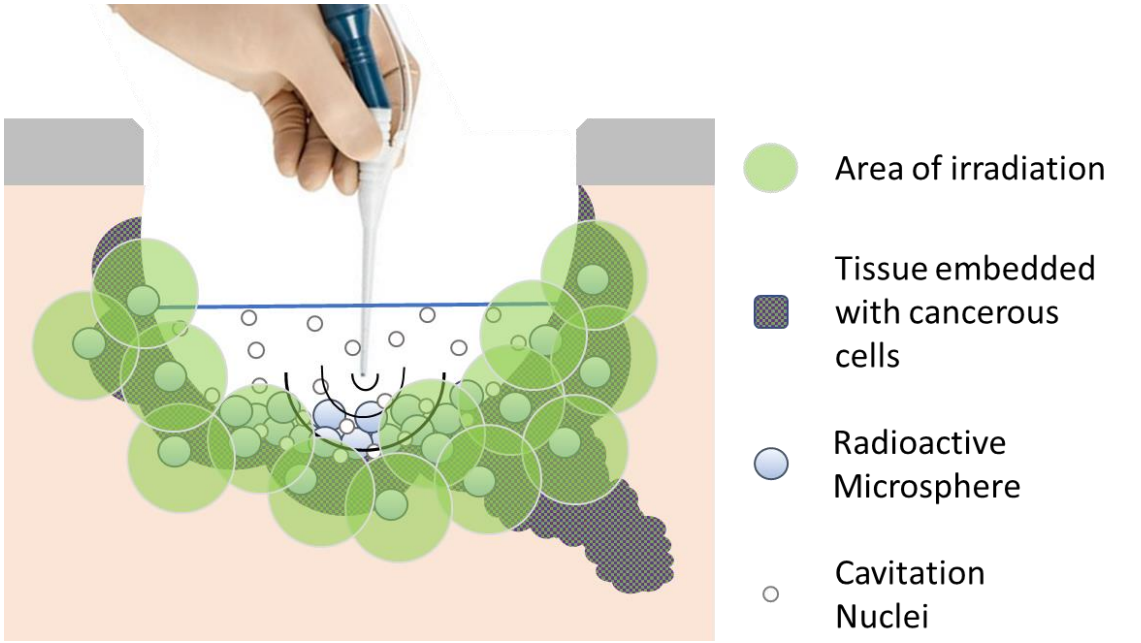


Figure 9: Diagram of envisioned adjuvant therapy. Radioactive microspheres are distributed within the tissue margins of the resection cavity. Image is not to scale. Margins may be up to a further 30-40mm outside of the central mass. Sonopet aspiration device image courtesy of Stryker®.

After removal of the central tumour mass, a slurry of radioactive microspheres and cavitation nuclei will be deposited in the resection cavity. An ultrasonic device, commercially available or specifically designed for this application, is then to be placed within the resection cavity. The acoustic field emitted from the device will cause the exogenous nuclei to cavitate and distribute the surrounding microspheres into the tissue margins. The distributions of the microspheres will need to be examined, quantified and modelled to isolate the ultrasound exposure parameters required. The field of radiation is to be estimated from the mean tissue penetration data of the radioactive microspheres.

Whilst there are other modalities (gels, resins, crystals) that could be used instead of the radioactive microspheres, the relative radioactivity and therefore therapeutic treatment, is directly proportional to the mass of the radioactive element. In order to deliver a high therapeutic dose, as seen with TheraSphere™, a high mass content is required. Using resin spheres, gels or specifically designed radioactive cavitation agents (utilising a porphyrin ring to encapsulate the radioactive metal) will ultimately produce a low therapeutic dose, undesirable

for this application. However, tailoring the size and distribution of the microspheres to the proposed procedure, is a foreseeable optimisation for translation of the technology. It could be argued that the optimal distribution of microspheres would have a separation distance equal to the or slightly less than the mean depth of beta irradiation from the TheraSphere™ microspheres (2.5mm). However, this assumption is based upon the microspheres being deposited in a ballistic fashion, which may not occur using cavitation activity as the mechanism for the microsphere extravasation. Further work is required to define what constitutes the optimum distribution of microspheres, particularly as the intended cellular target is 'invisible'.

Producing micro-channels using cavitation tunnelling phenomena, whilst destructive, removes significantly less tissue than extending the physical or mechanical extent of resection (EoR) during the surgery. The anticipated microsphere channels produced are necessary collateral damage, to enable the delivery of the more-selective radiotherapeutic. The volume of tissue irradiated by the microspheres is expected to be orders of magnitude larger than that of any additional tissue removed during the process of embedding the radioactive microspheres.

Inertial cavitation activity and associated phenomena have been demonstrated eroding hydrogel tissue phantoms several times stiffer than that of human brain parenchyma. Producing extravasation of various therapeutic agents, within a large ultrasound parameter space. The literature therefore suggests that cavitation should be a feasible mechanism to facilitate the transport of radioactive glass microspheres, such as those used in TheraSphere™ , towards the intra-operative adjuvant treatment of glioblastoma resection margins.

The aims of the thesis are therefore:

- To investigate the feasibility of producing microsphere extravasation in tissue mimicking material using ultrasound induced cavitation.
- To develop methods for imaging and quantifying the resulting distribution of microspheres in tissue/tissue phantoms.

- To identify the ultrasound exposure parameters critical to producing microsphere extravasation.
- To investigate the mechanisms responsible for the mass transport of microspheres.
- To evaluate whether ultrasound enhanced internal radiation therapy via the extravasation of radioactive glass microspheres is a plausible treatment modality for glioblastoma multiforme.

References

1. Helmberger, T. Overview of selective internal radiation therapy: From work-up to follow-up. Eur. J. Cancer, Suppl. 10, 48–50 (2012).

2. Pasciak, A. S. et al. The number of microspheres in Y90 radioembolization directly affects normal tissue radiation exposure. Eur. J. Nucl. Med. Mol. Imaging 47, 816–827 (2020).

3. Ostrom, Q. T. et al. CBTRUS statistical report: Primary brain and other central nervous system tumors diagnosed in the United States in 2009-2013. Neuro. Oncol. 18, v1–v75 (2016).

4. Gulati, S., Jakola, A. S., Johannesen, T. B. & Solheim, O. Survival and treatment patterns of glioblastoma in the elderly: A population-based study. World Neurosurg. 78, 518–526 (2012).

5. Woehrer, A., Bauchet, L. & Barnholtz-Sloan, J. S. Glioblastoma survival: Has it improved? Evidence from population-based studies. Curr. Opin. Neurol. 27, 666–674 (2014).

6. Weller, M., Cloughesy, T., Perry, J. R. & Wick, W. Standards of care for treatment of recurrent glioblastoma-are we there yet? Neuro. Oncol. 15, 4–27 (2013).

7. Gallego, O. Nonsurgical treatment of recurrent glioblastoma. Curr. Oncol. 22, e273–e281 (2015).

8. Hvizdos, K. M. & Goa, K. L. Temozolomide. 12, 237–243 (1999).

9. Kou, Y., Koag, M. C. & Lee, S. N7 Methylation Alters Hydrogen-Bonding Patterns of Guanine in Duplex DNA. J. Am. Chem. Soc. 137, 14067–14070 (2015).

10. Mao, X. & Shuman, S. Vaccinia virus mRNA (guanine-7-)methyltransferase: Mutational effects on cap methylation and AdoHcy-dependent photo-cross-linking of the cap to the methyl acceptor site. Biochemistry 35, 6900–6910 (1996).

11. Villani, G. Effect of Methylation on the Properties of the H-Bridges in DNA. A Systematic Theoretical Study on the Couples of Base Pairs. J. Phys. Chem. B 119, 7931–7943 (2015).

12. Trifiletti, D. M. et al. Leukoencephalopathy after stereotactic radiosurgery for brain metastases. Int. J. Radiat. Oncol. Biol. Phys. 93, 870–878 (2015).

13. Koncar, R. F. et al. PLK1 inhibition enhances temozolomide efficacy in IDH1 mutant gliomas. Oncotarget 8, 15827–15837 (2017).

14. Thanasupawat, T. et al. Dovitinib enhances temozolomide efficacy in glioblastoma cells. Mol. Oncol. 11, 1078–1098 (2017).

15. Hicks, J. et al. Intratumoral temozolomide in spontaneous canine gliomas: feasibility of a novel therapy using implanted microcylinders. Vet. Med. Sci. 5, 5–18 (2019).

16. Erwin G. Van Meir, PhD, Costas G. Hadjipanayis, MD, PhD, Andrew D. Norden, MD, MPH, Hui-Kuo Shu, MD, Patrick Y. Wen, MD, and Jeffrey J. Olson, M. Exciting New Advances in Neuro-Oncology: The Avenue to a Cure for Malignant Glioma. CA Cancer J Clin. 60, 166–193 (2010).

17. Larson, D. A. et al. Phase II study of high central dose Gamma Knife radiosurgery and marimastat in patients with recurrent malignant glioma. Int. J. Radiat. Oncol. Biol. Phys. 54, 1397–404 (2002).

18. Chaichana, K. L. et al. Risk of surgical site infection in 401 consecutive patients with glioblastoma with and without carmustine wafer implantation. Neurol. Res. 37, 717–726 (2015).

19. Goerig, N. et al. Klinisch relevante CMV-(Re-)Aktivierung während bzw. nach Bestrahlung/Chemotherapie des Gehirns: Korrelation mit neurologischer Verschlechterung und Besserung unter antiviraler Therapie. Strahlentherapie und Onkol. 192, 489–497 (2016).

20. Ene, C. et al. Safety and efficacy of carmustine (BCNU) wafers for metastatic brain tumors. Surg. Neurol. Int. 7, S295–S299 (2016).

21. Hsieh, J. et al. Tumor progression in patients receiving adjuvant whole-brain radiotherapy vs localized radiotherapy after surgical resection of brain metastases. Neurosurgery 76, 411–420 (2015).

22. LAURA M. KULIK, BASSEL ATASSI, LODEWIJK VAN HOLSBEECK, TAMEEM SOUMAN, ROBERT J. LEWANDOWSKI, MARY F. MULCAHY, RUSSELL D. HUNTER, ALBERT A. NEMCEK JR., MICHAEL M. ABECASSIS, KENNETH G. HAINES III, R. S. Yttrium-90 Microspheres (TheraSphere1) Treatment of Unresectable Hepatocellular Carcinoma: Downstaging to Resection, RFA and Bridge to Transplantation. J. Surg. Oncol. 94, 572–586 (2006).

23. Patel, D. M., Agarwal, N., Tomei, K. L., Hansberry, D. R. & Goldstein, I. M. Optimal Timing of Whole-Brain Radiation Therapy Following Craniotomy for Cerebral Malignancies. World Neurosurg. 84, 412–419 (2015).

24. Tian, Z. M. Stereotactic intracavitary irradiation of huge cystic craniopharyngiomas. Zhonghua Wai Ke Za Zhi 30, 102-103,125 (1992).

25. Idbaih, A. et al. Safety and feasibility of repeated and transient blood-brain barrier disruption by pulsed ultrasound in patients with recurrent glioblastoma. Clin. Cancer Res. 25, 3793–3801 (2019).

26. Nikfarjam, M., Muralidharan, V., Malcontenti-Wilson, C. & Christophi, C. Scanning electron microscopy study of the blood supply of human colorectal liver metastases. Eur. J. Surg. Oncol. 29, 856–861 (2003).

27. Kickingereder, P. et al. Low-dose rate stereotactic iodine-125 brachytherapy for the treatment of inoperable primary and recurrent glioblastoma: single-center experience with 201 cases. J. Neurooncol. 120, 615–623 (2014).

28. Hadi, I. et al. Radiation necrosis after a combination of external beam radiotherapy and iodine-125 brachytherapy in gliomas. Radiat. Oncol. 16, 1–9 (2021).

29. Parplys, A. C., Petermann, E., Petersen, C., Dikomey, E. & Borgmann, K. DNA damage by X-rays and their impact on replication processes. Radiother. Oncol. 102, 466–471 (2012).

30. Lomax, M. E., Folkes, L. K. & O'Neill, P. Biological consequences of radiation-induced DNA damage: Relevance to radiotherapy. Clin. Oncol. 25, 578–585 (2013).

31. Harper, J. V., Anderson, J. A. & O'Neill, P. Radiation induced DNA DSBs: Contribution from stalled replication forks? DNA Repair (Amst). 9, 907–913 (2010).

32. Thompson, L. H. Recognition, signaling, and repair of DNA double-strand breaks produced by ionizing radiation in mammalian cells: The molecular choreography. Mutat. Res. - Rev. Mutat. Res. 751, 158–246 (2012).

33. Caine, M. et al. Impact of Yttrium-90 Microsphere Density, Flow Dynamics, and Administration Technique on Spatial Distribution: Analysis Using an In Vitro Model. J. Vasc. Interv. Radiol. 28, 260-268.e2 (2017).

34. Gomaa, A. I., Khan, S. A., Toledano, M. B., Waked, I. & Taylor-Robinson, S. D. Hepatocellular carcinoma: Epidemiology, risk factors and pathogenesis. World J. Gastroenterol. 14, 4300–4308 (2008).

35. Eisenhauer, E. A. et al. New response evaluation criteria in solid tumours: Revised RECIST guideline (version 1.1). Eur. J. Cancer 45, 228–247 (2009).

36. Eisenbrey, J. R. et al. Sensitization of Hypoxic Tumors to Radiation Therapy Using Ultrasound-Sensitive Oxygen Microbubbles. Int. J. Radiat. Oncol. Biol. Phys. 101, 88–96 (2018).

37. Savage, A. E. O. United States Patent 5011677. vol. 19 (1985).

38. Hawkins, C. M., Kukreja, K., Geller, J. I., Schatzman, C. & Ristagno, R. Radioembolisation for treatment of pediatric hepatocellular carcinoma. Pediatr. Radiol. 43, 876–881 (2013).

39. Pei, X. Q. et al. Contrast-enhanced ultrasonography of hepatocellular carcinoma: Correlation between quantitative parameters and histological grading. Br. J. Radiol. 85, (2012).

40. Rossi, P. et al. X-rays Compton detectors for Biomedical application. AIP Conf. Proc. 1336, 356–360 (2011).

41. Mazaki, H., Nagatomo, T. & Shimizu, S. Effect of pressure on the decay constant of Tc99m. Phys. Rev. C 5, 1718–1724 (1972).

42. Abeles, R. D. et al. Multiple organ dysfunction syndrome (MODS), rather than the need for renal replacement therapy per se, dictates poor prognosis in patients with cirrhosis admitted to ICU. J Hepatol 56, S263–S264 (2012).

43. Kennedy, A. S., Nutting, C., Coldwell, D., Gaiser, J. & Drachenberg, C. Pathologic response and microdosimetry of 90Y microspheres in man: Review of four explanted whole livers. Int. J. Radiat. Oncol. 60, 1552–1563 (2004).

44. Sofocleous, C. T. et al. Phase i trial of selective internal radiation therapy for chemorefractory colorectal cancer liver metastases progressing after hepatic arterial pump and systemic chemotherapy. Clin. Colorectal Cancer 13, 27–36 (2014).

45. Gordon, A. C. Tuning Your RADIOembolization : Imaging-guidance of Yttrium-90 Radioembolization. (Evanson, Illinois, 2016).

46. Nezami, N. et al. Y90 radioembolization dosimetry using a simple semi-quantitative method in intrahepatic cholangiocarcinoma: Glass versus resin microspheres. Nucl. Med. Biol. 59, 22–28 (2018).

47. Attarwala, A. A. et al. Quantitative and qualitative assessment of yttrium-90 pet/ct imaging. J. Am. Ceram. Soc. 61, 247–249 (1978).

48. Wang, L. M., Jani, A. R., Hill, E. J. & Sharma, R. A. Anatomical basis and histopathological changes resulting from selective internal radiotherapy for liver metastases. J. Clin. Pathol. 66, 205–211 (2013).

49. Pellerin, O., Lin, M., Bhagat, N., Shao, W. & Geschwind, J.-F. Can C-Arm Cone-Beam CT Detect a Micro-Embolic Effect After TheraSphere Radioembolization of Neuroendocrine and Carcinoid Liver Metastasis? Cancer Biother. Radiopharm. 28, 459–465 (2013).

50. Vouche, M. et al. Unresectable solitary hepatocellular carcinoma not amenable to radiofrequency ablation: Multicenter radiology-pathology correlation and survival of radiation segmentectomy. Hepatology 60, 192–201 (2014).

51. Refaat, R. & Hassan, M. S. The relationship between the percentage of lung shunting on Tc-99m macroaggregated albumin (Tc-99m MAA) scan and the grade of hepatocellular carcinoma vascularity. Egypt. J. Radiol. Nucl. Med. 45, 333–342 (2014).

52. Dai, S. K., Wu, Y. C., Jan, Y. J. & Lin, S. C. The histological grading of HCC using fusion images. 2009 IEEE Int. Conf. Comput. Intell. Meas. Syst. Appl. CIMSA 2009 1, 186–189 (2009).

53. McKeown, S. R. Defining normoxia, physoxia and hypoxia in tumours—implications for treatment response. Br. J. Radiol. 87, 20130676 (2014).

54. Kwan, J. J. et al. Ultrasound-Propelled Nanocups for Drug Delivery. Small 11, 5305–5314 (2015).

55. William D. Callister, J. with special contributions by D. G. R. Materials science and engineering: an introduction. (New York: John Wiley & Sons, 2007).

56. Wells, P. N. T. & Liang, H. Medical Ultrasound - imaging of soft tissue strain and elasticity. J. R. Soc. Interface 8, 1521–1549 (2011).

57. Hoogenboom, M. et al. Mechanical High-Intensity Focused Ultrasound Destruction of Soft Tissue: Working Mechanisms and Physiologic Effects. Ultrasound Med. Biol. 41, 1500–1517 (2015).

58. Hsiao, Y. S., Kumon, R. E. & Deng, C. X. Characterization of lesion formation and bubble activities during high-intensity focused ultrasound ablation using temperature-derived parameters. Infrared Phys. Technol. 60, 108–117 (2013).

59. Dewhirst, M. W., Viglianti, B. L., Lora-Michiels, M., Hanson, M. & Hoopes, P. J. Basic principles of thermal dosimetry and thermal thresholds for tissue damage from hyperthermia. Int. J. Hyperthermia 19, 267–94 (2003).

60. Dewey, W. C., Hopwood, L. E., Sapareto, S. A. & Gerweck, L. E. Cellular responses to combinations of hyperthermia and radiation. Radiology 123, 463–74 (1977).

61. Moyer, L. C. et al. High-intensity focused ultrasound ablation enhancement in vivo via phase-shift nanodroplets compared to microbubbles. J. Ther. Ultrasound 3, 1–9 (2015).

62. Yarmolenko, P. S. et al. Thresholds for thermal damage to normal tissues: An update. Int. J. Hyperth. 27,

320–343 (2011).

63. Canney, M. S., Khokhlova, V. A., Bessonova, O. V., Bailey, M. R. & Crum, L. A. Shock-Induced Heating and Millisecond Boiling in Gels and Tissue Due to High Intensity Focused Ultrasound. Ultrasound Med. Biol. 36, 250–267 (2010).

64. Parsons, J. E., Cain, C. A., Abrams, G. D. & Fowlkes, J. B. Pulsed cavitational ultrasound therapy for controlled tissue homogenization. Ultrasound Med. Biol. 32, 115–129 (2006).

65. Engle, K. M.; Mei, T-S.; Wasa, M.; Yu, J.-Q. Development and Translation of Histotripsy: Current Status and Future Directions. Curr Opin Urol. 24, 104–110 (2014).

66. Roos, S. T. et al. Unexpected High Incidence of Coronary Vasoconstriction in the Reduction of Microvascular Injury Using Sonolysis (ROMIUS) Trial. Ultrasound Med. Biol. 42, 1919–1928 (2016).

67. Sheng, Y. et al. Magnetically responsive microbubbles as delivery vehicles for targeted sonodynamic and antimetabolite therapy of pancreatic cancer. J. Control. Release 262, 192–200 (2017).

68. Lake, A. M. et al. Histotripsy: Minimally Invasive Technology for Prostatic Tissue Ablation in an In vivo Canine Model. Urology 72, 682–686 (2008).

69. Shi, J., Zhang, X., Chen, R. & Zhang, G. Acoustic radiation force of a solid elastic sphere immersed in a cylindrical cavity filled with ideal fluid. Wave Motion 80, 37–46 (2018).

70. Sadeghi, S., Lin, C. Y. & Cortes, D. H. Narrowband Shear Wave Generation Using Sinusoidally-Modulated Acoustic Radiation Force. IEEE Trans. Ultrason. Ferroelectr. Freq. Control 66, 264–272 (2018).

71. Dadakova, T., Krafft, A. J., Özen, A. C. & Bock, M. Optimization of acoustic radiation force imaging: Influence of timing parameters on sensitivity. Magn. Reson. Med. 79, 981–986 (2018).

72. Leighton, T. G., Walton, A. J. & Pickworth, M. J. W. Primary Bjerknes forces. Eur. J. Phys. 11, 47–50 (1990).

73. Marin, A. et al. Three-Dimensional Phenomena in Microbubble Acoustic Streaming. Phys. Rev. Appl. 3, 1–5 (2015).

74. El Ghamrawy, A. et al. Acoustic Streaming in a Soft Porous Material. Ultrasound Med. Biol. 00, 1–10 (2018).

75. Khelif, A., Vasseur, J. O., Lambin, P., Djafari-Rouhani, B. & Deymier, P. A. Theory of acoustic scattering by supported ridges at a solid-liquid interface. Phys. Rev. E - Stat. Physics, Plasmas, Fluids, Relat. Interdiscip. Top. 65, 1–7 (2002).

76. Nyborg, W. L. M. Acoustic Streaming. Physical Acoustics vol. 2 (ACADEMIC PRESS INC., 1965).

77. Bader, K. B., Vlaisavljevich, E. & Maxwell, A. D. For Whom the Bubble Grows: Physical Principles of Bubble Nucleation and Dynamics in Histotripsy Ultrasound Therapy. Ultrasound Med. Biol. 45, 1056–1080 (2019).

78. Borkent, B. M., Gekle, S., Prosperetti, A. & Lohse, D. Nucleation threshold and deactivation mechanisms of nanoscopic cavitation nuclei. Phys. Fluids 21, (2009).

79. Atchley, A. A. & Prosperetti, A. The crevice model of bubble nucleation. J. Acoust. Soc. Am. 86, 1065–1084 (1989).

80. Jones, S. F., Evans, G. M. & Galvin, K. P. Bubble nucleation from gas cavities - A review. Adv. Colloid Interface Sci. 80, 27–50 (1999).

81. Versluis, M. Nonlinear behavior of ultrasound contrast agent microbubbles and why shell buckling matters. Proc. 20th Int. Congr. Acoust. 1–6 (2010).

82. Samarasinghe, S. Increasing the nonlinear character of microbubble oscillations at low acoustic pressures. 807–811 (2008) doi:10.1098/rsif.2008.0005.

83. Paul, S. et al. Material characterization of the encapsulation of an ultrasound contrast microbubble and its subharmonic response: Strain-softening interfacial elasticity model. J. Acoust. Soc. Am. 127, 3846–3857 (2010).

84. Abou-Saleh, R. H. et al. The influence of intercalating perfluorohexane into lipid shells on nano and microbubble stability. Soft Matter 12, 7223–7230 (2016).

85. Kwan, J. J. et al. Ultrahigh-Speed Dynamics of Micrometer-Scale Inertial Cavitation from Nanoparticles.

Phys. Rev. Appl. 6, 1–8 (2016).

86. Leighton, T. G. The Forced Bubble. Acoust. Bubble 287–438 (1994) doi:10.1016/b978-0-12-441920-9.50009-2.

87. Leighton, T. G. Cavitation Inception and Fluid Dynamics. Acoust. Bubble 67–128 (1994) doi:10.1016/b978-0-12-441920-9.50007-9.

88. Meng, Y. et al. Safety and efficacy of focused ultrasound induced blood-brain barrier opening, an integrative review of animal and human studies. J. Control. Release 309, 25–36 (2019).

89. Scott, D. J. et al. Development of an In vivo Tumor-Mimic Model for Learning Radiofrequency Ablation. J. Gastrointest. Surg. 4, 620–625 (2000).

90. MAuri, G. A. et al. Focused ultrasound: tumour ablation and its potential to enhance immunological therapy to cancer. Br. J. Radiol. 91, (2018).

91. Cha, G. D. et al. Advances in drug delivery technology for the treatment of glioblastoma multiforme. J. Control. Release 328, 350–367 (2020).

92. Tran, B. C. et al. Microbubble-Enhanced Cavitation for Noninvasive Ultrasound Surgery. IEEE Trans. Ultrason. Ferroelectr. Freq. Control 50, 1296–1304 (2003).

93. Eisenbrey, J. R. et al. Development of an ultrasound sensitive oxygen carrier for oxygen delivery to hypoxic tissue. Int. J. Pharm. 478, 361–367 (2015).

94. Song, J. H., Moldovan, A. & Prentice, P. Non-linear Acoustic Emissions from Therapeutically Driven Contrast Agent Microbubbles. Ultrasound Med. Biol. (2019) doi:10.1016/j.ultrasmedbio.2019.04.005.

95. Gu, Y. et al. Harmonic responses and cavitation activity of encapsulated microbubbles coupled with magnetic nanoparticles. Ultrason. Sonochem. 29, 309–316 (2016).

96. Mannaris, C. et al. Microbubbles, Nanodroplets and Gas-Stabilizing Solid Particles for Ultrasound-Mediated Extravasation of Unencapsulated Drugs: An Exposure Parameter Optimization Study. Ultrasound Med. Biol. 00, 1–14 (2019).

97. Kwan, J. J. et al. Ultrasound-induced inertial cavitation from gas-stabilizing nanoparticles. Phys. Rev. E - Stat. Nonlinear, Soft Matter Phys. 92, 1–5 (2015).

98. Borrelli, M. J. et al. Production of uniformly sized serum albumin and dextrose microbubbles. Ultrason. Sonochem. 19, 198–208 (2012).

99. Bailey, M. R. et al. Cavitation detection during shock-wave lithotripsy. Ultrasound Med. Biol. 31, 1245–1256 (2005).

100. Kyriakou, Z., Corral-Baques, M. I., Amat, A. & Coussios, C. C. HIFU-Induced Cavitation and Heating in Ex Vivo Porcine Subcutaneous Fat. Ultrasound Med. Biol. 37, 568–579 (2011).

101. Xu, Q., Holland, C. K. & Apfel, R. E. Measurement of cavitation thresholds for human blood. J. Acoust. Soc. Am. 91, 2432–2432 (1992).

102. Brujan, E. A. The role of cavitation microjets in the therapeutic applications of ultrasound. Ultrasound Med. Biol. 30, 381–387 (2004).

103. T. G. LEIGHTON. The Acoustic Bubble. J. Fluid Mech. 272, 407–409 (1994).

104. Loglio, G., Pandolfini, P., Liggieri, L., Makievski, A. & Ravera, F. Determination of Interfacial Properties by the Pendant Drop Tensiometry: Optimisation of Experimental and Calculation Procedure. Bubble Drop Interfaces 7 (2011).

105. Swanson, E. J., Mohan, V., Kheir, J. & Borden, M. A. Phospholipid-stabilized microbubble foam for injectable oxygen delivery. Langmuir 26, 15726–15729 (2010).

106. Needham, D. & Kim, D. H. PEG-covered lipid surfaces: Bilayers and monolayers. Colloids Surfaces B Biointerfaces 18, 183–195 (2000).

107. Kwan, J. J. & Borden, M. A. Lipid monolayer collapse and microbubble stability. Adv. Colloid Interface Sci. 183–184, 82–99 (2012).

108. van Rooij, T. et al. Non-linear Response and Viscoelastic Properties of Lipid-Coated Microbubbles: DSPC versus DPPC. Ultrasound Med. Biol. 41, 1432–1445 (2015).

109. Nittayacharn, P. et al. Enhancing Tumor Drug Distribution With Ultrasound-Triggered Nanobubbles. J. Pharm. Sci. (2019) doi:10.1016/j.xphs.2019.05.004.

110. Garg, S., Thomas, A. A. & Borden, M. A. The effect of lipid monolayer in-plane rigidity on invivo microbubble circulation persistence. Biomaterials 34, 6862–6870 (2013).

111. Sheng, Y. et al. Magnetically responsive microbubbles as delivery vehicles for targeted sonodynamic and antimetabolite therapy of pancreatic cancer. J. Control. Release 262, 192–200 (2017).

112. Guo, X., Li, Q., Zhang, Z., Zhang, D. & Tu, J. Investigation on the inertial cavitation threshold and shell properties of commercialized ultrasound contrast agent microbubbles. J. Acoust. Soc. Am. 134, 1622–1631 (2013).

113. Owen, J. et al. Understanding the Structure and Mechanism of Formation of a New Magnetic Microbubble Formulation. Theranostics 2, 1127–1139 (2012).

114. Mulvana, H., Stride, E., Tang, M. X., Hajnal, J. V. & Eckersley, R. J. The Influence of Gas Saturation on Microbubble Stability. Ultrasound Med. Biol. 38, 1097–1100 (2012).

115. Kratskin, I. L., Yu, X. & Doty, R. L. "Stable" Inertial Cavitation Charles. Ultrasound Med. Biol. 44, 199–203 (1997).

116. Wu, J. & Nyborg, W. L. Ultrasound, cavitation bubbles and their interaction with cells. Adv. Drug Deliv. Rev. 60, 1103–1116 (2008).

117. Bian, S., Seth, A., Daly, D., Carlisle, R. & Stride, E. A multimodal instrument for real-time in situ study of ultrasound and cavitation mediated drug delivery. Rev. Sci. Instrum. 88, (2017).

118. Prokop, A. F., Soltani, A. & Roy, R. A. Cavitational Mechanisms in Ultrasound-Accelerated Fibrinolysis. Ultrasound Med. Biol. 33, 924–933 (2007).

119. Bazan-Peregrino, M. et al. Cavitation-enhanced delivery of a replicating oncolytic adenovirus to tumors using focused ultrasound. J. Control. Release 169, 40–47 (2013).

120. Lv, H. et al. Facile Fabrication of Monodisperse Polymer Hollow Spheres. Langmuir 24, 13736–13741 (2008).

121. Vlaisavljevich, E., Durmaz, Y. Y., Maxwell, A., ElSayed, M. & Xu, Z. Nanodroplet-mediated histotripsy for image-guided targeted ultrasound cell ablation. Theranostics 3, 851–864 (2013).

122. Hannah, A. S., Luke, G. P. & Emelianov, S. Y. Blinking phase-change nanocapsules enable background-free ultrasound imaging. Theranostics 6, 1866–1876 (2016).

123. Lee, J. Y. et al. Nanoparticle-Loaded Protein-Polymer Nanodroplets for Improved Stability and Conversion Efficiency in Ultrasound Imaging and Drug Delivery. Adv. Mater. 27, 5484–5492 (2015).

124. Lee, J. Y. et al. Ultrasound-Enhanced siRNA Delivery Using Magnetic Nanoparticle-Loaded Chitosan-Deoxycholic Acid Nanodroplets. Adv. Healthc. Mater. 6, (2017).

125. Kasoji, S. K. et al. Cavitation enhancing nanodroplets mediate efficient DNA fragmentation in a bench top ultrasonic water bath. PLoS One 10, (2015).

126. Lee, J. Y. et al. Nanoparticle-Loaded Protein-Polymer Nanodroplets for Improved Stability and Conversion Efficiency in Ultrasound Imaging and Drug Delivery. Adv. Mater. 27, 5484–5492 (2015).

127. Paris, J. L. et al. Ultrasound-mediated cavitation-enhanced extravasation of mesoporous silica nanoparticles for controlled-release drug delivery. Chem. Eng. J. 340, 2–8 (2018).

128. Kaur, S., Prasad, C., Balakrishnan, B. & Banerjee, R. Trigger responsive polymeric nanocarriers for cancer therapy. Biomater. Sci. 3, 955–987 (2015).

129. Mo, S. et al. Increasing the density of nanomedicines improves their ultrasound-mediated delivery to tumours. J. Control. Release 210, (2015).

130. McLaughlan, J. R., Cowell, D. M. J. & Freear, S. Gold nanoparticle nucleated cavitation for enhanced high intensity focused ultrasound therapy. Phys. Med. Biol. 63, (2018).

131. Yoon, Y. Il, Pang, X., Jung, S., Zhang, G. & Kong, M. Smart gold nanoparticle-stabilized ultrasound microbubbles as cancer theranostics. 3235–3239 (2018) doi:10.1039/c8tb00368h.

132. Crum, L. A. Acoustic Cavitation Series: Part Five Rectified diffusion. Ultrasonics 22, 215–223 (1984).

133. Choi, J. J. & Coussios, C.-C. Spatiotemporal evolution of cavitation dynamics exhibited by flowing microbubbles during ultrasound exposure. J. Acoust. Soc. Am. 132, 3538–3549 (2012).

134. Myers, R. et al. Polymeric cups for cavitation-mediated delivery of oncolytic vaccinia virus. Mol. Ther. 24, (2016).

135. Park, K. Targeted delivery nano/micro particles to inflamed intestinal mucosa in human. J. Control. Release 165, 162 (2013).

136. Meng, J., Mei, D., Jia, K., Fan, Z. & Yang, K. Contactless and non-invasive delivery of micro-particles lying on a non-customized rigid surface by using acoustic radiation force. Ultrasonics 54, 1350–1357 (2014).

137. Yu, F. et al. Enteric-coated capsules filled with mono-disperse micro-particles containing PLGA-lipid-PEG nanoparticles for oral delivery of insulin. Int. J. Pharm. 484, 181–191 (2015).

138. Guiot, C. et al. Temperature monitoring using ultrasound contrast agents: In vitro investigation on thermal stability. Ultrasonics 42, 927–930 (2004).

139. Stride, E. P. & Coussios, C. C. Cavitation and contrast: The use of bubbles in ultrasound imaging and therapy. Proc. Inst. Mech. Eng. Part H J. Eng. Med. 224, 171–191 (2010).

140. Shevchenko, S. N. et al. Antimicrobial Effect of Biocompatible Silicon Nanoparticles Activated Using Therapeutic Ultrasound. Langmuir 33, 2603–2609 (2017).

141. Chu, X. et al. Exploration of TiO 2 nanoparticle mediated microdynamic therapy on cancer treatment. Nanomedicine Nanotechnology, Biol. Med. 18, 272–281 (2019).

142. Beranek, L. L. Handbook of Acoustics. American Journal of Physics vol. 77 (Business Media, New York, 2009).

143. Benjamin, T. B. ; Ellis, A. T. The Collapse of Cavitation Bubbles and the Pressures thereby Produced against Solid Boundaries. Philos. Trans. R. Soc. London. Ser. A, Math. Phys. Sci. 260, 221–240 (1966).

144. Shao, J. L., Wang, P. & He, A. M. Influence of shock pressure and profile on the microjetting from a grooved Pb surface. Model. Simul. Mater. Sci. Eng. 25, 1–19 (2017).

145. Goeller, J., Wardlaw, A., Treichler, D., O'Bruba, J. & Weiss, G. Investigation of Cavitation as a Possible Damage Mechanism in Blast-Induced Traumatic Brain Injury. J. Neurotrauma 29, 1970–1981 (2012).

146. Labbaf, S. et al. An encapsulated drug delivery system for recalcitrant urinary tract infection. J. R. Soc. Interface 10, (2013).

147. Culjat, M. O., Goldenberg, D., Tewari, P. & Singh, R. S. A review of tissue substitutes for ultrasound imaging. Ultrasound Med. Biol. 36, 861–873 (2010).

148. Mano, J. F. Designing biomaterials for tissue engineering based on the deconstruction of the native cellular environment. Mater. Lett. 141, 198–202 (2015).

149. Chanda, A., Callaway, C., Clifton, C. & Unnikrishnan, V. Biofidelic human brain tissue surrogates. Mech. Adv. Mater. Struct. 0, 1–7 (2016).

150. Yoon, H. J. et al. Cold water fish gelatin methacryloyl hydrogel for tissue engineering application. PLoS One 11, (2016).

151. Lea-Banks, H., Stride, E. & Coussios, C. C. Ultrasound-mediated transport of nanoparticles and the influence of particle density. University of Oxford (2016). doi:10.1121/1.4950210.

152. Li, T. et al. Pulsed high-intensity focused ultrasound enhances delivery of doxorubicin in a preclinical model of pancreatic cancer. Cancer Res. 75, 3738–3746 (2015).

153. Beguin, E. & Stride, E. SONODYNAMIC THERAPY OF HYPOXIC TUMOURS PRS Transfer Report. (2016).

154. Miller, D. L. & Quddus, J. Diagnostic ultrasound activation of contrast agent gas bodies induces capillary rupture in mice. Proc. Natl. Acad. Sci. U. S. A. 97, 10179–84 (2000).

155. Price, R. J., Skyba, D. M., Kaul, S. & Skalak, T. C. Delivery of colloidal particles and red blood cells to tissue through microvessel ruptures created by targeted microbubble destruction with ultrasound. Circulation 98, 1264–7 (1998).

156. Stieger, S. M. et al. Enhancement of vascular permeability with low-frequency contrast-enhanced ultrasound in the chorioallantoic membrane model. Radiology 243, 112–21 (2007).

157. Caskey, C. F., Qin, S., Dayton, P. A. & Ferrara, K. W. Microbubble tunneling in gel phantoms. J. Acoust. Soc. Am. 125, EL183 (2009).

158. Sukovich, J. R. et al. Temporally and spatially resolved imaging of laser-nucleated bubble cloud sonoluminescence. Phys. Rev. E - Stat. Nonlinear, Soft Matter Phys. 85, 3–6 (2012).

159. Edsall, C. et al. Bubble Cloud Behavior and Ablation Capacity for Histotripsy Generated from Intrinsic or Artificial Cavitation Nuclei. Ultrasound Med. Biol. 47, 620–639 (2021).

160. Lu, Y., Katz, J. & Prosperetti, A. Dynamics of cavitation clouds within a high-intensity focused ultrasonic beam. Phys. Fluids 25, (2013).

161. Caskey, C. F., Stieger, S. M., Qin, S., Dayton, P. A. & Ferrara, K. W. Direct observations of ultrasound microbubble contrast agent interaction with the microvessel wall. J. Acoust. Soc. Am. 122, 1191–1200 (2007).

162. Gerold, B., Rachmilevitch, I. & Prentice, P. Bifurcation of ensemble oscillations and acoustic emissions from early stage cavitation clouds in focused ultrasound. New J. Phys. 15, (2013).

163. Kallini, J. R. et al. Comparison of the Adverse Event Profile of TheraSphere ® with SIR-Spheres ® for the Treatment of Unresectable Hepatocellular Carcinoma: A Systematic Review. Cardiovasc. Intervent. Radiol. 40, 1033–1043 (2017).

164. Carlos, J., Vega, D. La, Esquinas, P. L., Rodríguez-rodríguez, C. & Bokharaei, M. Radioembolization of Hepatocellular Carcinoma with Built-In Dosimetry : First in vivo Results with Uniformly-Sized , Biodegradable Microspheres Labeled with 188 Re. Theranostics 9, 868–883 (2019).

165. Jakobs, T. Selective internal radiation therapy for other liver metastases. Eur. J. Cancer, Suppl. 10, 72–74 (2012).

166. Tchelebi, L. & Sharma, N. K. Selective Internal Radiation Therapy in the Multidisciplinary Management of Liver Metastases From Colorectal Carcinoma. Seminars in Nuclear Medicine (2019) doi:10.1053/j.semnuclmed.2019.01.002.

167. Pereira, P. L. FRI-03 Intraarterial therapies: SIRT or TACE. Dig. Liver Dis. 45, S241–S242 (2013).

168. Tchelebi, L. & Sharma, N. K. Selective Internal Radiation Therapy in the Multidisciplinary Management of Liver Metastases From Colorectal Carcinoma. Semin. Nucl. Med. doi:S000129981930008X.

169. Grabowski, S. F. et al. The Efficacy of Selective Internal Radiation Therapy (SIRT) With Yttrium-90 (Y90) is Enhanced When Given in Low Volume Disease and in Conjunction With Other Liver-Directed Therapies. Int. J. Radiat. Oncol. 81, S353–S354 (2011).

170. Kloeckner, R. et al. Selective internal radiotherapy (SIRT) versus transarterial chemoembolization (TACE) for the treatment of intrahepatic cholangiocellular carcinoma (CCC): Study protocol for a randomized controlled trial. Trials 15, 1–7 (2014).

171. Wright, G. P. et al. Liver Resection After Selective Internal Radiation Therapy with Yttrium-90 is Safe and Feasible: A Bi-institutional Analysis. Ann. Surg. Oncol. 24, 906–913 (2017).

172. Lyon, P. C. et al. Long-term radiological and histological outcomes following selective internal radiation therapy to liver metastases from breast cancer. Radiol. Case Reports 13, 1259–1266 (2018).

173. Quadri, S. M. et al. Preclinical evaluation of intravenously administered 111in- and 90y-labeled b72.3 immunoconjugate (GYK-DTPA) in beagle dogs. Nucl. Med. Biol. 20, 559–570 (1993).

174. Plöckinger, U. & Wiedenmann, B. Management of metastatic endocrine tumours. Best Pract. Res. Clin. Gastroenterol. 19, 553–576 (2005).

175. Krug, S. et al. Successful selective internal radiotherapy (SIRT) in a patient with a malignant solid pseudopapillary pancreatic neoplasm (SPN). Pancreatology 12, 423–427 (2012).

176. Attarwala, A. A. et al. Quantitative and qualitative assessment of yttrium-90 pet/ct imaging. PLoS One 9, 1–7 (2014).

177. Formenti, S. C. & Demaria, S. Combining radiotherapy and cancer immunotherapy: A paradigm shift. J. Natl. Cancer Inst. 105, 256–265 (2013).

178. Burnette, B., Fu, Y.-X. & Weichselbaum, R. R. The confluence of radiotherapy and immunotherapy. Front. Oncol. 2, 1–8 (2012).

179. Dillehay, L. E. et al. Use of bremsstrahlung radiation to monitor y-90 tumor and whole body activities during experimental radioimmunotherapy in mice. Cancer 73, 945–950 (1994).

180. Schäffer, M. et al. Differential expression of inflammatory mediators in radiation-impaired wound healing. J. Surg. Res. 107, 93–100 (2002).

181. Ter Haar, G. Therapeutic ultrasound. in European Journal of Ultrasound vol. 9 3–9 (1999).

182. Crezee, H. et al. Thermoradiotherapy planning: Integration in routine clinical practice. Int. J. Hyperth. 32, 41–49 (2016).

183. Tsilimigras, D. I. et al. Prognosis After Resection of Barcelona Clinic Liver Cancer (BCLC) Stage 0, A, and B Hepatocellular Carcinoma: A Comprehensive Assessment of the Current BCLC Classification. Ann. Surg. Oncol. 26, 3693–3700 (2019).

184. Van Rhoon, G. C. et al. CEM43°C thermal dose thresholds: A potential guide for magnetic resonance radiofrequency exposure levels? Eur. Radiol. 23, 2215–2227 (2013).

185. Singh, S. K. et al. Identification of human brain tumour initiating cells. Nature 432, 396–401 (2004).

186. Gimple, R. C., Bhargava, S., Dixit, D. & Rich, J. N. Glioblastoma stem cells: Lessons from the tumor hierarchy in a lethal cancer. Genes Dev. 33, 591–609 (2019).

187. Xie, Y. et al. The Human Glioblastoma Cell Culture Resource: Validated Cell Models Representing All Molecular Subtypes. EBioMedicine 2, 1351–1363 (2015).

188. Yang, W. et al. Sex differences in GBM revealed by analysis of patient imaging, transcriptome, and survival data. Sci. Transl. Med. 11, 1–15 (2019).

189. Galli, R. et al. Erratum: Isolation and characterization of tumorigenic, stem-like neural precursors from human glioblastoma (Cancer Research (October 2004) 64 (7011-7021). Cancer Res. 64, 8130 (2004).

190. Reifenberger, G., Wirsching, H. G., Knobbe-Thomsen, C. B. & Weller, M. Advances in the molecular genetics of gliomas-implications for classification and therapy. Nat. Rev. Clin. Oncol. 14, 434–452 (2017).

191. Garcia, C. A. et al. Functional characterization of brain tumor-initiating cells and establishment of GBM preclinical models that incorporate heterogeneity, therapy, and sex differences. Mol. Cancer Ther. 20, 2585–2597 (2021).

192. Trifiletti, D. M. et al. Prognostic Implications of Extent of Resection in Glioblastoma: Analysis from a Large Database. World Neurosurg. 103, 330–340 (2017).

193. Sun, T. et al. Sexually dimorphic RB inactivation underlies mesenchymal glioblastoma prevalence in males. J. Clin. Invest. 124, 4123–4133 (2014).

194. Hiraki, T. et al. Application of Genome-Wide DNA Methylation Analysis to Differentiate a Case of Radiation-Induced Glioblastoma From Late-Relapsed Medulloblastoma. J. Neuropathol. Exp. Neurol. 80, 552–557 (2021)

CHAPTER 2

In Vitro Extravasation of Glass Microspheres in Hydrogel Cavities

2. In Vitro Extravasation of Glass Microspheres in Hydrogel Cavities

Summary

Whilst it has been demonstrated that the extravasation of particles with diameters in the 50-500nm range can be enhanced using focused ultrasound, this has not been shown for particles in the micrometre range. The aim of this chapter is therefore to investigate the feasibility of ultrasound-induced extravasation of microspheres, with diameters of 5-100 µm for SIRT applications. Focussing on microspheres within this size range would be comparable to that of the commercially available TheraSphere® product, enabling faster technological translation should the technology platform be suitable. The design and fabrication of the required apparatus and development of the analytical methods used are described. The results are then presented and discussed.

2.1. Introduction

As described in Chapter 1, GBM is a particularly aggressive and persistent form of cancer which manifests as primary and secondary lower grade gliomas[1]. GBM cells are highly invasive and migrate quickly, producing metachronous lesions with the rapid growth of the disease, with undetectable individual cancerous cells extending into within otherwise healthy parenchyma[2]. Current treatments are palliative and aimed at minimising loss of brain function, and maintaining patient quality of life as the disease progresses[3–7]. Single tumour volumes can vary widely due to location and rate of disease progression, medium size tumours (30-40 cm^3) are common[8] but cases of particularly large tumours (>100 cm^3) are not infrequent[9].

2.1.1. Ultrasonic Aspiration for Tumour Resection

Complete removal of the rapidly growing tumour via resection, is technically challenging; with an improved survival rate only observed above a 98% extent of resection (EOR)[25]. Current medical devices include that of ultrasonic aspirators which use the displacement of the ultrasonic horns tip to erode the tissue directly in front of the tip, analogues to that of a pneumatic burr but with less mechanical feedback to the surgeon[26]. Tips are interchangeable, with different burr designs suited to different tissue stiffness, from bone through to brain with irrigation to aid in the removal of the homogenised debris.

Whilst the removal of soft tissue is straightforward, determining which tissue to remove remains a diagnostic challenge for most indications. Whilst cancerous tissue is stiffer than healthy parenchyma, tissue densities vary more between different tissue and organs than between healthy or diseased tissue. Fortunately in the case of GBM, 5-aminolevulinic dye (5-ALA) offers real-time visualisation of distinction between the two adjacent tissues[27–29]. Whilst delivered systemically, 5-ALA metabolism results in the accumulation of fluorescent protporphyrin IX molecule, solely within cancerous tumour cells causing the cancerous brain cells to selectively fluoresce under external excitation[27]. This enables the surgeon to confidently extend the resection intraoperatively, beyond what is currently visible in preoperative planning via MRI and CT[5,28]. All existing feeding vasculature is cauterised prior to mechanical erosion, to prevent further blood loss to the patient during the procedure. The cavity produced by ultrasonic erosion is then thoroughly irrigated with saline and aspirated repeatedly to clear the resection cavity of any emulsified tissue remaining. Despite this extensive protocol, true comprehensive resection remains unlikely due to the extreme level of cellular infiltration by the disease, at a low enough concentration as not to be detectable under selective fluorescence during the resection.

Adjuvant or follow up treatment with radio and/or chemo-therapy is frequently employed, particularly using treatment with Temozolomide (TMZ), but is rarely successful[1,5,9,30,31]. This may be in the form of a Rickham/Ommaya reservoir, a balloon containing the desired radio or chemotherapeutic agent situated beneath the scalp, used to locally deliver chemotherapy into the resection cavity[32,33].

Pseudoprogression of the disease is common in post-operative imaging of the patient every 2-3 months, brought about by blood-brain barrier disruption, oedema, and mass effect mimicking progression[34]. Despite the increased use of TMZ, only 6% of patients reach the 5 years survival mark despite early intervention[35]. Treatment failure and ultimately reoccurrence is largely due to the repair of TMZ DNA damage by protein O6-methylguanine-DNA-methyltransferase (MGMT), facilitating resistance to TMZ and recurrence of the GBM within the cavity[3,8,36,37].

2.1.2. Ultrasound Induced Cavitation as a Treatment Modality for Glioblastoma Multiforme

Stereotactic radiotherapy, although theoretically offering better targeting, is generally not used for GBM due to the risk of collateral damage resulting from the challenges involved in accurately defining the tumour volume in pre-operative imaging[34]. Multiple irradiations at lower doses are sometimes used as a palliative option, providing patient welfare is not compromised; but repeated treatment commonly lead to radioresistance[5,30]. A potential advantage of radioembolic microspheres is that they could offer a means of delivering an equivalent dose of radiation with a much lower risk of side effects and/or radioresistance. Distinct from the use of microspheres in embolic procedures, in this case they could be injected directly into the cavity created by the tumour resection without the need for any further surgical intervention.

Despite this, stereotactic radiation in the form of SIRT as initial adjuvant radiotherapy, holds the largest promise for increasing survival for GBM patients; reserving the use of WBRT for combatting further progression reoccurrences. The cavity produced by the intra cranial aspiration of the GBM central tumour mass, provides an opportunity for adjuvant therapy with a stereotactic radioactive product such as TheraSphere®. As the exact depth of the aggressive infiltration of cancerous cells into the healthy tumour margins is unknown, the 2.5 mm mean depth of irradiation from the glass microspheres may be insufficient; the microspheres themselves must therefore be placed within the tumour margins, to enlarge the volume of tissue irradiated. Ultrasound induced cavitation may prove to be the translational mechanism required for the mass transport of the radioactive glass microspheres.

The aim of the work described in this chapter was to design an experimental setup and associated data analysis, to test the feasibility of using ultrasound induced cavitation to extravasate glass SIRT microspheres from a cavity in a tissue mimicking phantom

2.2. Methods

2.2.1.Phantom Development

The first step was to design the phantom. The ideal tissue mimicking phantom would have a high water content, mechanical and acoustic properties close to those of the relevant tissue and be generated by a simple but robust fabrication process.

2.2.1.Malignancies of the Brain and Ex Vivo Surrogates

Malignant tissue is frequently stiffer than healthy surrounding tissue, with a higher corresponding Young's Modulus, an important differentiating criterion for pathology and tumour localisation using various methods[10]; including Vibro-Acoustography, Magnetic

Resonance Imaging (MRI) and x-ray computed tomography (CT)[11,12]. Therefore gel surrogates which mimic tumour tissue, must be chosen with a modulus as close to that of human tissue to accurately model factors effecting the dispersion of any radioembolic particle.

Brain matter is relatively soft[13,15], compared with other tissue, prone to permanent deformation and long lasting and damage as a result of acute injuries[18] or repeated stresses by the breakdown of the tau-microtubule complex e.g. chronic traumatic encephalopathy (CTE)[19,20] . The primary reason for this degree of damage is due to the low solid content of the parenchyma. Liquids will oppose applied stress in volume but not in shape[21], whereas solids will tend to oppose stress in both volume and shape. Liquids therefore only have a bulk whereas solids also have elastic (Young's) and shear moduli.

Young's modulus describes the relationship between the stress (unit of force per area) and the strain (degree of proportional deformation as a result of the force) on a solid object, in a linear elastic model from a single axis[22]. Human brain tissue has reported Young's modulus of 0.17-16.06 kPa for various pathologies with Human glioma (2.75 ± 1.40 kPa) and metastatic lymphoma (2.10 ± 0.57 kPa) marginally stiffer but similar to isolated mouse brain (3.97 ± 3.66 kPa)[13]; including a non-linear elastic component due to the presence of cerebrospinal fluid (CSF)[14]. The low modulus of brain tissue, is independent of the displacement of CSF by the tissue, which occurs before deformation of the cerebral matter[15].

Several surrogates have been previously investigated, primarily for modelling drug-distribution within the brain. They include Agarose gelatine, Alginates, Sylgard 527 Silicone gel, Hyaluronic acid (HA) and Polyvinyl alcohol (PVA) [16]. Readily available inexpensive animal surrogates for brain tissue include chicken liver (0.44 ± 0.13 kPa) which has similar mechanical properties to normal brain tissue and chicken gizzard tissue (3.00 ±0.65 kPa) with a similar Young's Modulus to that of varying gliomas[13]. The use of domestic animal tissue allows for the observation of potential radiation damage on glioma surrogates with a similar stiffness. *Ex vivo* tissue does

not offer the same mechanism for decay as necrosis or apoptosis *in vivo*[17], however it does offer a more suitable medium for observing the depth of radiation penetration compared to *in vitro* hydrogel models.

Tissue mimics which are too stiff may inhibit the intended delivery of the surrogate microspheres, reducing the feasibility of the ultrasound initiated cavitation as an effective method for facilitating the mass transport of the radioactive microspheres. Whilst selecting a material which is too soft may incorrectly increase the penetration depth, invalidating any successful results. A literature survey indicated that hydrogels were most likely to meet the requirements for this work[14,38–42]. Hydrogels e.g. Salt crossed alginate hydrogels[43–45], which had reported moduli larger than that of healthy brain tissue[13,14,46–48,48] were initially excluded and were not considered. PVA and Agar-agar hydrogels were investigated in detail.

2.2.2.Poly Vinyl Alcohol Freeze-Thaw Hydrogels

PVA-based tissue substitutes have the advantages of indefinite longevity and particularly low cost for the volume of gel produced. As a biocompatible polymer, PVA has been used in various medical device applications for years[49,50] as well as tissue phantoms[14,24,46,51–53] for academic research. PVA solutions are liquid at room temperature, but can be turned into physically cross-linked PVA hydrogels by heat cycling the solution between ambient and <0°C, known as freeze-thaw[24,50,52,54]. As the water within the polymer solution begins to crystallise, PVA is concentrated in supercooled microdomains between growing ice crystals. The increase in relative concentration as well as the growing surrounding pressure causes the repeating units within the polymer to adopt a more repetitive, crystalline lattice. The degree of crystallinity increases with the degree of symmetry (hydrolysis) and length (molecular weight) of the polymer used.[50] As the solution is brought back to ambient temperature and the ice crystals melt, the increased degree of crystallinity and concentration of the PVA remains,

physically crosslinking the semi-crystalline PVA chains together producing a hydrogel network. The PVA's degree of hydrolysis, its molecular weight and the number of thermal cycles all act to increase the degree of crystallinity and hydrogel network strength. After one freeze-thaw cycle the ultrasound attenuation coefficient of the PVA hydrogel is 0.075 dB/cm-MHz and increases to 0.28 dB/cm-MHz after 4 cycles[55].

As PVA freeze-thaw hydrogels can be tuned in various ways, PVA seemed ideally suited as tissue mimic for healthy brain parenchyma, a particularly soft and deformable tissue[13–15,47,48].

The fabrication time for production of freeze-thawed PVA gels is long due to the high temperatures and long periods of time required to dissolve the polymer granules, and the hours needed to freeze and thaw large volumes of water. In order to minimise variation between phantoms, it is important to closely control the ambient temperature and subsequently the rate of cooling and thawing of the PVA gels, as the crystallinity of the PVA chains and therefore the material properties of the gel, is directly proportional to the duration of the freeze-thaw cycles and temperatures used[24,52,54] as well as its molecular weight (Mw). Solutions containing PVA of increasing polymer chain length have higher elastic moduli and tensile strength, due to the increase in crystallinity in each polymer chain as well as the increased physical crosslinking of the gel by the longer chains.

PVA gels were produced using a previously reported method[14] by dissolving PVA (146-186 kDa Mw, Sigma Aldrich) in deionised water (Millipore-Q Type 1) to produce a 10% weight/volume concentration of the PVA after microwave irradiation (1200W, 600s) with intermittent agitation. The solutions were poured into the desired mould (See Section 2.2.4) cooled to 4^{o}C for 12h before freezing at -20^{o}C for 18h and thawing at 4^{o}C for a further 6 hours. PVA hydrogels produced in this manner were stored at 4^{o}C until required. It was impossible to degas the solution of PVA (required to prevent cavitation within the hydrogel under ultrasound exposure) due to the polymer acting as a foaming agent under reduced pressure. Only a single

freeze-thaw cycle was required to form each gel. The gels produced were far stiffer than expected from the literature, especially when compared to mammalian brain tissue and undesirably opaque and radiopaque in addition to the lengthy fabrication time, preventing any µCT analysis (See Section Micro Computed Tomography (µCT). The opacity of the gel also hid signs of unwanted cavitation within the gel, stemming from gas bubbles which remained trapped within the gel after completion of the heat cycles. As the degassing of the hydrogel medium was critical for ultrasound experimentation, PVA was deemed to be unsuitable as a tissue mimic for brain parenchyma and the use of PVA freeze-thaw gels was abandoned.

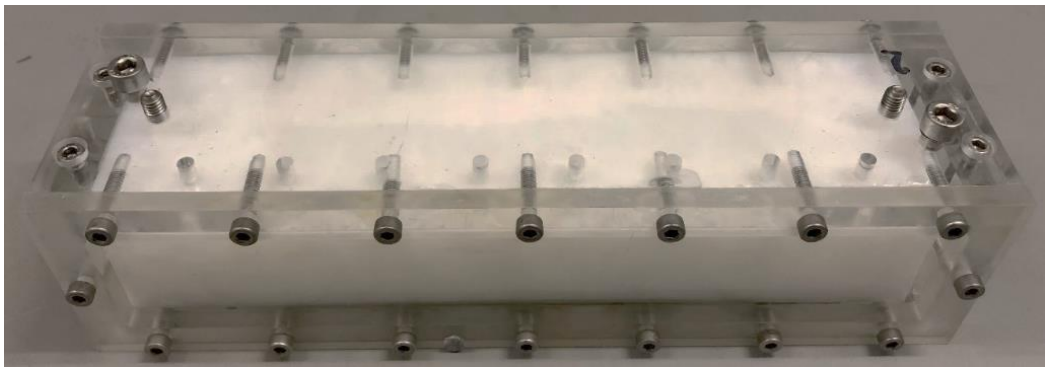


Figure 10: Freeze-thaw PVA opaque hydrogel in serial phantom mould with stainless steel screws.

2.2.3.Agar-Agar

Agar based phantoms have been widely used as tissue mimics, primarily due to their ease of production, optical clarity and having an acoustic impedance akin to that of mammalian tissue (2%, 1490 m/s)[23,56–61]. Agar gels are comprised of two compounds, agarose and agaropectin which adopt a threefold double helix confirmation once in a gel state[62], achieved by van der Waals forces, hydrogen bonding and electrostatic interactions between the agar polymer and entrapped water molecules. To create a gel, agar is dissolved in hot water, which upon cooling undergoes a sol-gel transition. The intermolecular forces of the polymer act to entrap water within the polymer network forming a hydrogel at room temperature.

Agar phantoms have been shown to be suitable for studying bubble "tunnelling"[58], nanoparticle projections and extravasations[60,63,64] produced by ultrasound and cavitation, whilst remaining stiff enough to simulate arterial or venous vessels for flow simulations[23,42,58]. They can be generated with much better reproducibility than PVA phantoms and modification of the gel stiffness is easily achieved by varying the concentration and molecular weight of the agar. Unfortunately, even at concentrations as low as 1 or 0.5% agar w/v, the resulting hydrogels are significantly stiffer than brain tissue[14,15,40,48,56,57]; whilst very low concentration solutions (< 0.5% w/v agar) do not form a gel matrix upon cooling.

Material	Mean Elastic Modulus (kPa)
PVA (14%) Freeze Thaw Hydrogel [14]	2.73
PVA (7%) Freeze Thaw Hydrogel [14]	0.34
0.2% agarose [13]	2.35 ± 0.39
0.4% agarose [13]	6.31 ± 0.96
0.6% agarose [13]	12.93 ± 2.99
Human Brain Parenchyma [46]	0.58
Human glioma [13]	2.75 ± 1.40
Human meningiomas [13]	3.97 ± 3.66
Fresh Mouse Brain [13]	1.56 ± 0.75
Mouse Tumours [13]	7.64 ± 4.73

Table 1: Mechanical stiffness values for tissue mimicking phantom candidates, healthy and cancerous human and mouse tissues.

Nevertheless, despite the reported values for the freeze-thaw PVA hydrogels, in the interest of time and as the use of ex vivo tissues was foreseen, agar was chosen as the material for the initial *in vitro* investigations.

2.2.4.Tissue Phantom Mould

It was important that the experimental setup and protocol would enable both consistency and high throughput to quantify microsphere extravasation over a large range of ultrasound exposure parameters.

An 8 well rectangular mould (internal volume 225 x 60 x 10 x 40mm) was designed and fabricated from 10mm polymethyl methacrylate (PMMA, Perspex®) with Mylar (polyethylene terephthalate) sheet 'windows' at the front and rear of the mould (Figure 11). The thin mylar 'windows' in the mould allow for propagation of ultrasound waves through the window and into the tissue phantom (speed of 2400ms^{-1})[65]. The phantom mould was assembled using nylon screws to reduce the need for high density materials in the construction, critical for x-ray analysis post exposure. Wells were cast in the moulds using suspended stainless steel rods with modified tips, in a range of diameters (4mm, 2mm, and 1mm) in order to simulate the effect of varying the excised cavity dimensions. The wells were offset from the front of the mould to allow extravasating microspheres to pass into the bulk of the phantom, with minimal interference from adjacent wells or boundaries.

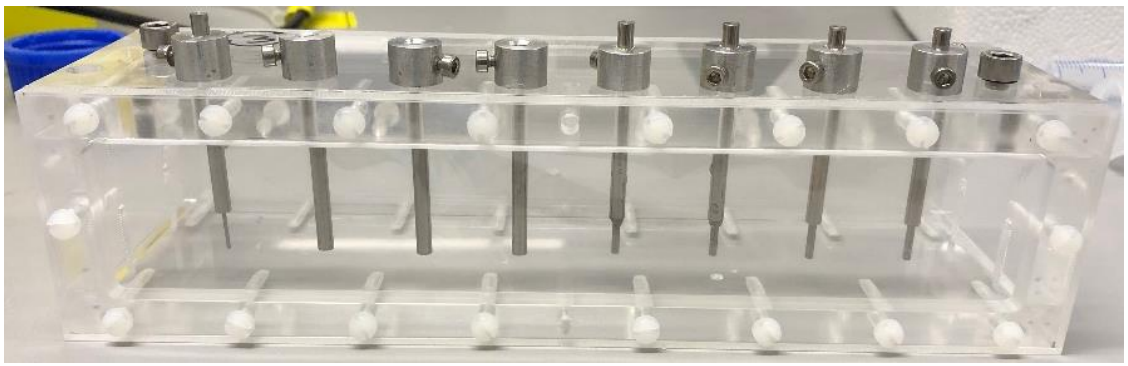


Figure 11: Tissue phantom mould. Internal volume 225 x 60 x 10 x 40m using 10mm thick PMMA acrylic.

A suspension of agar (0.5% w/v, Sigma Aldrich, w201201, Mw 500-1500 Da) in deionised water (Millipore-Q Type 1) was degassed under reduced pressure for 90 minutes. After which it was microwave irradiated for 390s to dissolve the agar with minimal agitation in order to avoid

boiling of the aqueous solution. Moulds were filled with hot (>85°C) agar liquid and set at 4°C for a minimum of 12 hours before use. The stainless steel rods were removed once the hydrogel had formed, leaving cavity wells with volumes corresponding to those of the rods.

2.2.5.Fabrication of Bespoke Ultrasound Tank and Movement Stages

In collaboration with the IBME Engineering workshop, an ultrasound tank of medium size (310 x 365 x 150mm, 16L capacity) was designed and built from PMMA. The joining faces of the tank were sealed with a clear silicone gel and screwed togetehr with stainless steel screws to prevent leaks. A aluminum bread board (3 x 12, 2.5mm pitch, M4 screw thread) was screwed into the walls on top of one end of the tank, and fitted with three individual multidirectional Newport® (MKS Instruments) modular movement stages, capable of mm adjustments in all three axes. Suspended from the modular stage was a poloxomethylene (Delrin®) holder designed to hold a range of therapeutic ultrasound transducers (See Figure 13).

An aluminium cross member was used to suspend the mould within the tank, aligning the focus of the transducer with the bottom (45mm ±0.5mm from the top of the mould) of each well. Once filled with 10µm filtered, deionised water (Type 1, MilliQ®) the ultrasound apparatus and gel phantom were immmersed in the tank, avoiding the entrapment of any air bubbles, submerging the face of the transducer completely whilst not allowing the water level to rise above that of the front mould face and into the wells.

Securing the positioning stage and the gel phantom into the tank walls, allowed for a reduction in setup time between well exposures, whilst improving reproducibility between runs. Aligning the increments of the breadboard to that of the gel phantom, allowed for increased throughput with minimal adjustments between runs.

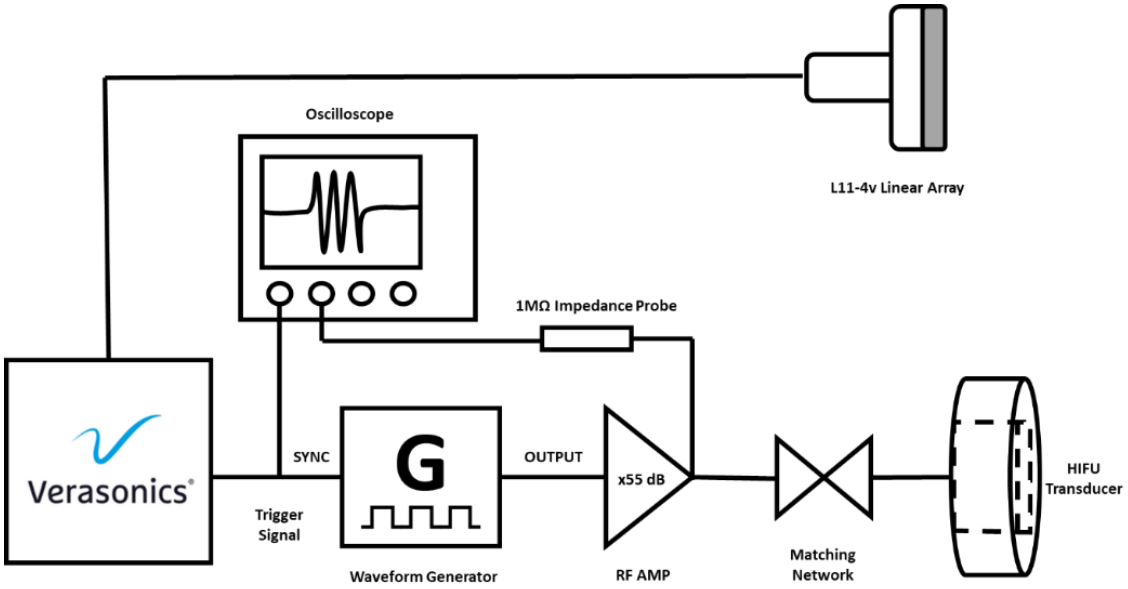


Figure 12: Electronic diagram for the ultrasound setup used to produce microsphere projections

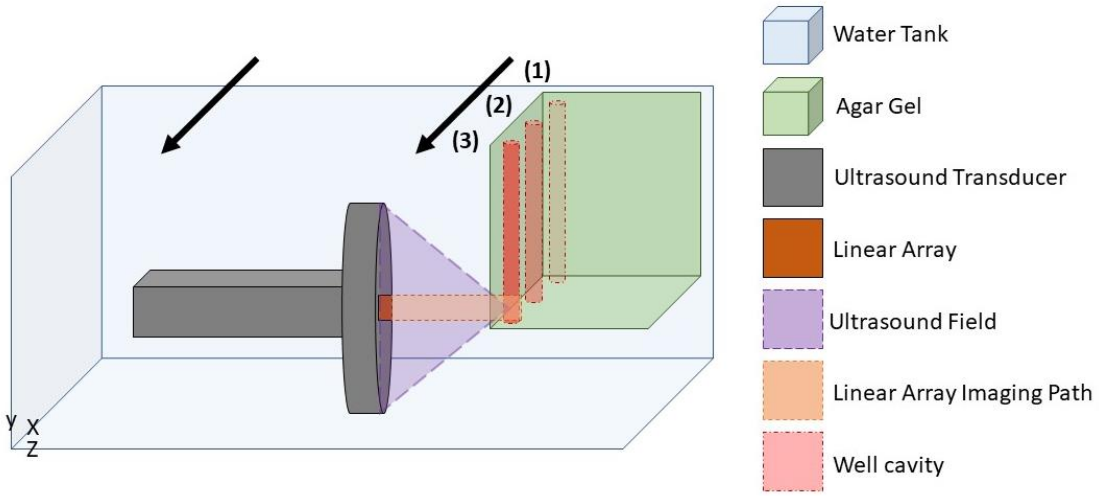


Figure 13: Diagram of the physical setup of the ultrasound transducer, linear array and agar mould with well cavities within the water tank. Not to scale. The wells are exposed in order 1,2,3 moving across from left to right (black arrows) in the mould. The ultrasound field is not on during relocation of the ultrasound transducer.

2.2.6. Ultrasound Transducer Setup and Calibration

The suspended circular Delrin® holder accommodated a series of high intensity focused ultrasound (HIFU) transducers (H107/B02 series, Sonic Concepts Bothell, WA, USA), all with an outer diameter of 64mm, a central rectangular cut out measuring 48 x 17mm for a coaxially aligned linear array (128 elements, 0.3mm pitch, 18mm elevation focus, L11-4v Verasonics®).

The HIFU transducers had fundamental frequencies of 0.55 or 1.10 MHz with corresponding third harmonic outputs (1.65 and 3.30 MHz) and individual impedance matching networks.

A large (600 x 630 x 370 mm) thoroughly degassed water tank with motorised stages (±0.1mm, UMS3, Precision Acoustics) was used for the calibration of the transducers. The rectangular cut-out transducers (H107 and 102BB series) were calibrated as follows. The centre of the transducer focus was found by pressure scans in the XY and XZ axis using a 1.2 mm tip diameter needle hydrophone (100-100-1, Muller-Platte) for the 0.5/1.5MHz pressure calibrations. A 31-step voltage ramp from 10 to 610mV was used in combination with a 55dB gain amplifier (E&I, 1140LA, 1000W) to produce and record pressure and voltage traces over two consecutive tests, for each transducer at its centre frequency and third harmonic.

For the 1.1 and 3.3 MHz pressure calibrations (102BB-022 transducer) a hydrophobic fibre optic hydrophone (FOH, Precision acoustics 250 kHz – 50 MHz, 10kPa to 15MPa, 10 µm tapered tip) was used over the needle hydrophone to perform the planar focus (Figures 14 and 15) and pressure scans (Figure 16), reducing the likelihood of cavitation on the surface of the hydrophone.

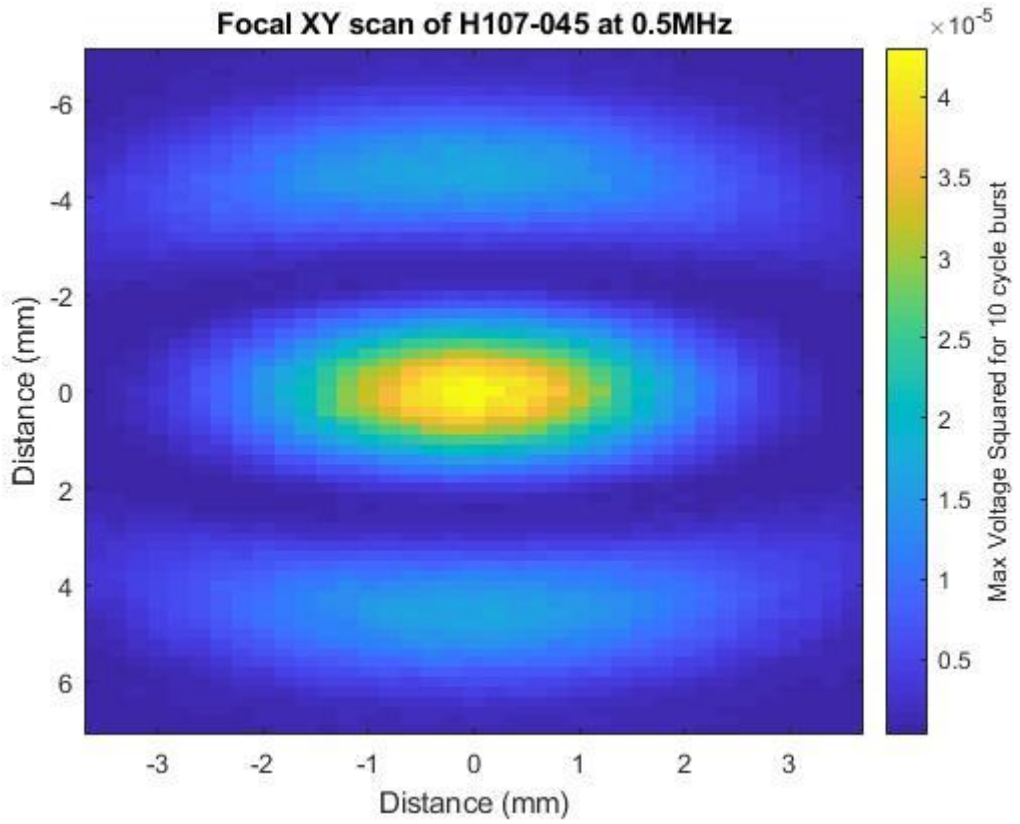


Figure 14: XY planar scan at the focus of H107-045 (0.500 MHz at a resolution of 0.2mm per pixel, showing the side lobes above and below the focus of the transducer in the y plane using a needle hydrophone.

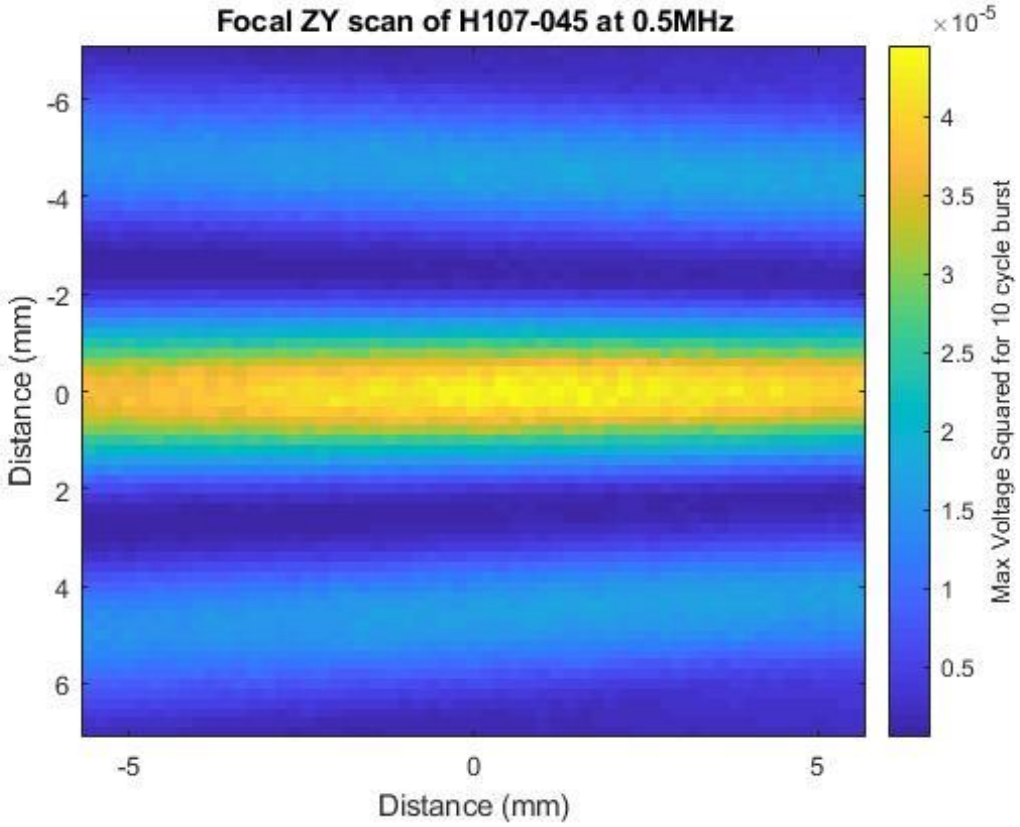


Figure 15: ZY plane scan for H107-045 (0.500 MHz) at a resolution of 0.2mm per pixel, showing the side lobes above and below the focus of the transducer in the z plane using a needle hydrophone.

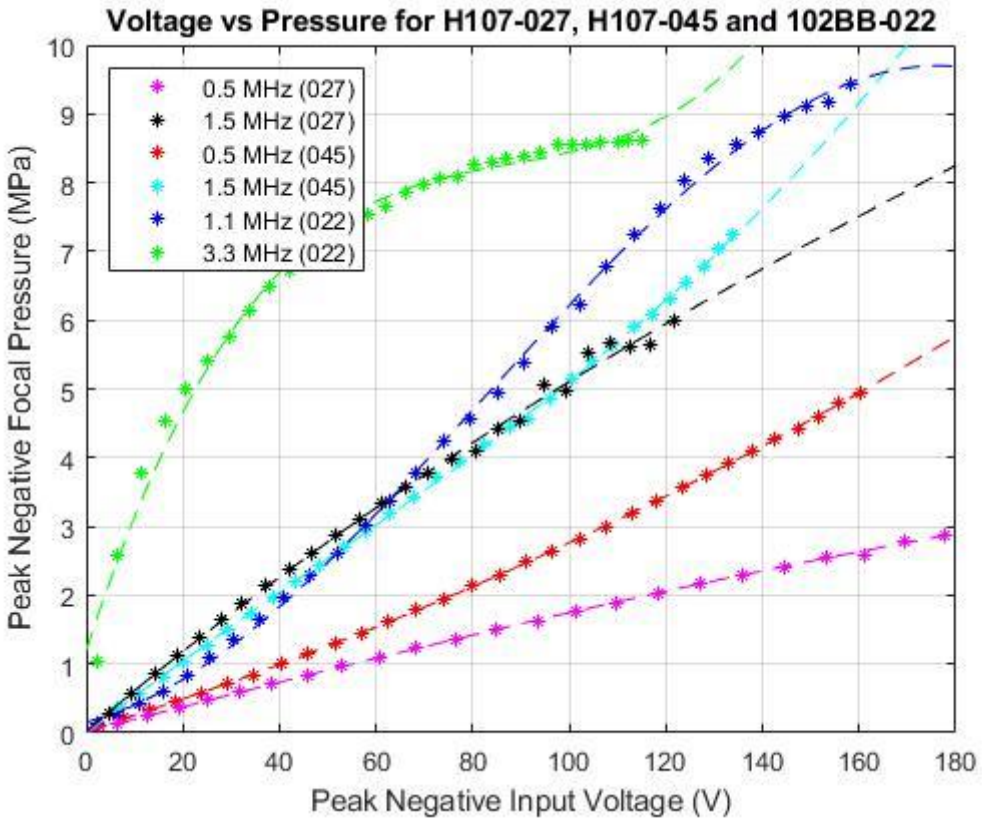


Figure 16: Calibration data for H107027, H107-045 and 102BB-022. A third order polynomial was fitted to each data series, which fitted the recorded data best. The polynomial for the 3.3 MHz data series should plateau at higher pressures and does not fit a 2nd or 3rd order polynomial correctly.

Monitoring of acoustic emissions was achieved with passive acoustic mapping using signals recorded on a L11-4 linear array (centre frequency 6.25 MHz, bandwidth 4-11MHz, 128 elements, pitch 0.298-0.302mm, Verasonics Inc., Redmond, WA), aligned coaxially with the FUS transducer. The linear array was connected to a Verasonics Vantage 256 channel ultrasound research system (Verasonics Inc., Redmond, WA) on which signals received by each element were recorded for offline processing.

2.2.7. Ultrasound Transducer Alignment

Alignment of the transducer and coaxially aligned linear array proceeded by first aligning the focus of the transducer with a 1mm stainless steel tipped rod, which was inserted into the well to be tested (See Figure 11). A pulser-receiver (JSR Ultrasonics, DPR300) was used initially to send a short, low energy pulse to the transducer, so that the soft hydrogel was not unnecessarily exposed to HIFU. The transducer position was adjusted in sub millimetre increments until the maximum amplitude of the received signal was observed on the oscilloscope. Next, a B-mode image was captured (using the Verasonics® system) of the alignment rod. This was used as a reference point for alignment when manually moving the transducer and array to adjacent wells within the same agar phantom. Alignment of the next well in the same mould, could then be checked using the x,y coordinates of the B-mode image, visually confirmed before proceeding with ultrasound exposure.

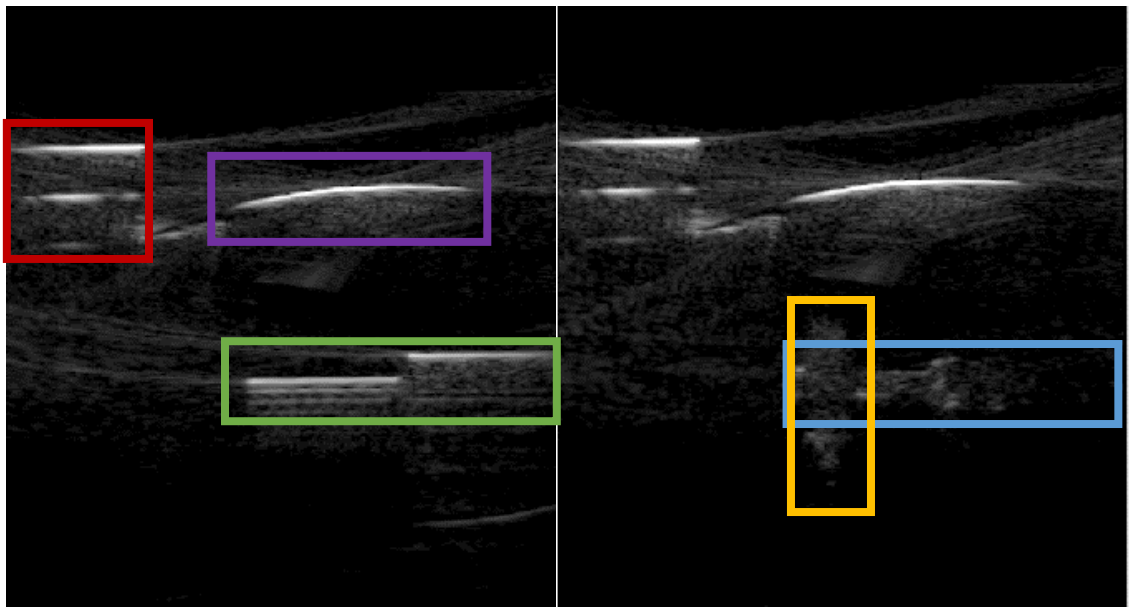


Figure 17: B-mode images of the stainless steel 1mm alignment rod within a 4mm diameter well (green, plastic mould (red), mylar sheet (purple) and the same 4mm well with deposited microspheres (blue) and microsphere extravasation (yellow).

After initial alignment, the pulser-receiver was replaced with an arbitrary waveform generator. All of the ultrasound exposure parameters were manually controlled using the waveform generator, the signal output from the Verasonics dictated the pulse repetition frequency and

was coded at 0.33s (3.3 Hz PRF). A wide variety of ultrasound parameter combinations were tested (See Appendix 1, Section 3.2.3.2) which included a range of fundamental frequency, peak negative pressure and duty cycle. The parameter space investigated was defined from previously reported literature values for the ultrasound induced extravasation of nanoparticles[58,60,66], microbubble tunnelling[67,68] and inertial cavitation of various cavitation agents[63,69–72].

2.3. Experimental Procedure and Analysis Techniques

Once the mould and transducer were successfully aligned, the experimental procedure was as follows. 250µL suspension of cavitation agent (See section 3.2.3.2), of known concentration was added to a glass vial containing a known mass of glass YAS microspheres in one of three diameter distributions (<20, 15-35, >32 µm). A 'cold' non-radioactive glass microsphere of equivalent density and size was used as a surrogate in this body of work to mitigate any associated unnecessary exposure to radioactive isotopes.

The glass microspheres and cavitation agent were swirled and withdrawn as a single aliquot to avoid sedimentation of the microspheres. The aliquot was pipetted directly into the well aligned to the ultrasound transducer and linear array. The well was exposed to ultrasound and acoustic emissions monitored over the exposure period. A second B-mode image was captured post exposure and the ultrasound transducer and array relocated by 25mm. This was repeated for wells 2 through 8 on each iterative mould, with well 1 used as an exposure control between moulds. After all exposures had been completed, the mould and its cross-member were disconnected from the tank and the mould stored at 4^{o}C awaiting further analysis.

2.3.1.Micro Computed Tomography (µCT)

Analysis of the phantoms and any bead extravasation produced, was performed via X-ray computed tomography (CT). CT generates a map of X-ray absorption with objects of high density and hence X-ray absorbance appearing brighter than those of lower absorbance. µCT is capable of imaging objects to micrometre resolution and enables visualisation of incredibly fine and detailed structures such as bone remodelling and calcification[73–75].

The YAS glass microspheres have a relative density of 3.6 gmL^{-1} making them easily distinguishable from the surrounding hydrogel matrix, acrylic mould and any entrapped gas remaining within the cast wells, but not from other metal objects e.g. steel screws. A Perkin Elmer Quantum FX µCT system, located within the Kennedy Institute of Rheumatology was used. A bespoke acrylic sample holder, with a recessed bed was used to fix the position of the sequential mould within the chamber and reduce variation between moulds analysed. The mould bed could be moved incrementally in any direction using the integrated electrical movement stage of the Quantum FX µCT.

The µCT system bore can hold one of three acrylic cylinder inserts, which protect the x-ray detector from the adjustable sample tray. The bore of the acrylic insert determines the proximity of the detector to the sample bed and therefore the maximum spatial resolution of the image, by increasing the field of view (FOV).

The FOV of the Quantum FX machine is defined by a square at the centre of the image, the dimensions of which dictate the size of the sample imaged and the subsequent resolution of the image obtained. At 73 and 10 mm FOV, the pixel resolution of the square in focus is 148 and 20µm respectively. Therefore, for the majority of experiments studied (30 mm FOV), an individual bright pixel or voxel is not representative of one, but rather a cluster of microspheres either adjacent or in close proximity, so as to increase the average density and provide sufficient contrast for the given volume.

For all µCT scans obtained, the maximum available voltage and current (90 kV and 160 µA) were used to produce the largest exposure and resulting contrast in the images produced. The only parameter that was changed in the acquisition parameters was that of the FOV. Individual wells were imaged at 30mm FOV as standard, unless otherwise stated.

2.3.2. µCT Image Analysis

The Quantum FX µCT uses DICOM (Digital Imaging and Communications in Medicine) files to export the X-ray exposure images for interpretation. Two free open source programs (RadiAnt and InVersalius) were used as DICOM viewers, for initial experiments to gauge approximately the effect of the different parameters investigated. Both software packages allowed for basic 3D reconstruction of the 512x512 pixel by 512 image stacks obtained from the Quantum FX machine, allowing for simple contrasting and image manipulation to observe the bright contrasting microspheres from the dark background of the agar hydrogel phantom and acrylic holder. Images can be filtered by brightness, falsely coloured to highlight areas of interest and manipulated to orientate the exposures to the same viewpoint in either software. Initial images reported were created using maximum intensity projections (MIP), highlighting the voxels in the desired plane of observation and overlaying them to produce an image with substantially greater contrast than the corresponding spatially correct 3D images[75–77]; for the analysis of the glass YAS microspheres MIPs were found to be useful for characterising microsphere extravasation.

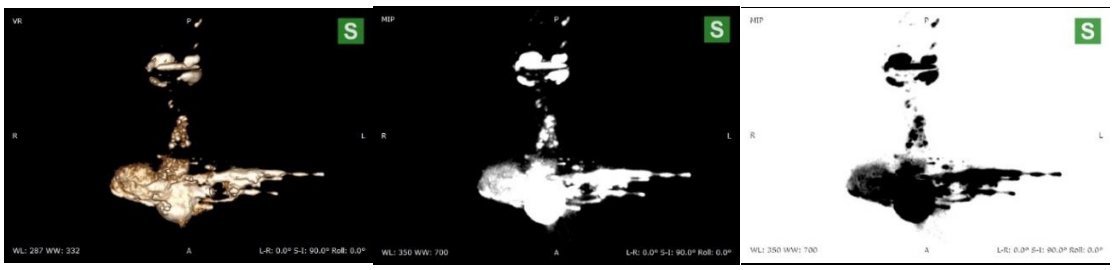


Figure 18: 3D image reconstructions using radiant DICOM viewer (left) and MIPs of the same 3D reconstruction (middle and right).

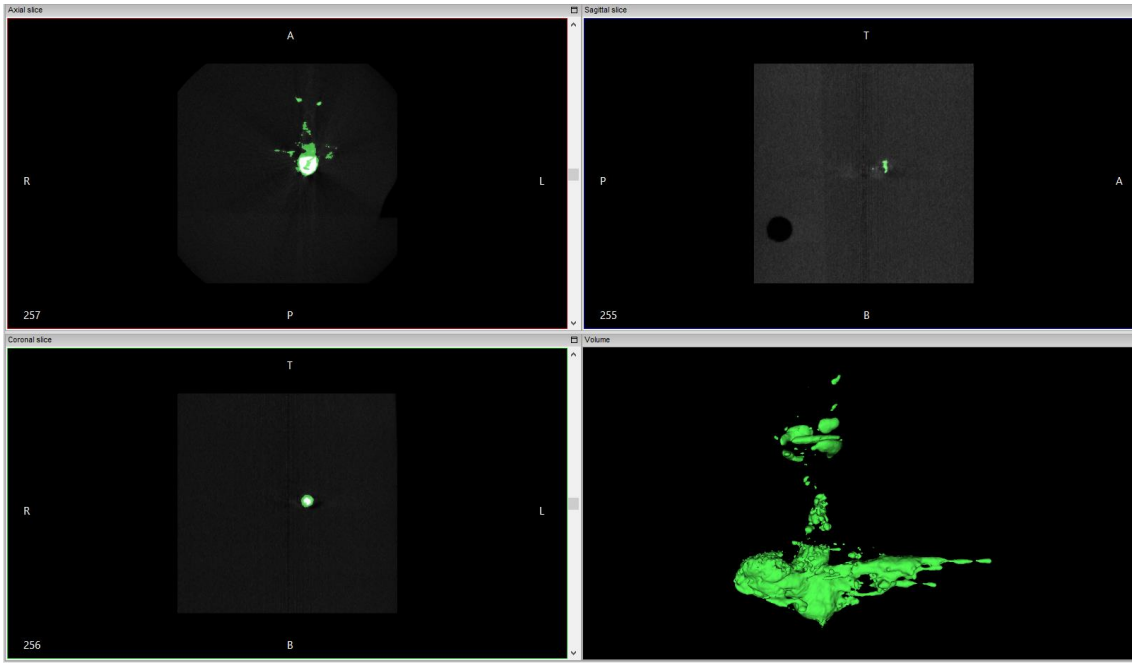


Figure 19: Image reconstruction using InVersalius showing items of high radiopacity highlighted in each image slice in each plane, with a 3D reconstruction of the total image (bottom right).

2.4. Characterisation of Microsphere Extravasation

There were several common features of the patterns produced by the extravasating microspheres. These are illustrated in Figure 20 together with the nomenclature that will be used in the remainder of the thesis.

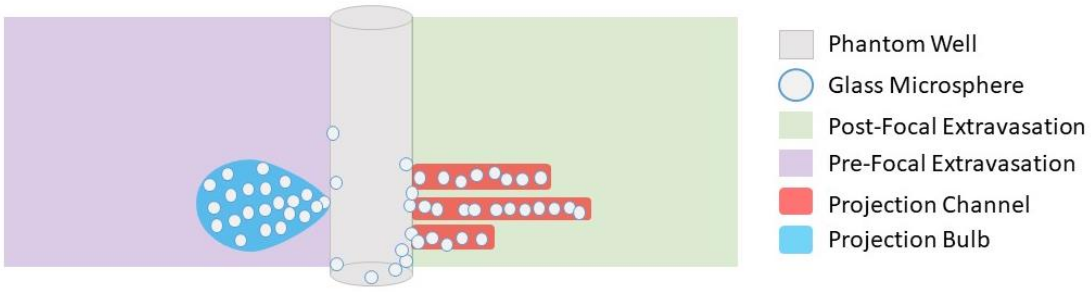


Figure 20: Schematic for the labelling of microsphere extravasation from a vertical cavity (well). Ultrasound is applied from left to right in the image above. The projection bulb is thought to be brought about by pre-focal turbulence of the glass microspheres eroding the soft pre-focal agar.

2.4.1.Phantom Well

This is the void or cavity created by the removal of the stepped cylindrical stainless steel rod from the fixed hydrogel phantom (See Section 2.2.4), simulating the cavity created during tumour resection. Upon injection into the well, the microspheres settle to the bottom due to their weight and the vertical orientation of the well.

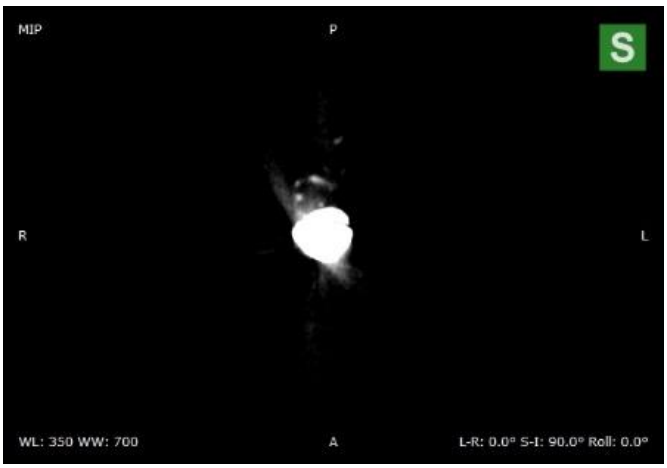


Figure 21: Microspheres sedimented at the bottom of a vertically orientated 4mm well, appearing bright white after MIP of a 3D reconstruction acquired via µCT analysis. MIP from a 3D reconstruction, FOV 30mm.The rounded bottom edge is as a result of the agar boundary flexing under the additional weight of the microspheres and cavitation nuclei.

2.4.2.Microsphere Projection

"Projection" in this context describes the movement of a microsphere or cluster of microspheres outside of the original well, and includes both the pre-focal and post-focal extravasation of microspheres. Both linear and planar projections were observed. Linear projections extend at a fixed angle and in a single direction away from the well; appearing as lines or streaks away from their original position in the CT images (Figure 22 a). Planar projections extend in a singular plane at a random angle away from a fixed point, not necessarily at the well or boundary interface. These appear as flat elliptical shapes, with

radiopaque microspheres distributed towards the outermost edge of the projection (Figure 22 b).

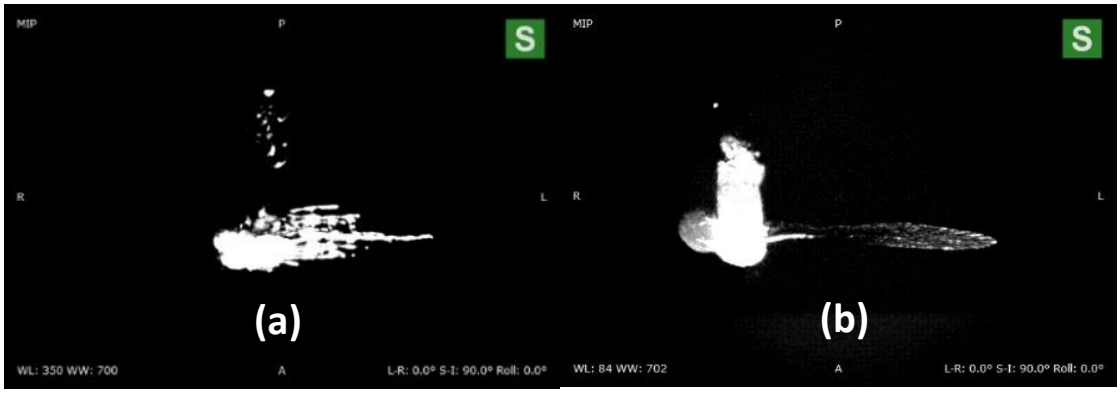


Figure 22: Cavitation enhanced microsphere projection examples, linear (a) and planar (b). Ultrasound field is from left to right of the image. MIPs from 3D reconstructions, FOV's 30mm.

2.4.3.Projection Channels

Within the post-focal extravasation region distinct lines can be seen. These lines are glass microspheres which have been propelled though the agar and now reside within agar tunnels or 'projection channels' which have been formed (Figure 23). The channels are of various lengths, originate from various independent positions on the well edge. Projection channels may intersect and combine to form a single channel as the projection progresses. Projection channels always start at the well edge and extend solely into the post-focal region. Uneven microsphere distribution within the channel produced, causes some sections of the channel lumen to be invisible under µCT due to lack of radiopaque material. The 'tip' of the projection channel is the furthermost point away from the well boundary edge for any single projection channel and is often highlighted by concentrated microsphere packing, appearing as bright objects under µCT.

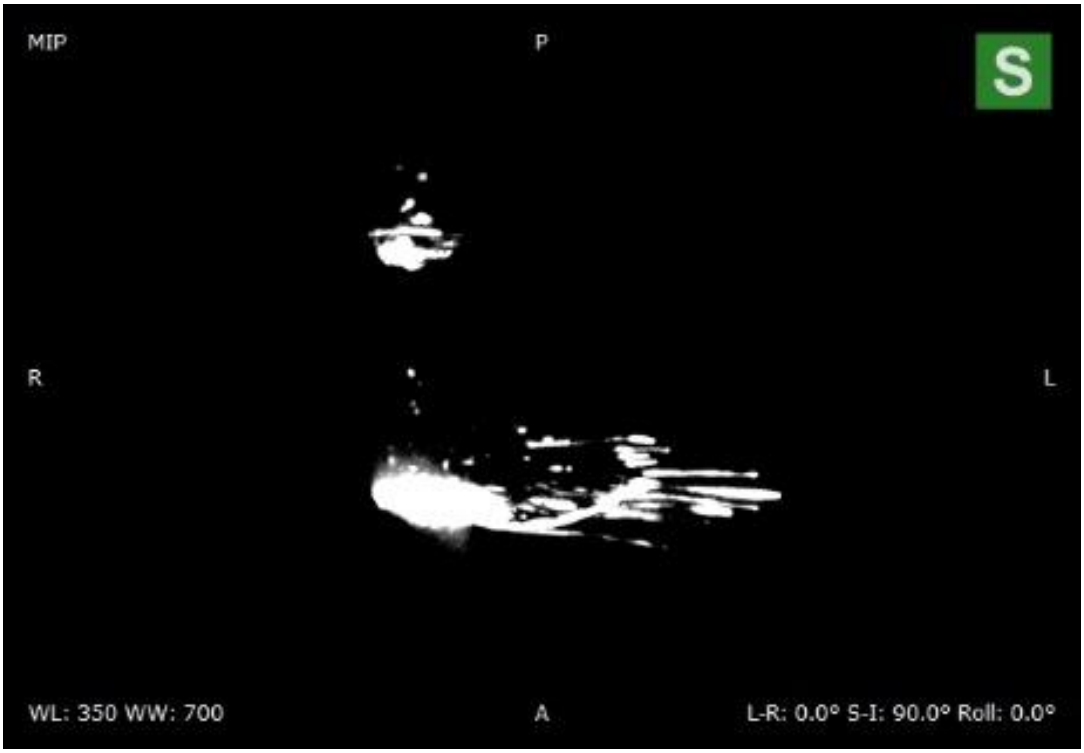


Figure 23: Numerous post-focal projection channels within a single microsphere projection. Individual channels are seen as straight white lines. In places where the channel has not been completely filled with radiopaque microspheres section of a channel appears black due to a lack of radiopaque material.

2.4.4.Projection Bulbs

Projection bulbs consist of a large void within the agar gel, with microspheres embedded at the edge of the void, which appear as large teardrop or spherical shapes within the pre-focal region (Figure 24). The size of the void created can be larger in diameter than the terminal diameter of the well cavity and may be accompanied by post-focal projections of various shapes and sizes. Projection bulbs are most frequently seen in combination with planar projections. The mechanisms by which the different features are formed are discussed in Chapter 4.

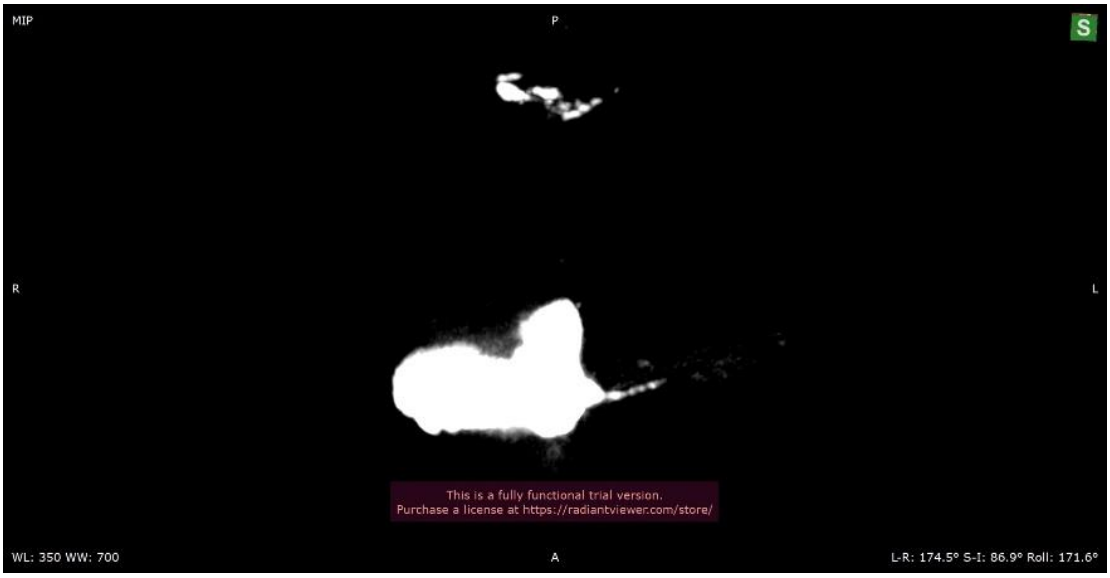


Figure 24: Large pre-focal projection bulb with single post projection channel. Relative density of the glass microspheres under µCT limits the view beneath the surface of the microsphere embedded projection bulb.

2.5. Discussion

Despite the limited resolution and FOV trade-off, the imaging and resolution of the projections produced has been shown to be sufficient for quantifying microsphere distribution. The interpretation of the images produced however still poses a significant challenge. Without un-biased, repeatable and preferably automated interpretations of the projections, it is impossible to determine the impact of different ultrasound exposure conditions. The next chapter will therefore focus on the development of method for analysing and quantifying the microsphere projections.

It should also be noted that the simple uniform hydrogel, whilst analogous in terms of its mechanical acoustic properties, does also not accurately represent the target organ architecture. There are no voids, folds, feeding vessels, inter cranial fluid or irrigation fluids in the wells currently used. Whilst a range of well diameters was investigated to simulate the effect on microsphere extravasation, the cavities used are far smaller than that of a GBM resection cavity. It is expected that adjustments to the current practise will therefore need to

be made; to produce a cavity of the intended size within the target area, allowing the ultrasound enhanced distribution of the radioembolic microspheres. With the removal and aspiration of the remaining malignant tissue and subsequent aspiration of the final resection cavity, occurring after the radioactive microspheres have been adequately distributed.

The pre-focal projection bulbs are an undesirable phenomenon which should be avoided and removed where possible. This is because the tear-drop shape of the bulb is an example of poor microsphere distribution within a given volume and dramatically increases the amount of collateral tissue removed from the patient; this approach is mechanically destructive, non-selective and not the intended, more selective radiotherapy approach.

Nonetheless, the results presented do confirm that ultrasound induced cavitation can be used to promote extravasation of microspheres using commercially available microbubbles and ultrasound exposure parameters comparable to those used in current therapeutic applications.

2.6. Conclusion

Two potential tissue mimicking phantoms were investigated, with agar found be the most consistent, reliable and suitable hydrogel for this application. Apparatus for creating phantoms containing cavities to simulate a post-resection tumour cavity and exposing them to ultrasound was designed and built. Ultrasound parameters were identified under which microsphere extravasation could be observed and a method for imaging the resulting spatial distribution of microspheres using µCT was developed. Descriptive nomenclature for the observed microsphere extravasation was also defined. In the next chapter a method for analysing the µCT images of the projections and quantifying microsphere transport and the anticipated radiation field is proposed. Statistical models are produced for the attributes measured, allowing separation and weighting of the key factors which contribute to the

extravasation of the microspheres. Parameter trends are discussed for translation towards the intra-cranial deposition of radioembolic microspheres, for the treatment of GBM.

2.6.1.Limitations

Whilst the work within this chapter is largely positive, there are a few key limitations to the work produced. Firstly, the use of an agar-agar hydrogel does not fully imitate the intended tissue architecture and is an oversimplification only of the elastic modulus. There are no elements of the tissue phantom design which address the tissue vascularity, the supporting structures (cerebral fluid and skull) or the innate homogeneity of the brain tissue.

The phantom wells are an order of magnitude smaller, than the average resection cavity produced (approximately 40 mm) and exploit the directionality of the focussed ultrasound transducer. Whereas the envisioned therapy is expected to use an un-focussed ultrasonic device, which may also reduce the occurrence of the unwanted pre-focal extravasation. It is foreseeable however that the order of the resection procedure could be altered, so that channels or wells could be produced if needed in the malignant tissue via ultrasonic erosion and aspiration. Creating voids akin to that of the wells used in the tissue phantom. Changing the size of the cavity however will influence the settling of the microspheres and may impact the resultant projections formed.

Finally, images of the microsphere distributions are unlikely to be visible *in vivo* using CT. SPECT imaging of the 0.01% gamma ray emissions from the glass microspheres is possible, although the subsequent image quality obtained is likely to be insufficient due to the low gamma energy output of the radioactive microspheres. Alternative intra-cranial imaging techniques may have to be investigated in order to be able to map the distribution of the glass microspheres post-operation.

References

1. Vellayappan, B. *et al.* Re-Irradiation for Recurrent Glioblastoma Multiforme (GBM) : Systematic Review and Meta-Analysis. *Int. J. Radiat. Oncol.* **99**, E114 (2017).

2. Dumitru, C. A., Sandalcioglu, I. E. & Karsak, M. Cannabinoids in glioblastoma therapy: New applications for old drugs. *Front. Mol. Neurosci.* **11**, 1–7 (2018).

3. Gallego, O. Nonsurgical treatment of recurrent glioblastoma. *Curr. Oncol.* **22**, e273–e281 (2015).

4. Gulati, S., Jakola, A. S., Johannesen, T. B. & Solheim, O. Survival and treatment patterns of glioblastoma in the elderly: A population-based study. *World Neurosurg.* **78**, 518–526 (2012).

5. Cha, G. D. *et al.* Advances in drug delivery technology for the treatment of glioblastoma multiforme. *J. Control. Release* **328**, 350–367 (2020).

6. Krieg, S. M. *et al.* Surgery of highly eloquent gliomas primarily assessed as non-resectable: Risks and benefits in a cohort study. *BMC Cancer* **13**, 1 (2013).

7. Thanasupawat, T. *et al.* Dovitinib enhances temozolomide efficacy in glioblastoma cells. *Mol. Oncol.* **11**, 1078–1098 (2017).

8. Chaichana, K. L. *et al.* Risk of surgical site infection in 401 consecutive patients with glioblastoma with and without carmustine wafer implantation. *Neurol. Res.* **37**, 717–726 (2015).

9. Grabowski, M. M. *et al.* Residual tumor volume versus extent of resection: predictors of survival after surgery for glioblastoma. *J. Neurosurg.* **121**, 1115–1123 (2014).

10. Maccabi, A. *et al.* An examination of the elastic properties of tissue-mimicking phantoms using vibro-acoustography and a muscle motor system. *Rev. Sci. Instrum.* **87**, 1–7 (2016).

11. Wolbarst, Anthony B., et al. Sketches of the Standard Imaing Modalities. in *Medical Imaging: Essentials for Physi* 1–36 (2013).

12. Vinet, L. & Zhedanov, A. A 'missing' family of classical orthogonal polynomials. *J. Phys. A Math. Theor.* **44**, 085201 (2011).

13. Stewart, D. C., Rubiano, A., Dyson, K. & Simmons, C. S. Mechanical characterization of human brain tumors from patients and comparison to potential surgical phantoms. *PLoS One* **12**, 1–19 (2017).

14. Forte, A. E., Galvan, S., Manieri, F., Rodriguez y Baena, F. & Dini, D. A composite hydrogel for brain tissue phantoms. *Mater. Des.* **112**, 227–238 (2016).

15. Franceschini, G., Bigoni, D., Regitnig, P. & Holzapfel, G. A. Brain tissue deforms similarly to filled elastomers and follows consolidation theory. *J. Mech. Phys. Solids* **54**, 2592–2620 (2006).

16. Goeller, J., Wardlaw, A., Treichler, D., O'Bruba, J. & Weiss, G. Investigation of Cavitation as a Possible Damage Mechanism in Blast-Induced Traumatic Brain Injury. *J. Neurotrauma* **29**, 1970–1981 (2012).

17. Opitz, A., Falchier, A., Linn, G. S., Milham, M. P. & Schroeder, C. E. Limitations of ex vivo measurements for *in vivo* neuroscience. *Proc. Natl. Acad. Sci.* **114**, 5243–5246 (2017).

18. Goldstein, L. E. *et al.* Chronic traumatic encephalopathy in blast-exposed military veterans and a blast neurotrauma mouse model. *Sci. Transl. Med.* **4**, (2012).

19. Grashow, R. *et al.* Premortem Chronic Traumatic Encephalopathy Diagnoses in Professional Football. *Ann. Neurol.* **88**, 106–112 (2020).

20. van den Bedem, H. & Kuhl, E. Molecular mechanisms of chronic traumatic encephalopathy. *Curr. Opin. Biomed. Eng.* **1**, 23–30 (2017).

21. Reintjes, M. A Note on Incompressibility of Relativistic Fluids and the Instantaneity of their Pressures. *Reports Math. Phys.* **82**, 113–120 (2018).

22. William D. Callister, J. with special contributions by D. G. R. *Materials science and engineering: an introduction*. (New York: John Wiley & Sons, 2007).

23. Wells, P. N. T. & Liang, H. Medical Ultrasound - imaging of soft tissue strain and elasticity. *J. R. Soc. Interface* **8**, 1521–1549 (2011).

24. Jiang, S., Liu, S. & Feng, W. PVA hydrogel properties for biomedical application. *J. Mech. Behav. Biomed. Mater.* **4**, 1228–1233 (2011).

25. Patel, D. M., Agarwal, N., Tomei, K. L., Hansberry, D. R. & Goldstein, I. M. Optimal Timing of Whole-Brain Radiation Therapy Following Craniotomy for Cerebral Malignancies. *World Neurosurg.* **84**, 412–419 (2015).

26. Fatemi, P., Zhang, M., Miller, K. J., Robe, P. & Li, G. How Intraoperative Tools and Techniques Have Changed the Approach to Brain Tumor Surgery. *Curr. Oncol. Rep.* **20**, (2018).

27. Smith, S. J. *et al.* The invasive region of glioblastoma defined by 5ALA guided surgery has an altered cancer stem cell marker profile compared to central Tumour. *Int. J. Mol. Sci.* **18**, 1–13 (2017).

28. Roessler, K., Becherer, A., Donat, M., Cejna, M. & Zachenhofer, I. Intraoperative tissue fluorescence using 5- aminolevolinic acid (5-ALA) is more sensitive than contrast MRI or amino acid positron emission tomography (18F-FET PET) in glioblastoma surgery. *Neurol. Res.* **34**, 314–317 (2012).

29. and Claudins (. 2018 (2018).

30. Cho, D. Y. *et al.* The role of cancer stem cells (CD133+) in malignant gliomas. *Cell Transplant.* **20**, 121–125 (2011).

31. Tang, Z. *et al.* Deep Learning of Imaging Phenotype and Genotype for Predicting Overall Survival Time of Glioblastoma Patients. *IEEE Trans. Med. Imaging* **39**, 2100–2109 (2020).

32. Boiardi, A. *et al.* Treatment of recurrent glioblastoma: Can local delivery of mitoxantrone improve survival? *J. Neurooncol.* **88**, 105–113 (2008).

33. Frosina, G. Advances in drug delivery to high grade gliomas. *Brain Pathol.* **26**, 689–700 (2016).

34. Weller, M., Cloughesy, T., Perry, J. R. & Wick, W. Standards of care for treatment of recurrent glioblastoma-are we there yet? *Neuro. Oncol.* **15**, 4–27 (2013).

35. Hegi, M. E. *et al.* MGMT Gene Silencing and Benefit from Temozolomide in Glioblastoma . *N. Engl. J. Med.* **352**, 997–1003 (2005).

36. Hicks, J. *et al.* Intratumoral temozolomide in spontaneous canine gliomas: feasibility of a novel therapy using implanted microcylinders. *Vet. Med. Sci.* **5**, 5–18 (2019).

37. Hvizdos, K. M. & Goa, K. L. Temozolomide. **12**, 237–243 (1999).

38. Yoon, H. J. *et al.* Cold water fish gelatin methacryloyl hydrogel for tissue engineering application. *PLoS One* **11**, (2016).

39. Markert, C. D. *et al.* Characterizing the micro-scale elastic modulus of hydrogels for use in regenerative medicine. *J. Mech. Behav. Biomed. Mater.* **27**, 115–127 (2013).

40. Huang, D. *et al.* Viscoelasticity in natural tissues and engineered scaffolds for tissue reconstruction. *Acta Biomater.* doi:10.1016/j.actbio.2019.08.013.

41. Liu Tsang, V. & Bhatia, S. N. Three-dimensional tissue fabrication. *Adv. Drug Deliv. Rev.* **56**, 1635–1647 (2004).

42. Long, R. & Hui, C. Y. Fracture toughness of hydrogels: Measurement and interpretation. *Soft Matter* **12**, 8069–8086 (2016).

43. Ouwerx, C., Velings, N., Mestdagh, M. M. & Axelos, M. A. V. Physico-chemical properties and rheology of alginate gel beads formed with various divalent cations. *Polym. Gels Networks* **6**, 393–408 (1998).

44. Chan, E. S. *et al.* Effect of formulation of alginate beads on their mechanical behavior and stiffness. *Particuology* **9**, 228–234 (2011).

45. Cendon, F. V., Salomão, B. B., Jorge, R. M. M. & Mathias, A. L. Mechanical and optical evaluation of alginate hydrospheres produced with different cross-linking salts for industrial application. *Colloid Polym. Sci.* **299**, 693–703 (2021).

46. McGarry, C. K. *et al.* Tissue mimicking materials for imaging and therapy phantoms: a review. *Phys. Med. Biol.* (2020) doi:10.1088/1361-6560/abbd17.

47. Wang, C., Tong, X. & Yang, F. Bioengineered 3D brain tumor model to elucidate the effects of matrix stiffness on glioblastoma cell behavior using peg-based hydrogels. *Mol. Pharm.* **11**, 2115–2125 (2014).

48. Chanda, A., Callaway, C., Clifton, C. & Unnikrishnan, V. Biofidelic human brain tissue surrogates. *Mech. Adv. Mater. Struct.* **0**, 1–7 (2016).

49. Kumar, A. & Han, S. S. PVA-based hydrogels for tissue engineering: A review. *Int. J. Polym. Mater. Polym. Biomater.* **66**, 159–182 (2017).

50. Daza Agudelo, J. I., Badano, J. M. & Rintoul, I. Kinetics and thermodynamics of swelling and dissolution of PVA gels obtained by freeze-thaw technique. *Mater. Chem. Phys.* **216**, 14–21 (2018).

51. Meirza, B. Development of Vessel Phantoms for Ultrasound Methods. *Thesis Lund Univ.* 73 (2017).

52. Ye, M., Mohanty, P. & Ghosh, G. Morphology and properties of poly vinyl alcohol (PVA) scaffolds: Impact of process variables. *Mater. Sci. Eng. C* **42**, 289–294 (2014).

53. Culjat, M. O., Goldenberg, D., Tewari, P. & Singh, R. S. A review of tissue substitutes for ultrasound imaging. *Ultrasound Med. Biol.* **36**, 861–873 (2010).

54. Fukumori, T. & Nakaoki, T. High-tensile-strength polyvinyl alcohol films prepared from freeze/thaw cycled gels. *J. Appl. Polym. Sci.* **131**, n/a-n/a (2014).

55. Drakos, T., Giannakou, M., Menikou, G., Constantinides, G. & Damianou, C. Characterization of a soft tissue-mimicking agar/wood powder material for MRgFUS applications. *Ultrasonics* **113**, (2021).

56. Maccabi, A. *et al.* Quantitative characterization of viscoelastic behavior in tissue-mimicking phantoms and ex vivo animal tissues. *PLoS One* **13**, 1–18 (2018).

57. Cafarelli, A. *et al.* Tuning acoustic and mechanical properties of materials for ultrasound phantoms and smart substrates for cell cultures. *Acta Biomater.* **49**, 368–378 (2017).

58. Lea-Banks, H., Stride, E. & Coussios, C. C. Ultrasound-mediated transport of nanoparticles and the influence of particle density. *University of Oxford* (2016). doi:10.1121/1.4950210.

59. Suomi, V., Edwards, D. & Cleveland, R. Optical Quantification of Harmonic Acoustic Radiation Force Excitation in a Tissue-Mimicking Phantom. *Ultrasound Med. Biol.* **41**, 3216–3232 (2015).

60. Paris, J. L. *et al.* Ultrasound-mediated cavitation-enhanced extravasation of mesoporous silica nanoparticles for controlled-release drug delivery. *Chem. Eng. J.* **340**, 2–8 (2018).

61. Hall, L. M. Bassel Rifai Cavitation-Enhanced Delivery of Therapeutics to Solid Tumors. (2011).

62. Boral, S., Saxena, A. & Bohidar, H. B. Universal growth of microdomains and gelation transition in agar hydrogels. *J. Phys. Chem. B* **112**, 3625–3632 (2008).

63. Mannaris, C. *et al.* Microbubbles, Nanodroplets and Gas-Stabilizing Solid Particles for Ultrasound-Mediated Extravasation of Unencapsulated Drugs: An Exposure Parameter Optimization Study. *Ultrasound Med. Biol.* **00**, 1–14 (2019).

64. Yemane, P. T. *et al.* Effect of Ultrasound on the Vasculature and Extravasation of Nanoscale Particles Imaged in Real Time. *Ultrasound Med. Biol.* **45**, 3028–3041 (2019).

65. Rajagopal, S., Sadhoo, N. & Zeqiri, B. Reference Characterisation of Sound Speed and Attenuation of the IEC Agar-Based Tissue-Mimicking Material Up to a Frequency of 60MHz. *Ultrasound Med. Biol.* **41**, 317–333 (2015).

66. Yao, L. *et al.* Facilitated brain delivery of poly (ethylene glycol)-poly (lactic acid) nanoparticles by microbubble-enhanced unfocused ultrasound. *Biomaterials* **35**, 3384–3395 (2014).

67. Caskey, C. F., Qin, S., Dayton, P. A. & Ferrara, K. W. Microbubble tunneling in gel phantoms. *J. Acoust. Soc. Am.* **125**, EL183 (2009).

68. Acconcia, C., Leung, B. Y. C., Manjunath, A. & Goertz, D. E. Interactions between Individual Ultrasound-Stimulated Microbubbles and Fibrin Clots. *Ultrasound Med. Biol.* **40**, 2134–2150 (2014).

69. Yamakoshi, Y. & Miwa, T. Observation of microhollows produced by bubble cloud cavitation. *Jpn. J. Appl. Phys.* **51**, (2012).

70. Song, J. H., Moldovan, A. & Prentice, P. Non-linear Acoustic Emissions from Therapeutically Driven Contrast Agent Microbubbles. *Ultrasound Med. Biol.* **45**, 2188–2204 (2019).

71. Lin, Y. *et al.* Effect of acoustic parameters on the cavitation behavior of SonoVue microbubbles induced by pulsed ultrasound. *Ultrason. Sonochem.* **35**, 176–184 (2017).

72. Song, J. H., Moldovan, A. & Prentice, P. Non-linear Acoustic Emissions from Therapeutically Driven Contrast Agent Microbubbles. *Ultrasound Med. Biol.* (2019) doi:10.1016/j.ultrasmedbio.2019.04.005.

73. Althomali, M. A. M., Wille, M. L., Shortell, M. P. & Langton, C. M. Estimation of mechanical stiffness by finite element analysis of ultrasound computed tomography (UCT-FEA); a comparison with X-ray µCT based FEA in cancellous bone replica models. *Appl. Acoust.* **133**, 8–15 (2018).

74. Hagenmüller, H. *et al.* Non-invasive time-lapsed monitoring and quantification of engineered bone-like tissue. *Ann. Biomed. Eng.* **35**, 1657–1667 (2007).

75. Spin-Neto, R., Marcantonio, E., Gotfredsen, E. & Wenzel, A. Exploring CBCT-based DICOM files. A systematic review on the properties of images used to evaluate maxillofacial bone grafts. *J. Digit. Imaging* **24**, 959–966 (2011).

76. Garea-Rodríguez, E. *et al.* Visualizing dopamine transporter integrity with iodine-123-FP-CIT SPECT in combination with high resolution MRI in the brain of the common marmoset monkey. *J. Neurosci. Methods* **210**, 195–201 (2012).

77. Ackerly, T., Geso, M., O'Keefe, G. & Smith, R. Stereotactic radiosurgery planning with ictal SPECT images. *Australas. Phys. Eng. Sci. Med.* **27**, 136–147 (2004).

CHAPTER 3

In Silico Analysis and Interpretation of Cavitation Induced Projections of Glass Microspheres

3. In Silico Analysis and Interpretation of Cavitation Induced Projections of Glass Microspheres

3.1. Introduction

Current guidelines do not recommend the post-delivery imaging of YAS microspheres, due to the risk of legal action if off target delivery is identified. As previously mentioned, only preliminary arterial mapping using macro-aggregated albumin (^{99m}Tc-MAA) is used to plan the delivery procedure and predict what fraction of the spheres may be lost via lung shunting. Moreover, at the spatial resolution available in typical clinical scanners it is not possible to visualise individual glass YAS microspheres, only clusters of microspheres in close proximity to one another. In order to quantify the distribution of any microsphere extravasation, whether in vitro or *in vivo*, a suitable imaging modality is required. In a research context, various analytical methods (CT[1–6], SPECT[2,7–10], PET[1,2,5–8,11,12], Fluoroscopy[13,14])have been employed with the aim of imaging YAS microspheres, but to date no single technique has been capable of resolving individual YAS beads within patients to an acceptable level. Whilst x-ray computed tomography has the potential to image objects smaller than a micrometre, the technique's resolution is limited by the need for a relatively wide field of view (FOV). Decreasing the FOV dramatically increases the scan time as well as the post-imaging processing required to 'stitch' multiple acquisitions together for analysis.

In the previous chapter, the feasibility of producing projections of glass microspheres using ultrasound enhanced cavitation events and imaging them using microcomputed tomography (μCT), was demonstrated. The interpretation and thresholding of these images was however found to be heavily biased by the user.

The work within this chapter therefore focusses on the production of a method and associated MATLAB code, to automate the interpretation of 3D reconstructed images obtained using the

DICOM file stacks produced from the Quantum FX µCT instrument. The data generated are then used to determine which experimental parameters are key to producing microsphere extravasation.

A debt of gratitude is given to Cameron Smith (BUBBL group, IBME, Oxford University, UK), for his considerable patience with the author and continued support regarding the interpretation automation. Areas of collaborative work with are highlighted where appropriate.

3.2. Methods

As tumour volumes are approximated in size by physicians [15,16] due to the margins of the tumour mass, it is important to be confident in the coverage of radiation dose encompassing the tumour margins beyond the anticipated resection cavity. The diameter of the individual microspheres is 15-32 µm and the depth of irradiation from each sphere is ~2.5 mm.

Whilst initial experiments in Chapter 2 using the Quantum FX µCT machine produced images suitable for qualitative analysis of the microsphere extravasation, current commercially available software for medical imaging is largely orientated towards the image filtering and measurements of a single large object within a given volume (e.g. tumour mass). Here, however, it is necessary to use multiple image points and measurements to estimate a given volume, i.e. the therapeutically relevant levels of radiation emitted from the YAS glass microspheres. The limitations of the measurement systems available in the commercial software (e.g. RadiAnt, Inversalius) meant that a bespoke MATLAB script needed to be written to import, interpret and measure the image stacks obtained from the µCT to produce un-biased quantitative measurement data of the microsphere distributions produced from each experimental run.

3.2.1.Minimum-volume enclosed ellipsoid (MVEE)

Previous work by Thompson et al[17] compared the use of *in vivo* cone beam CT under various peak kilovoltages (kVp) against excised tissue samples for µCT images of radiopaque beads (ROBs) after hepatic embolization in a swine model. Due to the natural variation of anatomy within the study, the authors coined a novel term to describe the volume which encompassed the total distribution of the static radiopaque microspheres, the minimum-volume enclosed ellipsoid (MVEE). The use of MVEE as a metric was initially used to compare the total volume of tissue which contained ROBs via differing imaging techniques and not to produce quantitative measurements of objects within the volume encompassed. The Khachiyan algorithm script was kindly provided by the authors (Nima Moshtagh, University of Pennsylvania, Appendix 1).

Whilst the cold surrogate spheres used previously (See Chapter 2) do not occupy a particularly large volume within the agar hydrogel, their high relative density and subsequent radiopacity produce images with particularly high contrast. Using the MVEE metric, we can simulate volume distribution of the encompassed microspheres and the subsequent radiation coverage. This differs to current approach used for TheraSphere® of inter-arterial delivery of the radioembolic spheres which rely on extensive pre-planning and mapping of the vasculature using MAA.

3.3. Single Well Elimination Microsphere Projection Interpretation

The majority of the images obtained from the Quantum FX µCT machine correspond to a circular field of view (FOV) 30 mm in diameter chosen by the operator. Each image capture produces 512 image slices of 512x512 pixels slices along a 30 mm long cylinder. As the X-ray detector moves around the centrally fixed object in a circular fashion, the 3D reconstruction is therefore a cylinder, 30mm in diameter and 30mm in length, not a perfect 30mm cuboid. A 30

mm FOV was sufficient to capture a single well and the majority of projections observed, including the pre and post focal extravasation, whilst maximising resolution of the images obtained. Projections which were particularly large and which required an increased FOV, used the same method for interpretation but with adjustments made for the change in relative distance observed.

With help a MATLAB algorithm was produced to identify the microspheres distributed within the projections produced using the in vitro setup (Section 2.2.4) and quantify their distances from one another. Measurements of the microspheres are split into pre and post focal extravasation, with both quantified in terms of their respective height, width and length (See Section 2.4, Figure 20). The angle of extravasation through the tissue phantom, perpendicular to the acrylic mould, would be generated in addition to the MVEE of the entire projection (pre and post focal). The MVEE volume would be used to extrapolate the anticipated beta radiation field over the anticipated tumour margins.

Using a script in MATLAB (See Appendix 2), each DICOM image series, corresponding to a single well and projection, is imported as a 3D array. The values within the array correspond to the intensity (brightness) of the voxels and are thresholded between 1521 (226 HU) and 4366 (3071 HU), using a 11586 scale (-1295 to 10290, including zero, defined by the Quantum FX μCT). This creates a binary array, with 1 corresponding to the presence of beads; segregating the voxels containing any radiopaque dense material (YAS glass microspheres) from the surrounding soft hydrogel.

To remove artefacts caused by the presence of screws or distant leaks in the gel, which caused microsphere pooling on the base of the mould, voxels that are more than 6 mm away from the bulk microsphere extravasation from the well were excluded. To identify these artefact voxels, each binary voxel is increased in size by 3 mm, whilst keeping its original central position, voxels which are close to one another overlap. The overlapping voxels produce a single large

connected object, all other unconnected points are reduced to a value of zero, removing them from the reconstruction.

The stainless steel rods used for the formation of well cavities (See Section 2.2.4), have a terminal section with diameters of either 1 or 2mm (the diameter at the end of the well) which changes to 4 mm after 10 mm of height. This abrupt diameter step produces a ledge in the agar, which microspheres frequently stick to (Figure 25). Additionally, microspheres occasionally stick to the vertical well walls during deposition; both observations cause imaging artefacts during the reconstruction, as they are not a part of the intended microsphere extravasation and distort quantification measurements. To remove the voxels corresponding to the volume of the well, the code searches for a 4 mm cylindrical object (corresponding to the stainless steel rods maximum diameter) at the top of the image using a circular shape detection algorithm. As all the images are acquired in a vertical orientation, this corresponds to the widest point of the stainless steel rod used to form the well.

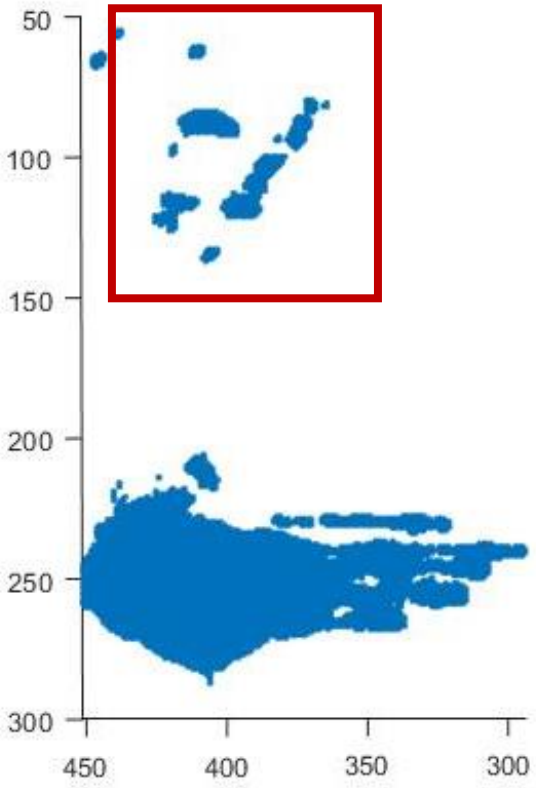


Figure 25: Mould 26 well 3 voxel reconstruction. Area highlighted in red show deposition artefacts, not part of the main projection at the bottom of the well, which need removal for projection processing and quantification.

This identification is done by summing the 3D binary space to produce a 2D intensity map showing the axial and lateral positions of the beads. This is then convolved with a circular shape where 3.5 to 4.5 mm diameter = 1 (to account for slight discrepancies in the rod manufacture), 3.2 to 3.5 mm diameter = -1, and 4.5 to 4.8 mm = -1. This convolved image will have a maximum at the centre of the well. Microspheres within the 4mm cylindrical well are removed throughout the entire 3D image, along with any microspheres in the top half of the image.

As the exact placement of the well within the image changes, due to manual operation of the Quantum FX machine, the centre of the 4mm well is used as a point of reference for further measurements.

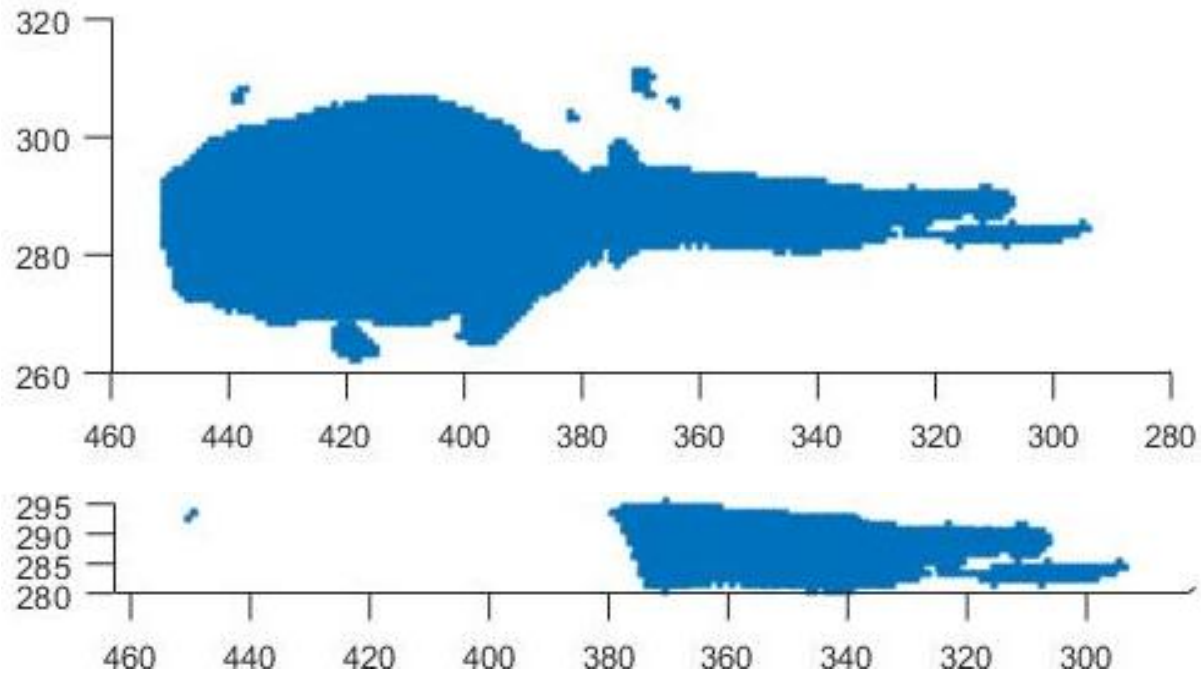


Figure 26: Removal of the 4mm cylindrical well from mould 26, well 3.

A surface mesh of the 3D matrix was found to reduce computation time and memory requirements for the later parts of this procedure. The reconstructed image skin is split using the central point of the well, into the pre and post microsphere extravasations. With the width and height measured by the distance from the fifth greatest (max-5) to the fifth smallest (min+5) voxels containing microspheres, in both planes. This is achieved by summing the 3D binary matrix in the direction of the ultrasound propagation, to produce a 2D matrix with values greater than one, representing the number of voxels which contained microspheres. For the depth measurement the same method was used, but the fifth greatest voxel was compared to the centre point of the well. The fifth value was chosen for all axes to improve the robustness of the algorithm's measurements, by initially manually counting the number of spheres that were frequently disconnected from the end of the largest surface mesh object.

3.3.1.Predicting ^{90}Yttrium β Radiation Emission from Glass Microspheres

To estimate the area of radiation exposure or 'kill zone' the voxels of the image were dilated by 2 mm, a conservative beta radiation penetration depth in human tissue[18]. Following which the Khachiyan algorithm is used to place a MVEE around the voxels containing microspheres in the projection image, with a 5% tolerance. The voxel location furthest from the centre of the ellipse is found, a straight line is fitted between this point and the centre of the ellipse, providing the dominant angle for the bulk of the microsphere projection.

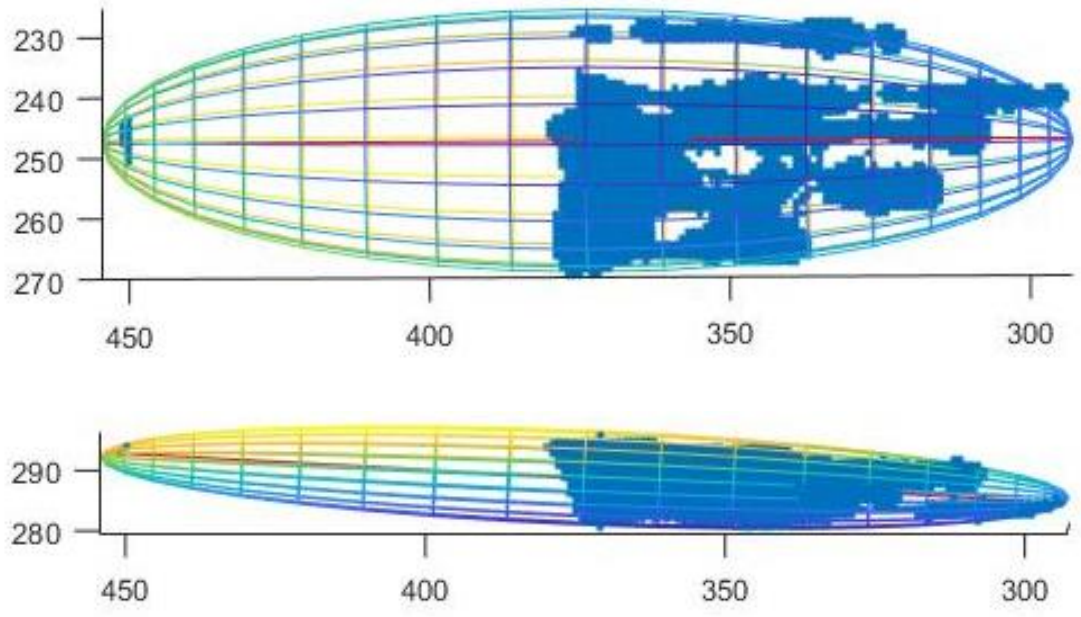


Figure 27: MVEE fitted to mould 26 well 3 after removal of the 4 mm well cylinder. Angle of the bulk microsphere projection can be seen more clearly on the bottom image. Colours are a visual aid for the reader only.

The killzone % is defined as the percentage of the MVEE volume, which is covered by the kill zone volume, the field of the radiation emitted from the microspheres contained within the enclosed ellipsoid. The values are then saved as an output MATLAB file for manual transfer to an Excel spreadsheet, for import into MiniTab (See Section 3.3.1).

3.3.2.Factorial Design – Response Surface

Producing ultrasound induced microsphere projection uses a number of both physical and acoustic parameters as experimental variables, the majority of which are continuous as numerical values e.g. fundamental frequency, peak negative pressure, in order to model the effects of how each parameter responds over a variety of input conditions. To produce a full factorial of all of the potential parameter combinations an immense number of experimental runs would be required. This is calculated as the number of levels to the power of the number of factors i.e. investigating 3 factors each with 2 levels would be $2^3 = 8$ to cover all combinations, ignoring required run iterations[19].

Statistical design of experiments (DoE)[20,21] can be used to evaluate parameter interactions whilst reducing the total number of experimental runs required, by estimating the remaining replicate data required using the data gathered based upon the observed variance. The variation of the data and model is statistically analysed to highlight key areas of interest or change within the input design space, typically as a factorial design[22] or reduced factorial design[23]; this enables order analysis of the response (linear, exponential, cubic etc).

A linear factorial design can be explained as the total of all possible first order products arising from a series of manually defined input arguments, with two levels (high and low), producing a long polynomial defining the relationships (factors) between the input arguments and the observed outputs[19]. The model tests all possible combinations of both the high and low levels, with the model (block) replicated, normally for a minimum of 40 samples, to test variability at each of the cubic points measured. In a simple linear model (Plackett-Burman[24]), the polynomial can be used to predict untested input arguments to accurately predict outcomes of interactions where the variation in the model is small, normally within the input ranges experimentally tested. This orientates the design towards optimisation of a known set of conditions, ideal for process improvement.

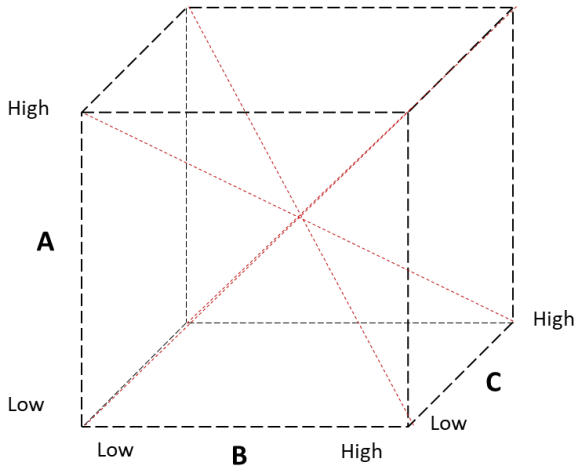


Figure 28: Cubic Factorial Design with high and low values, for three input variables. Red lines indicate primary interactions.

Traditional linear investigations varying a single parameter e.g. ultrasound duty cycle (DC) while fixing all other parameters, are unsuitable for investigating a wide number of parameters within a short space of time particularly when multiple parameters are collinear with each other. Collinearity changes the response of a single parameter based upon parameters that it is dependent upon, so data obtained under one given set of conditions will not be representative if the co-linear factor is also changed. Multi-collinearity produces highly complex parameter spaces with highly entangled factors and interactions making analysis of single parameters extremely difficult.

A surface response design[25] is a second order design which can be employed where there is less knowledge about the parameter space or interactions within it, frequently using parameters with more than two levels for each factor. It can be used to locate areas of interest with subsequently tighter parameter spaces, for further stringent investigation. Frequently this is in the form of a central composite design[26], which uses data points outside that of the desired ranges in combination with central points, to map the rate of change of a factor within the desired investigation parameter space. This utilises input arguments with more than two levels to each output argument.

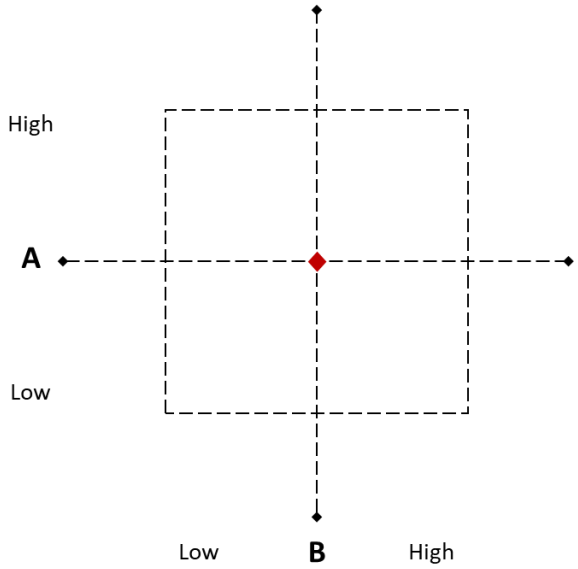


Figure 29: A single face of a central composite design. Values outside of the high low range are used to enable multiple levels within the high low range. Red indicates the centre point, used to assess non-linear factor response over the surface area.

3.3.3.Parameters Investigated

A variety of input parameters was investigated to generate the design space for investigation, these can be separated into two categories: physical and acoustic parameters. The acoustic parameters investigated were: fundamental frequency, peak negative pressure, duty cycle and the total number of cycles each phantom well was exposed to. The pulse repetition frequency (PRF) for all exposures was fixed at 3.3 Hz for all tests, as this was controlled independently from the waveform generator by the Verasonics® software and associated coding (See Fig. 3, Section 2.2.3).

The physical parameters investigated included: Microsphere size (within a given distribution), mass of microspheres deposited, cavitation agent, cavitation agent concentration and terminal well diameter (See section 2.2.2).

Outputs for the modelling were the variables generated by the code in Section 3.2.2. The height, width and length of the pre and post focal projections were analysed independently.

The total microsphere volume and expected irradiation volume of the projection as a whole were also measured.

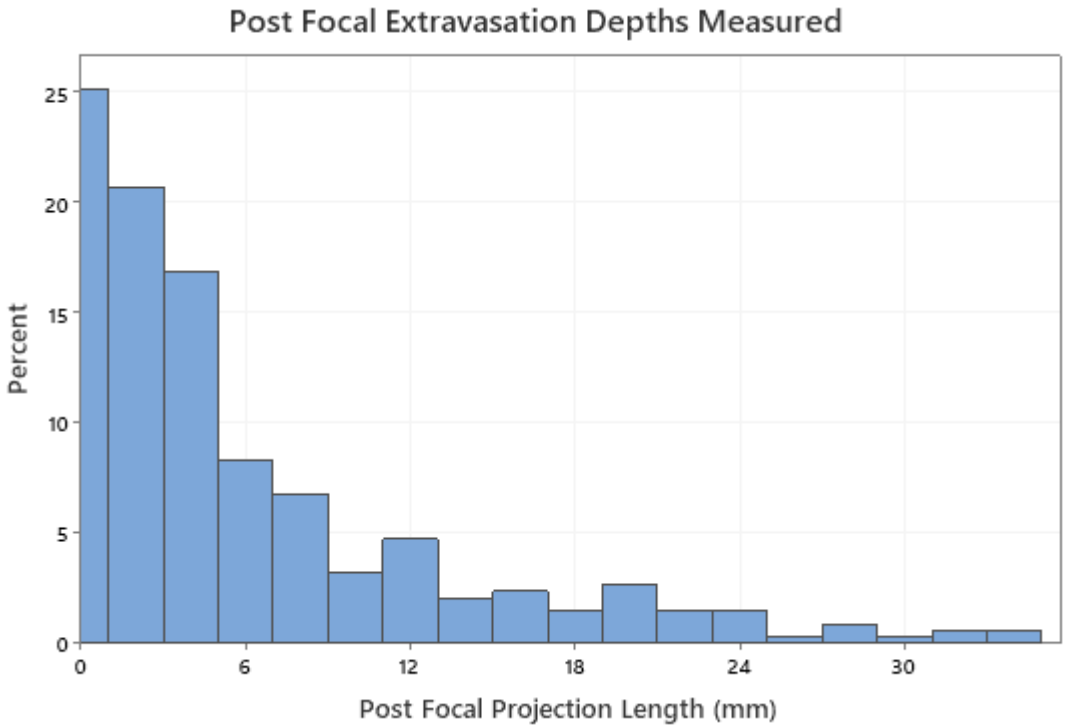
Initial discussions with Professor Plaha, a consultant neuro-oncology surgeon in the John Radcliffe Hospital, Oxford, stressed the importance of penetration depth as a key deliverable for the new technology if it were to be used intra-operatively as an adjuvant to the existing GBM resection practice. For example, previous investigations using intra-operative iodine-125 crystals for brachytherapy were unsuccessful, due to the low dose of irradiation (35 keV vs 2.28 MeV for ^{90}Y) to the surrounding area from the inserted crystals[27,28]. To improve the likelihood of success, the microspheres would need to be lodged within the brain tissue several millimetres or more beyond the original cavity generated by the aspiration of the tumour mass and with higher radiation emission.

This chapter therefore focusses primarily on how the variation of the input parameters affects the measured post-focal penetration depth, and the subsequent volume of tissue irradiated by the microspheres.

Some variables could not be estimated and are highlighted as such. This normally occurs for two cases; either a lack of data or repetitions for correct estimate of a sub population within each category (i.e. n is too low) or multicollinearity of the terms, where the independent terms themselves are dependent upon each other and cannot be separated, e.g. the driving frequency and cavitation agent, where a nanodroplet requires a different peak negative pressure to vaporise and then cavitate compared to a microbubble. As a large number of factors within the model, particularly the ultrasound parameters, are multicollinear (as indicated by the reported Variance Inflation Factor (VIF) value) this is a known limitation of the linear regression model and an oversimplification of the reported data, which is to be expected. Values above 5 for VIF are deemed multicollinear[29], some of the values in this model which could be calculated were in the thousands, indicating extreme co-dependency.

3.3.4.Post Focal Projection Depth Surface Design

Measurements obtained via the MATLAB algorithm in Section 3.2.2. were imported into MiniTab as a worksheet (Figure 30). A total of 9 primary factors, 7 of which were continuous (Frequency (A), peak negative pressure MPa (B), duty cycle % (C), total number of cycles (D), mass input g (F), cavitation concentration (H), terminal well diameter mm (J) and 2 categorical (YAS microsphere size distribution µm (E) and Cavitation agent (G)).



Statistics

Variable	N	N*	Mean	SE Mean	StDev	Minimum	Q1	Median	Q3	Maximum
Post Length (mm)	338	7	6.027	0.388	7.136	0.000	0.930	3.216	8.231	33.158

Figure 30: Post focal projection depths recorded over all parameter inputs (N = 338). N denotes the number of cells which did not have a numerical value in them, in this case n/a.*

Whilst it would have been preferable to use the microsphere diameter as a continuous variable, no supporting information were provided by the Supplier (MoSci) on each of the microsphere batches provided (chemical composition, relative density, surface finish, population distribution etc.) and so this would have only further increased the already large number of variables. Each batch was therefore deemed 'unique' and categorised as such to

minimise further unneeded complexity in the already heavily congested design space. Mould number was used to block the recorded data against the standard and run order. Blocking or grouping of certain experimental runs together is a useful tool for evaluating change over time where it is not possible to perform the entire DoE at a given time. Particularly useful for monitoring changes in equipment, operators or in this case variability in the agar used for each phantom mould.

Data entries with a standard residual larger than 3 were removed over 3 iterations, to remove extreme outliers from the data set, which could produce misleading results by changing the weighting of the model's coefficients. This can result in otherwise significant terms or interactions becoming insignificant due to extreme outliers. This resulted in the data set being reduced from N=338 down to N=325. No further reductions to the data set were made thereafter during the linear regression model analysis.

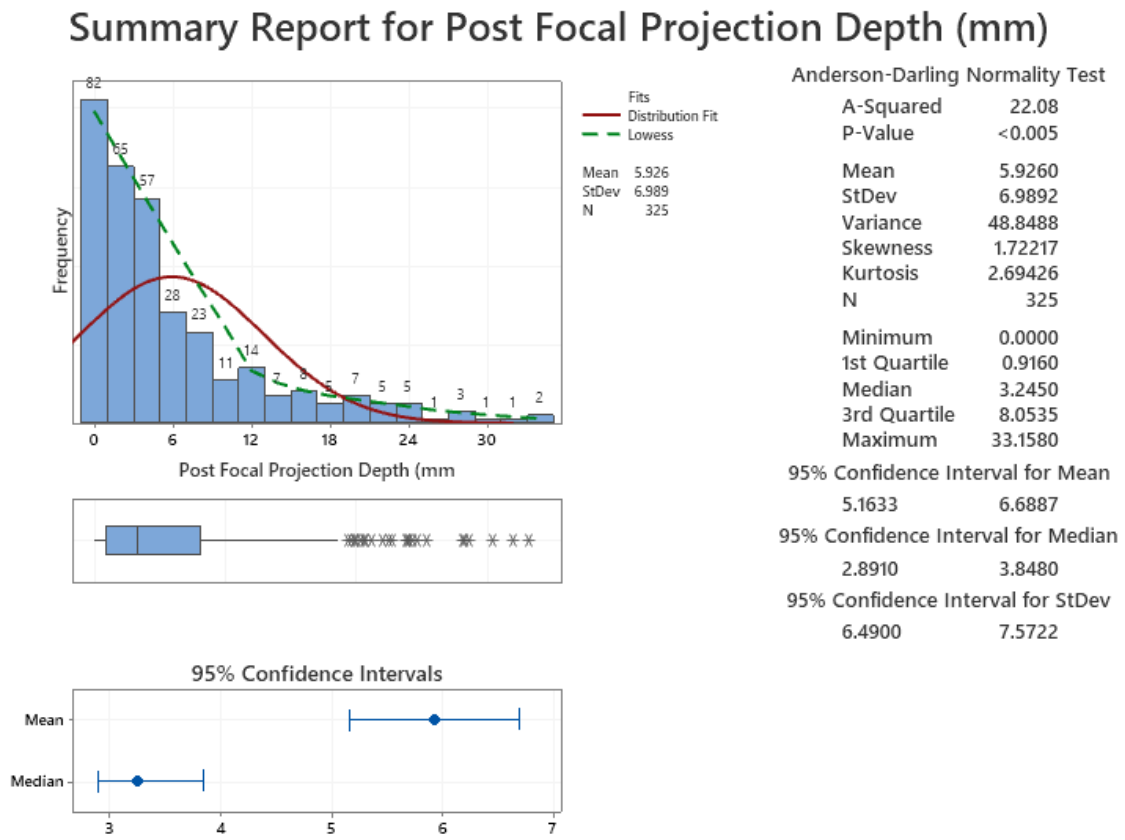


Figure 31: Frequency data for post focal projection depth after removal of large (>3) residuals over 3 iterations.

The recorded data are exponential, as indicated by the Anderson-Darling value being large (Figure 31, A-squared 22.08, p-value <0.005), with the mode (0) of the sample set being skewed away from the mean value (5.7737). Whilst removing all 0.000 values generated by the code would improve the normality of the data (AD 16.00, p<0.005) the data set would still appear exponential but would be subsequently suitable for transformations e.g. BOX-COX or Johnson transformations[30]. As the data can be fit to a second order polynomial, they are suitable for surface response linear regression but this is not the optimal approach. The non-linearity is caused by the multicollinearity of the input factors (variables). Isolating the factor with the highest weight was therefore used for further non-linear regression methods to generate a more accurate model of the post focal projection depth.

A response surface model was used to define the design of experiment (DOE) using the data set in Figure 31, initially using all primary factors and possible square and secondary terms (S 4.06, R-sq 76.6%, R-sq(adj) 66.3%, R-sq(pred) 44.2%). Secondary terms, either as cross products or squares, were removed in order of largest p-value to improve the surface response model (S 4.1, R-sq 76.6%, R-sq(adj) 66.0%, R-sq(pred) 56.0%) with all remaining terms being significant (p<0.05). Whilst driving frequency, cavitation agent concentration and YAS microsphere size could not be estimated in the model, these terms were kept in to maintain a hierarchical model for their respective secondary interactions.

Analysis of Variance

Source	DF	Adj SS	Adj MS	F-Value	P-Value
Model	61	11452.6	187.75	11.25	0.000
Blocks	42	7660.2	182.39	10.93	0.000
Linear	5	543.1	108.62	6.51	0.000
Pressure (MPa)	1	290.1	290.06	17.38	0.000
Duty Cycle (%)	1	109.6	109.60	6.57	0.011
Total Number of Cycles	1	221.1	221.07	13.25	0.000
Mass Input (g)	1	89.6	89.63	5.37	0.021
Well Diameter (mm)	1	131.1	131.10	7.86	0.005
2-Way Interaction	14	1200.3	85.74	5.14	0.000
Frequency (MHz)*Duty Cycle (%)	1	87.4	87.42	5.24	0.023
Frequency (MHz)*Total Number of Cycles	1	632.7	632.75	37.92	0.000
Frequency (MHz)*Mass Input (g)	1	130.3	130.25	7.81	0.006
Pressure (MPa)*Duty Cycle (%)	1	95.5	95.48	5.72	0.017
Pressure (MPa)*Total Number of Cycles	1	278.8	278.83	16.71	0.000
Pressure (MPa)*Well Diameter (mm)	1	78.3	78.34	4.69	0.031
Duty Cycle (%)*Total Number of Cycles	1	72.7	72.69	4.36	0.038
Total Number of Cycles*TheraSphere Size (um)	6	490.0	81.66	4.89	0.000
Cavitation Concentration*Well Diameter (mm)	1	75.0	75.01	4.50	0.035
Error	262	4371.8	16.69		
Lack-of-Fit	261	4336.2	16.61	0.47	0.856
Pure Error	1	35.6	35.59		
Total	323	15824.4			

Figure 32: Analysis of variance for parameters in the optimised surface response linear regression model for post focal projection depth (mm). Degrees of freedom (DF), adjusted sum of squares (Adj SS) and adjusted mean of squares (Adj MS).

A Pareto chart ($\alpha = 0.05$) was generated for the standardised effects, for comparing the influence of the various factors in our model, critical to using a non-linear regression method with a single variable for predicting the post focal penetration depth afterwards.

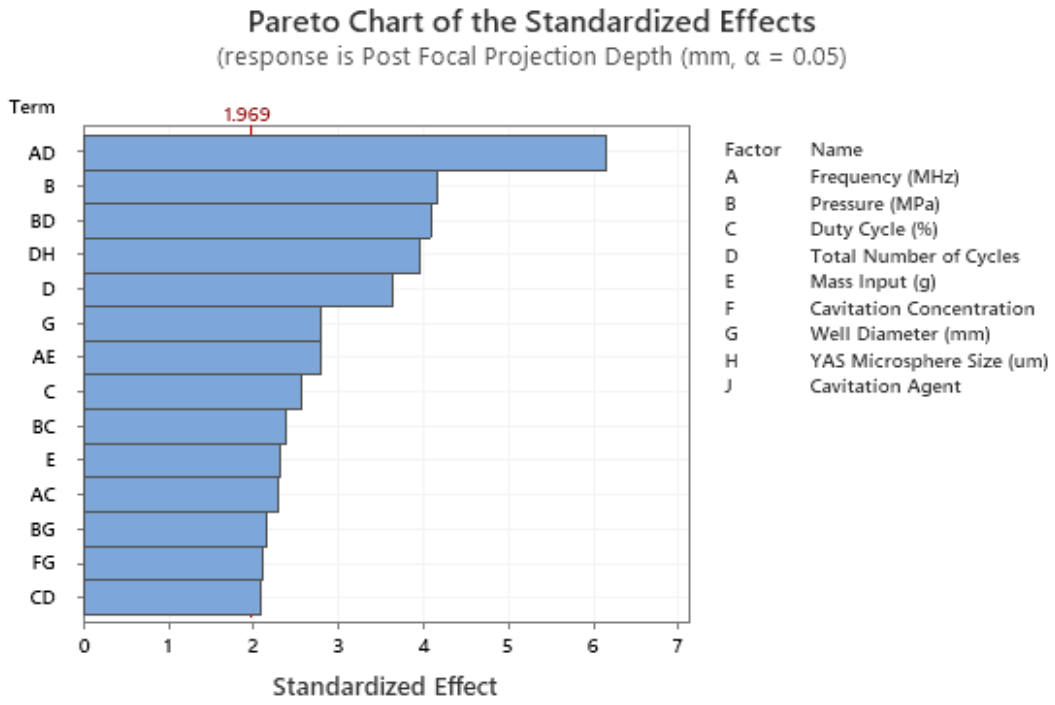


Figure 33: Pareto chart for standardised effects of the optimal linear regression model for post focal projection depth (mm).

Whilst Frequency (A) as a factor cannot be estimated in the linear model, the interaction between frequency (A) and the total number of cycles (D) is the highest absolute value contributing factor to the model with a coefficient of -37.53, pressure has the largest and second largest absolute coefficient at 33.43.

Unfortunately, as the linear model failed to estimate the coefficient for fundamental frequency (MHz) due to multicollinearity, we cannot calculate values for Frequency*Total number of cycles for use in a non-linear model (AD). Frequency remains a parameter critical to the future efforts in designing a device for the intended therapy (See Chapter 5, Appendix 7). A boxplot of the penetration depths over fundamental frequency displays the undulating non-linear response of post focal projection depth to the applied ultrasound frequency (Figure 34).

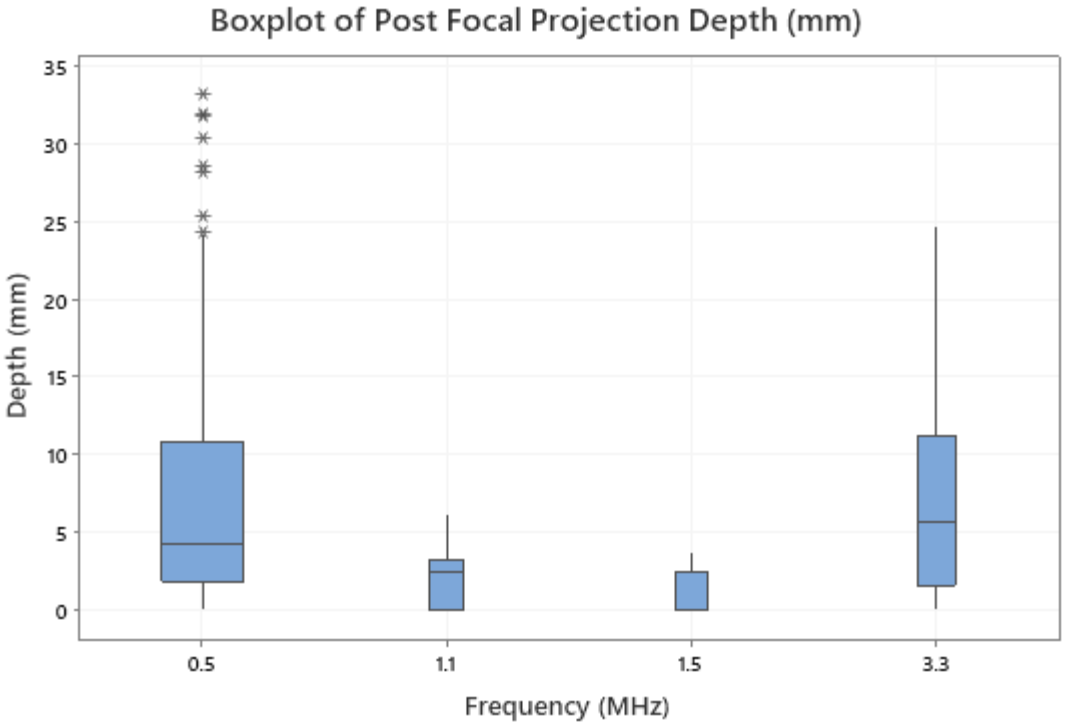


Figure 34: Post-focal projection penetration depth (mm). Mean values are notated by each box plot. 0.5MHz (n= 218), 1.1MHz (n=40), 1.5 MHz (n= 32), 3.3MHz (n=48). Outliers are indicated with an asterisk. The mean of each frequency is highlighted in the box plot.

Plotting the same data as histograms for post focal projection penetration depth (mm) over frequency (MHz) in Figure 35 highlights this further. The overlapping population curves are indicative of a minimum of two different response distributions within the same output data series. In this instance 0.5 and 3.3MHz appear to have a different population distribution compared to 1.1/1.5MHz, although this may be skewed due to a low sample number above 0.5 MHz.

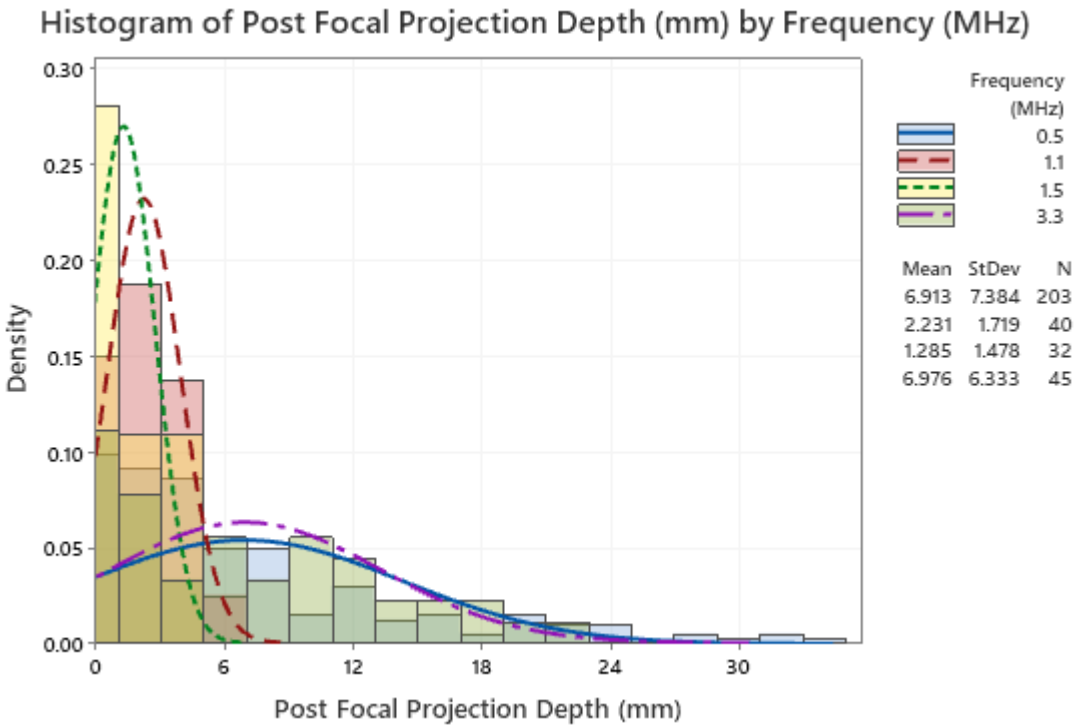


Figure 35: Histogram of post focal penetration depth (mm) for 0.5, 1.1, 1.5 and 3.3 MHz.

Separating data sets based on the apparent difference in data populations for further analysis did not yield an improvement in the linear model. Combining 0.5 and 3.3 MHz drastically reduced the predictive power of the unreduced model from 44.21 to 29.8% whilst increasing the standard deviation (S) from 4.06 to 4.27, indicating a broadening of the data set to the parameters, not tightening the spread as the distributions may suggest. It was not possible to isolate the 1.1/1.5 MHz data for independent evaluation due to a poor sample population (N=72) for the number of variables investigated.

3.4. Results

3.4.1.0.5 MHz Non-linear Regression

Using linear regression, peak negative pressure (MPa) was highlighted as the most influential primary input parameter which could be estimated. Frequency however seemed to have the most significant effect (non-linearly) within the design space, producing bi-modal distributions

of data within the larger output data set. It therefore seemed appropriate to standardise the non-linear regression using peak negative pressure to a single frequency, to see if pressure alone could be used as the sole predictor for post focal projection depth. 0.5MHz contained the largest number of data points, largest recorded penetration depth as well as the broadest distribution of data and so was selected as the frequency of choice.

Fitting a cubic line plot to the entire 0.5 MHz data set for post focal penetration depth (mm), we see that the majority of the data (95%, p=0.05) fall within the predictive interval (PI) or twice that of the confidence interval (CI). Importantly the S value, the % average distance of the data from the fitted line is relatively small at 6.5% (Figure 36), indicating a good agreement.

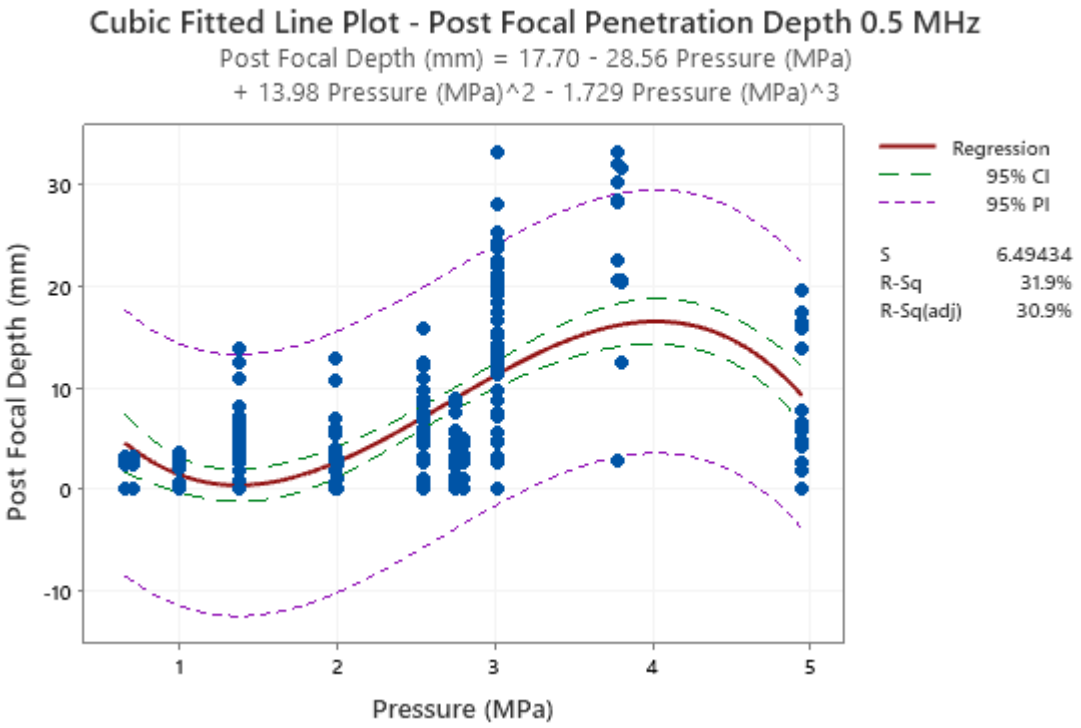


Figure 36: Cubic polynomial line plot for post focal penetration depth (mm) for 0.5MHz. The regression equation is:

Post Focal Depth (mm) = 17.70 - 28.56 Pressure (MPa) + 13.98 Pressure (MPa)^2 - 1.729 Pressure (MPa)^3.

Whilst the cubic model is a crude assumption, the data more closely resemble an asymmetrical Bragg peak. This highlights the apparent optimum pressure for extravasation at 0.5MHz between 3.7 and 5 MPa peak negative pressure before the additional increase in peak negative pressure becomes counterproductive, leading to a reduction in post focal penetration depth (Figures 36). Theta values based on the initial cubic analysis (Figure 36) were selected as initial inputs for identifying a Bragg peak with a Gauss-Newton convergence algorithm to find the final parameter estimates by minimising the sum of the squared function values[31].

Starting Values for Parameters

Parameter	Value
Theta1	0.35
Theta2	35
Theta3	1
Theta4	3.78

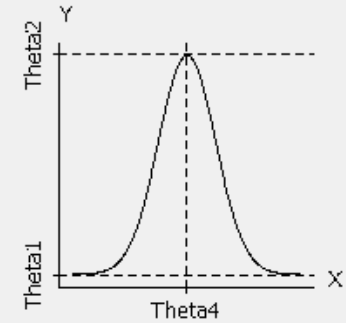


Figure 37: Starting theta values for the gauss-newton convergence algorithm (left) and the position of the theta levels within an example Bragg peak (right).

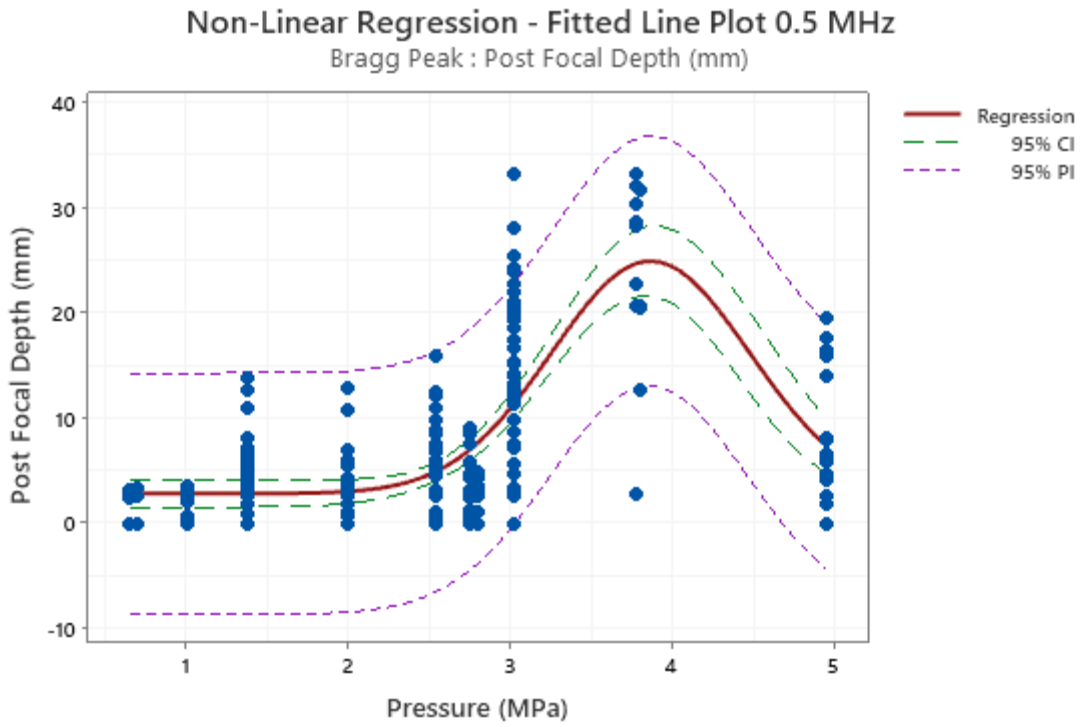


*Figure 38: Gauss-Newton non-linear regression of post focal penetration depth for 0.5MHz after 10 iterations. S 5.78629. Equation: Post Focal Depth (mm) = 2.79384 + (24.9075 - 2.79384) * exp(-1.33648 * ('Pressure (MPa)' - 3.86696) ^ 2).*

The improvement in the S value from 6.5 to 5. 8 reflects the improved regression line fit to the data set. More importantly it provides a far simpler equation for prediction of post focal penetration depth (88.4% to a 95% PI) at 0.5MHz using a single variable parameter compared to that of the linear regression, which had far poorer predictive capabilities for all fundamental frequencies (40.8%) and (0% for 0.5MHz, due to non-linearity). All without removing extreme standard residuals (>3) and reducing the dataset (n=214 for 0.5MHz). Removal of outliers (R>2) over three iterations, reducing the spread of data into the non-linear regression using the Gauss-Newton Algorithm, did also tighten the S value to 5.0 (n=151) but was deemed an insignificant improvement for a loss of 30% of the sample data set.

Parameter Estimates

Parameter	Estimate	SE Estimate	95% CI
Theta1	2.7938	0.65095	(1.5178, 4.0321)
Theta2	24.9075	1.69958	(21.6851, 28.2247)
Theta3	1.3365	0.18244	(1.0322, 1.9653)
Theta4	3.8670	0.05100	(3.7178, 3.9652)

*Post Focal Depth (mm) = Theta1 + (Theta2 - Theta1) * exp(-Theta3 * ('Pressure (MPa)' - Theta4) ^ 2)*

Figure 39: Parameter estimate outputs and intervals for Figure 38, generated by the Gauss-Newton algorithm for a Bragg peak.

3.5. Discussion

3.5.1. Experimental Order

As with any new *in vitro* experiment, benchmarking of results is important for making future improvements to the system and its design, to remove both type I and type II errors[32]. Whilst the MATLAB code despite its large memory requirements minimised human error and bias in the quantification measurements, it did not improve human error associated with the experimental ultrasound exposure. A run order versus the standard error of each observation (Figure 40) shows the reproducibility error of the operator.

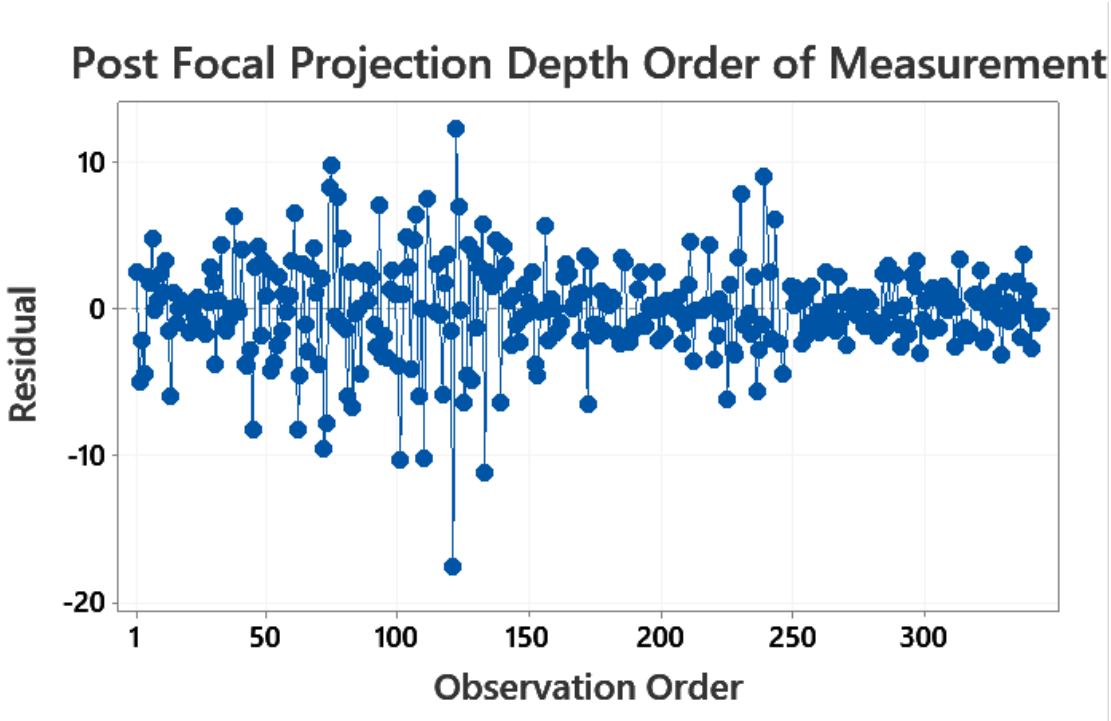


Figure 40: Run order versus residual for post focal projection depth (mm) across all frequencies.

As experience with the system grows as does the operator's competence. This is particularly relevant for transducer alignment. As the transducer is manually moved across the breadboard for further exposures in each mould (See Section 2.2.2 and 2.2.3), the transducer has to be manually repositioned so that the face of the transducer remains parallel with the mould. This certainly contributed to the observed error and variation of early experiments (observations <150). The reduction variation seen in later experiments (>150) is due to the use of a metal pin used to measure the distance from the face of the transducer to the gel mould, reducing operator error by minimising misalignment.

3.5.2.Primary Factor Responses Using Linear Regression

Running a Plackett-Burman factorial may have helped identify exactly which factors were critical to producing post focal extravasation. Running these screening tests prior to the surface response design would have been futile however due to the multicollinearity of a

number of the primary factors, leading to the screening tests being approximately the same size as the final response surface design. The surface response also allowed for a much higher degree of flexibility regarding levels and parameter combinations without producing needless or redundant data, which would have been the case in a Plackett-Burman design, allowing for initial screening and feasibility tests runs to contribute to the design reported.

Whilst the frequency component of the surface response could not be estimated, we can see that from figures 34 and 35 previously, that the post projection length is non-linearly related to frequency. The remaining primary factors that were deemed significant in the linear regression model are highlighted below (Figure 41).

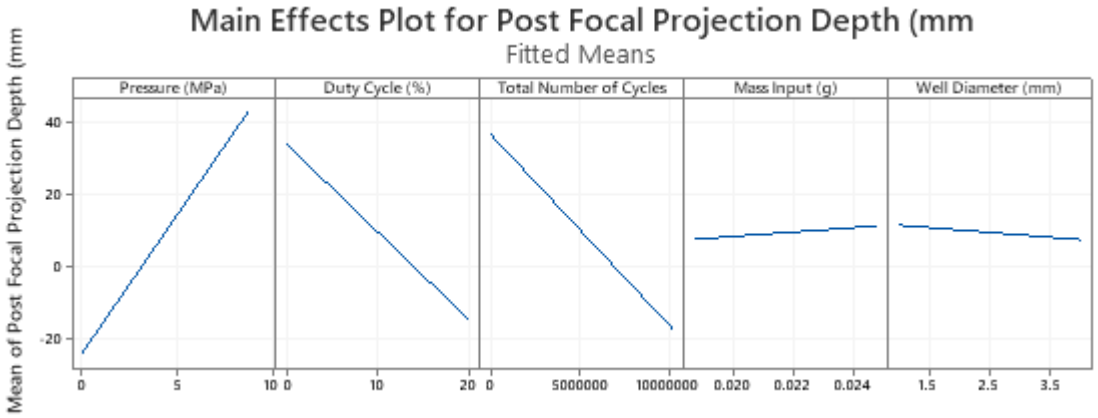


Figure 41: Primary factor effects on the significant remaining factors for post focal projection depth (mm) using the optimised surface response linear regression method.

It is unsurprising that peak negative pressure correlates to a significant increase in post focal extravasation, as the peak negative pressure and frequency of the acoustic field primarily dictate the likelihood of inertial cavitation of a microbubble via the intensity of the acoustic wave and its acoustic radiation force[33–40]. Whilst cavitation agent and cavitation concentration could not be estimated, due to multicollinearity, it is interesting to see that the total number of cycles or duty cycle negatively affect the post focal projection depth. Whilst theoretically maintaining a higher cavitation agent concentration leads to a higher chance of inertial cavitation and post focal microsphere movement, practically we realise that to produce

projections particularly those of longer lengths require time (total number of cycles) and a minimum duty cycle (5%) to form. Runs with less than 5% DC were not observed to produce any significant post focal microsphere extravasation. None the less, it highlights the temporal significance of the mechanism at play; smaller infrequent but intense pulses seem to provide the best conditions for producing projections of varying lengths.

The positive influence of mass input, whilst minor is not surprising as increasing the mass and therefore number of microspheres of a given distribution within the agar well, is required for x-ray detection of the larger projections. This is because of the associated measure error with the µCT instrument (see section 2.3.1) requiring ~30µm of material at a 30mm FOV for sufficient x-ray absorption and is therefore detecting clusters of microspheres rather than individual microspheres for some tested distributions. This in combination with mass loss via the manual deposition of the cavitation agent and microsphere slurry (see section 3.3.2) during the experimentation, means that the addition of more material is unlikely to directly contribute to the microsphere extravasation mechanism and is more likely to be a false positive as a result of the methods and analysis used to generate the data.

Increasing well diameter negatively affects the post focal length of the projections produced. For all well diameters, particularly at the lower (0.5MHz) frequencies used, the majority of the diameter of the well is encompassed by the focal region of the transducer. The detrimental effect of well diameter can therefore be explained by reducing the free space between the boundary edges, brought about by decreasing diameter of the well, reducing the degrees of freedom for the microspheres to travel from within the agar well. This phenomenon can be observed during the ultrasound exposure particularly with a combination of large microspheres, high pressures, low frequencies and a large well diameter; as a pulsing vortex of microspheres causing turbulence within the well cavity. Each subsequent pulse causes

agitation within the well and the otherwise sedimented microspheres to ‘jump’ upon exposure.

3.5.3.Factor Interaction Responses Using Linear Regression

A full interaction plot can be found in Appendix 3. Whilst the majority of secondary interactions follow the dominant primary factor, there are some secondary interactions which offer insight into the formation of the microsphere projections.

The positive interaction between frequency and pressure diminishes as frequency increases. Increasing duty cycle or the total number of cycles a well is exposed to both produce detrimental effects with increasing frequency.

Whilst the effect of cavitation agent concentration could not be independently assessed, its interactions with pressure, duty cycle, total number of cycles, mass input and well diameter are all positive.

For YAS microsphere Size*Total number of cycles, the top two largest distributions (200-400 and 106µm) have the largest negative effects on post focal microsphere extravasation depth. The data also suggests that different microsphere populations respond differently to the number of cycles each sample is exposed to. As the remaining distributions are relatively even this suggests that not only does the diameter of each individual microsphere contribute to the post focal projection depth, but other uncharacterised attributes e.g. range of distribution relative to the mean size, surface finish and exact chemical composition, may also have a small but limited interaction with the applied ultrasound field.

3.5.4. Comparison of Predictive Outputs for Regression Models

The linear model can be used to optimise the parameter inputs to maximise the measured output (Figure 42). The linear model indicates that within the defined design space, a 110 mm post focal penetration depth would be possible using a fundamental frequency of 0.5MHz and 8.7 MPa. The linear model predicts a completely non-sensical solution of -16.2 mm using 3.85 MPa at 0.5 MHz. The non-linear modelling suggests that there is an optimum peak negative pressure around 3.85 MPa and exceeding this is not optimal, most likely due to consumption of the cavitation agent nuclei at a rate faster than the extension of the microsphere projection.

Multiple Response Prediction

Variable	Setting
Frequency (MHz)	0.5
Pressure (MPa)	8.7
Duty Cycle (%)	20
Total Number of Cycles	10230000
Mass Input (g)	0.0187
Cavitation Concentration	1.00000E+10
Well Diameter (mm)	1
TheraSphere Size (um)	<20

Response	Fit	SE Fit	95% CI	95% PI
Post Focal Projection Depth (mm	110.3	17.9	(75.1, 145.5)	(74.2, 146.4)

Figure 42: Maximal prediction optimising all parameters within the design space for 0.5MHz.

Settings

Variable	Setting
Frequency (MHz)	0.5
Pressure (MPa)	3.85
Duty Cycle (%)	5
Total Number of Cycles	1500000
Mass Input (g)	0.022
Cavitation Concentration	1000000000
Well Diameter (mm)	1
TheraSphere Size (um)	15-32

Prediction is averaged over blocks.

Figure 43: Parameter inputs for linear prediction using the surface response

Prediction

Fit	SE Fit	95% CI	95% PI
-16.2372	3.77126	(-23.6630, -8.81138)	(-27.1843, -5.29014) X

X denotes an unusual point relative to predictor levels used to fit the model.

Figure 44: Results of the linear prediction using parameter inputs from figure 43.

Whereas using the non-linear regression equation produced in earlier (Section 3.3.3) with an estimated input pressure of 3.85 MPa at 0.5 MHz, we can calculate a response of 24.90 mm with a 95% confidence interval of 21.3, 27.6 and a 95% prediction interval of 19.9, 29.1. A far more logical solution, demonstrating the frequency dependency of producing a microsphere projection with a large post focal depth, which also explains why frequency as a component was not able to be estimated using linear regression.

3.6. Conclusion

In this chapter a method for interpretation of microsphere projections has been developed. The un-biased quantitative outputs have been used to investigate the parameter space tested for maximising post focal depth of the microsphere projections. Using statistical methods, two

methods (linear and non-linear) have been used to identify the parameters and their interactions critical to maximising post focal projection depth. The linear regression analysis provided more insight into the secondary interactions and nuances within the model, whereas the simpler non-linear method had increased predictive capabilities. Both models suggest both peak negative pressure and fundamental frequency as key criteria for maximising post-focal projection depth, with an optimal peak negative pressure at a given frequency, highlighting their collinearity. Drastically increasing the peak negative focal pressure, may cause cauterised vessels within the resection cavity to be reopened. Although this is highly unlikely this could inadvertently force spheres into the circulatory system, causing downstream health and toxicity concerns. This failure mode needs to be considered during further *in vivo* experimentation, when evaluating the peak negative pressure offset for mammalian tissue compared to that of the over-simplified agar-agar hydrogel.

For clinical translation the post focal penetration depth of the microspheres can be tailored by varying the applied peak negative pressure. Whilst the radius of the irradiation field produced largely static at ~2.5 mm, based upon the mean depth of beta irradiation. It appears that smaller infrequent but intense pulses seem to provide the best conditions for producing projections of varying lengths, not too dissimilar to conditions used in ultrasound histotripsy[40–47]. Smaller microspheres not only offer increased coverage but also appear to travel the furthest, with the largest post focal projection lengths. In order to treat the margins of a particularly large resection, the ultrasound focus must be able to move to encompass the interior surface of the resection cavity or the aspiration of the tumour mass performed in stages. Performing the adjuvant therapy in stages would allow for improved localised dosimetry via increased directional control of the microsphere projection under ultrasound exposure; using the cavities produced by the ultrasonic aspiration as ‘wells’ for microsphere and cavitation agent deposition.

As the work to date has used only focussed ultrasound transducers for producing microsphere extravasation, the largest directional component measured has always been in the same direction as the applied ultrasound filed or acoustic radiation force. Therefore, using post focal projection depth (mm) as the key measurable output does indeed maximise any minimum-volume enclosed ellipsoid produced and also therefore maximises and volume of irradiation around the microspheres extravasated into the anticipated tumour margins. However, as the well does not reflect the size or shape of the cavity produced during the resection procedure, nor the potential use of an un-focussed ultrasonic horn rather than focussed transducer; Considerations need to be made for the relative thickness of the in vivo slurry produced compared to the size and shape of the ultrasound field used during translation, a noticeable change in geometries from those used within the agar-agar phantom.

3.6.1.Limitations

Whilst there are other µCT machines commercially available, we could only gain access to the Perkin Elmer Quantum FX machine for this project. As a result, the resolution of the images produced are 59 and 140 µm, for the 30 and 72 mm FOV's respectively. Ultimately the images used for quantifying the microsphere distributions using the 15-32 µm microspheres, rely on clustering of the microspheres to be detected for a given pixel. It is assumed therefore that there are some microspheres which are delivered beyond that of the mapped projections and may be cause for concern in future translation of the technology. The exact number of microspheres delivered beyond the imaged projects will need quantifying, via histology during ex vivo experiments.

Additionally, it has not been possible to investigate the potential effects of the ultrasound focus size independent of the applied ultrasound frequency. This is because the focus region is dictated by the physical curvature of the transducer and the applied fundamental frequency,

which cannot be manipulated on each device. The use of a smaller focal region particularly at higher pressures, appears to produce less controllable projections compared to that of larger focal regions (See Chapter 1) and is therefore largely undesirable towards translation of the technology. Preference is given to the use of larger focal regions e.g 0.5 MHz.

3.6.2.Future Work

As shown in both this and the preceding chapter, extravasation of microspheres into agar at various depths can be achieved using a variety of parameters from focussed ultrasound transducers. This new method for distributing microspheres using cavitation activity however is very sensitive to frequency. Further work is needed to more accurately identify the non-linear relationships and corresponding sensitivities between the fundamental frequency and the peak negative pressure required to achieve the required degree of extravasation.

Future work is also needed to design of a device to produce the intended microsphere projections within an intra-operative setting. Fundamental frequency and peak negative pressure will be key elements moving forward however other considerations including the physical use, ergonomics and safety concerns of the device must also be considered. This will be discussed further in Chapter 5. Investigation of the mechanism(s) by which cavitation produces extravasation is also required and this will be the subject of Chapter 4.

Further feedback from physicians will be required to establish key output criteria of the device e.g. focussed or unfocussed acoustic field, time allocation for the intervention, availability of cavitation agents and radioembolic material.

References

1. Ng, S. C. *et al.* Patient dosimetry for 90Y selective internal radiation treatment based on 90Y PET imaging. *J. Appl. Clin. Med. Phys.* **14**, 212–221 (2013).

2. Kafrouni, M. *et al.* Analysis of differences between 99mTc-MAA SPECT- and 90Y-microsphere PET-based dosimetry for hepatocellular carcinoma selective internal radiation therapy. *EJNMMI Res.* **9**, (2019).

3. Gordon, A. C. Tuning Your RADIOembolization : Imaging-guidance of Yttrium-90 Radioembolization. (Evanson, Illinois, 2016).

4. Attarwala, A. A. *et al.* Quantitative and qualitative assessment of yttrium-90 pet/ct imaging. *PLoS One* **9**, 1–7 (2014).

5. Knešaurek, K., Tuli, A., Pasik, S. D., Heiba, S. & Kostakoglu, L. Quantitative comparison of pre-therapy 99mTc-macroaggregated albumin SPECT/CT and post-therapy PET/MR studies of patients who have received intra-arterial radioembolization therapy with 90Y microspheres. *Eur. J. Radiol.* **109**, 57–61 (2018).

6. Auditore, L. *et al.* Monte Carlo 90 Y PET/CT dosimetry of unexpected focal radiation-induced lung damage after hepatic radioembolisation . *Phys. Med. Biol.* **65**, 235014 (2020).

7. Kafrouni, M. *et al.* Analysis of differences between 99mTc-MAA SPECT- and 90Y-microsphere PET-based dosimetry for hepatocellular carcinoma selective internal radiation therapy. *EJNMMI Res.* (2019) doi:10.1186/s13550-019-0533-6.

8. Elschot, M. *et al.* Quantitative Comparison of PET and Bremsstrahlung SPECT for Imaging the *In vivo* Yttrium-90 Microsphere Distribution after Liver Radioembolization. *PLoS One* **8**, (2013).

9. Wang, X. D., Yang, R. J., Cao, X. C., Tan, J. & Li, B. Dose delivery estimated by bremsstrahlung imaging and partition model correlated with response following intra-arterial radioembolization with 32p-glass microspheres for the treatment of hepatocellular carcinoma. *J. Gastrointest. Surg.* **14**, 858–866 (2010).

10. Wondergem, M. *et al.* 99mTc-macroaggregated albumin poorly predicts the intrahepatic distribution of 90Y resin microspheres in hepatic radioembolization. *J. Nucl. Med.* **54**, 1294–1301 (2013).

11. Walrand, S., Hesse, M., Chiesa, C., Lhommel, R. & Jamar, F. The low hepatic toxicity per gray of 90Y glass microspheres is linked to their transport in the arterial tree favoring a nonuniform trapping as observed in posttherapy PET imaging. *J. Nucl. Med.* **55**, 135–140 (2014).

12. Maughan, N. M. *et al.* Phantom study to determine optimal PET reconstruction parameters for PET/MR imaging of 90Y microspheres following radioembolization. *Biomed. Phys. Eng. Express* **2**, 15009 (2016).

13. Pasciak, A. S. *et al.* The number of microspheres in Y90 radioembolization directly affects normal tissue radiation exposure. *Eur. J. Nucl. Med. Mol. Imaging* **47**, 816–827 (2020).

14. Pasciak, A. S. *et al.* The number of microspheres in Y90 radioembolization directly affects normal tissue radiation exposure. *Eur. J. Nucl. Med. Mol. Imaging* **47**, 816–827 (2020).

15. Gallego, O. Nonsurgical treatment of recurrent glioblastoma. *Curr. Oncol.* **22**, e273–e281 (2015).

16. Erwin G. Van Meir, PhD, Costas G. Hadjipanayis, MD, PhD, Andrew D. Norden, MD, MPH, Hui-Kuo Shu, MD, Patrick Y. Wen, MD, and Jeffrey J. Olson, M. Exciting New Advances in Neuro-Oncology: The Avenue to a Cure for Malignant Glioma. *CA Cancer J Clin.* **60**, 166–193 (2010).

17. Thompson, J. G. *et al.* Distribution and Detection of Radiopaque Beads after Hepatic Transarterial Embolization in Swine: Cone-Beam CT versus MicroCT. *J. Vasc. Interv. Radiol.* **29**, 568–574 (2018).

18. Westcott, M. A., Coldwell, D. M., Liu, D. M. & Zikria, J. F. The development, commercialization, and clinical context of yttrium-90 radiolabeled resin and glass microspheres. *Adv. Radiat. Oncol.* **1**, 351–364 (2016).

19. Statistics, B. & Improvement, C. <3-s2.0-B9780750647090500077-main.pdf>.

20. Collins, L. M., Dziak, J. J. & Li, R. Design of Experiments With Multiple Independent Variables: A Resource Management Perspective on Complete and Reduced Factorial Designs. *Psychol. Methods* **14**, 202–224

(2009).

21. Montgomery, D. C. *Design and analysis of experiments*. (2013).

22. Antony, J. Fundamentals of Design of Experiments. *Des. Exp. Eng. Sci.* 7–17 (2014) doi:10.1016/b978-0-08-099417-8.00002-x.

23. Federer, W. T. & Raktoe, B. L. Fractional Factorial Designs. *Wiley StatsRef Stat. Ref. Online* **2**, (2014).

24. Briefs, A. M. C. T. Experimental design and optimisation (4): Plackett-Burman designs. *Anal. Methods* **5**, 1901–1903 (2013).

25. Bhatra Charyulu, N. C. & Ameen Saheb, S. Note on reduction of dimensionality for second-order response surface design model. *Commun. Stat. - Theory Methods* **46**, 3520–3525 (2017).

26. Sukriti *et al.* Surface response methodology-central composite design screening for the fabrication of a Gx-psy-: G -polyacrylicacid adsorbent and sequestration of auramine-O dye from a textile effluent. *RSC Adv.* **6**, 74300–74313 (2016).

27. Hadi, I. *et al.* Radiation necrosis after a combination of external beam radiotherapy and iodine-125 brachytherapy in gliomas. *Radiat. Oncol.* **16**, 1–9 (2021).

28. Kickingereder, P. *et al.* Low-dose rate stereotactic iodine-125 brachytherapy for the treatment of inoperable primary and recurrent glioblastoma: single-center experience with 201 cases. *J. Neurooncol.* **120**, 615–623 (2014).

29. Craney, T. A. & Surles, J. G. Model-dependent variance inflation factor cutoff values. *Qual. Eng.* **14**, 391–403 (2002).

30. Transformations, B. Box-Cox Transformations. (1964).

31. Argyros, I. K. *Iterative Methods and Their Dynamics with Applications.* (CRC Press, 2017).

32. Greenland, S. *et al.* Statistical tests, P values, confidence intervals, and power: a guide to misinterpretations. *Eur. J. Epidemiol.* **31**, 337–350 (2016).

33. Kratskin, I. L., Yu, X. & Doty, R. L. "Stable" Inertial Cavitation Charles. *Ultrasound Med. Biol.* **44**, 199–203 (1997).

34. Guo, X., Li, Q., Zhang, Z., Zhang, D. & Tu, J. Investigation on the inertial cavitation threshold and shell properties of commercialized ultrasound contrast agent microbubbles. *J. Acoust. Soc. Am.* **134**, 1622–1631 (2013).

35. Lauterborn, W. & Kurz, T. Physics of bubble oscillations. *Reports Prog. Phys.* **73**, (2010).

36. Versluis, M. Nonlinear behavior of ultrasound contrast agent microbubbles and why shell buckling matters. *Proc. 20th Int. Congr. Acoust.* 1–6 (2010).

37. Prosperetti, A. Bubble phenomena in sould fields: part two. *Ultrasonics* **22**, 115–124 (1984).

38. Samarasinghe, S. Increasing the nonlinear character of microbubble oscillations at low acoustic pressures. 807–811 (2008) doi:10.1098/rsif.2008.0005.

39. Lauterborn, W., Kurz, T., Geisler, R., Schanz, D. & Lindau, O. Acoustic cavitation, bubble dynamics and sonoluminescence. *Ultrason. Sonochem.* **14**, 484–491 (2007).

40. Bader, K. B., Vlaisavljevich, E. & Maxwell, A. D. For Whom the Bubble Grows: Physical Principles of Bubble Nucleation and Dynamics in Histotripsy Ultrasound Therapy. *Ultrasound Med. Biol.* **45**, 1056–1080 (2019).

41. Edsall, C. *et al.* Bubble Cloud Behavior and Ablation Capacity for Histotripsy Generated from Intrinsic or Artificial Cavitation Nuclei. *Ultrasound Med. Biol.* **47**, 620–639 (2021).

42. Engle, K. M.; Mei, T-S.; Wasa, M.; Yu, J.-Q. Development and Translation of Histotripsy: Current Status and Future Directions. *Curr Opin Urol.* **24**, 104–110 (2014).

43. Lake, A. M. *et al.* Histotripsy: Minimally Invasive Technology for Prostatic Tissue Ablation in an *In vivo* Canine Model. *Urology* **72**, 682–686 (2008).

44. Vlaisavljevich, E. *et al.* Effects of tissue stiffness, ultrasound frequency, and pressure on histotripsy-induced cavitation bubble behavior. *Phys. Med. Biol.* **60**, 2271–2292 (2015).

45. Hendley, S. A., Bollen, V., Anthony, G. J., Paul, J. D. & Bader, K. B. In vitro assessment of stiffness-dependent histotripsy bubble cloud activity in gel phantoms and blood clots. *Phys. Med. Biol.* **64**, ab25a6 (2019).

46. Hendley, S. A., Bollen, V., Anthony, G. J., Paul, J. D. & Bader, K. B. In vitro assessment of stiffness-dependent histotripsy bubble cloud activity in gel phantoms and blood clots. *Phys. Med. Biol.* **64**, (2019).

47. Hoogenboom, M. *et al.* Mechanical High-Intensity Focused Ultrasound Destruction of Soft Tissue: Working Mechanisms and Physiologic Effects. *Ultrasound Med. Biol.* **41**, 1500–1517 (2015).

CHAPTER 4

High-speed Imaging of Cavitation Enhanced Projection Events

4. High-speed Imaging of Cavitation Enhanced Projection Events

4.1. Introduction

Several studies have shown that ultrasound induced cavitation can promote convection of small molecule drugs[1,2] and nanoparticles[3–6] both in tissue mimicking phantoms and *in vivo*[4,6,7]. It was established in Chapters 2 and 3 that enhanced extravasation could also be achieved with glass microspheres having diameters in the range 10 - 100μm in agar phantoms. Interestingly, despite the ultrasound exposure conditions being comparable in terms of frequency, peak negative pressure, duty cycle and pulse repetition frequency, the distances travelled by the microspheres were found to be significantly larger than those reported for nanoparticles[5,8] . This could potentially be explained by the fact that the larger particles will have greater inertia and/or that they will be subject to larger acoustic radiation forces and/or that the microspheres may themselves promote cavitation activity. The aim of the work described in this chapter was to attempt to gain insight into the mechanisms by which microsphere transport is facilitated, by using a high-speed camera to directly observe the process.

4.2. Methods

4.2.1.Mould Design

For this series of experiments, an acrylic mould for an agar gel block measuring 80 x 40 x 40mm was fabricated, with a wall thickness of 10mm in all directions. A blind M4 thread was tapped into the top surface of the mould to allow for a metal supporting rod to be attached so that the mould could be suspended in the water tank. Nylon screws were used to hold the gel mould together during alignment and experimentation, to avoid unwanted B-mode imaging artefacts. A 4mm hole was drilled through the acrylic lid near the front right corner of the

mould, 4mm from the right edge of the mould to the centre and 10mm from the front of the mould to the centre of the hole. This allowed for a 4mm stainless-steel modified rod to be inserted, in a similar fashion to previous experiments (See Section 2.2.4) to produce a blind ended channel or well within the gel. An initial pilot study showed that the optimum terminal dimensions of the rod were 1x10mm in size for this set of experiments.

The gel was comprised of 0.5% agar and was fabricated in the same manner as previously reported (Section 2.2.3). The moulds were set on a slight incline whilst cooling, to prevent ingress of air into the cavity near the stainless-steel rod. Initial experiments included an acrylic supporting column with a partial relief on the front right of the mould; this was removed to increase the gel thickness around the well and reduce the frequency of tears in the mould when removing the stainless-steel rod insert.

Once the gel had solidified, two faces of the mould were removed, the front face and the right edge, to enable access for the high magnification objectives. With the stainless-steel rod carefully removed to produce the gel cavity, a mixture of undiluted Sonovue® (310µL, Bracco) and black glass microspheres (15-35µm, 106µm, 200-400µm) were injected into the well, which was the sealed with a rubber bung to prevent water ingress. The glass microspheres were manufactured by MoSci (TheraSphere® manufacturer) and were produced in that the same way as TheraSphere™ giving them identical surface properties and density but increased brightfield contrast.

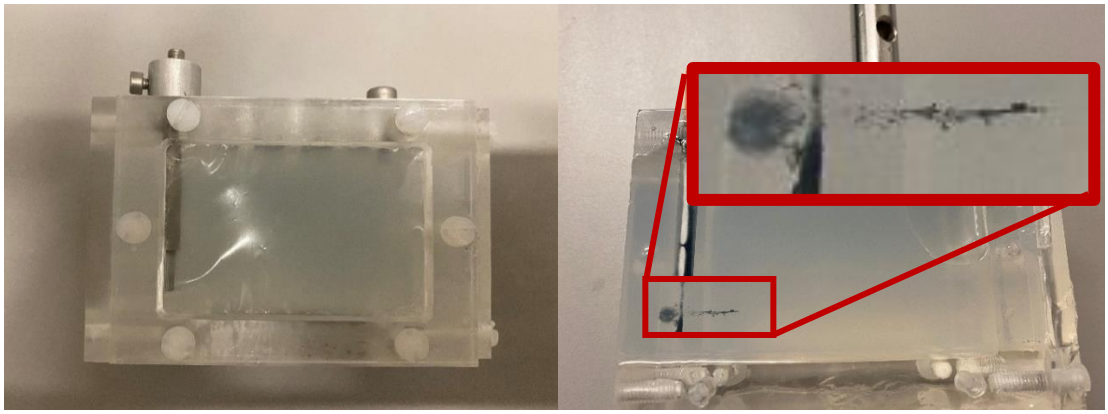
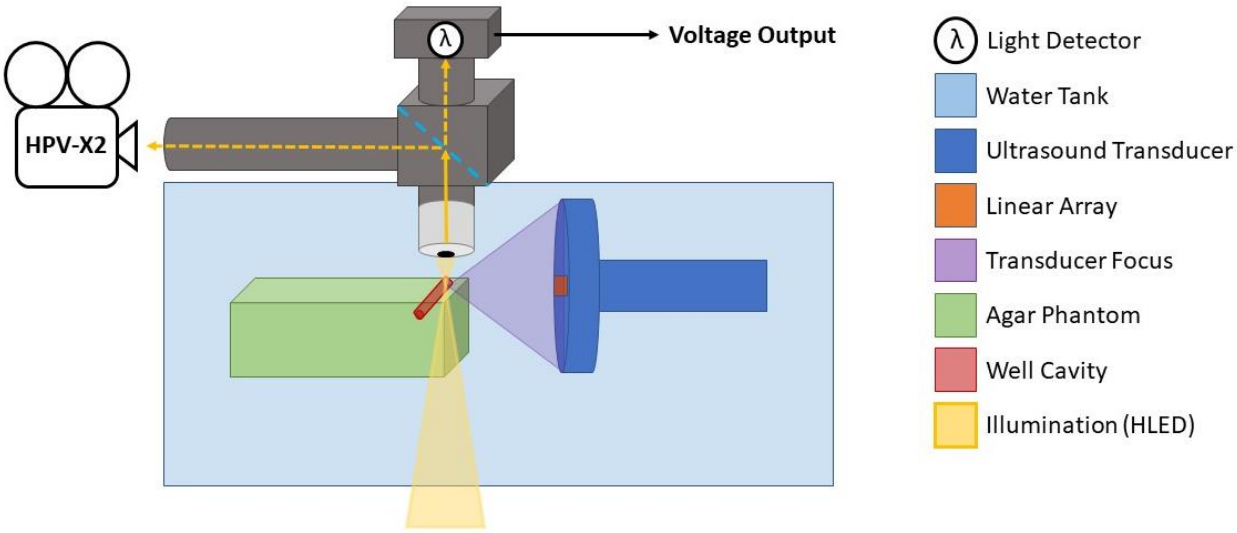


Figure 45: Acrylic gel mould used for high-speed imaging experiments before (left), after (right). Ultrasound exposure from left (front) to right (back). Extravasation of black microspheres (outlined in red). Gel block measures 80 x 40 x 40mm, with 10mm thick acrylic walls, excluding the front and back faces (left and right faces of the images above) which were 5mm acrylic brackets with mylar sheet in the middle.

4.2.2. Ultrasound Tank and Movement Stages

A transparent acrylic water tank measuring 445mm x 445mm x 175mm mounted on an aluminium breadboard with two rows of M6 thread holes pitched 25mm apart on its edges, was used for this series of experiments (Figure 46 below).



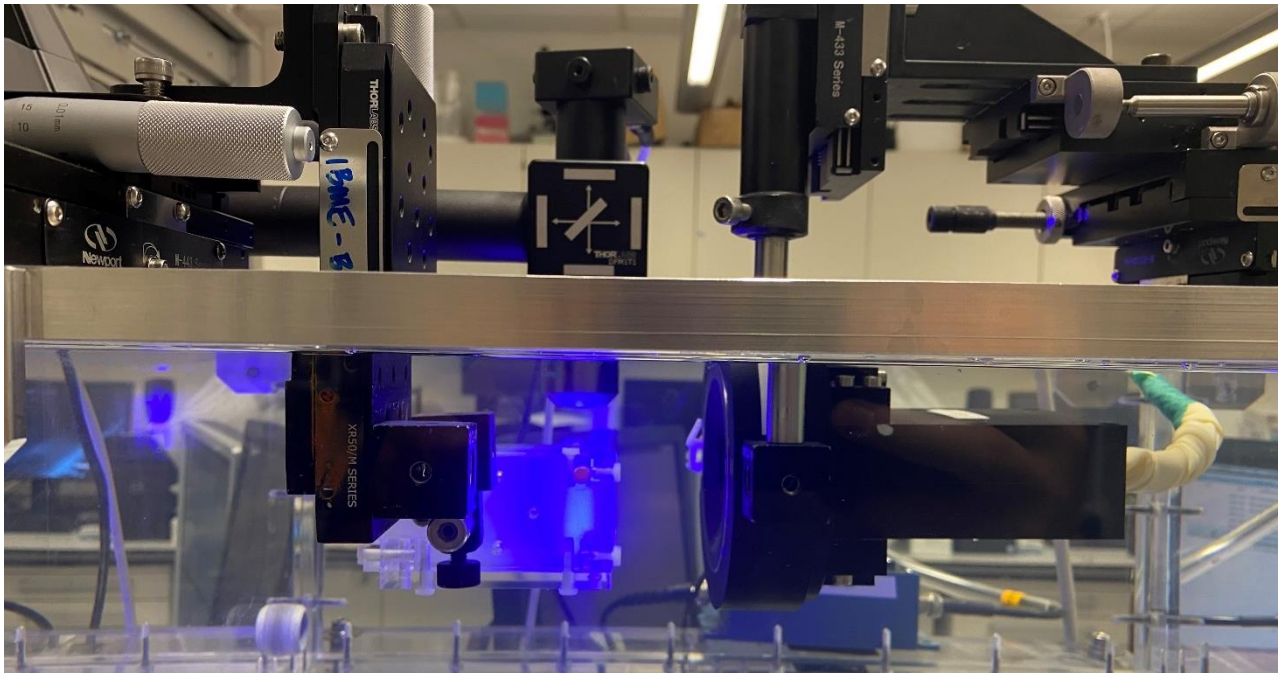


Figure 46: Equipment setup for high-speed camera experiments. Diagram (not to scale, above) actual (below). For details of the electronics, please see Figure 47.

Two sets of xyz movement stages were constructed from crossed-roller bearing aluminium manual linear movement stages (Newport®, MKS Instruments) allowing for fine adjustment ±0.01mm within a 50 mm range of travel. One assembly was used to suspend the rotated gel mould in the water tank, using the holding rod to avoid entrapment of gas bubbles on the surface as the mould passed through the air-water interface. Each experimental test run used a new gel mould, warmed to room temperature (~ 20°C) before exposure.

A second assembly was used to support the single element transducer (64mm, 0.50MHz, H107 Series, Sonic Concepts, Bothell, WA) with a rectangular cutout measuring 48 x 17mm in the centre for a coaxially aligned linear array (centre frequency 6.25 MHz, bandwidth 4-11MHz, 128 elements, 0.3mm pitch, 18mm elevation focus, L11-4v Verasonics®, Redmond, WA). Pressure calibrations for this transducer are as previously reported (Section 2.2.6). The tank was filled each day with degassed deionised water (Millipore-Q Type 1).

4.2.3.Shimadzu Hypervision HPV-X2 High-speed Camera

A Solis® High-Power LED (445 nm Royal Blue, 48.3mm clear aperture, 5.4 W Min, Thor Labs, UK) with a Plug-and-Play Solis® LED driver (Thor Labs, UK) was placed beneath the tank to provide illumination. The driver automatically detects and sets the current limit to the value stored in each LED's internal memory to protect it from being overdriven; maintaining a constant level of light emission throughout each experiment.

To capture cavitation events at a sufficient rate for driving frequencies 0.5 - 3.3 MHz, a Hypervision HPV-X2 (Shimadzu, Tokyo, Japan) high-speed camera was chosen based on its capability and availability. The HPV-X2 is capable of recording from 60 to 10 million frames per second, with variable exposure times, and can record a maximum of 256 frames within a single capture

To the front of the camera was attached a 25mm ID lens tube with a 552 nm edge LaserMUX™ single-edge laser dichroic beam splitter lens (LM01-552-25, Semrock®, Rochester, NY) placed 175mm from the HPV-X2 detector. At a distance of 200mm from the face of the high-speed camera was placed a 30 mm Cage-Compatible, Kinematic Fluorescence Filter Cube (DFM1T1, Thor Labs, UK) allowing for a 90-degree reflection to be transmitted to the HPV-X2. In the direct path of light was placed an aspheric condenser lens with diffuser surface (ACL2520U, 600 Grit, Ø25 mm) followed by a light detector (PDA36A2 Si Switchable gain detector, 400 - 1000 nm, Thor Labs, UK) which produced an output voltage trace for monitoring of the transmitted light, this was later used to develop a light responsive trigger signal for the Shimadzu camera. The diffuser lens was required to reduce the intensity of the received light to the diode as not to damage the oscilloscope input and reduce the detector's fidelity, a reduction which could be compensated for by the internal gain of the detector.

At the base of the cube, an adaptor ring for attachment of two NIKON (Tokyo, Japan) CFI Plan Fluor series air objectives; a 4x (0.13 NA, 17.2mm WD) and a 10x (0.30 NA, 16.00mm WD).

Over which was placed a 100ml borosilicate glass beaker with a polystyrene insert between the edge of the glass wall and outermost edge of the objective, to prevent water ingress into the two objectives and to centre the objective in the middle of the protective glass beaker. Whilst the base of the beaker was not perfectly flat, nor designed for this application; a water immersible objective of the correct magnification and working distance could not be sourced. Ingress of water either as droplets or vapour causes a hazing of the objective surface and a subsequent reduction in clarity, contrast and resolution as well as being potentially damaging to the objective.

4.2.4.High Speed Camera Triggering

Cavitation events occurring on the nanosecond to microsecond time scale have been studied extensively using high-speed cameras[9–16]. The cavitation induced microsphere transport observed in this study, however, were found to occur after a variable multi-second delay. This posed a considerable challenge for triggering the high-speed camera. The size and optical contrast of the microspheres enabled them to be observed by the naked human eye. Unfortunately attempts to manually trigger the high-speed camera in time with the projection events were only successful with imaging frame rates up to 10,000 fps. In order to capture events at 100,000 fps and above, an electronic trigger signal was required.

Initial attempts used a photo-detector to convert the received transmitted light into an output voltage (Figure 46) to produce a voltage trace over the exposure time, used to monitor the change in image contrast during the formation of a microsphere projection (See Appendix 4). An average of the corresponding voltage-time trace was then used to set a manual delay onto the second waveform generator, so that the input trigger signal to the high-speed camera would coincide with the microsphere projection. Due to the variable nature of the delay, however, this approach was of limited success, with the delay frequently being either

insufficient (i.e. only capturing the very beginning of the projection event) or too long (only capturing the end of the event or mid-way through a projection).

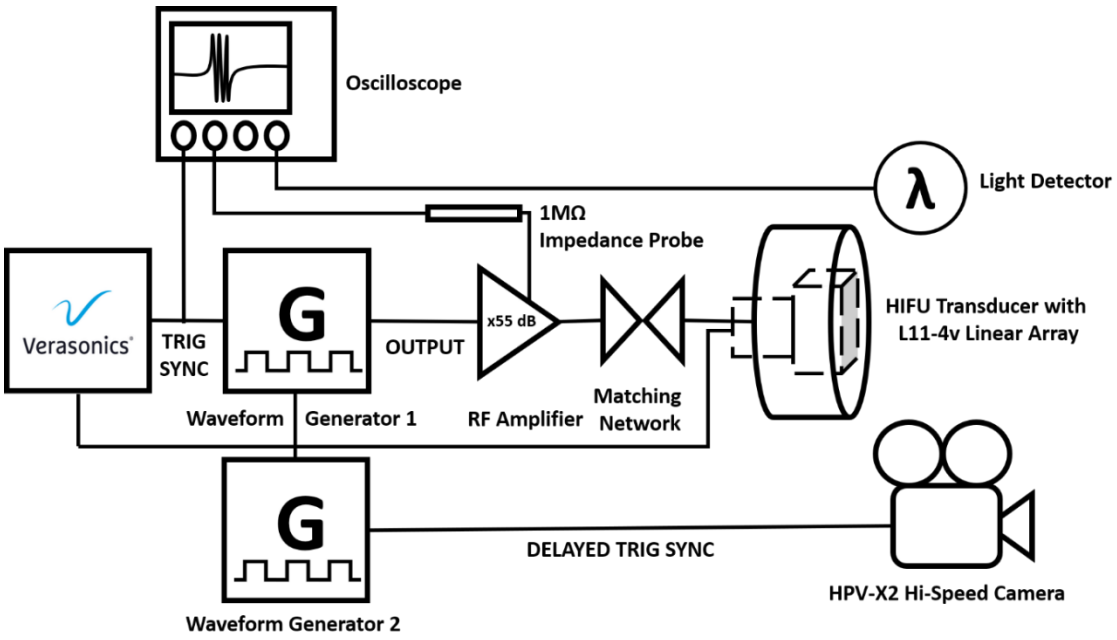


Figure 47: Electronic setup for manually gated delay of the HPV-X2 high-speed Camera

A second more responsive electronic setup was therefore devised. The voltage trace generated from the output of the light detector was split between oscilloscopes, one for monitoring of the voltage signal (overlaid on the Verasonics™ trigger and waveform out of the RF amplifier) with a second to produce another output signal independent of the ultrasound trigger, when the oscilloscope detected a drop in the observed voltage from the detector trace. This allowed any electronic delay, caused by processing or transmission, to be removed by setting the trigger frame (from 1-256) to later within the capture sequence, allowing more frames to be recorded before the delayed trigger signal was received. The second trigger output signal was triggered by exceeding a voltage window (positive or negative) or by using a falling edge (negative only) manually set by the operator for each ultrasound exposure from the mean resting voltage prior to ultrasound exposure. Each exposure required manual editing

of the mean voltage required for the trigger, even for subsequent exposures. Further information on development of the triggering methods can be found in Appendix 2.

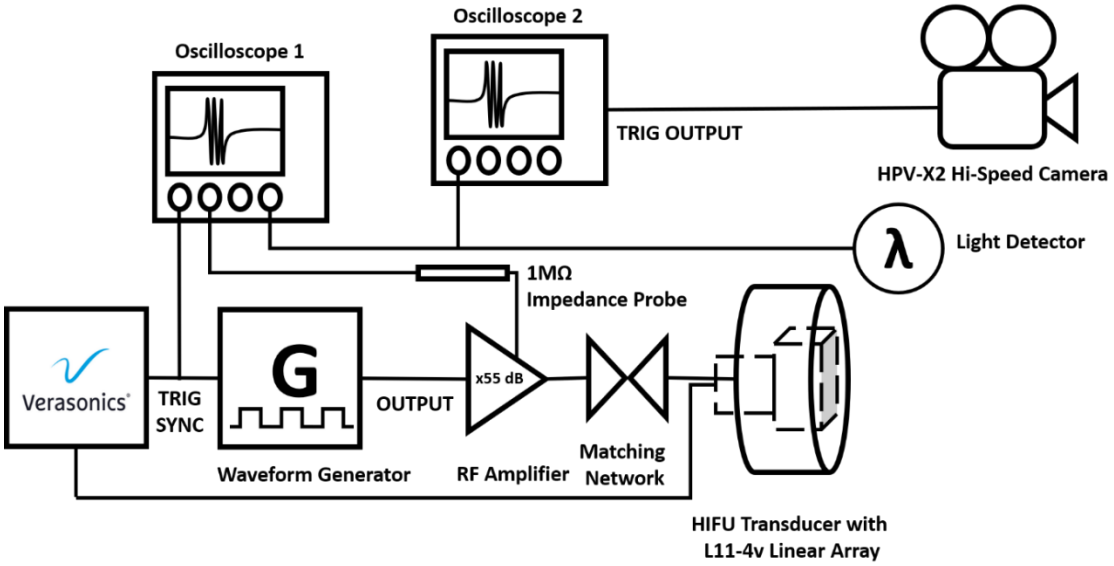


Figure 48: Light detector voltage gated trigger electronic setup for use with dual oscilloscopes.

4.2.5. Ultrasound Exposure Conditions to Facilitate High-speed Imaging

The exposure conditions investigated were based on the work described in the previous chapter (See section 3.2.6) and the limitations imposed by the maximum imaging frame rate and the optical field of view and depth of focus. During initial testing with pressures up to 3.9 MPa it was found that the well shook violently, moving in and out of the field of view, and thus capturing consecutive frames at these pressures was particularly difficult. All of the subsequent experiments therefore used the same ultrasound exposure conditions unless otherwise stated; 0.50 MHz, 1.9 MPa, 5% DC, 3.3Hz PRF at a room temperature ~20^{o}C. It was hoped that the smaller peak negative pressure, despite producing shorter projections overall in the direction of US transmission, would provide clearer images to help elucidate the mechanism by which the projections are formed. Constant exposure to the HLED even at maximum light output, did not appear to have any effect on microbubble stability, i.e., no destruction of microbubbles or coalescence/foaming was observed.

The elasticity of the 0.5% agar, despite its low material strain[17–23], is not overcome by a single flux of pressure, does not tear and retains the integrity of the well. The applied ultrasound field is therefore not directly responsible for the perforation of the gel boundary and extravasation of microspheres, validating agar as a suitable choice of body tissue mimic.

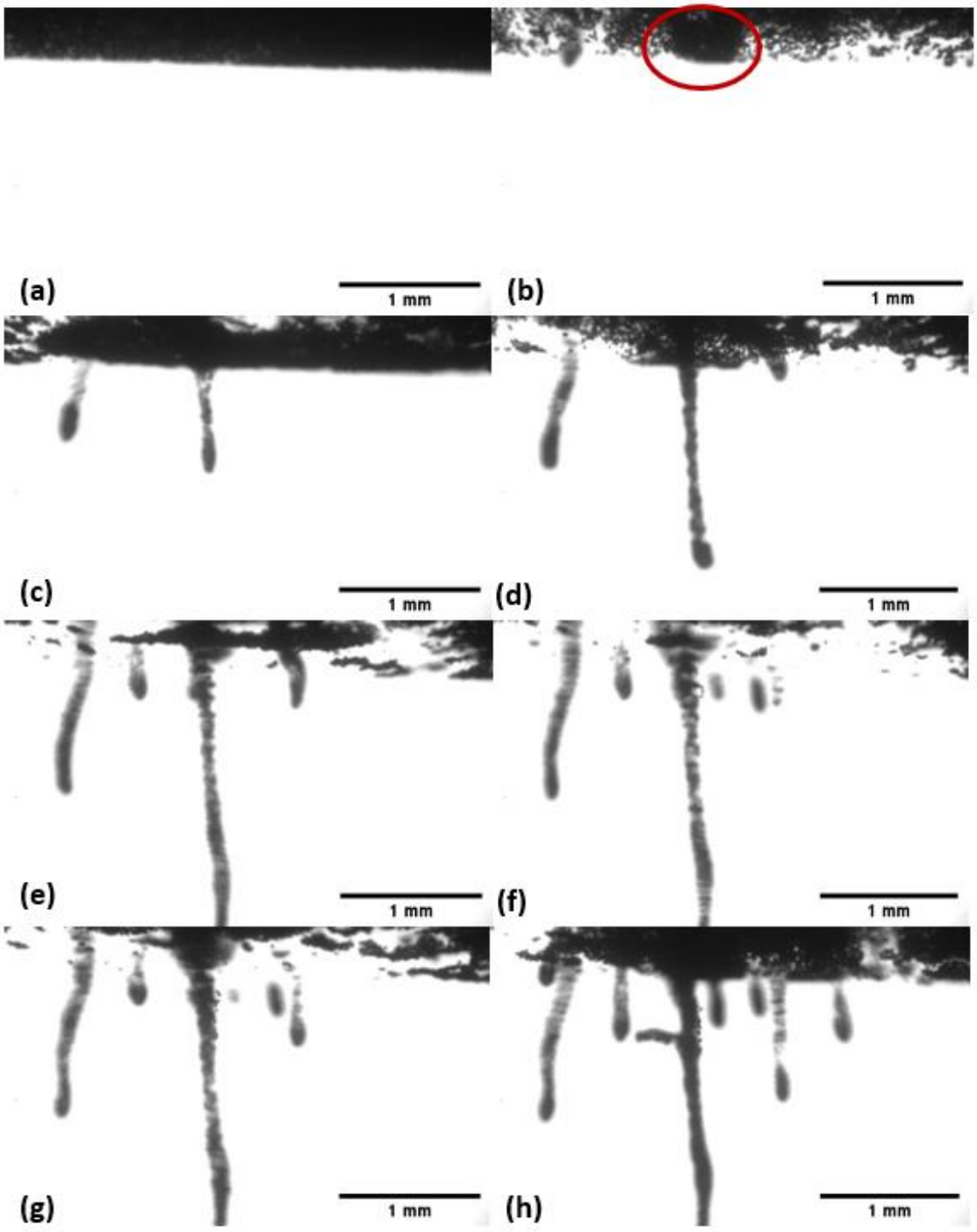
4.3. Results

As the majority of results within this chapter are recorded as video files, an unlisted YouTube channel (https://youtube.com/playlist?list=PL2ZKtYn85C-Qd5WOQkOu7OdbEONlxrU1S) has been created for the reader(s) to help visualise the dynamic movements of the microbubbles, microspheres and cavitation activity. Hyperlinks to videos discussed are embedded throughout the text and Figures for convenience.

4.3.1.Extravasation of Glass Microspheres through Agar Phantoms

Figure 49 shows an example of a typical glass microsphere projection caused by ultrasound mediated cavitation observed using low magnification (4x). The series of images demonstrates the various events which occur to produce the numerous channels which contribute to entirety of the single microsphere projection. The 4x NIKON objective was primarily used to visualise the macroscopic appearance of the multi-channel cavitation induced projections. Low magnification videos were captured at relatively low frame rates (2-10,000 fps) to enable observations of microsphere extravasation, projection channel formation and growth across the image frames; with the microsphere filled channels appearing as large black streaks against a white-grey background. Please note that for ease of viewing, all images are shown in the same orientation with the upper edge corresponding to the edge of the well closest to the transducer, i.e. the direction of ultrasound propagation is from top to bottom; gravity acts

perpendicular to the plane of the image, preventing microspheres from sinking into the projection channels.



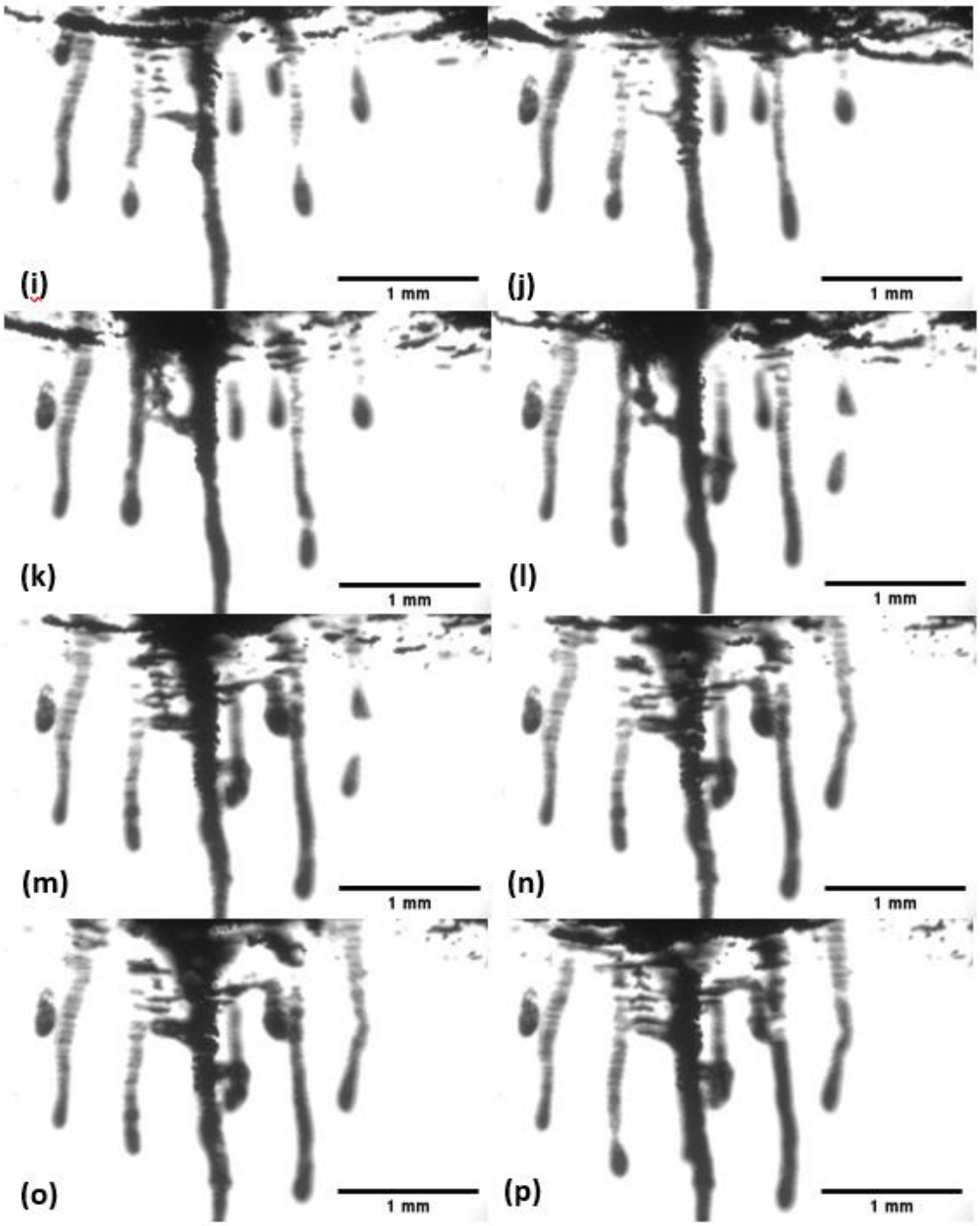


Figure 49: Series of images (a-p) captured during HIFU exposure for Mould 86. Each image is frame number 256 of 256 of each individual video capture, taken manually approximately 5 seconds apart. 0.500 MHz fundamental frequency, 1.9 MPa peak negative focal pressure, 5% Duty Cycle, 3.3 Hz PRF, 20 mg of 15-32 black glass microspheres with 310 µL of reconstituted SonoVue® microbubbles (3 x 10^8).

For this series, each image is the last frame captured from each video recorded, in chronological order over the whole course of the exposure. The videos were captured at 2,000 fps, for a total of 128ms per video over ~ 80 seconds, with each video being ~5s apart from one another (corresponding to the save time of the HPV-X2) using the 4x NIKON objective. Please note that at 4x magnification, the microbubbles themselves are not visible and Figure 49 is therefore only representative of the extravasation of microspheres through the agar medium and not of the microbubble movements within the ultrasound field.

Figure 49 shows the start of the projection in more detail. Each projection starts with a disruption to the packing of the microspheres, presumably brought about by the ultrasound induced motion of the intermingled microbubbles (although this cannot be resolved at 2000 fps). A 'bolus' of microspheres, highlighted in red, can be seen forming within the well at the centre of the frame (Figure 49, b, YouTube). With each new pulse, a group of microspheres is seen to collide with the well boundary, distributing other microspheres along it and initiating projection channels (Figure 49, c, YouTube). As the ultrasound exposure continues and further microsphere collisions occur, these channels extend in the direction of the applied ultrasound field and more channels form (Figure 49, b:p), A single tightly packed bolus of microspheres can be seen at the tip of each channel with a varying number of microspheres along the rest of its length. With each successive pulse the channels are increasingly filled with further microspheres (Figure 490, e:h).

As might be expected, those channels most closely aligned with the central axis of ultrasound propagation appear to grow the fastest, regardless of the order in which the channels are initially formed. As the channels grow in length, the number of microspheres available in the well diminishes and the previously obvious boundary edge is no longer visible, only the microspheres behind the central channel of the projection (Figure 49, i:p) are discernible. This channel is the broadest and most densely packed with microspheres. In channels with a lower

density of microspheres, a loose banding is now observable after the bolus at the tip of each projection (Figure 49, i:p, See Appendix 5 for further detail).

In the example shown in Figure 49, the central projection continues to progress beyond the edge of the image frame (the height of the frame is 2.2 mm) and continues linearly with the direction of the applied ultrasound field for several mm. The longer the ultrasound is applied for, the greater the length of the channels, increasing the overall length of the projection formed (See Chapter 3.2.6).

4.3.2.Microsphere Bolus Speed Measurements

By comparing distances within the frame and knowing the frame rate, estimates can be made of the speed at which a bolus of microspheres is propelled through the agar phantom. It is not possible to track individual microspheres in frame, due to the spatial resolution at this magnification (4x, 8.93 µm $pixel^{-1}$).

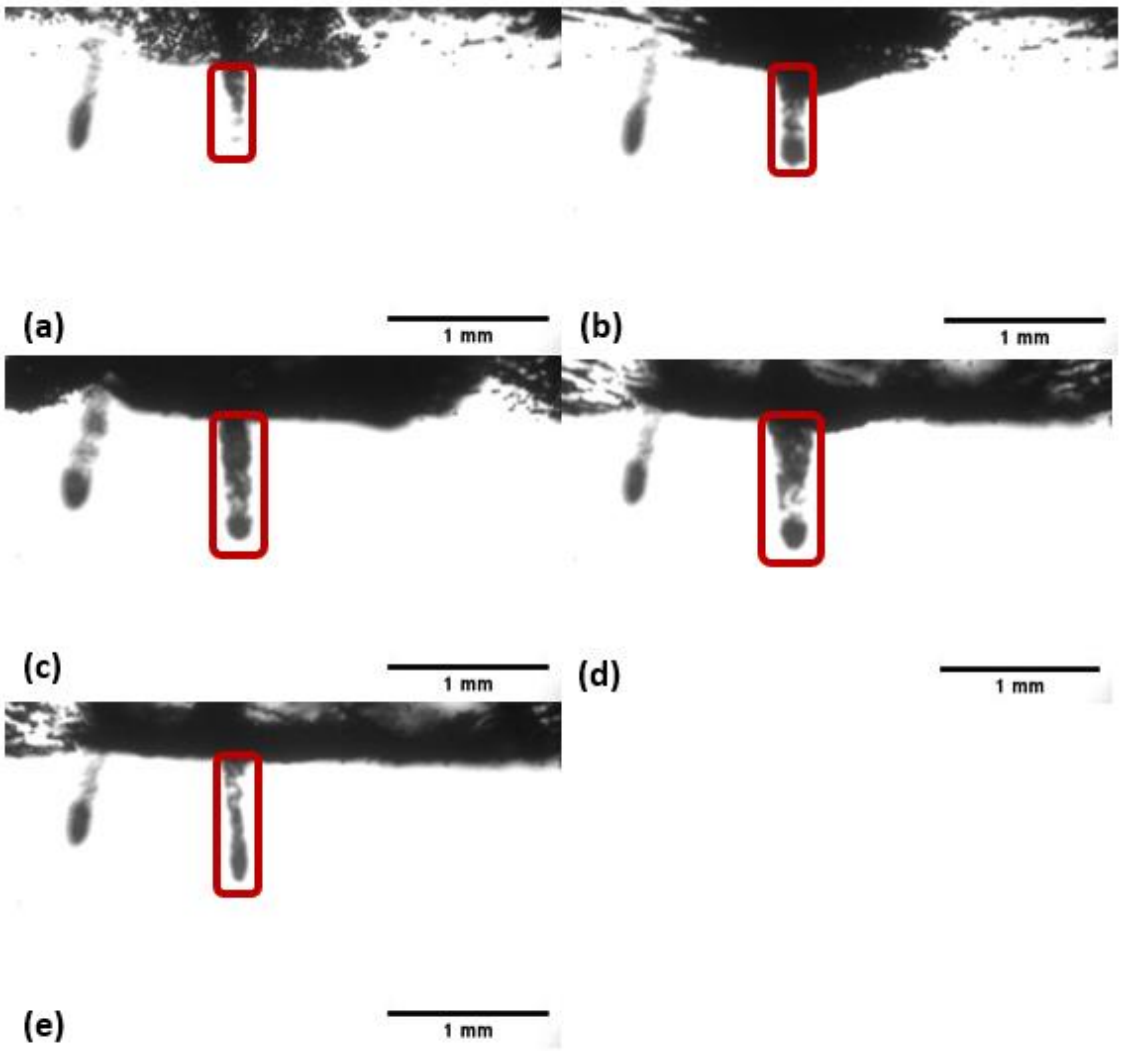


Figure 50: Frames 238-242 of mould 86 (YouTube) used to calculate the speed at which the bolus of microspheres travels through the agar to produce the most central channel. 5,000 fps, 200µs a frame). 0.500 MHz fundamental frequency, 1.9 MPa peak negative focal pressure, 5% Duty Cycle, 3.3 Hz PRF, 20 mg of 15-32 black glass microspheres with 310 µL of reconstituted SonoVue® microbubbles (3 x 10^8).

Figure 50 illustrates the extension of a projection channel. The projection in the middle of the image, shown by the red rectangle, measures 474 µm. As the channel grows over the next 4 frames it extends it to a length of 816 µm via the collision of the microsphere bolus with the end of the channel. In the fifth frame (Figure 50e), however, the ultrasound is off and the agar at the tip of the channel compressed by the impingement of the microspheres recovers, reducing the total length of the channel produced to 753 µm (i.e. an elastic relaxation of 63 µm). The average speed of the microsphere bolus in this case is therefore ~ 0.4275 m/s (427.5 mm/s). The width of the channel is also observed to increase (Figure 50, b:d), from 146 to 291

µm, with the widest point being at the most proximal end to the ultrasound or 'mouth' of the channel. This reduces to a width of 208µm after the ultrasound is switched off.

Measurements were taken for the pitch of multi-channel projections, to ascertain if there was any consistency in their spacing. As might be expected for a cavitation related process, there was no consistency in the spacing over multiple experimental runs, despite identical ultrasound parameters, phantom composition and geometry, microbubble and microsphere concentration.

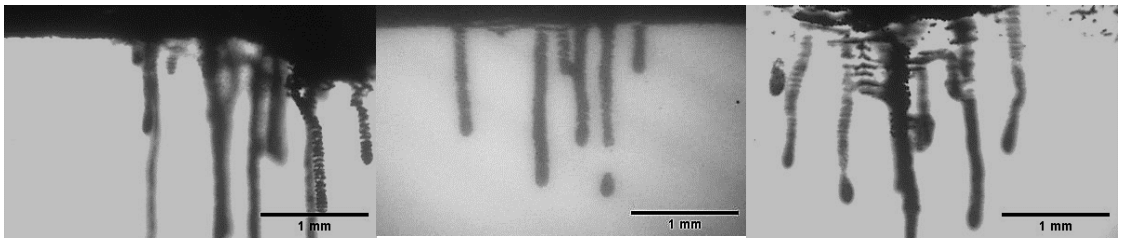


Figure 51: Examples of multi-channel microsphere projections using a 4x objective. Achieved using identical ultrasound parameters (See Section 4.1.8) Min 123.00, Max 739.00, Mean 365.459, STD 164.43; 26 measurements, 6 projections total. 0.500 MHz fundamental frequency, 1.9 MPa peak negative focal pressure, 5% Duty Cycle, 3.3 Hz PRF, 20 mg of 15-32 black glass microspheres with 310 µL of reconstituted SonoVue® microbubbles (3 x 10^8).

4.3.3.Rippling of the Edge of the Well

Prior to the extravasation of microspheres and the formation of projection channels, an oscillation or 'rippling' can be seen of the agar water interface at the edge of the well (Figure 52).

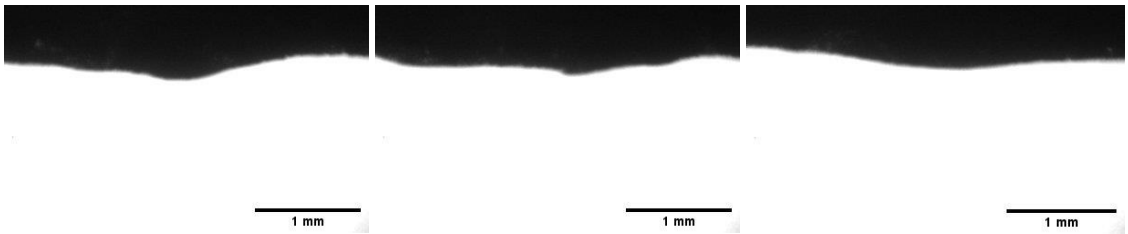
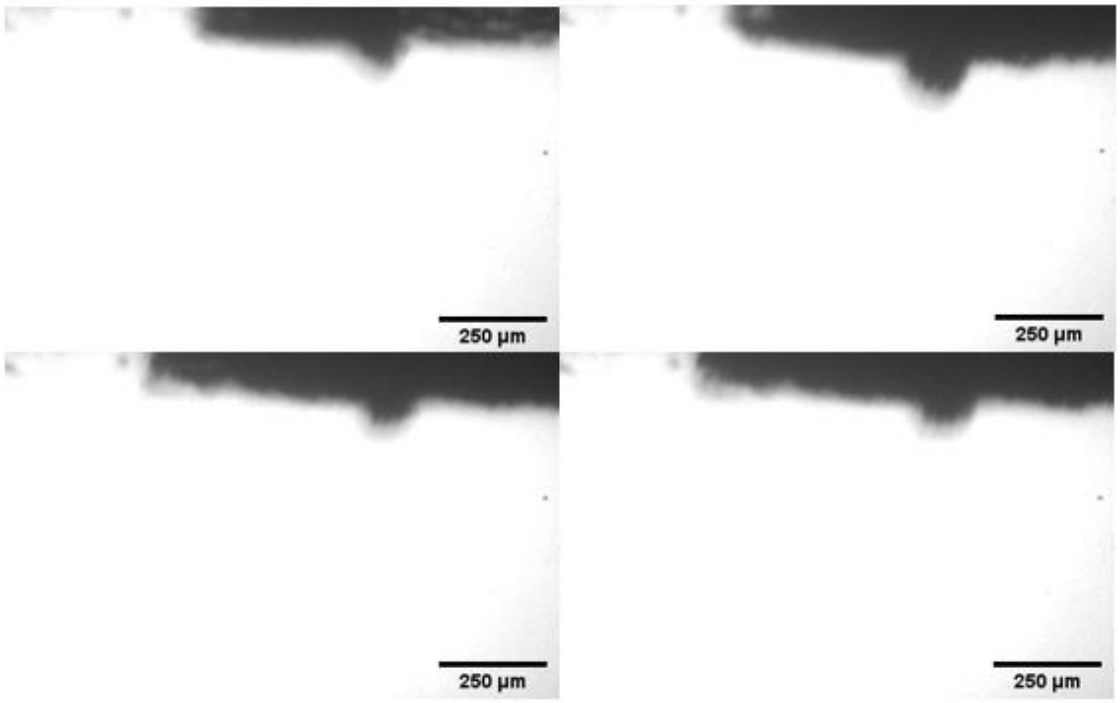


Figure 52: Rippling of the well edge under first ultrasound pulse at 2,000 fps. Frames 141, 142 and 143 of mould 86 (YouTube). Time between frames is 0.5ms. 0.500 MHz fundamental frequency, 1.9 MPa peak negative focal pressure, 5% Duty Cycle, 3.3 Hz PRF, 20 mg of 15-32 black glass microspheres with 310 µL of reconstituted SonoVue® microbubbles (3 x 10^8).

The timescale of this rippling phenomenon does not appear to correspond directly to the ultrasound exposure as the duration of the event is in the order of milliseconds, orders of magnitude longer than the period of the ultrasound (2 μs) and shorter than that of the PRF (3.3 Hz, 300 ms). Increasing the magnification (10x) and imaging frame rate (100,000 fps) indicated that this movement was in fact due to the formation and motion of a microbubble cloud (Figure 53, YouTube).



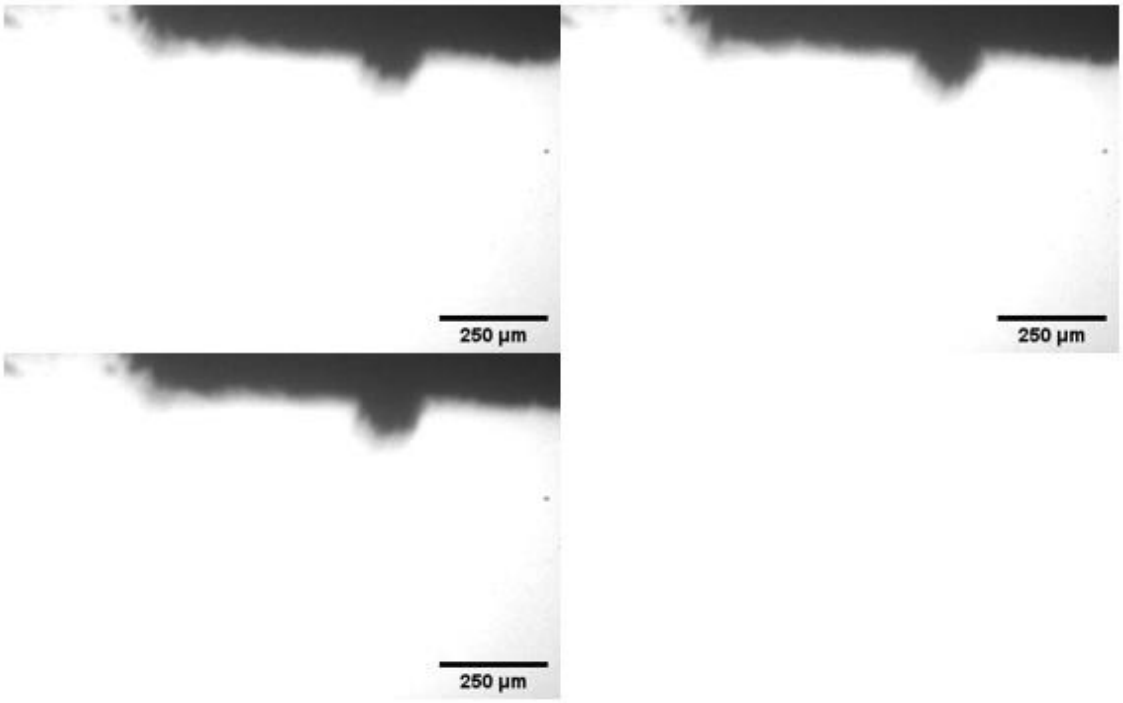


Figure 53: Rippling of the boundary edge as a result of a microbubble cloud. 10x objective, 100,000 fps, 15-32µm microspheres. Frames 132, 201, 240, 244, 248, 252 and 256 of 256 frame capture. Image frames within the figure are therefore 250ns apart, total time recorded 2560 µs. The increased packing density of the microspheres within the well cavity and loss of resolution at higher magnification when using <15 µm microspheres, inhibits resolving any further activity within the agar well. YouTube

During an ultrasound pulse the microbubble cloud moves throughout the frame within the voids created by the phantom well or projection channels. Whilst the microbubble cloud does not move across the frame between pulses, cavitation activity within the cloud and associated bead movements around the microbubble cloud continue; presumably sustained by scavenging of other microbubble in close proximity to the microbubble cloud which prolongs cloud cavitation between pulses (invisible at this magnification).

4.3.4.Observations of Bubble Cloud and Microsphere Interactions

Observing movement within the intermingled microbubbles and microspheres was particularly difficult with the smaller microspheres using the higher magnification objective. Using a lower magnification (4x) and much larger microspheres (106µm), which move more slowly due to their increased inertia, made it possible to track their individual movements within a

projection. Increasing the relative mass of each particle by an order of magnitude, requires an increase in focal pressure to induce movement for the same driving frequency (Figure 41, Section 3.5.4). Therefore, all images produced using the larger (106µm) microspheres used a focal pressure of 2.8 MPa. In addition to the increased focal pressure and microsphere diameter, it was necessary to increase the frame rate of video capture (to-200,000 fps) with the aim of observing microbubble cavitation effects rather than large-scale microsphere movements. In Figure 54. the smaller circular objects are cavitating microbubbles, expanding and contracting in response to the applied ultrasound field and consequently changing in appearance between frames. Bubbles in close proximity to each other can be seen forming a 'cloud'. In Figure 54, this bubble cloud has a maximum diameter of 329 µm (shown by the red rectangle), several times larger than that of the microspheres surrounding it; with its exact size depending on the phase of the ultrasound.

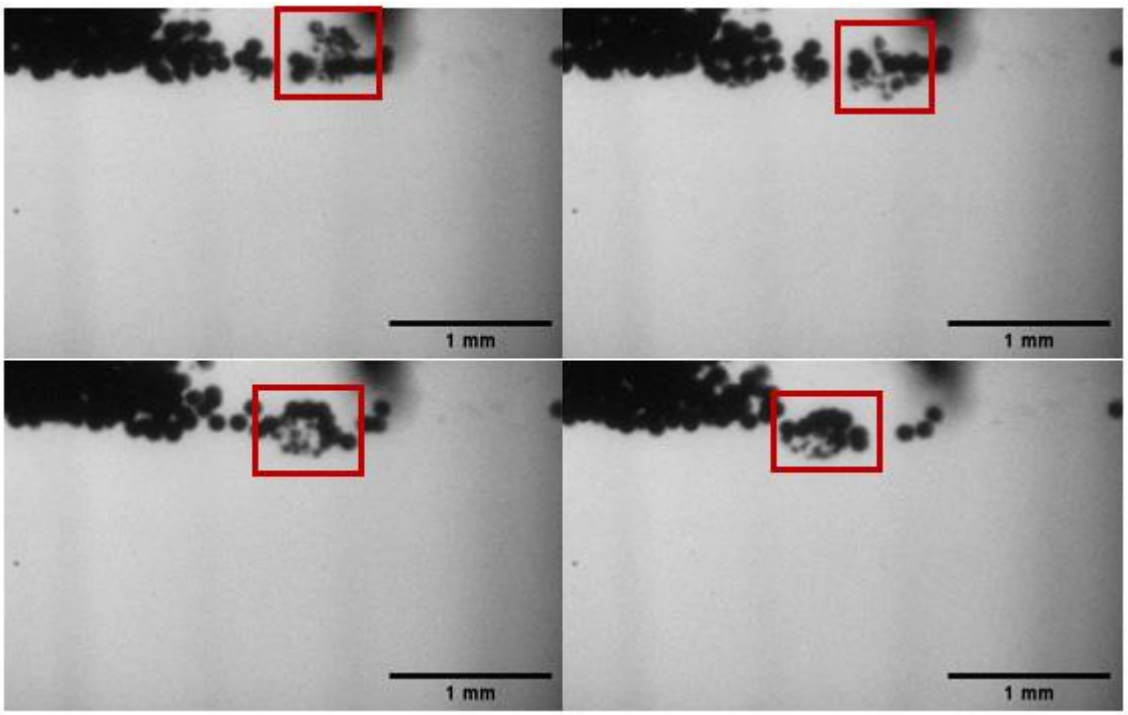
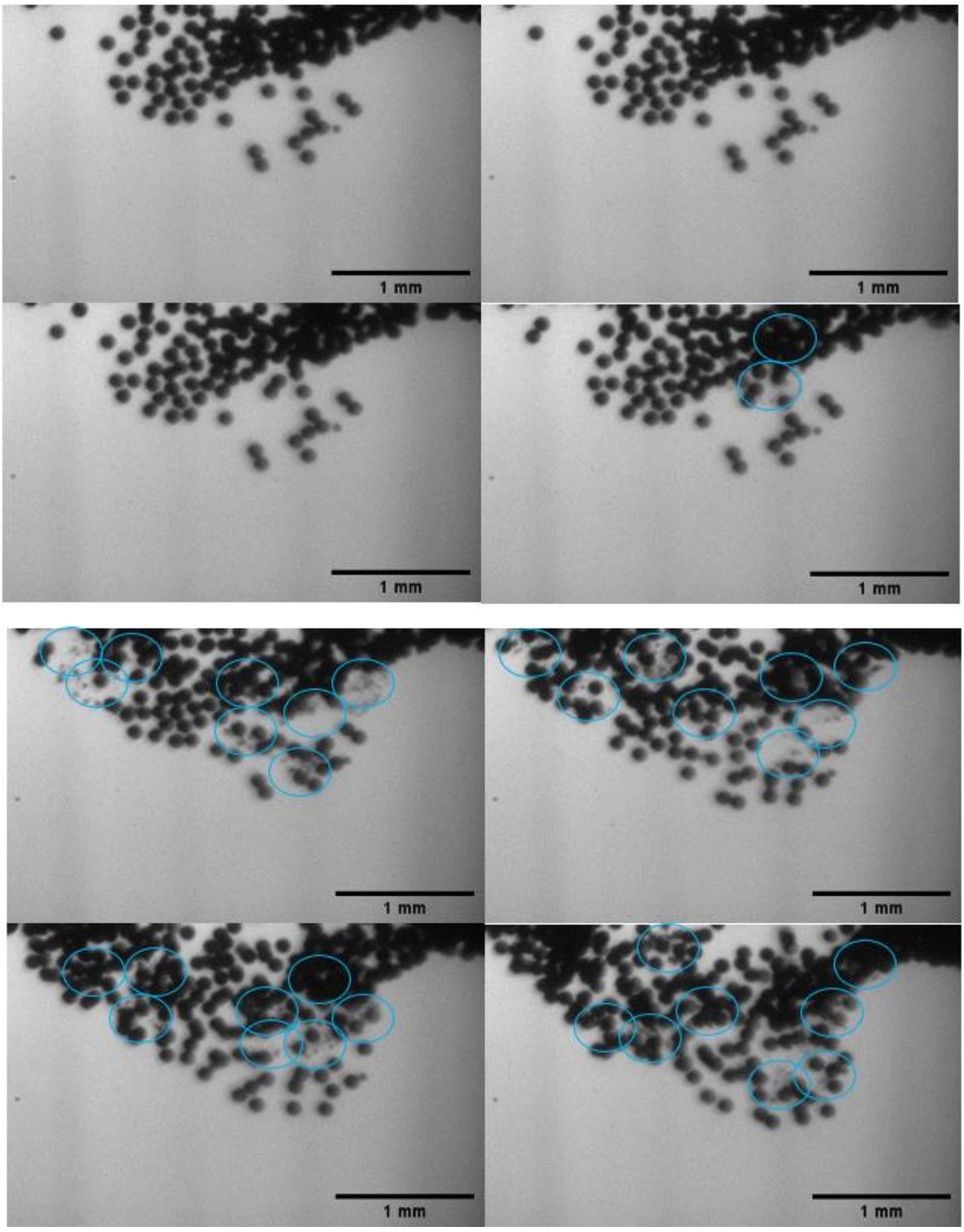


Figure 54: Movements of a cavitating bubble cloud, which attracts and gathers nearby microspheres (106µm). Microspheres can be seen gravitating towards the clouds (red) and travel with the cloud, rebounding off the surface. Mould 188, 2.8MPa focal pressure. YouTube

In the video of Figure 54, the microbubble cloud can be seen travelling to the forefront of the boundary edge from outside of the frame, propelled by the primary acoustic radiation force from the applied ultrasound. Despite their close proximity to the boundary edge, the microspheres appear unable to cross the boundary threshold without assistance from the cloud cavitation and remain dotted along the edge of the agar well.

The projection bolus, previously identified as a single dark amorphous mass, is now clearly identifiable as the combination of microbubble cloud and associated microspheres (Figure 54, red). Microspheres can be seen being drawn towards the cloud and rebounding off its surface. Due to the increased separation between the larger microspheres, individual microbubbles within the cloud can be seen oscillating, in and out of phase with one another sustaining the cloud activity and microsphere movements.

At 2.8MPa peak negative pressure, multiple clouds were observed (Figure 55, circled in blue), which travel to the front of the well simultaneously extending the length of the microsphere projection, across the image series (YouTube). Resulting in the formation of a large broad singular channel, approximately equal in width to the transducer focus (1mm for 0.5 MHz, See section 2.2.4). It is difficult to ascertain with absolute certainty how many clouds are formed, expire, coalesce or are sustained throughout the time captured; as at these frame rates (100,000-200,000 fps) and magnification, it is not possible to temporally or spatially resolve oscillations of individual microbubbles within the cloud; nor is it possible to record the activity of the microbubble cloud over the entire pulse length at this capture rate, due to the maximum number of frames allowed using the HPV-X2.


1 mm
1 mm
1 mm
1 mm
1 mm
1 mm
1 mm
1 mm

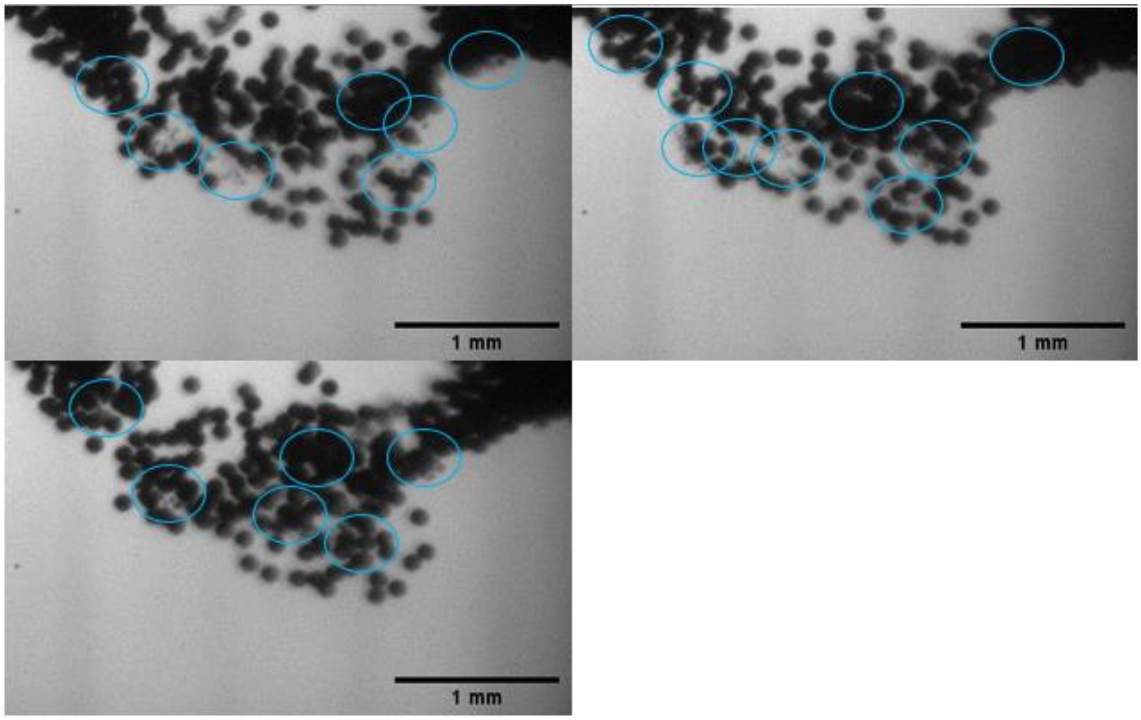
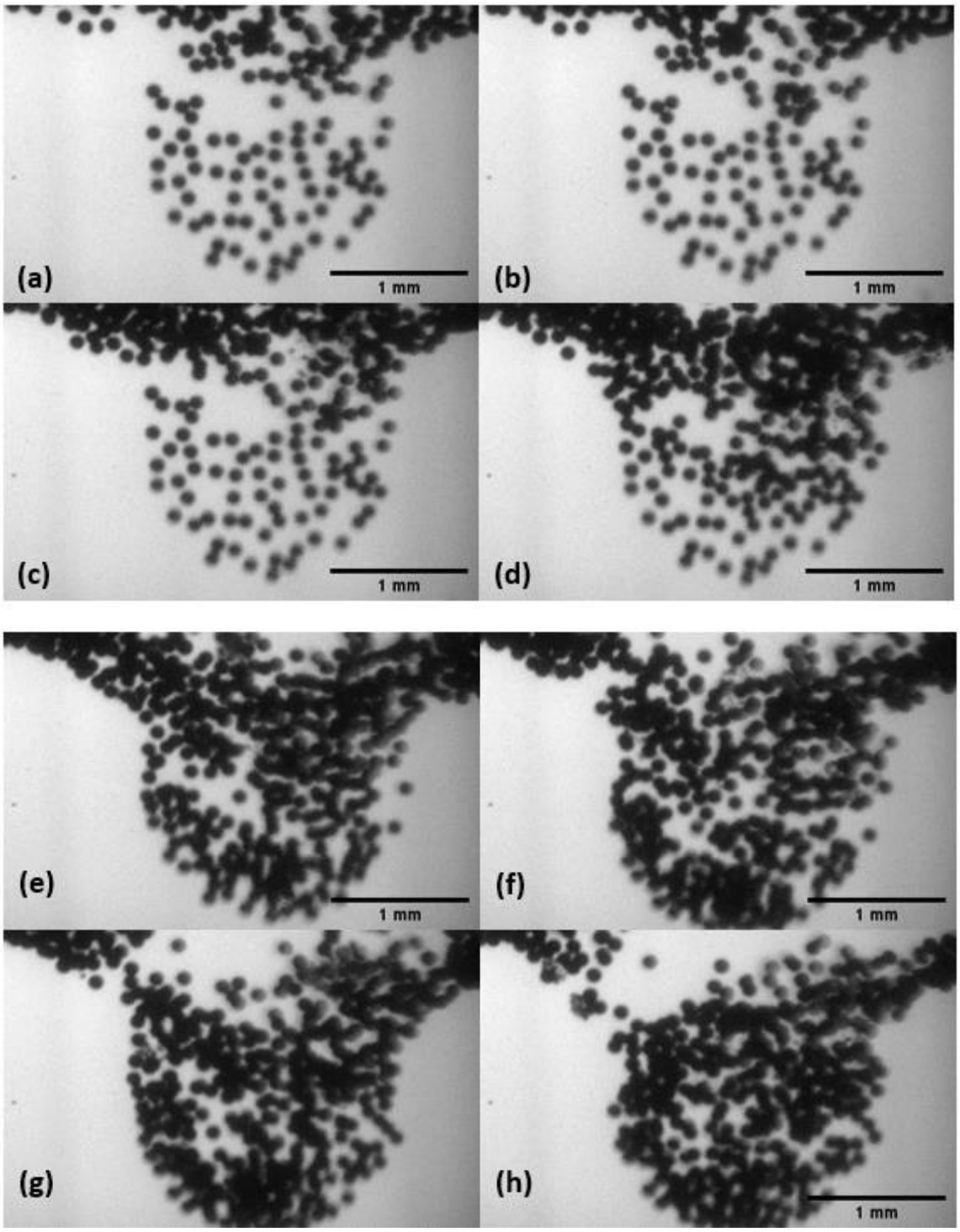


Figure 55: Frames 001, 026, 051, 076, 101, 126, 151, 176, 201, 226 and 251 of mould 188. 100,000 fps using a 4x objective, 106µm microspheres. Propulsion of multiple cavitating microbubble clouds (blue) being drawn to the front of the well cavity as a 'wave' which extends the microsphere projection. With further microbubble clouds joining the channel progression over time. YouTube

Between Figures 54 and 55, it is clear that the microbubble clouds which travel from within the well to the boundary edge of the agar, are directly responsible for the erosion of the agar and the formation of the projection channel(s). As the ultrasound pulse is applied to the well behind, the acoustic radiation force acting upon the bubble cloud drives the cavitating bubble cloud further into the agar (Figure 54) as seen by the extension of the boundary interface, eroding more of the agar and forming the beginnings of a channel, with the microspheres back-filling the voids created by the cavitating microbubble clouds.

Between ultrasound pulses the cavitation within individual microbubble clouds wanes, some clouds coalesce and bring together microspheres to a single focal point of increased density (Figure 56, h). As the activity within the microbubble cloud wave ceases, and the majority of the microbubble clouds disappear, a large single bolus of microspheres is now visible at the tip

of the projection channel (Figure 56, h:k), with a lower concentration of microspheres in its wake (as previously seen in sections 4.3.2 and 4.3.4).



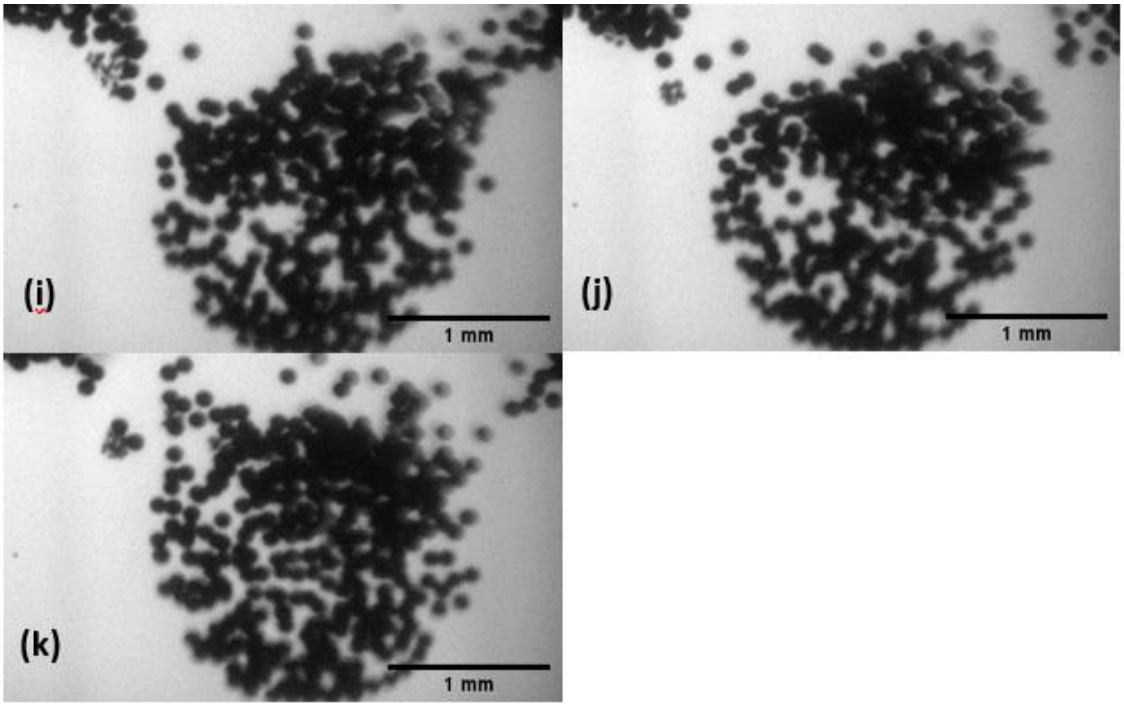


Figure 56: Frames 001, 026, 076, 101, 126, 151, 126, 151, 176, 201, 226 and 256 of mould 189. Captured at 50,000 fps using a 4x objective and 106 µm microspheres. Example images of how the multiple cavitating microbubble clouds group together to form a single microsphere bolus at the tip of the projection. YouTube

With the increased microsphere diameter (106 µm, 15-32 µm previously) and interstitial spacing of the microspheres, there are fewer physical restrictions to prevent bubble clouds to traversing between microspheres and coalescing with one another to form larger microbubble clouds (Figure 57).

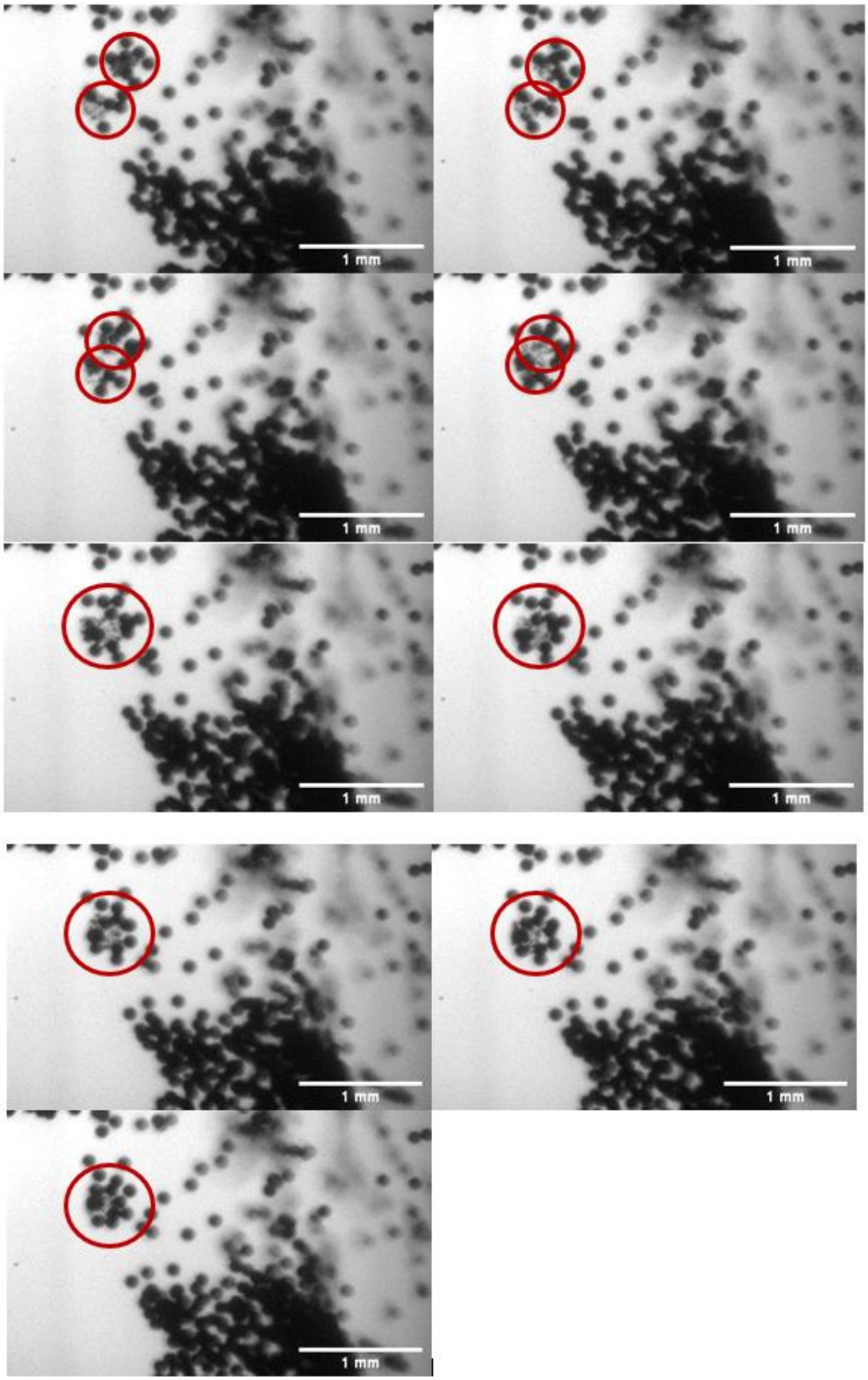

1 mm
1 mm
1 mm
1 mm
1 mm
1 mm
1 mm
1 mm
1 mm

Figure 57: Frames 125, 127, 129, 131, 133, 135, 137, 139 and 141 of mould 191. Captured at 50,000 fps using s 4x objective and 106µm microspheres. Coalescence of individual bubble clouds is highlighted in red. YouTube

Both coalescence of microbubble clouds and cloud formation were observed. The latter appears have been promoted by the collision of the glass microspheres, potentially because the contact between the two curved surfaces, creates a nucleation site between the two microspheres[24,25] (Figure 58).

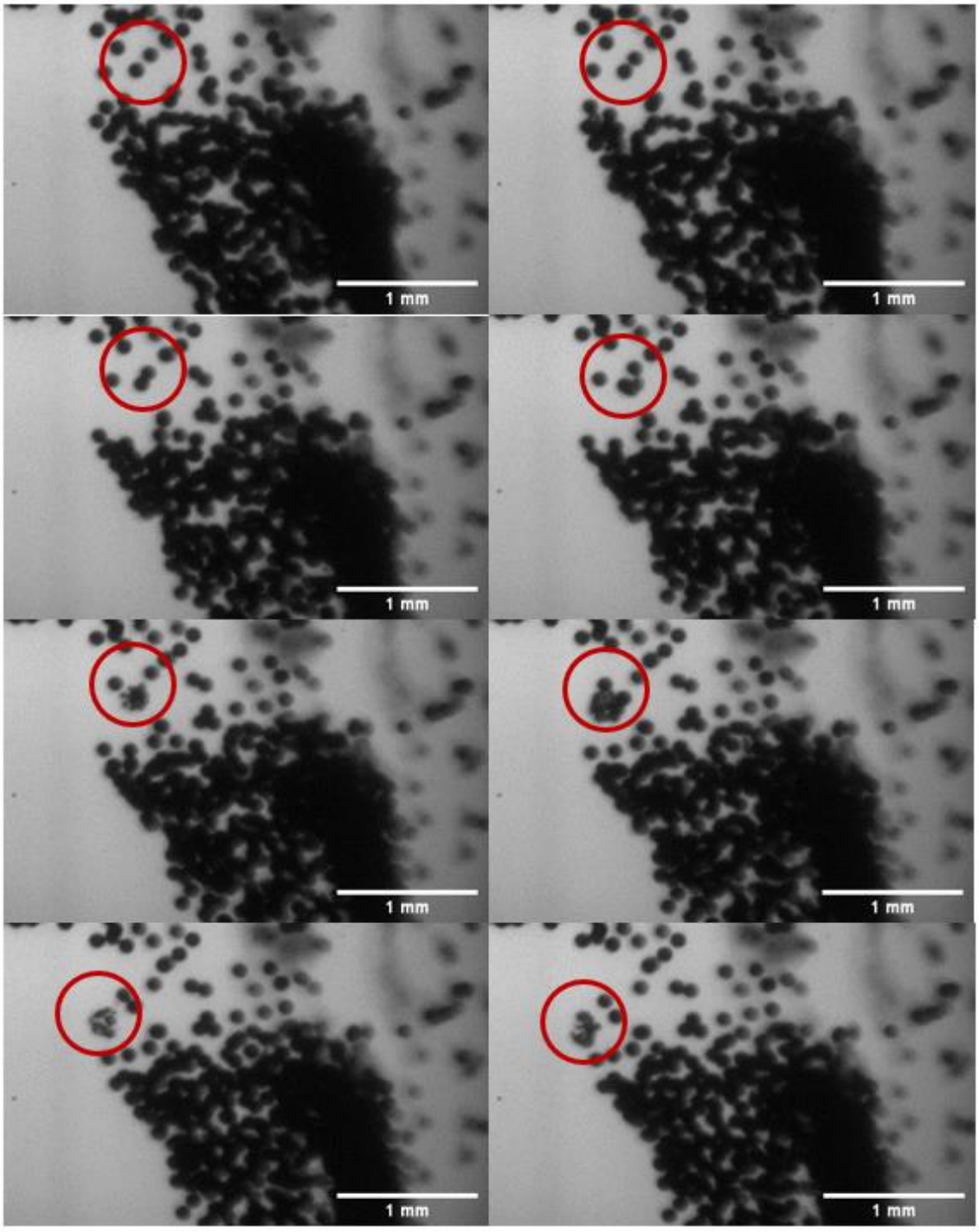


Figure 58: Frames 033, 037, 043, 045, 047, 049, 051 and 053 from mould 190. Captured at 50,000 fps using a 4x objective and 106µm microspheres. Collision of microspheres results in the formation of a new bubble cloud and subsequent microsphere-cloud cluster (circled in red). YouTube

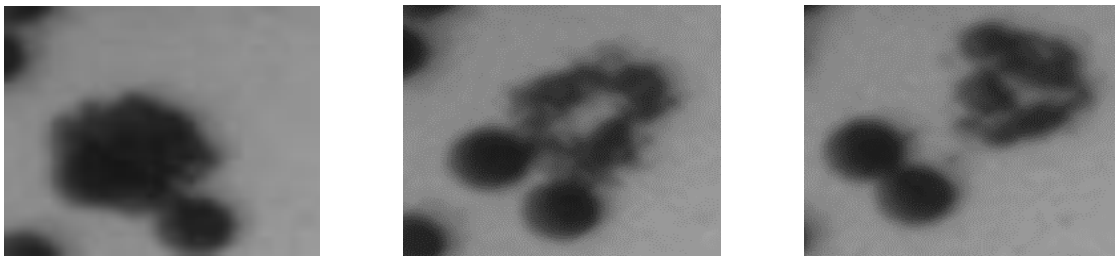


Figure 59: Close up images of microbubble cloud dissociation, from mould 190 (Figure 14). Frames 049, 050 and 051 of 256. Microspheres are 106 µm for reference. The formed microbubble cloud can clearly be seen forming between the microspheres and separating from the nucleation site between them.

Once formed, the new clouds appear to grow and drive the microspheres apart, freeing the cloud to travel in the direction of ultrasound propagation towards the tip of the projection (Figure 59) and further assisting the movement of the microspheres in this direction.

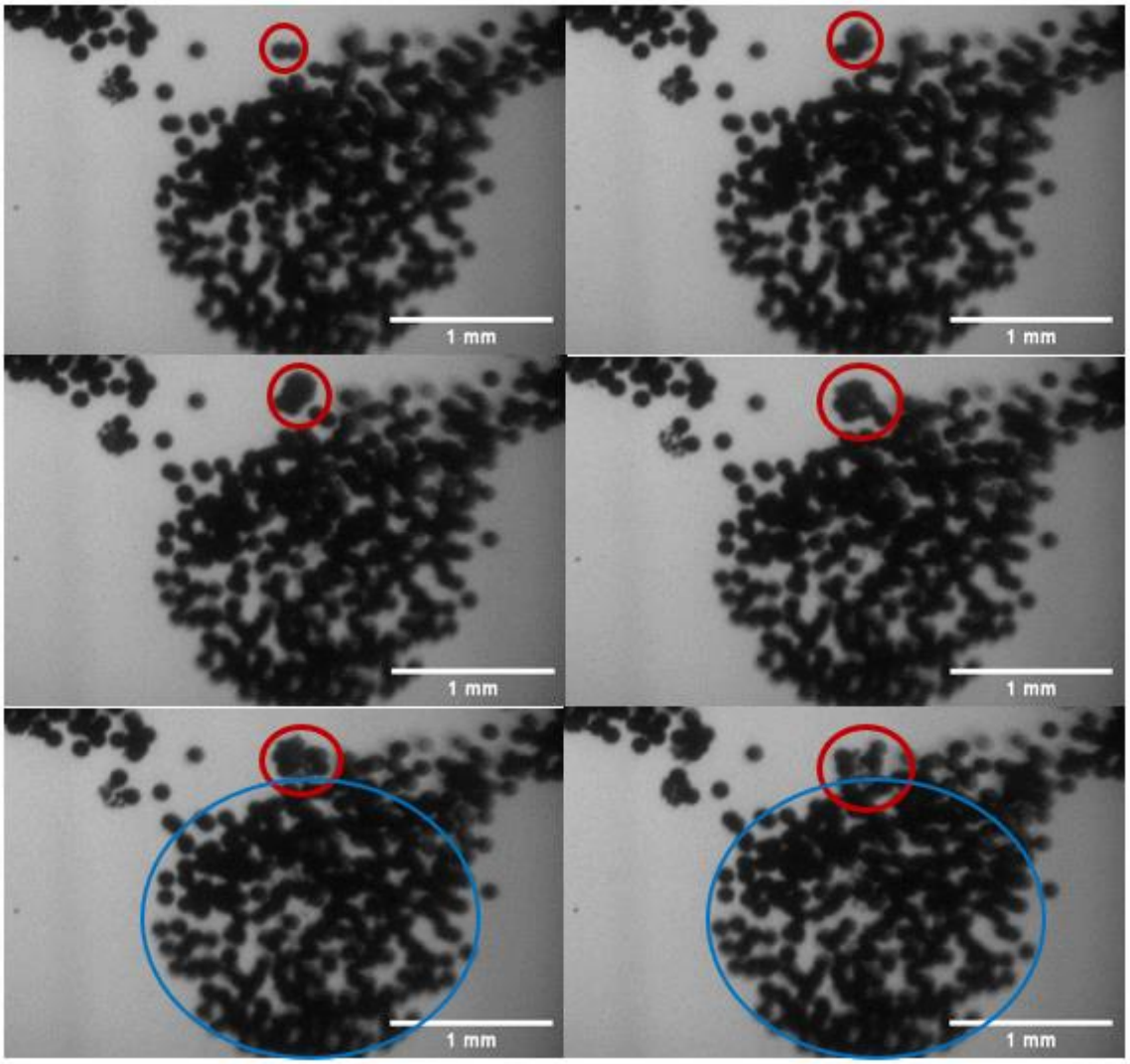
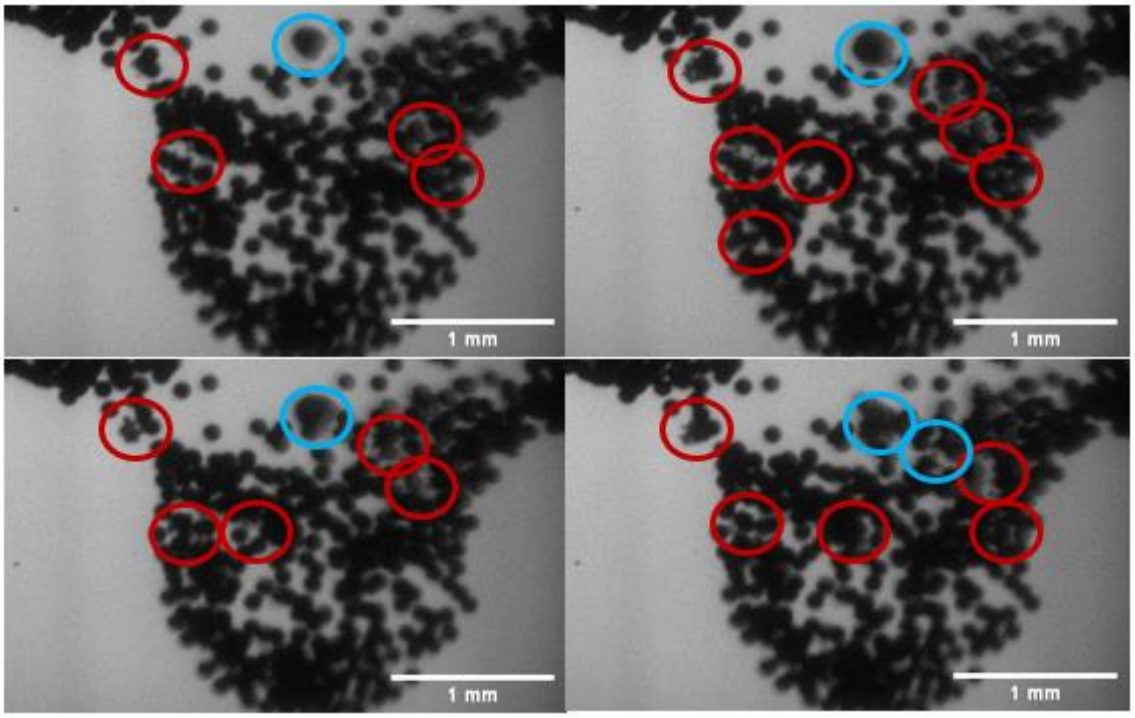


Figure 60: Frames 191 to 196 of mould 191. Captured at 50,000 fps using a 4x objective and 106µm microspheres. Images show the collision of microspheres acting as a nucleation site for microbubble cloud formation (red), which in turn moves to join the bolus of other microsphere cloud clusters within it (blue). YouTube

The creation of microbubble clouds via the collision of microsphere, is not limited to microspheres outside the projection bolus at the tip of the projection channel. Indeed, it seems to have been promoted by the increased packing density of microspheres at the projection tip. Each microbubble cloud which joins the bolus at the tip of the projection disrupts the packing density of the resting microspheres causing further collisions, and formation of microbubble clouds. In Figure 61 microbubble clouds (blue and orange) join the bolus from the agar well out of frame in the direction of the primary acoustic radiation force. The microbubble cloud highlighted in blue, causes a microsphere collision and formation of another microbubble cloud. The newly formed cloud (blue) connects with pre-existing microbubble clouds (red) sustaining the cavitation activity. The cavitation activity within the bolus is sustained in this way until either the ultrasound is tuned off or the cavitation nuclei are depleted.



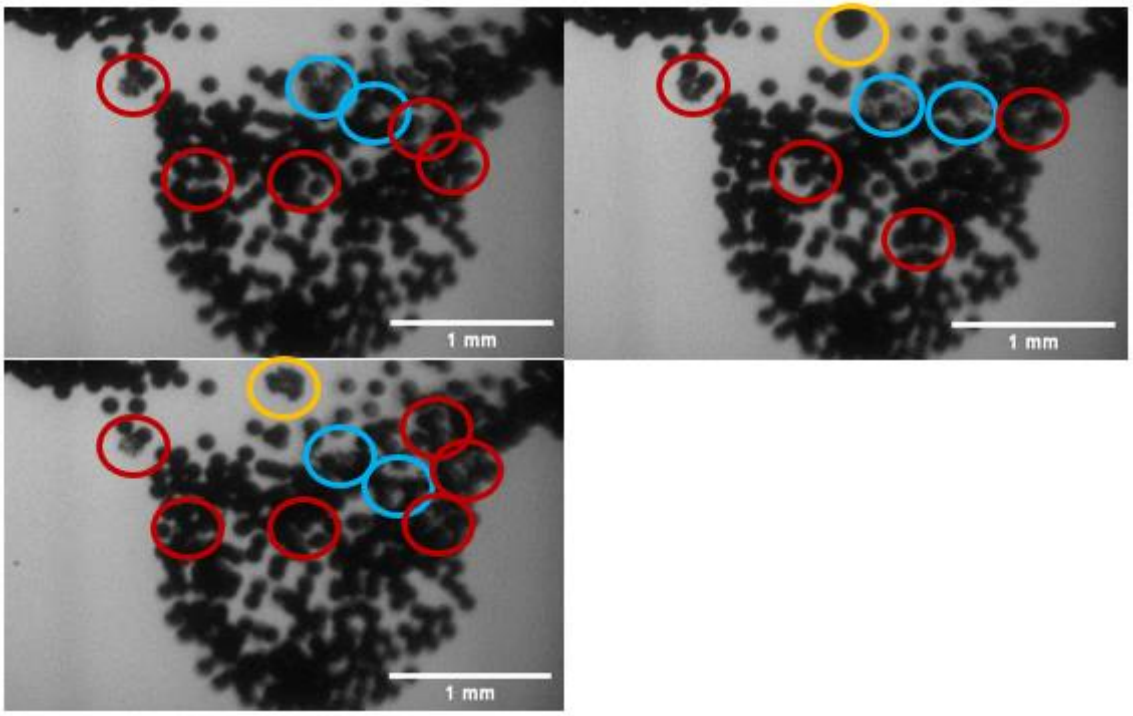


Figure 61: Frames 155-161 of mould 191. 50,000 fps using a 4x objective 106 µm microspheres. Collision of microspheres produces a cavitating microbubble cloud (blue) which under the influence of primary acoustic radiation force, joins the collection of other microbubble clouds within the bolus of microspheres, seeding further cloud cavitation. The formation of another microbubble cloud is seen (orange) repeating the cycle of growth. YouTube

4.3.5.Microsphere Bolus Movement

Whether or not a bolus enters a pre-existing channel appears to be entirely random with boluses that are initially not in frame suddenly appearing and travelling past visible boluses to entering a channel (Figure 62) [26].

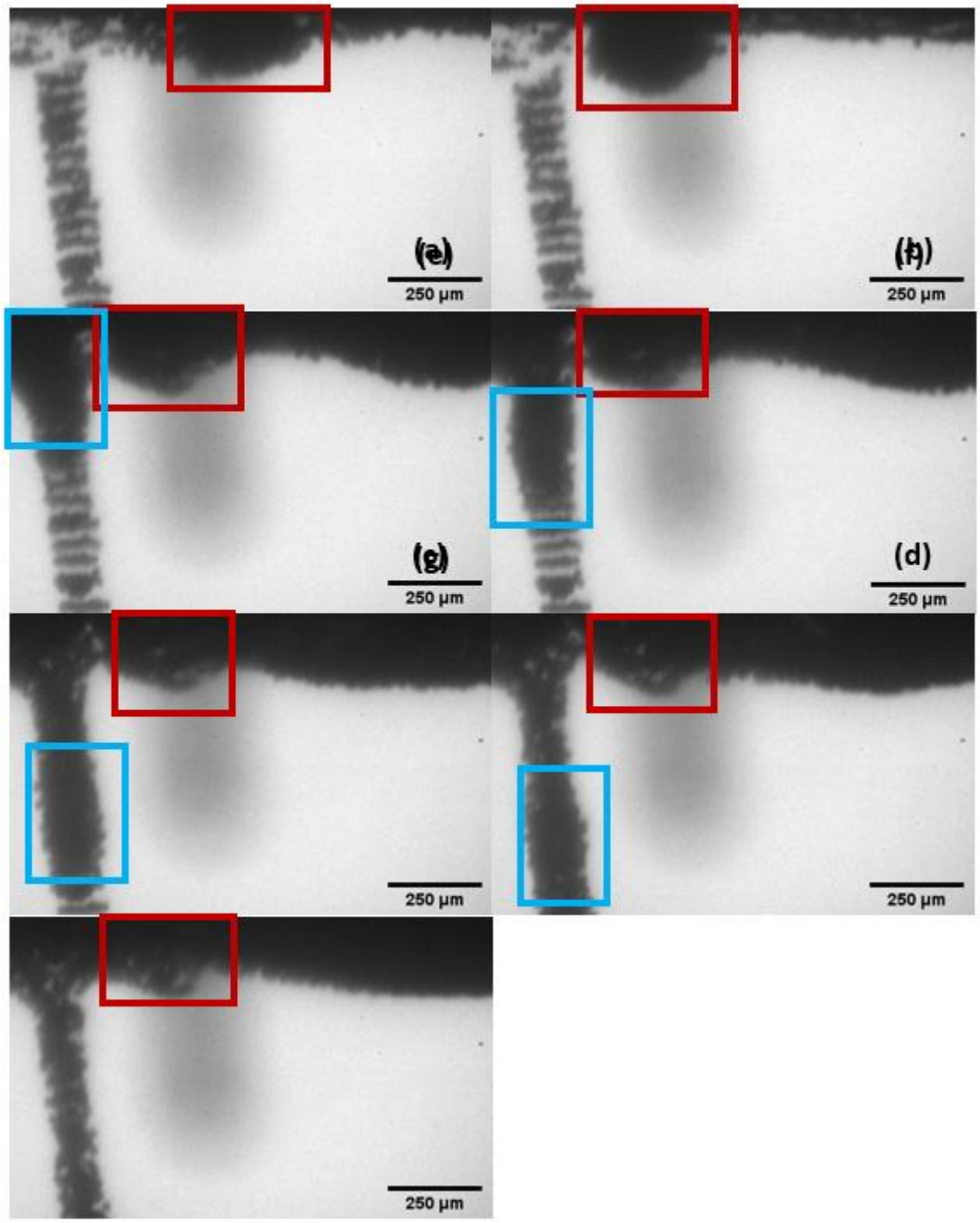


Figure 62: Frames 125, 135, 240, 242, 244, 246 and 253 of mould 155 (YouTube). Captured at 10,000 fps. Images show the movement of a single bolus (red) which comes to a halt near the opening of a pre-existing channel, only for another faster moving bolus out of frame (blue) to pass by in close proximity travelling down the channel's lumen and out of the image frame. It is unclear if the cloud cavitation in the first bolus continues for the entire length of the recording. Another channel of the microsphere projection at a different depth can be seen forming out of focus in the middle of the frame, causing the blurring in the centre of the image.

As a bolus travels down a channel, the channel widens in diameter to accommodate it (as previously seen in Section 4.3.2) contracting back to its original size after the bolus has passed. The elasticity of the agar acts as a one-way valve, trapping the bolus and preventing it from returning to the bulk of the well cavity. The microspheres in the wake of the bolus's movement appear to be more densely.

Whilst the microbubble clouds are sustained by the applied ultrasound field, boluses traversing the well or channel lumen act as single entities, although there is some exchange between microspheres in bolus and those in the surrounding medium. Unfortunately, it is not possible to discernible whether the exchange of microspheres enables the microbubble cloud to pass down the channel, displacing the solid medium in its path.

In between ultrasound pulses, the bubble clouds do not immediately disappear and the bolus continues to move along the channel. Eventually this movement ceases, and the microspheres gently settle usually at the furthermost tip of the channel. Channels which are constantly supplied with fresh boluses increase the most in length, with each new aggregate of microspheres and microbubbles destroying more agar at the tip of each channel, increasing the channels total length (Figure 63). Boluses continue to erode the agar boundary interface until the energy provided by the cloud cavitation ceases, at which point the channel ceases to increase in size. The same bubble cloud activity is also responsible for each projection channel formation but requires additional energy to overcome the elastic interface of the agar and sufficiently allow for a cavitating cloud to fit with its lumen.

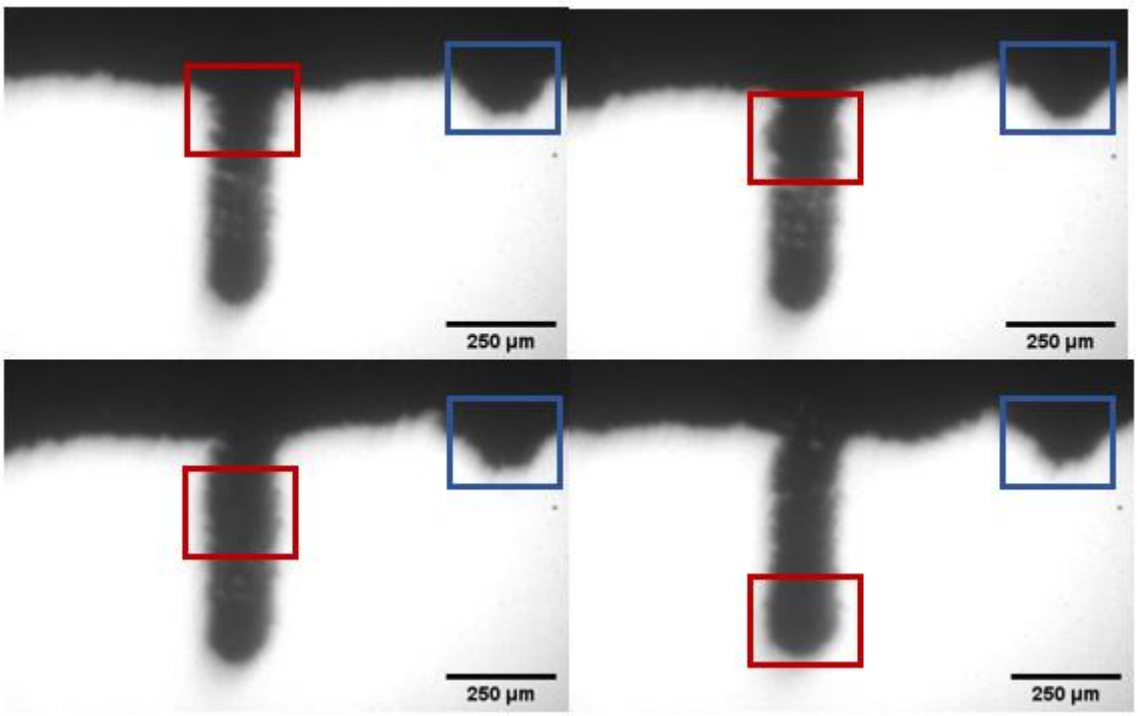


Figure 63: Frames 001, 163, 175 and 245 of mould 167 (YouTube) captured at 100,000 fps, 15-32 µm microspheres. Cluster cloud cavitation extends a smaller channel (blue), whilst a cluster travels down the longest, central channel to continue eroding agar at the channels furthest most point (red). Both channels are formed by the same mechanism of action, but in different time scales, determined via the number of clusters delivered and energy used to destroy the hydrogel.

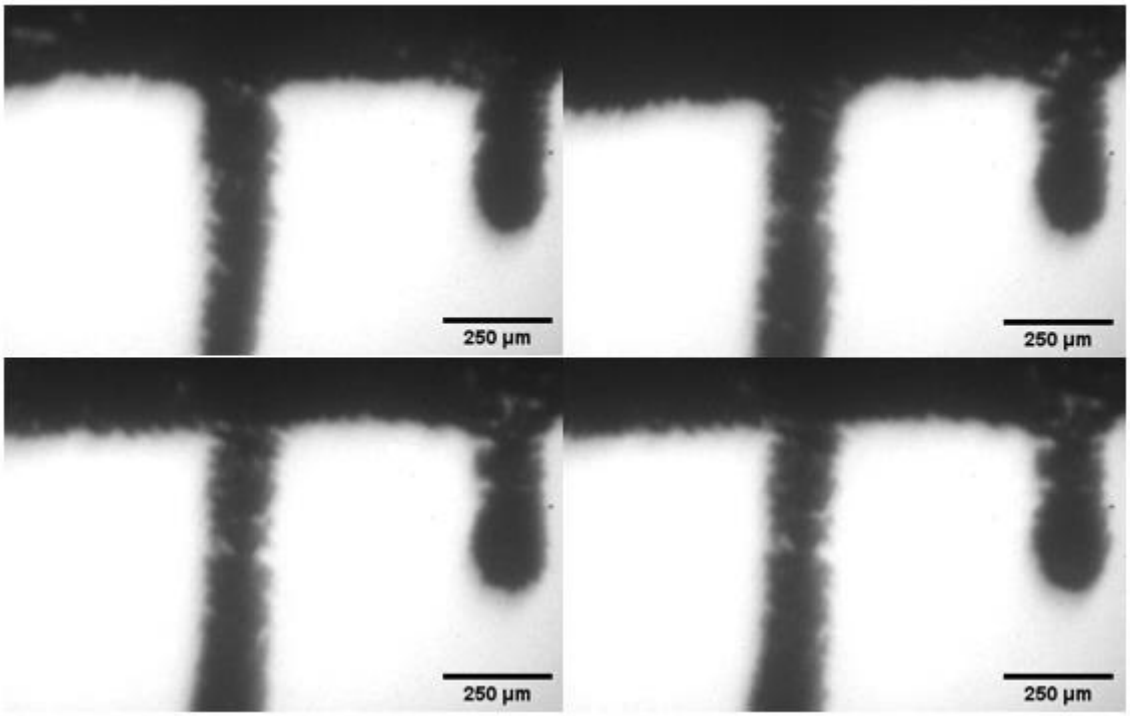


Figure 64: Frames 002, 161, 249 and 256 of Mould 167 (YouTube). Captured at 100,000 fps, 15-32 µm microspheres, approximately 10s after figure 63. The immature projection channel (top right in images) has now extended disproportionately to that of the central projection, which is now long enough to continue out of frame (>782µm).

4.4. Discussion

4.4.1. Order of Events Leading to Microsphere Extravasation

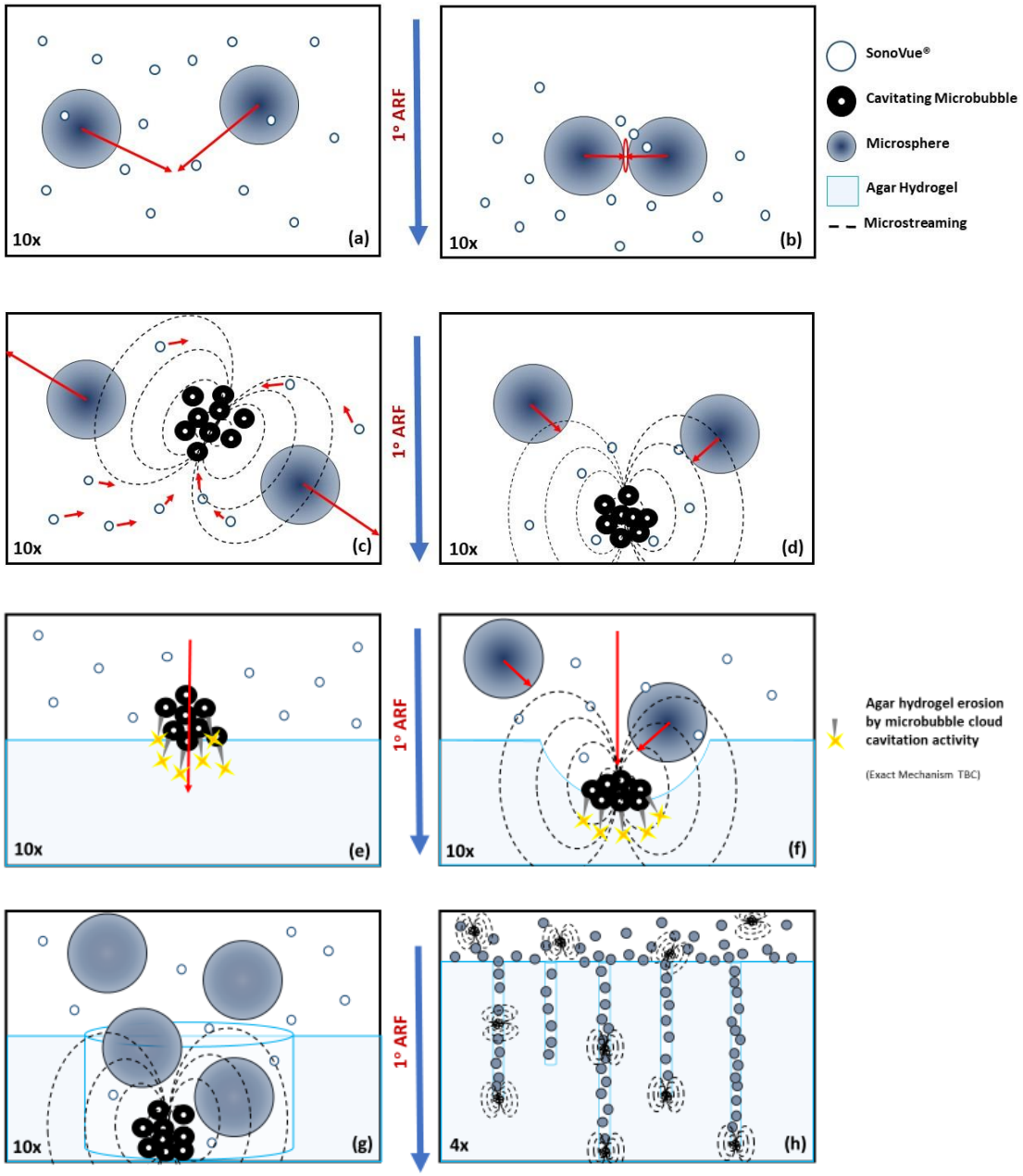


Figure 65: Events occurring within the well of a hydrogel mould to produce microsphere extravasation. Microsphere collision (a) brought about by ultrasound exposure, promotes formation of (b) a cloud of oscillating SonoVue® bubbles which in turn generate microstreaming(c). The primary ARF dissociates the microbubble cloud (c, d) from the microspheres and presses it into the agar boundary interface (e). The oscillating microbubble cloud causes mechanical erosion of the agar (e, erosion highlighted in yellow), producing a channel within it (f), the void created is filled with microspheres and additional cavitation nuclei via a combination of microstreaming and radiation force (g). Further microsphere collisions occur, producing additional bubble clouds and extending the channel. These events occur at multiple locations throughout the well cavity, producing a multitude of microbubble clouds and a number of projection channels (h). The primary acoustic radiation force from the applied ultrasound acts from top to bottom in all image panes. Objects are not to scale. The approximate magnification corresponding

to the high speed videos is indicated in the lower left hand corner of all image panes. Red arrows denote the direction of microsphere and/or microbubble movement. Dotted lines indicate microstreaming.

4.4.2.Microsphere Imaging Capability and Clarity

It was serendipitous that the existing TheraSphere™ size distribution of 15-32 µm was well suited to this setup, producing clear images of microsphere distribution under various magnifications. The use of larger microspheres (106 µm) and a lower magnification objective (4x), however, ultimately proved to be the most useful for observing cavitation activity and the interactions with microspheres leading to projection formation. This was because the glass cover used in the equipment setup (Section 4.4.2), scattered the transmissible light, resulting in increasingly less focused images at higher magnifications (See Appendix 4, for further details).

Irrespective of whether or not smaller microspheres would be more favourable for extending the post-focal projection length, it would not have been possible to image microbubble cloud activity with smaller (<106 µm) microspheres using the currently proposed setup. This is because microspheres smaller than 106 µm, had an increased packing density, reducing the light transmitted between microspheres, making resolving cavitation activity and microsphere movements difficult, reducing overall image quality and the image resolution of within the channels of the projections produced. Using microspheres greater in size (>35µm) also reduced image quality at increased magnification as only a fraction of the microsphere's depth could be in focus at any given point using the 10x objective, with the remaining proportion of the microsphere out of focus which obscured finer details in front or behind the larger microspheres e.g. gel edges, cloud oscillations or reverberations within the gel channel(s). This shadowing effect of the larger microspheres under the 10x objective (Figure 66, b) was mitigated by switching to the 4x objective (See Section 4.3.1) enabling capture of the microbubble cloud directly.

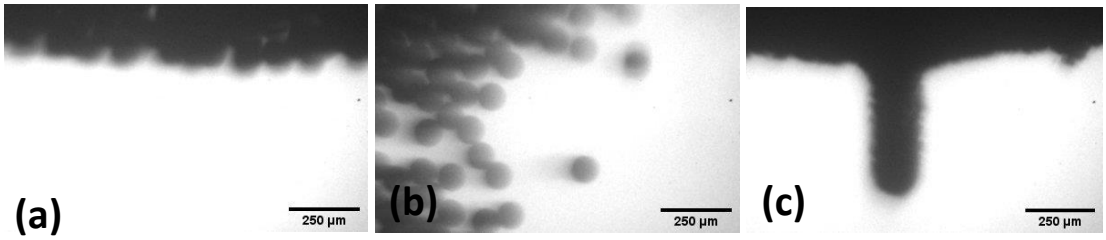


Figure 66: Poor focusing of microspheres due to casting of shadows by large microspheres at higher magnification (a and b). A reduction in image sharpness due to focussing and resolution on small microspheres (<15um, c).

Changing the total mass of microspheres added to the well (5 – 100 mg), had no effect on the relative distribution of microspheres within any projections produced. It was hoped that lowering the mass, would increase visibility of the bubble cloud dynamics behind the spheres at within the channels produced but this was not the case, irrespective of the mass added the packing density of the microspheres remained the same. Only the number of microspheres visible within the well (top of each image frame) changed. It is unclear whether the reduction in microsphere mass, reduced the number of projection channels formed. The only noticeable difference was an increase in the minimum pressure required for the formation of the projections, for the 106 µm microspheres (See Section 4.3.2).

Despite the slight loss of image quality from the glass objective cover, the combination of increased microsphere diameter (106µm) and spacing between the individual microspheres meant that bubble-cloud activity was easily visible and distinguishable from the microsphere movements under low magnification (4x). The obvious difference in size between the larger microspheres, microbubbles and clouds thereof, allowed for improved identification of effects and movements which the smaller microspheres obscured. The use of the higher magnification objective (10x) and the combination of smaller microspheres (<106µm) decreased the image quality to such an extent as to prevent clear imaging of the microbubble cloud at lower peak negative pressures (1.9 MPa), it is therefore assumed that the bolus movements at the lower peak negative pressure are the result of a single microbubble cloud rather than a ‘wave’ of

clouds, despite it not being possible to image individual oscillations of the microbubbles within the cloud. This is because multiple channels with a reduced lumen diameter were produced using a lower peak negative pressure (1.9 MPa) rather than a single oversized channel observed at high pressures (2.9MPa) with multiple microbubble clouds interacting with the agar interface as a 'wave' (See Section 4.3.2).

It is unclear whether the increase in diameter of the microspheres and subsequent increase in peak negative pressure (2.9 MPa) used, increased the overall projection length compared with smaller (<106µm) microspheres with equivalent pressure, as the number and activity of the microbubble clouds also increases with the increased peak negative pressure used. As shown in Chapter 3 (Section 3.2.6) increasing the total mass of microspheres added to the injection site does increase the total post focal projection length, presumably increasing the total number of microspheres also increases the number of collisions and microbubble clouds produced, sustaining the cavitation activity between pulses. It remains unclear whether it is favourable to use a fewer number of larger microspheres with a higher individual mass or a greater number of smaller microspheres with a smaller individual microsphere mass.

4.4.3.Microbubble Cloud Erosion of the Agar Medium

The images produced in this chapter show microsphere extravasation occurring as the result of a microbubble cloud activity rather than of individual microbubbles. It appears from the images shown in the previous section (4.3.2), that the microbubble clouds erode the agar interface, with the dense glass microspheres back filling the void produced a combination of microstreaming and primary and secondary acoustic radiation forces.

Whilst for smaller microspheres and lower pressures (1.9MPa) the number and size of the channels produced appear to resemble tunnelling phenomena[15] of individual microbubbles, there appears to be no loss in activity of the microbubble cloud at a boundary interface

(Section 4.3.3). Microbubble cloud boluses can 'rest' on the agar boundary surface, whilst the microbubble population of the cloud continues to cavitate; implying no penetration and subsequent erosion of the agar hydrogel by microbubbles within the microbubble cloud.

Prentice reports jetting of the surface of the cavitation cloud, with microbubbles collapsing from the periphery towards the centre of the cloud[27]. Micro-jetting has been observed eroding various hard rigid boundaries[28–30] and may explain why erosion of the agar boundary is observed without a dramatic decrease in cloud cavitation activity, which would be obvious in tunnelling phenomena where the cavitation nuclei are expended to produce the gel channels[15]. In practice microjets are preferentially formed towards the most rigid boundary and away from the pressure relief surface; which in this case would be the glass microspheres. The surface of the microspheres however is convex, resulting in two opposing jetting forces, the jet and counter jet, drastically diminishing the impact force on the microspheres[31]. This may explain why despite significant cavitation activity, no microsphere fragmentation is observed in any of the microsphere distributions tested. It is more likely therefore that the microbubble cloud must dissociate from surrounding microspheres, to enable erosion of the soft agar boundary. In theory this would enabling micro-jetting to take place and suggests that the primary acoustic radiation force plays a key role in dissociation of the microbubble cloud from the microspheres.

Increasing the minimum required peak negative pressure (2.8 MPa from 1.9 MPa) and therefore the primary acoustic radiation force applied upon a microbubble cloud, demonstrated this dissociation by the formation of a 'wave' of microbubble clouds travelling together towards the boundary edge (See Section 4.3.2) which was not apparent at the lower pressure (1.9 MPa) used; where microbubble clouds were encased by numerous smaller microspheres preventing dissociation of the cloud from the solid particles. This reduction in

dissociation resulted in shorter more discrete projection channels at the lower pressures tested (1.9 MPa) akin to microbubble tunneling[15].

The increased frequency of microsphere collisions and microbubble cloud nucleation at higher peak negative pressures certainly plays a role in initiating and sustaining the cavitation activity of the agar erosion but the inclusion of the microspheres further complicates an already complex mechanistic model. Irrespective of the exact mechanism of agar erosion, increasing the number of clouds cavitating at the boundary edge produces more channels which can subsequently overlap, to produce one large channel at higher pressures.

To directly observe the mechanism responsible for the erosion of the agar, modifications would have to be made to the current setup to improve the level of transmitted light to enable a higher rate of image capture (See section 4.5.1). However, it is most likely a combination of effects including microbubble jetting[27,32,33], embedding[34–36] and tunnelling [15] of the hydrogel surrounding the cavitation microbubble cloud[34,36] that causes the erosion. It is clear however that the erosion is not caused by the microspheres physically eroding the surface of the agar gel, as it is preceded by the microbubble cloud (Figures 54 & 56).

4.4.4.Microsphere Projection Wake Banding

Several experimental exposures produced projection channels which showed distinctive "banding" of the microspheres. This banding was only observed after several seconds of ultrasound exposure and was not visible in all projections produced. It is unclear if the banding is a result of interstitial packing of microspheres, supply of microspheres to the projection produced or standing wave phenomena from the acrylic mould or the enclosing water tank. Banding was disrupted by further delivery of boluses to the projection channel (See Figure 67) which increased the number of microspheres present in the channel; banding could however be restored after the bolus had travelled further down the lumen.

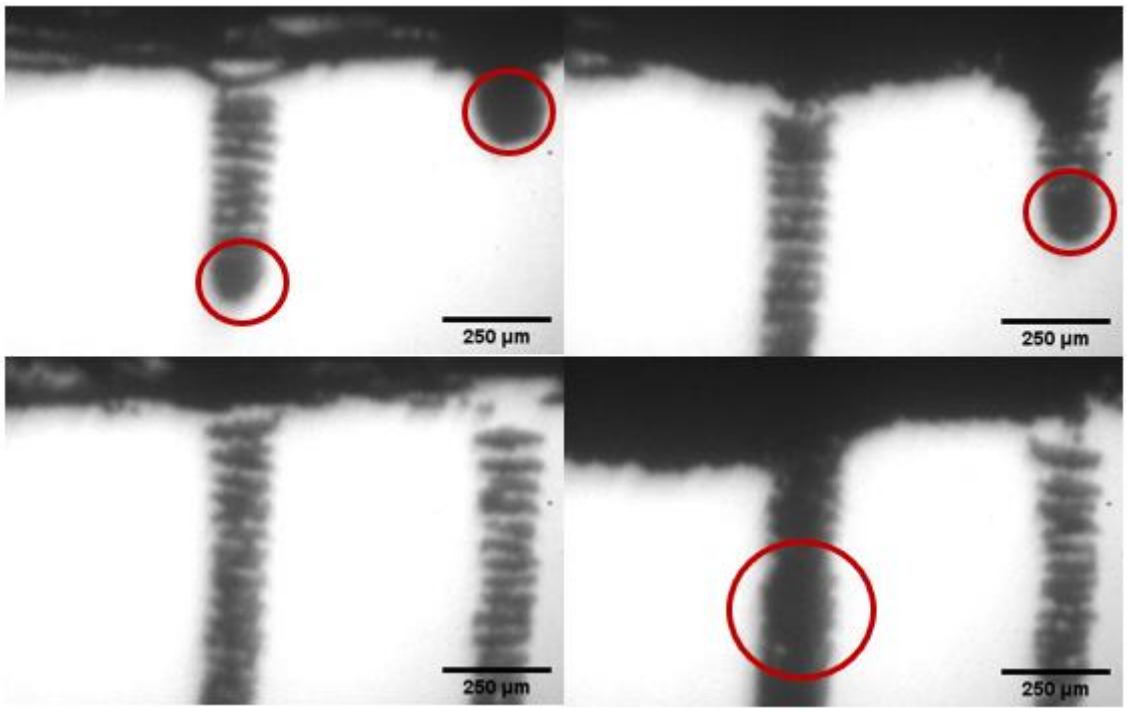


Figure 67: Frames from four sequential videos taken from mould 167. Distinctive microsphere banding can be observed in the lumen of the projection channels produced, where the microspheres have settled. Taken using a 10x objective and 15-32µm microspheres. Bolus of microspheres (red) can be seen passing down the projection channels with distinctive microsphere banding left in its wake.

Banding pitch measurements were taken from three individual gel moulds (Table 2). Measurements were taken over the entire frame, to maximise the number of measurements and reduce experimental uncertainty due to blurring and distortion in the images, although this was problematic with the 10x objective.

Mould Number	Mean Banding Distance (µm)	Standard Deviation (µm)	Minimum Banding Distance (µm)	Maximum Banding Distance (µm)	Count Number (n)
167	48	12	28	81	55
176	47	11	25	90	155
178	54	14	38	106	33

Table 2:Banding measurements for moulds 167, 176 and 178 which displayed significant banding throughout the image frames captured.

The banding observed within the channels (circa 50 µm) is far too tight in pitch to be related to the fundamental driving frequency (0.500MHz, λ 686 µm, λ/2 353µm) or any of its detectable harmonics up to the 8th harmonic at 4.00MHz .

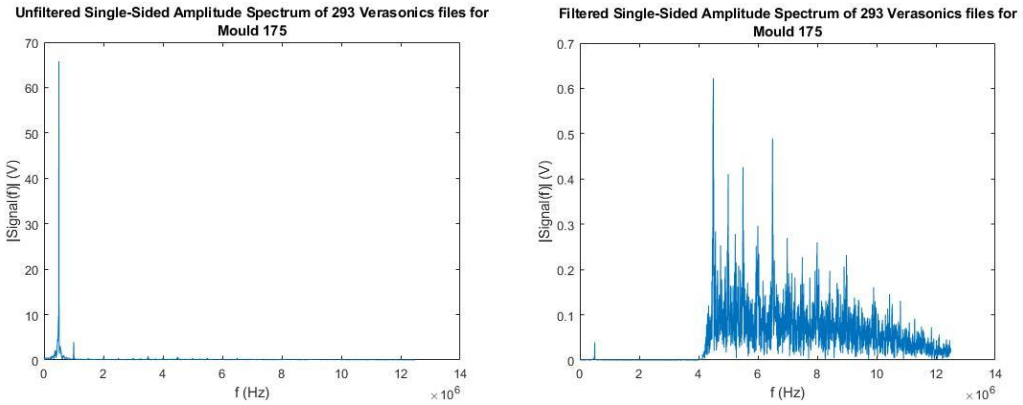


Figure 68: Example spectra of unfiltered Fast-Fourier Transformation (fft) of the frequency data received by the L11-4v linear array for mould 175, which has minimal banding. Unfiltered (left) and hi-pass filtered (right).

It is unlikely therefore that the microsphere banding is formed via standing waves, within the mould or ultrasound tank, as there was no notable emission beyond that of the broadband signal, of which the peaks at 4.498 MHz (λ 76.3µm) and 6.494 MHz (λ 52.83µm) predominate for this example (Figure 68).

Whilst the fundamental signal and the first harmonic encompass the majority of the data, applying a hi-pass filter (Stop at 4.00MHZ, Pass at 4.5MHz, no upper limit, Figure 68) reveals the comparatively small amount of broadband noise produced by the cavitation phenomena observed. To produce the banding pitch via a standing wave, a standing wave to be formed at 6.86 MHz for the ~50µm distance (edge to edge) to be accurate.

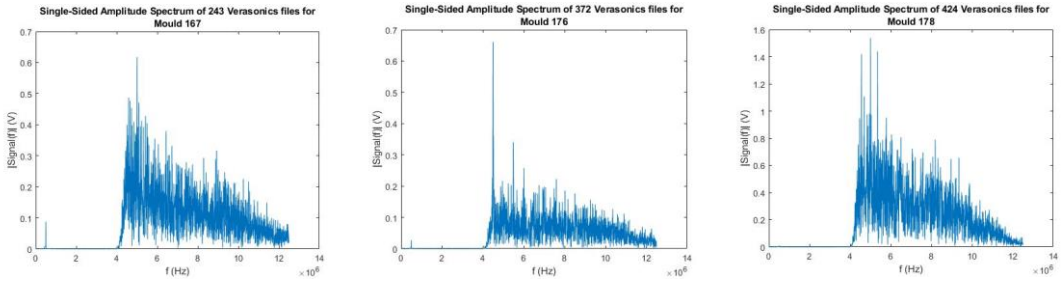


Figure 69: Filtered Frequency content of experimental moulds 167, 176, 178 with significant microsphere banding throughout. Primarily broadband noise associated with inertial cavitation of microbubbles inside or outside of bubble clouds. Signal strength is higher in mould 178 due to the length of exposure being significantly more.

Whilst there is a peak of 6.494 MHz in Figure 68 this is not seen in further examples (Figure 69). If a standing wave was being setup, a consistent frequency component should be visible in all spectra for samples with significant banding.

A simulation (Appendix 6) of the standing waves produced near the 0.500 MHz fundamental frequency, by Dr. Bernard Shieh (BUBBL, IBME, Oxford University, UK) also corroborated these findings. Dr. Shieh found no evidence of any excited modes near the fundamental could be responsible for the pitch distance associated with the microsphere banding observed; confirmed by the unfiltered fft of the frequency content recorded.

4.5. Conclusion

This chapter reports the design, fabrication and optimisation of a bespoke high-speed brightfield imaging setup for the observation of the movement of glass microspheres and microbubbles under focussed ultrasound exposure. Two methods of triggering the camera capture were developed, which led to preliminary projection timings and tracking of microsphere extravasation over time via the change in transmitted light. Multiple cavitation phenomena were imaged at various frame rates, the findings of which correlated well with similar findings in the literature.

The order of events leading to the extravasation of microspheres through agar as the result of ultrasound induced cavitation is now clear. Microbubble clouds are produced initially by the insonation of microbubbles which undergo inertial cavitation, under sufficient peak negative pressure. The primary acoustic radiation force from the applied ultrasound presses active microbubble clouds into the agar boundary surface, where they erode the agar phantom. The oscillations of each microbubble cloud produce a region of microstreaming around the microbubble cloud, drawing in nearby microspheres and additional cavitation nuclei which sustain the activity of the microbubble clouds. Microsphere are pulled into the channels in the agar behind the active microbubble clouds, backfilling the channel lumen. The collection of numerous microspheres in close proximity to one another, causes microspheres to collide. These microsphere collisions act as transient nucleation sites, increasing the number of microbubble clouds produced, the coalescence of which sustains cavitation activity in between external ultrasound pulses. It is unclear if the collision of microspheres, initially by the primary radiation force of the applied ultrasound, initiates the cavitation cascade microbubble clouds.

The acoustic radiation force of the applied ultrasound aids the formation of the projection channels by forcing the microbubble clouds, and microspheres, down the lumen of pre-existing channels further elongating them over time. The total length of the projection, is influenced by the total time under of which the gel mould and its contents, are exposed to the applied ultrasound field which is consistent with earlier work (Total Number of Cycles, Figure 33, See Section 3.3.4). However, it has not been possible to determine exactly how the microbubble cloud erodes the surface of the hydrogel material at the boundary interface.

From the images captured, it is now apparent why increasing the focal pressure produces projections of increased length and width. The formation of additional microbubble clouds determines the number and size of the channels produced. This observation was not discernible from the statistical modelling performed earlier (Chapter 3) as the computational

interpretation of the projection images used a surface interpretation or 'skin' of the projection. As a result, the volumetric analysis could not definitively separate individual channels from within the same projection.

The change in well orientation did not initially appear to influence the formation of projections provided. Using a horizontal arrangement for this set of experiments, appears to have been detrimental to the length of the projections produced; however, it was not possible to image the projections produced from the high-speed setup using μCT due to restrictions during the COVID-19 pandemic, prohibiting access the required equipment and associated quantification required for comparisons to earlier work.

In a vertical setup, the well acts as a silo for the microspheres which are gravity fed to the projection channels as the microbubble clouds erode the agar hydrogel, backfilling the voids with microspheres. Increasing the packing density of the microspheres presumably increases the chances of collision and therefore nucleation for microbubble clouds. Assisted by the primary acoustic radiation, the increased number of clouds travel to the tip of the projection channel thus extending its length. This agrees with previous findings on the effect of microsphere mass and total projection length (See Section 3.3.4).

Whilst isolated cloud activity and cavitation induced extravasation have been independently observed; neither of these has been documented in combination with one another, nor have they been reported with the co-delivery of relatively large dense glass microspheres. The findings in this chapter differ from those previously reported in the context thrombolysis[34–36] and micro-tunnelling[5,8,15] which relate to the activity single microbubbles and not that of a microbubble cloud or multiple microbubble cloud 'waves'.

The back-filling of the channels produced by the cavitation cloud activity are uniformly filled with microspheres, with channels evenly distributed from the acoustic focus, producing an even anticipated radiation field beyond the channels produced; ideal for future translation. As

the cavitation cloud activity and subsequently the post focal depth of the channels is directly related to the post focal pressure applied (See Chapter 3), the delivery approach is suitable for the envisioned intra-operative adjuvant therapy, unlike that of co-administered arterial delivery. As is evident by the order of events leading to the production of projection channels, a proximity relationship between the microbubble clouds and microspheres is evident. This relationship not only back-fills the cavities produced using the secondary acoustic radiation forces but also increases the number of cavitation clouds, brought about by collisions of microspheres. This proximity dependency means that for arterial delivery approaches, where the cavitation nuclei and microspheres are distant from one another, there will be diminished cavitation cloud activity, reduced backfilling of microspheres and a dramatic increase of off target delivery within the circulatory system.

4.5.1.Limitations

The largest limitation to the work within this chapter relates to the objective and glass cover used (See Appendix 4). The use of the glass beaker cover, to prevent water ingress into the air objective, which resulted in distortion of the images at even relatively low magnification (x10). This meant that it was impossible to independently track small bead movements at high magnification, very high capture rates (e.g. 1 million fps) or see fine cavitation phenomena, key to understanding the exact mechanism of agar erosion by the bubble cloud. Some of this was mitigated by the use of larger microspheres which bias the results and conclusions, i.e the exact cavitation phenomena may change based on the size of glass microspheres used, particularly regarding the observed microsphere collisions which produced additional cavitation clouds upon impact.

The work within this chapter also only uses one particular cavitation agent, microbubbles. Whilst the majority of cavitation nuclei behave very similarly there are some subtle differences

which may influence the exact cavitation phenomena, e.g. the use of nanocups rather than microbubbles may enhance the activity or duration of microbubble clouds observed by reducing the rate of cavitation nuclei depletion. Whilst use of a commercially available cavitation agent may enable faster translation of the technology, but it may be preferable to design a cavitation agent suited to the operating parameters of the ultrasound device or produce a radioactively labelled microbubble which would eliminate the impact of microsphere size.

4.5.2.Future Work

Overall, the experimental setup performed well and facilitated the planned experimental work. Future bright field imaging of bubble cloud activity could be improved however by increasing the clarity of the images produced, by the design and development of either a new bespoke long distance, water immersible, high magnification objective or the development of an optically flat glass case to cover commercially available air objectives. Neither of these options was available during the current project due to the ongoing COVID-19 pandemic and associated disruption. To date there are no long distance, water immersible, high magnification objectives available off-the-shelf from major commercial sources (Olympus, NIKON, Thor, Mitutoyo etc.).

Individual microsphere movements were near impossible to track due to the positional exchange of microspheres within the projection channels with the existing setup but may be possible in future with a bespoke objective discussed earlier (Section 4.4.2). This could be improved using fluorescently tagged microspheres mixed within the microsphere population, to enable tracking of individual sphere movements. It remains to be seen if this contrast enhancement under excitation, would be sufficient for video capture using the HPV-X2, as the camera is only capable of greyscale image capture. It may be possible to exploit the

sonoluminescence of the bubble cloud[37–42] or use high speed ultrasound imaging[43–45] to provide the necessary image contrast to that of the surrounding microspheres to help elucidate exactly how the microbubble cloud erodes the agar interface.

The extravasation of surrogate glass microspheres through agar gel, as a tissue mimicking phantom for soft grey matter, has now been demonstrated; and the processes leading to extravasation elucidated. The next project aim is to utilise the findings thus far towards producing a device capable of extravasating the YAS microspheres for the envisaged GBM therapy; and in an ex vivo tissue model with a more clinically representative architecture.

References

1. Li, T. *et al.* Pulsed high-intensity focused ultrasound enhances delivery of doxorubicin in a preclinical model of pancreatic cancer. *Cancer Res.* **75**, 3738–3746 (2015).

2. Bian, S., Seth, A., Daly, D., Carlisle, R. & Stride, E. A multimodal instrument for real-time in situ study of ultrasound and cavitation mediated drug delivery. *Rev. Sci. Instrum.* **88**, (2017).

3. Yemane, P. T. *et al.* Effect of Ultrasound on the Vasculature and Extravasation of Nanoscale Particles Imaged in Real Time. *Ultrasound Med. Biol.* **45**, 3028–3041 (2019).

4. Paris, J. L. *et al.* Ultrasound-mediated cavitation-enhanced extravasation of mesoporous silica nanoparticles for controlled-release drug delivery. *Chem. Eng. J.* **340**, 2–8 (2018).

5. Lea-Banks, H., Stride, E. & Coussios, C. C. Ultrasound-mediated transport of nanoparticles and the influence of particle density. *University of Oxford* (2016). doi:10.1121/1.4950210.

6. Yao, L. *et al.* Facilitated brain delivery of poly (ethylene glycol)-poly (lactic acid) nanoparticles by microbubble-enhanced unfocused ultrasound. *Biomaterials* **35**, 3384–3395 (2014).

7. Park, K. Targeted delivery nano/micro particles to inflamed intestinal mucosa in human. *J. Control. Release* **165**, 162 (2013).

8. Mannaris, C. *et al.* Microbubbles, Nanodroplets and Gas-Stabilizing Solid Particles for Ultrasound-Mediated Extravasation of Unencapsulated Drugs: An Exposure Parameter Optimization Study. *Ultrasound Med. Biol.* **00**, 1–14 (2019).

9. Prokop, A. F., Soltani, A. & Roy, R. A. Cavitational Mechanisms in Ultrasound-Accelerated Fibrinolysis. *Ultrasound Med. Biol.* **33**, 924–933 (2007).

10. Bezer, J. H., Koruk, H., Rowlands, C. J. & Choi, J. J. Elastic Deformation of Soft Tissue-Mimicking Materials Using a Single Microbubble and Acoustic Radiation Force. *Ultrasound Med. Biol.* **46**, 3327–3338 (2020).

11. Yamakoshi, Y. & Miwa, T. Observation of microhollows produced by bubble cloud cavitation. *Jpn. J. Appl. Phys.* **51**, (2012).

12. Keller, S., Bruce, M. & Averkiou, M. A. Ultrasound Imaging of Microbubble Activity during Sonoporation Pulse Sequences. *Ultrasound Med. Biol.* **45**, 833–845 (2019).

13. Choi, J. J. & Coussios, C.-C. Spatiotemporal evolution of cavitation dynamics exhibited by flowing microbubbles during ultrasound exposure. *J. Acoust. Soc. Am.* **132**, 3538–3549 (2012).

14. Song, J. H., Moldovan, A. & Prentice, P. Non-linear Acoustic Emissions from Therapeutically Driven Contrast Agent Microbubbles. *Ultrasound Med. Biol.* (2019) doi:10.1016/j.ultrasmedbio.2019.04.005.

15. Caskey, C. F., Qin, S., Dayton, P. A. & Ferrara, K. W. Microbubble tunneling in gel phantoms. *J. Acoust. Soc. Am.* **125**, EL183 (2009).

16. Lin, Y. *et al.* Effect of acoustic parameters on the cavitation behavior of SonoVue microbubbles induced by pulsed ultrasound. *Ultrason. Sonochem.* **35**, 176–184 (2017).

17. Valery Normand, Didier L. Lootens, Eleonora Amici, Kevin P. Plucknett, Aymard, P. New Insight into Agarose Gel Mechanical Properties. *Biomacromolecules* **1**, 730–738 (2000).

18. Ramzi, M., Rochas, C. & Guenet, J. M. Structure-properties relation for agarose thermoreversible gels in binary solvents. *Macromolecules* **31**, 6106–6111 (1998).

19. Brewin, M. P. *et al.* Characterisation of Elastic and Acoustic Properties of an Agar-Based Tissue Mimicking Material. *Ann. Biomed. Eng.* **43**, 2587–2596 (2015).

20. Schiavi, A., Cuccaro, R. & Troia, A. Strain-rate and temperature dependent material properties of Agar and Gellan Gum used in biomedical applications. *J. Mech. Behav. Biomed. Mater.* **53**, 119–130 (2016).

21. Ross, K. A., Pyrak-Nolte, L. J. & Campanella, O. H. The effect of mixing conditions on the material properties

of an agar gel - Microstructural and macrostructural considerations. *Food Hydrocoll.* **20**, 79–87 (2006).

22. Cafarelli, A. *et al.* Tuning acoustic and mechanical properties of materials for ultrasound phantoms and smart substrates for cell cultures. *Acta Biomater.* **49**, 368–378 (2017).

23. Culjat, M. O., Goldenberg, D., Tewari, P. & Singh, R. S. A review of tissue substitutes for ultrasound imaging. *Ultrasound Med. Biol.* **36**, 861–873 (2010).

24. Borkent, B. M., Gekle, S., Prosperetti, A. & Lohse, D. Nucleation threshold and deactivation mechanisms of nanoscopic cavitation nuclei. *Phys. Fluids* **21**, (2009).

25. Atchley, A. A. & Prosperetti, A. The crevice model of bubble nucleation. *J. Acoust. Soc. Am.* **86**, 1065–1084 (1989).

26. Leighton, T. G. The Sound Field. *Acoust. Bubble* 1–66 (1994) doi:10.1016/b978-0-12-441920-9.50006-7.

27. Gerold, B., Rachmilevitch, I. & Prentice, P. Bifurcation of ensemble oscillations and acoustic emissions from early stage cavitation clouds in focused ultrasound. *New J. Phys.* **15**, (2013).

28. Brujan, E. A. The role of cavitation microjets in the therapeutic applications of ultrasound. *Ultrasound Med. Biol.* **30**, 381–387 (2004).

29. Shao, J. L., Wang, P. & He, A. M. Influence of shock pressure and profile on the microjetting from a grooved Pb surface. *Model. Simul. Mater. Sci. Eng.* **25**, 1–19 (2017).

30. Lechner, C., Koch, M., Lauterborn, W. & Mettin, R. Pressure and tension waves from bubble collapse near a solid boundary: A numerical approach. *J. Acoust. Soc. Am.* **142**, 3649–3659 (2017).

31. Tomita, Y., Robinson, P. B., Tong, R. P. & Blake, J. R. Growth and collapse of cavitation bubbles near a curved rigid boundary. *J. Fluid Mech.* **466**, 259–283 (2002).

32. Karri, B. *et al.* High-speed jetting and spray formation from bubble collapse. *Phys. Rev. E - Stat. Nonlinear, Soft Matter Phys.* **85**, 1–5 (2012).

33. Prabowo, F. & Ohl, C. D. Surface oscillation and jetting from surface attached acoustic driven bubbles. *Ultrason. Sonochem.* **18**, 431–435 (2011).

34. Hendley, S. A., Bollen, V., Anthony, G. J., Paul, J. D. & Bader, K. B. In vitro assessment of stiffness-dependent histotripsy bubble cloud activity in gel phantoms and blood clots. *Phys. Med. Biol.* **64**, ab25a6 (2019).

35. Kelsey C. Martin Mhatre V. Ho, J.-A. L. 基因的改变NIH Public Access. *Bone* **23**, 1–7 (2012).

36. Acconcia, C., Leung, B. Y. C., Manjunath, A. & Goertz, D. E. Interactions between Individual Ultrasound-Stimulated Microbubbles and Fibrin Clots. *Ultrasound Med. Biol.* **40**, 2134–2150 (2014).

37. Levinsen, M. T. Concomitance in single bubble sonoluminescence of period doubling in emission and shape distortion. *Ultrasonics* **54**, 637–643 (2014).

38. Didenko, Y. T., McNamara, W. B. & Suslick, K. S. Molecular emission from single-bubble sonoluminescence. *Nature* **407**, 877–879 (2000).

39. Xu, H. & Suslick, K. S. Molecular emission and temperature measurements from single-bubble sonoluminescence. *Phys. Rev. Lett.* **104**, 1–4 (2010).

40. Lauterborn, W., Kurz, T., Geisler, R., Schanz, D. & Lindau, O. Acoustic cavitation, bubble dynamics and sonoluminescence. *Ultrason. Sonochem.* **14**, 484–491 (2007).

41. Sukovich, J. R. *et al.* Temporally and spatially resolved imaging of laser-nucleated bubble cloud sonoluminescence. *Phys. Rev. E - Stat. Nonlinear, Soft Matter Phys.* **85**, 3–6 (2012).

42. Didenko, Y. T. & Suslick, K. S. The energy efficiency of formation of photons, radicals and ions during single-bubble cavitation. *Nature* **418**, 394–397 (2002).

43. Kauer, M., Belova-Magri, V., Cairós, C., Linka, G. & Mettin, R. High-speed imaging of ultrasound driven cavitation bubbles in blind and through holes. *Ultrason. Sonochem.* **48**, 39–50 (2018).

44. Mulvana, H., Stride, E., Tang, M., Hajnal, J. V. & Eckersley, R. Temperature-Dependent Differences in the Nonlinear Acoustic Behavior of Ultrasound Contrast Agents Revealed by High-Speed Imaging and Bulk Acoustics. *Ultrasound Med. Biol.* **37**, 1509–1517 (2011).

45. Ketterling, J. A. *et al.* High-speed, high-frequency ultrasound, in utero vector-flow imaging of mouse embryos. *Sci. Rep.* **7**, 1–9 (2017).

CHAPTER 5

Conclusions & Future Projects

5. Conclusions

Glioblastoma Multiforme remains the most aggressive primary central nervous system cancer[1,1,2] with disheartening mortality rates (<5% 5-year survival) despite significant advances in surgical intervention and combination therapies[1,1,3]. New approaches are required to transform patient survival in the future.

Current external beam therapies lack the supporting accuracy from imaging techniques (MRI, 18F-FET PET[4]) compared to pre-operative 5-ALA and selective tumour fluorescence currently employed during surgical intervention[5]. Current adjuvant treatment using external beam radiotherapy[6–10] or chemotherapy (Temozolomide[11–13], Carmustine[14,15]) struggles to control the aggressive progression of the disease and frequently lowers quality of life for patients in advanced stages of the disease[6,16]. Whilst proton beam radiotherapy offers significant benefits over EBR by minimising exit doses, the treatment remains largely inaccessible due to its high cost per patient[17].

Selective internal radiotherapy (SIRT) remains an under-utilised and under-investigated approach as an intra-operative adjuvant for glioblastoma surgical resection. SIRT offers localised radiotherapy via biocompatible radioactive glass[18–22] or resin[23–25] microspheres currently approved for use in hepatocellular carcinoma (HCC) and metastases from colorectal carcinoma[25–30].

The main objective of this research was to investigate whether ultrasound induced cavitation of various cavitation agents (microbubble, nanocups, nanodroplets) has the capability to propel surrogate glass microspheres through a soft tissue phantom; and hence assess its potential for translation as an adjuvant therapy for glioblastoma resection surgery. In Chapter 1, the indication of glioblastoma multiforme and its therapeutic regimens was described, with emphasis on the patient's welfare and quality of life. The concept of selective internal

radiation therapy, radioembolic products and existing practices were presented as were their potential benefits over more commonplace external beam therapies[25,26,31–33]. Ultrasound as a non-invasive therapy, including the use of cavitation nuclei was explored as means of delivering various adjuvants and solid particles suitable for the mass transport of radioembolic products.

Chapter 2 focussed primarily on the design and fabrication of an experimental setup and analysis method to investigate the feasibility of ultrasound enhanced cavitation as a potential means of delivering radioactive microspheres within the margins of a tumour resection cavity. Suitable soft tissue phantoms were investigated as surrogates for human brain tissue with 0.5% agar selected as the most suitable and robust candidate. The mould, tank and equipment setup proved to be suitable and initial findings were promising demonstrating the formation of microsphere projections over a wide range of parameters which warranted further, deeper investigation. Nomenclature for describing different aspects of the projections was produced to standardise the analysis. The x-ray imaging performed via µCT enabled visualisation of the projections, as well as the limitations of the mould design and bias within the image analysis.

Chapter 3 focussed on exploring the parameter space under which ultrasound induced cavitation produced microsphere projections. Nine different parameters were highlighted for investigation, over a multitude of levels and combinations. In order to remove the inherent operator bias from the results, a bespoke MATLAB algorithm was used to identify, filter and measure the projections formed in manner previously reported for radioembolic products[34]. The quantitative result was then analysed using DoE methods, specifically surface response linear regression to produce a Pareto chart of weighted factor contributions to the model for post focal projection depth. Primary and secondary interactions were discussed to assess their role in the formation of microsphere projections, using the setup designed in Chapter 2. Pressure was identified as the most significant parameter that could be estimated by the

model and was used to perform non-linear regression, using a Bragg Peak model and a Gauss-Newton least sum squares algorithm to find the coefficient values from initial estimates. Post focal projection depth (mm) was significantly correlated to Peak Negative Pressure (PNP) to such an extent that predications for post focal projection depth could be made within 88.4% of the input pressure value for 95% of predictions made.

Chapter 4 reported the design of an experimental set up to use a high-speed camera (>1 million fps) to observe cavitation activity and its role in microsphere extravasation. A high powered LED was used to illuminate the samples, whilst the microsphere movements and cavitation activity were recorded by the high-speed camera. A light responsive trigger system was designed to capture microbubble activity up to 200,000 frames per second. The videos obtained indicated that the agar channels produced were the result of the microbubble cloud cavitation activity eroding the agar boundary and not the propulsion of microspheres as projectiles through the soft tissue phantom.

The physical mechanisms by which microsphere projections were initiated and extended were captured for the first time, demonstrating that the presence of the microspheres themselves plays a key role in sustaining acoustically initiated microbubble cloud activity and transport.. Other interesting phenomena were observed and recorded using the high-speed setup. For example, microbubble cloud activity was observed between ultrasound pulses, an original finding which is key to explaining why projections of microspheres can be produced an order of size greater than cavitation agents alone. Limitations of the setup prevented observation of small scale cavitation activity and thus the exact mechanism for the agar erosion and microsphere projection channel formation still require elucidation.

The body of work within this thesis demonstrates that ultrasound enhanced selective internal radiotherapy is feasible. Proof of concept work has produced findings which are not only repeatable but can be controlled via various acoustic and physical parameters.

Microbubble cloud cavitation activity has been observed as primarily responsible for the erosion of the agar boundary surface and draws, rather than pushes, microspheres behind it in its wake. Back filling the agar channels with the microspheres from within the bulk well cavity. The erosion of the agar hydrogel by the microbubble cloud cavitation activity, raises questions as to whether the same unobserved mechanism will occur *in vivo* and whether this will cause collateral mechanical damage to the healthy parenchyma within the resection margins; especially crucial as brain tissue is softer than the 0.5% agar hydrogel used in the tissue phantom.

5.1. Publications

Due to the Coronavirus pandemic and travel restrictions, no formal presentations of the work have been produced to date. A priority patent submission has been completed and submitted to the British Patent office titled 'DISTRIBUTING MICROPARTICLESDISTRIBUTING MICROPARTICLES', GB GB2106412.6. Filed May 11, 2021.

Two papers are currently in writing aimed at Radiology and Physics in Medicine and Biology or Ultrasound in Medicine and Biology. The first paper will be orientated towards the technology findings, translation potential and indication obstacles; the second paper will primarily focus on the work within Chapter 4. Discussing the cavitation phenomena findings, the associated methods and implications for cavitation nuclei when co-delivered with microparticles.

5.2. Limitations

Overall the body of work has some key limitations. The agar-agar hydrogel used for the majority of the work does not accurately reflect the target tissue architecture and it is unclear how transitioning from a focussed to an unfocussed ultrasound device will impact the

cavitation mechanisms and transport of the radioactive microspheres. The hypothesis is an oversimplification of a dynamic and multi domain disease. It is unclear what impact changing the type or material of the microspheres will have on the subsequent projections and distributions. Whilst the gravitational effects on the microspheres and slurry composition are mitigated by the applied ultrasound field, microspheres which are not embedded within the tissues margins and remain within the cavity, are mobile and will continue to irradiate the cavity in which they are deposited; a potential safety concern to be considered. Although these could be removed via irrigation and aspiration, using the same equipment already used within theatre; particularly Stryker's Sonopet device, which offers both ultrasonication and aspiration within a single handheld device.

Mapping the distribution of the microspheres *in vivo*, will need further work evaluating other imaging techniques. The safety profile of the envisioned therapy also needs further consideration, primarily around the erosion of soft tissue, the impact of ultrasound and cavitation phenomena within the brain; in addition to impact of the high radioactivity of the TheraSphere™ microspheres within the targeted organ.

The indication also provides some future challenges to address, primarily how to map the invasion of the cancerous cells within the healthy tissue and ultimately decide what constitutes a reasonable volume of irradiation outside that of the resection cavity. This is further compounded by GBM tendrils which exist as extensions of the central tumour mass, currently invisible by current imaging techniques.

5.3. Future Projects

Review and critique of the work to date is overdue as a result of limited faculty contact in wake of the Coronavirus-19 pandemic. As surgical consultant Mr. Plaha has not been updated in the last 18 months, there is a large body of information to digest and assess as to whether or not

the emerging new technology has real-world implications. Should there be sufficient interest, funding and personnel available there are numerous avenues to be explored all of which may be fruitful in further developing the efficacy of the envisioned therapy.

5.3.1.Tumour Inhomogeneity

Future testing must now move towards a more representative tissue model than that of agar, particularly the use of ovine and porcine brain tissue which is commonly available. Whilst some initial testing was performed using these tissue substitutes, microsphere projections formed via cavitation activity could not be recreated at low pressures (<3.0 MPa). It expected that the tissue architecture as well as the supporting microvasculature plays an important part in supporting and solidifying the otherwise incredibly soft 'pockets' of gelatinous brain cells. Whilst there is expected to be differences in the delivery of the microspheres *in vivo*, which require further parameter optimisation, the underlying physics is unlikely to change. The work contained within this thesis therefore is designed to be a foundation for further optimisation and translation to build upon for use within *ex vivo* and *in vivo* research.

The heterogenous nature of GBM means even with sufficient even distribution of the high activity radioactive microspheres, there is no guarantee that the proposed approach will result in an increase in overall survival. Radiation success is linked with the availability of radical carriers (primarily O_2) which are limited in hypoxic regions of the central tumour mass. Assuming the surrounding parenchyma is healthy, there should be sufficient availability of oxygen for radical propagation within the tumour margins. Producing projections channels may also increase the availability of oxygen to the irradiated volume but is unlikely to be a key contributor. Exposing a patient to particularly high acoustic peak negative pressures using a focussed ultrasound transducer is highly likely to be damaging to the immediate cellular environment, invoking cellular stress, short term inflammation and swelling as well as

promoting a variety of cellular cascades and immune responses. By transitioning from a focussed to an unfocussed (radial) ultrasonic device, the majority of these concerns are drastically reduced. This is primarily achieved by designing a bespoke unfocussed ultrasonic device, better suited to the application (See sections 5.3.2 and Appendix 7). An unfocussed device can be designed to operate at much lower frequencies and subsequently far lower pressures than a focussed transducer whilst also removing issues surrounding pre-focal extravasation. As a result there is expected to be a trade-off between a lack of directional control when using an unfocussed horn device and the safety concerns of using a precise focussed transducer; which will eventually have to be investigated in a pre-clinical small mammal model to be evaluated properly.

GBM tumours are incredibly heterogeneous; with pockets of varying densities, vascular networks, shapes of the central tumour mass and associated tendrils which make modelling the indication very challenging. It means that the distributions observed within the agar-agar tissue phantoms may not be representative of those *in vivo* and will require further gap analysis work to identify the root cause of the projection variability *in vivo*. This may result in either under delivery of microspheres leading to disease progression or over-delivery of radioactive microspheres into otherwise healthy areas of the brain, off-target delivery with dire consequences as a result of the varying tissues densities outside the initial cavity. This is further compounded by heterogeneity within the patient pool, disease staging, disease progression between planning and intervention as well as previous treatment regimes.

Off-target downstream delivery of microspheres may occur due to extravasation of the microparticles into nearby vasculature, brought about by the applied ultrasound field and associated cavitation activity. This may result in unwanted downstream embolisation and is a design concern particularly with larger more compressible resin based microspheres however as the arterial and venous walls are far stiffer than the surrounding tissue, it is unlikely that the

microspheres (glass or resin) will pass through into the circulatory system. It is more likely that the microspheres which encounter any feeding vessels, will most likely deposit themselves adjacent to stiffer structures, as they are impenetrable to the cavitation activity. This is because of the microspheres being 'pulled not pushed' by the cavitation cloud activity as highlighted in Chapter 4.

It is assumed that the use of selective stereotactic radiation within the tumour margins will be sufficient to eradicate the remaining cancerous cells surrounding the central tumour mass however success is not guaranteed. Whilst the proposed approach may reduce local reoccurrence it does not address progression of the disease elsewhere in the brain, potential long term radio-resistance or complications arising from combination therapy. This work is therefore only suitable for extending the short term (<2 year) survival and should not be considered a curative approach. However the mechanical damage caused by the microbubble clouds may illicit expression of cancerous material and in combination with the localised irradiation and up-signalling, set off various immunotherapeutic cascades and could result in treatment of malignant tissue elsewhere in the organ via the Abscopal effect. Whilst unlikely this modality should be considered in the technology's translation and future potential combination therapies.

The efficacy of Y-90 is already being investigated for glioblastoma but via an intra-arterial route of administration in a canine model[58], the results which demonstrate the technical feasibility and safety of ^{90}Y in canines, whereby treatment of individual hemispheres showed promising results despite poor localisation of microspheres, radiation doses were tolerated very well leading to increased overall survival. Developments of in this area will be of particular interest to those who intend to build upon the work within this thesis. Whether or not arterial administration of SIRT products for indications within the brain is a suitable choice, remains to be seen.

5.3.2.Prototype Optimisation

As the concept of ultrasound enhanced microsphere delivery appears promising, a series of lightweight ultrasonic horn prototypes were designed and developed for intraoperative use; this work is captured in Appendix 7. Due to delays brought about by the global pandemic, the prototype device remains unoptimised. Therefore, work to optimise the pressure output of the current x3c prototype needs to be completed and the issues surrounding the variable impedances of the prototype devices resolved. Review of the current prototypes and critical analysis is required to evaluate if the prototypes are remotely suitable for the envisioned therapy or whether a complete redesign, focussed on critical parameters not investigated (e.g. safety concerns, useability, ergonomics) have not been addressed adequately. Particularly as there is no insulation of the high voltage, ultrasonic vibrations or noise of the device from the intended user, apart from standard PPE.

Should these prototypes gather significant interest as to warrant further research, initial work should focus on eliminating or at a minimum reducing the impedance issues experiences by designing a circular clamp for the horn prototypes; in hope that exerting equal pressure upon the ultrasonic driver, would allow for a more accurate pressure calibrations and potentially an increase in peak negative pressure of the x3c device. This may lead to the current prototypes being useable, in a limited fashion, as to orientate a second design iteration with user orientated specific improvements.

In the medium to long term, a large body of work akin to that performed in Chapter 3 (In Silico Analysis and Interpretation of Cavitation Induced Projections of Glass Microspheres) is required for ultrasonic horns and frequencies from 20-500 kHz. As from previous work (Section 3.4.4) it is understood that the cavitation and therefore microsphere projection depth is highly responsive to frequency. Identifying a narrower range, in the 10’s of kHz rather than ± 0.5 MHz, will help further prototype designs elicit an improved response. This is particularly key as

it appears that focussed transducers operating at high frequencies (3.3 MHz) appear to produce the same 2d planar projections (See Section 2.4.2) as very low frequency (20 kHz) ultrasonic horns, implying that there is more than one mechanism involved in the production of microsphere projections, not observed in Chapter 4.

This large body of work may lead to the device prototypes needing a complete overhaul or redesign as the data and knowledge supporting the ultrasound enhanced distribution of microspheres grows. This will most likely require further dedicated personnel and significant funding in order to be suitable for a clinical setting.

References

1. Grabowski, M. M. *et al.* Residual tumor volume versus extent of resection: predictors of survival after surgery for glioblastoma. *J. Neurosurg.* **121**, 1115–1123 (2014).

2. Gallego, O. Nonsurgical treatment of recurrent glioblastoma. *Curr. Oncol.* **22**, e273–e281 (2015).

3. Carpentier, A. *et al.* Clinical trial of blood-brain barrier disruption by pulsed ultrasound. *Sci. Transl. Med.* **8**, (2016).

4. Roessler, K., Becherer, A., Donat, M., Cejna, M. & Zachenhofer, I. Intraoperative tissue fluorescence using 5- aminolevolinic acid (5-ALA) is more sensitive than contrast MRI or amino acid positron emission tomography (18F-FET PET) in glioblastoma surgery. *Neurol. Res.* **34**, 314–317 (2012).

5. Smith, S. J. *et al.* The invasive region of glioblastoma defined by 5ALA guided surgery has an altered cancer stem cell marker profile compared to central Tumour. *Int. J. Mol. Sci.* **18**, 1–13 (2017).

6. Patel, D. M., Agarwal, N., Tomei, K. L., Hansberry, D. R. & Goldstein, I. M. Optimal Timing of Whole-Brain Radiation Therapy Following Craniotomy for Cerebral Malignancies. *World Neurosurg.* **84**, 412–419 (2015).

7. Hsieh, J. *et al.* Tumor progression in patients receiving adjuvant whole-brain radiotherapy vs localized radiotherapy after surgical resection of brain metastases. *Neurosurgery* **76**, 411–420 (2015).

8. Montay-Gruel, P. *et al.* Long-term neurocognitive benefits of FLASH radiotherapy driven by reduced reactive oxygen species. *Proc. Natl. Acad. Sci.* **116**, 10943–10951 (2019).

9. Welzel, G. *et al.* Memory Function Before and After Whole Brain Radiotherapy in Patients With and Without Brain Metastases. *Int. J. Radiat. Oncol. Biol. Phys.* **72**, 1311–1318 (2008).

10. Erwin G. Van Meir, PhD, Costas G. Hadjipanayis, MD, PhD, Andrew D. Norden, MD, MPH, Hui-Kuo Shu, MD, Patrick Y. Wen, MD, and Jeffrey J. Olson, M. Exciting New Advances in Neuro-Oncology: The Avenue to a Cure for Malignant Glioma. *CA Cancer J Clin.* **60**, 166–193 (2010).

11. Koncar, R. F. *et al.* PLK1 inhibition enhances temozolomide efficacy in IDH1 mutant gliomas. *Oncotarget* **8**, 15827–15837 (2017).

12. Hvizdos, K. M. & Goa, K. L. Temozolomide. **12**, 237–243 (1999).

13. Hegi, M. E. *et al.* MGMT Gene Silencing and Benefit from Temozolomide in Glioblastoma . *N. Engl. J. Med.* **352**, 997–1003 (2005).

14. Ene, C. *et al.* Safety and efficacy of carmustine (BCNU) wafers for metastatic brain tumors. *Surg. Neurol. Int.* **7**, S295–S299 (2016).

15. Chaichana, K. L. *et al.* Risk of surgical site infection in 401 consecutive patients with glioblastoma with and without carmustine wafer implantation. *Neurol. Res.* **37**, 717–726 (2015).

16. Andrews, D. W. *et al.* Whole brain radiation therapy with or without stereotactic radiosurgery boost for patients with one to three brain metastases: phase III results of the RTOG 9508 randomised trial. *Lancet (London, England)* **363**, 1665–72 (2004).

17. Levin, W. P., Kooy, H., Loeffler, J. S. & DeLaney, T. F. Proton beam therapy. *Br. J. Cancer* **93**, 849–854 (2005).

18. LAURA M. KULIK, BASSEL ATASSI, LODEWIJK VAN HOLSBEECK, TAMEEM SOUMAN, ROBERT J. LEWANDOWSKI, MARY F. MULCAHY, RUSSELL D. HUNTER, ALBERT A. NEMCEK JR., MICHAEL M. ABECASSIS, KENNETH G. HAINES III, R. S. Yttrium-90 Microspheres (TheraSphere1) Treatment of Unresectable Hepatocellular Carcinoma: Downstaging to Resection, RFA and Bridge to Transplantation. *J. Surg. Oncol.* **94**, 572–586 (2006).

19. Kallini, J. R. *et al.* Comparison of the Adverse Event Profile of TheraSphere ® with SIR-Spheres ® for the Treatment of Unresectable Hepatocellular Carcinoma: A Systematic Review. *Cardiovasc. Intervent. Radiol.* **40**, 1033–1043 (2017).

20. Kulik, L. M. *et al.* Yttrium-90 microspheres (TheraSphere) treatment of unresectable hepatocellular

carcinoma: downstaging to resection, RFA and bridge to transplantation. *J. Surg. Oncol.* **94**, 572–86 (2006).

21. Pellerin, O., Lin, M., Bhagat, N., Shao, W. & Geschwind, J.-F. Can C-Arm Cone-Beam CT Detect a Micro-Embolic Effect After TheraSphere Radioembolization of Neuroendocrine and Carcinoid Liver Metastasis? *Cancer Biother. Radiopharm.* **28**, 459–465 (2013).

22. Schilling, W. R., Hammond, P. Y. & Snyder, G. H. The "New Look" of 1953. *Strateg. Polit. Def. Budgets* **43**, 379–524 (2019).

23. Attarwala, A. A. *et al.* Quantitative and qualitative assessment of yttrium-90 pet/ct imaging. *J. Am. Ceram. Soc.* **61**, 247–249 (1978).

24. Attarwala, A. A. *et al.* Quantitative and qualitative assessment of yttrium-90 pet/ct imaging. *PLoS One* **9**, 1–7 (2014).

25. Pardo, F. *et al.* The Post-SIR-Spheres Surgery Study (P4S): Retrospective Analysis of Safety Following Hepatic Resection or Transplantation in Patients Previously Treated with Selective Internal Radiation Therapy with Yttrium-90 Resin Microspheres. *Ann. Surg. Oncol.* **24**, 2465–2473 (2017).

26. Pereira, P. L. FRI-03 Intraarterial therapies: SIRT or TACE. *Dig. Liver Dis.* **45**, S241–S242 (2013).

27. Tchelebi, L. & Sharma, N. K. Selective Internal Radiation Therapy in the Multidisciplinary Management of Liver Metastases From Colorectal Carcinoma. *Semin. Nucl. Med.* doi:S000129981930008X.

28. Lee, B. Q. *et al.* Radiosensitivity of colorectal cancer to 90Y and the radiobiological implications for radioembolisation therapy. *Phys. Med. Biol.* **64**, (2019).

29. Sofocleous, C. T. *et al.* Phase i trial of selective internal radiation therapy for chemorefractory colorectal cancer liver metastases progressing after hepatic arterial pump and systemic chemotherapy. *Clin. Colorectal Cancer* **13**, 27–36 (2014).

30. Lyon, P. C. *et al.* Long-term radiological and histological outcomes following selective internal radiation therapy to liver metastases from breast cancer. *Radiol. Case Reports* **13**, 1259–1266 (2018).

31. Jakobs, T. Selective internal radiation therapy for other liver metastases. *Eur. J. Cancer, Suppl.* **10**, 72–74 (2012).

32. Krug, S. *et al.* Successful selective internal radiotherapy (SIRT) in a patient with a malignant solid pseudopapillary pancreatic neoplasm (SPN). *Pancreatology* **12**, 423–427 (2012).

33. Garrean, S., Hering, J., Helton, W. S. & Espat, N. J. A primer on transarterial, chemical, and thermal ablative therapies for hepatic tumors. *Am. J. Surg.* **194**, 79–88 (2007).

34. Thompson, J. G. *et al.* Distribution and Detection of Radiopaque Beads after Hepatic Transarterial Embolization in Swine: Cone-Beam CT versus MicroCT. *J. Vasc. Interv. Radiol.* **29**, 568–574 (2018).

35. Pellow, C. *et al.* Simultaneous Intravital Optical and Acoustic Monitoring of Ultrasound-Triggered Nanobubble Generation and Extravasation. *Nano Lett.* **20**, 4512–4519 (2020).

36. Lea-Banks, H., Mannaris, C., Grundy, M., Stride, E. P. & Coussios, C. Enhanced delivery of a density-modified therapeutic using ultrasound: Comparing the influence of micro- and nano-scale cavitation nuclei. *J. Acoust. Soc. Am.* **141**, 4011–4011 (2017).

37. Paverd, C., Lyka, E., Elbes, D. & Coussios, C. Passive acoustic mapping of extravasation following ultrasound-enhanced drug delivery. *Phys. Med. Biol.* **64**, (2019).

38. Yildirim, A., Blum, N. T. & Goodwin, A. P. Colloids, nanoparticles, and materials for imaging, delivery, ablation, and theranostics by focused ultrasound (FUS). *Theranostics* (2019) doi:10.7150/thno.32424.

39. Nittayacharn, P. *et al.* Enhancing Tumor Drug Distribution With Ultrasound-Triggered Nanobubbles. *J. Pharm. Sci.* (2019) doi:10.1016/j.xphs.2019.05.004.

40. Pasciak, A. S. *et al.* Correction to: Yttrium-90 radioembolization as a possible new treatment for brain cancer: proof of concept and safety analysis in a canine model (EJNMMI Research, (2020), 10, 1, (96), 10.1186/s13550-020-00679-1). *EJNMMI Res.* **10**, 1–16 (2020).

41. Gordon, A. C. Tuning Your RADIOembolization : Imaging-guidance of Yttrium-90 Radioembolization. (Evanson, Illinois, 2016).

42. Auditore, L. *et al.* Monte Carlo 90 Y PET/CT dosimetry of unexpected focal radiation-induced lung damage after hepatic radioembolisation . *Phys. Med. Biol.* **65**, 235014 (2020).

43. Hickey, R., Lewandowski, R. & Salem, R. Yttrium-90 Radioembolization is a Viable Treatment Option for Unresectable, Chemorefractory Colorectal Cancer Liver Metastases: Further Evidence in Support of a New Treatment Paradigm. *Ann. Surg. Oncol.* **22**, 706–707 (2015).

44. Knešaurek, K., Tuli, A., Pasik, S. D., Heiba, S. & Kostakoglu, L. Quantitative comparison of pre-therapy 99mTc-macroaggregated albumin SPECT/CT and post-therapy PET/MR studies of patients who have received intra-arterial radioembolization therapy with 90Y microspheres. *Eur. J. Radiol.* **109**, 57–61 (2018).

45. Hawkins, C. M., Kukreja, K., Geller, J. I., Schatzman, C. & Ristagno, R. Radioembolisation for treatment of pediatric hepatocellular carcinoma. *Pediatr. Radiol.* **43**, 876–881 (2013).

46. Paladini, A. *et al.* Delivery of selective internal radiation therapy complicated by variant hepatic vascular anatomy. *Radiol. Case Reports* **14**, 662–672 (2019).

47. Liu, T. I. *et al.* Radiotherapy-Controllable Chemotherapy from Reactive Oxygen Species-Responsive Polymeric Nanoparticles for Effective Local Dual Modality Treatment of Malignant Tumors. *Biomacromolecules* **19**, 3825–3839 (2018).

48. F., B. & Sonveaux, P. Targeting Tumor Perfusion and Oxygenation Modulates Hypoxia and Cancer Sensitivity to Radiotherapy and Systemic Therapies. *Adv. Cancer Ther.* (2012) doi:10.5772/23332.

49. Chu, X. *et al.* Exploration of TiO 2 nanoparticle mediated microdynamic therapy on cancer treatment. *Nanomedicine Nanotechnology, Biol. Med.* **18**, 272–281 (2019).

50. Hou, H. *et al.* Effect of a Topical Vasodilator on Tumor Hypoxia and Tumor Oxygen Guided Radiotherapy using EPR Oximetry. *Radiat. Res.* **173**, 651–658 (2010).

51. Fraisl, P., Mazzone, M., Schmidt, T. & Carmeliet, P. Regulation of Angiogenesis by Oxygen and Metabolism. *Dev. Cell* **16**, 167–179 (2009).

52. Dumitru, C. A., Sandalcioglu, I. E. & Karsak, M. Cannabinoids in glioblastoma therapy: New applications for old drugs. *Front. Mol. Neurosci.* **11**, 1–7 (2018).

APPENDIX

1. Khachiyan Algorithm - Minimum Volume Enclosed Ellipse

Code

```
function [A , c] = MinVolEllipse(P, tolerance)
% [A , c] = MinVolEllipse(P, tolerance)
% Finds the minimum volume enclsing ellipsoid (MVEE) of a set of data
% points stored in matrix P. The following optimization problem is
solved:
%
% minimize       log(det(A))
% subject to     (P_i - c)' * A * (P_i - c) <= 1
%
% in variables A and c, where P_i is the i-th column of the matrix P.
% The solver is based on Khachiyan Algorithm, and the final solution
% is different from the optimal value by the pre-spesified amount of
'tolerance'.
%
% inputs:
%---------
% P : (d x N) dimnesional matrix containing N points in R^d.
% tolerance : error in the solution with respect to the optimal value.
%
% outputs:
%---------
% A : (d x d) matrix of the ellipse equation in the 'center form':
% (x-c)' * A * (x-c) = 1
% c : 'd' dimensional vector as the center of the ellipse.
%
% example:
% --------
%      P = rand(5,100);
%      [A, c] = MinVolEllipse(P, .01)
%
%      To reduce the computation time, work with the boundary points
only:
%
%      K = convhulln(P');
%      K = unique(K(:));
%      Q = P(:,K);
%      [A, c] = MinVolEllipse(Q, .01)
%
%
% Nima Moshtagh (nima@seas.upenn.edu)
% University of Pennsylvania
%
% December 2005
% UPDATE: Jan 2009



%%%%%%%%%%%%%%%%%%%% Solving the Dual
problem%%%%%%%%%%%%%%%%%%%%%%%%%%%%%5
% ----------------------------------
% data points
% ----------------------------------
[d N] = size(P);
```

```
Q = zeros(d+1,N);
Q(1:d,:) = P(1:d,1:N);
Q(d+1,:) = ones(1,N);


% initializations
% --------------------------------
count = 1;
err = 1;
u = (1/N) * ones(N,1);          % 1st iteration


% Khachiyan Algorithm
% --------------------------------
while err > tolerance,
    X = Q * diag(u) * Q';       % X = \sum_i ( u_i * q_i * q_i')  is a
(d+1)x(d+1) matrix
    M = diag(Q' * inv(X) * Q);  % M the diagonal vector of an NxN
matrix
    [maximum j] = max(M);
    step_size = (maximum - d -1)/((d+1)*(maximum-1));
    new_u = (1 - step_size)*u ;
    new_u(j) = new_u(j) + step_size;
    count = count + 1;
    err = norm(new_u - u);
    u = new_u;
end



%%%%%%%%%%%%%%%%%%% Computing the Ellipse
parameters%%%%%%%%%%%%%%%%%%%%%%
% Finds the ellipse equation in the 'center form':
% (x-c)' * A * (x-c) = 1
% It computes a dxd matrix 'A' and a d dimensional vector 'c' as the
center
% of the ellipse.

U = diag(u);

% the A matrix for the ellipse
% --------------------------------------------
A = (1/d) * inv(P * U * P' - (P * u)*(P*u)' );


% center of the ellipse
% --------------------------------------------
c = P * u;
```

2. Single Well Elimination Microsphere Projection Interpretation Code

```
clear variables;close all;clc;
folList = dir;
whichFols = [];
for i = 3:size(folList,1)
    if folList(i).isdir == 1
        whichFols = [whichFols; i];
    end
end

for n = 1:length(whichFols)
tic
folName = folList(whichFols(n)).name;
rRadius = 2.5; %Rod Radius mm
whichHighest = 5;

addpath(folName);

fol = dir([folName '/*.dcm']);
temp = dicomread(fol(1).name);
dinfo = dicominfo(fol(1).name);
pmm = dinfo.SliceThickness;
KillRp = round(2/pmm);
rData =
ones(size(temp,1)+KillRp*2,size(temp,2)+KillRp*2,length(fol)+KillRp*2)
*4000;

for i = (KillRp+1):(size(rData,3)-KillRp)
    rData((KillRp+1):(size(rData,1)-KillRp),(KillRp+1):(size(rData,2)-
KillRp),i) = dicomread(fol(i-KillRp).name);
end
rmpath(folName);

%1521 to 4366 (bone)
thresholded = (rData>=(1521+min(rData(:))-
1))&(rData<=(4366+min(rData(:))-1));
thresholded(1:10,:,:) = 0;
if sum(thresholded(:)) > 0
Sphere = strel('sphere',round(KillRp*1.5));
dThresholded = imdilate(thresholded,Sphere);
CC = bwconncomp(dThresholded);
numPixels = cellfun(@numel,CC.PixelIdxList);
[~,idx] = max(numPixels);
filtered_vol = false(size(dThresholded));
filtered_vol(CC.PixelIdxList{idx}) = true;
thresholded = thresholded.*filtered_vol;

%P = zeros(3,sum(thresholded(:)));
clear P
count = 1;
for i = 2:(size(rData,1)-1)
    for j = 2:(size(rData,2)-1)
        for k = 2:(size(rData,3)-1)
```

```
            if (thresholded(i,j,k) == 1)&&((thresholded(i-
1,j,k)==0)||(thresholded(i+1,j,k)==0)||(thresholded(i,j-
1,k)==0)||(thresholded(i,j+1,k)==0)||(thresholded(i,j,k-
1)==0)||(thresholded(i,j,k+1)==0))
                P(:,count) = [i,j,k];
                count = count + 1;
            end
        end
    end
end

% tThresholded = zeros(size(thresholded));
% tThresholded(min(P(1,:)):round((max(P(1,:))-
min(P(1,:)))/2+min(P(1,:))),:,:) =
thresholded(min(P(1,:)):round((max(P(1,:))-
min(P(1,:)))/2+min(P(1,:))),:,:);
tThresholded = thresholded;
stThresholded = squeeze(sum(tThresholded));
short = ((max(P(1,:))-min(P(1,:)))*pmm)<10;

circ = zeros(101,101);
for i = 1:size(circ,1)
    for j = 1:size(circ,2)
        if (((i-size(circ,1)/2)^2+(j-size(circ,2)/2)^2) >=
(3.5/pmm/2)^2) && (((i-size(circ,1)/2)^2+(j-size(circ,2)/2)^2) <=
(4.5/pmm/2)^2)
            circ(i,j) = 1;
        elseif (((i-size(circ,1)/2)^2+(j-size(circ,2)/2)^2) >
(4.5/pmm/2)^2) && (((i-size(circ,1)/2)^2+(j-size(circ,2)/2)^2) <=
(4.8/pmm/2)^2)
            circ(i,j) = -1;
        elseif (((i-size(circ,1)/2)^2+(j-size(circ,2)/2)^2) <
(3.5/pmm/2)^2) && (((i-size(circ,1)/2)^2+(j-size(circ,2)/2)^2) >=
(3.2/pmm/2)^2)
            circ(i,j) = -1;
        end
    end
end

circFit = conv2(stThresholded,circ,'same');
[circx, circy] = find(ismember(circFit, max(circFit(:))));

circx = round(mean(circx));
circy = round(mean(circy));

count = 1;
countPre = 1;
countPost = 1;
PreVol = 0;
PostVol = 0;
clear PsPre
clear PsPost
clear Ps
for i = 2:(size(rData,1)-1)
    for j = 2:(size(rData,2)-1)
        for k = 2:(size(rData,3)-1)
            if (thresholded(i,j,k) == 1)&&((thresholded(i-
1,j,k)==0)||(thresholded(i+1,j,k)==0)||(thresholded(i,j-
1,k)==0)||(thresholded(i,j+1,k)==0)||(thresholded(i,j,k-
1)==0)||(thresholded(i,j,k+1)==0))&&((((j-circx)*pmm)^2+((k-
```

```
circy)*pmm)^2)>((rRadius)^2))&&((i>((max(P(1,:))-
min(P(1,:)))/2+min(P(1,:))))||short)
                Ps(:,count) = [i,j,k];
                count = count + 1;
            end
            if (thresholded(i,j,k) == 1)&&((((j-circx)*pmm)^2+((k-
circy)*pmm)^2)>((rRadius)^2))&&((i>((max(P(1,:))-
min(P(1,:)))/2+min(P(1,:))))||short)&&((j-circx)>=0)
                PsPre(:,countPre) = [i,j,k];
                PreVol = PreVol + 1;
                countPre = countPre + 1;
            elseif (thresholded(i,j,k) == 1)&&((((j-circx)*pmm)^2+((k-
circy)*pmm)^2)>((rRadius)^2))&&((i>((max(P(1,:))-
min(P(1,:)))/2+min(P(1,:))))||short)&&((j-circx)<0)
                PsPost(:,countPost) = [i,j,k];
                PostVol = PostVol + 1;
                countPost = countPost + 1;
            end
        end
    end
end

% count = 1;
% for i = 2:(size(rData,1)-1)
%     for j = 2:(size(rData,2)-1)
%         for k = 2:(size(rData,3)-1)
%             if ((((j-circx)*pmm)^2+((k-circy)*pmm)^2)<((2.5)^2))
%                 Ps2(:,count) = [i,j,k];
%                 count = count + 1;
%             end
%         end
%     end
% end
if count > whichHighest
sPsx = sortrows(Ps',2);
PreDistxcirc = sPsx((size(sPsx,1)-whichHighest+1),2);
PostDistxcirc = sPsx(whichHighest,2);
PreDistxcirc = (PreDistxcirc-circx)*((PreDistxcirc-circx)>0)*pmm;
PostDistxcirc = (circx-PostDistxcirc)*((circx-PostDistxcirc)>0)*pmm;

if countPre > whichHighest
    sPsPrex = sortrows(PsPre',3);
    sPsPrey = sortrows(PsPre',1);
    sPsPrez = sortrows(PsPre',2);
    MWidthPre = (sPsPrex((size(sPsPrex,1)-whichHighest+1),3)-
sPsPrex(whichHighest,3))*pmm;
    MHeightPre = (sPsPrey((size(sPsPrey,1)-whichHighest+1),1)-
sPsPrey(whichHighest,1))*pmm;
    MDepthPre = (sPsPrez((size(sPsPrez,1)-whichHighest+1),2)-
circx)*pmm;
else
    MWidthPre = 0;
    MHeightPre = 0;
    MDepthPre = 0;
end

if countPost > whichHighest
sPsPostx = sortrows(PsPost',3);
sPsPosty = sortrows(PsPost',1);
sPsPostz = sortrows(PsPost',2);
```

```
MWidthPost = (sPsPostx((size(sPsPostx,1)-whichHighest+1),3)-
sPsPostx(whichHighest,3))*pmm;
MHeightPost = (sPsPosty((size(sPsPosty,1)-whichHighest+1),1)-
sPsPosty(whichHighest,1))*pmm;
MDepthPost = (circx-sPsPostz(whichHighest,2))*pmm;
else
    MWidthPost = 0;
    MHeightPost = 0;
    MDepthPost = 0;
end

PreProj = zeros(size(thresholded,1),size(thresholded,2));
PostProj = zeros(size(thresholded,1),size(thresholded,2));
Ps3D = zeros(size(thresholded));

countPre = 1;
countPost = 1;
clear PrPre
clear PrPost
for i = 1:size(Ps,2)
    if (Ps(2,i)-circx)>=0
        PrPre(1:3,countPre) = Ps(:,i);
        PrPre(4,countPre) = sqrt((Ps(2,i)-circx)^2+(Ps(3,i)-circy)^2);
        PreProj(Ps(1,i),Ps(3,i)) = PreProj(Ps(1,i),Ps(3,i))+1;
        countPre = countPre + 1;
    else
        PrPost(1:3,countPre) = Ps(:,i);
        PrPost(4,countPost) = sqrt((Ps(2,i)-circx)^2+(Ps(3,i)-
circy)^2);
        PostProj(Ps(1,i),Ps(3,i)) = PostProj(Ps(1,i),Ps(3,i))+1;
        countPost = countPost + 1;
    end
    Ps3D(Ps(1,i),Ps(2,i),Ps(3,i)) = 1;
end
% if countPost > 1
%     sPrPost = sortrows(PrPost(4,:)',1);
%     PostDistR = sPrPost(size(sPrPost,1)-whichHighest+1)*pmm;
% else
%     PostDistR = 0;
% end
% if countPre > 1
%     sPrPre = sortrows(PrPre(4,:)',1);
%     PreDistR = sPrPre(size(sPrPre,1)-whichHighest+1)*pmm;
% else
%     PreDistR = 0;
% end

Ps3DKill = zeros(size(Ps3D));
for i = 1:size(Ps3D,1)
    for j = 1:size(Ps3D,2)
        for k = 1:size(Ps3D,3)
            if Ps3D(i,j,k) == 1
                Ps3DKill((i-KillRp):(i+KillRp),(j-
KillRp):(j+KillRp),(k-KillRp):(k+KillRp)) = 1;
            end
        end
    end
end
% count = 1;
% for i = KillRp:(size(Ps3D,1)-KillRp)
%     for j = KillRp:(size(Ps3D,2)-KillRp)
```

```
%         for k = KillRp:(size(Ps3D,3)-KillRp)
%             if Ps3DKill(i,j,k) == 1
%                 PKill(:,count) = [i,j,k];
%                 count = count + 1;
%             end
%         end
%     end
% end

[A , C] = MinVolEllipse(Ps, 0.05);
figure;
plot3(Ps(1,:),Ps(2,:),Ps(3,:),'.');
daspect([1 1 1]);
hold on
Ellipse_plot(A,C);

Ellipse3D = zeros(size(thresholded));
count = 1;
MaxR = 0;
MaxRC = [0;0;0];
NMaxR = 1;
clear PE
for i = 1:size(Ellipse3D,1)
    for j = 1:size(Ellipse3D,2)
        for k = 1:size(Ellipse3D,3)
            if ([i;j;k]-C)'*A*([i;j;k]-C)<=1
                Ellipse3D(i,j,k) = 1;
                PE(:,count) = [i,j,k];
                count = count+1;
                if (sqrt((i-C(1))^2+(j-C(2))^2+(k-C(3))^2))>=MaxR
                    if (sqrt((i-C(1))^2+(j-C(2))^2+(k-C(3))^2))==MaxR
                        MaxR = (sqrt((i-C(1))^2+(j-C(2))^2+(k-
C(3))^2));
                        MaxRC = MaxRC + [i;j;k];
                        NMaxR = NMaxR + 1;
                    else
                        MaxR = (sqrt((i-C(1))^2+(j-C(2))^2+(k-
C(3))^2));
                        MaxRC = [i;j;k];
                        NMaxR = 1;
                    end
                end
            end
        end
    end
end
MaxRC = round(MaxRC/NMaxR);
MVEE = sum(Ellipse3D(:))*pmm^3/1e3;
% count = 1;
% clear PEs
% for i = 2:(size(rData,1)-1)
%     for j = 2:(size(rData,2)-1)
%         for k = 2:(size(rData,3)-1)
%             if (Ellipse3D(i,j,k) == 1)&&((Ellipse3D(i-
1,j,k)==0)||(Ellipse3D(i+1,j,k)==0)||(Ellipse3D(i,j-
1,k)==0)||(Ellipse3D(i,j+1,k)==0)||(Ellipse3D(i,j,k-
1)==0)||(Ellipse3D(i,j,k+1)==0))
%                 PEs(:,count) = [i,j,k];
%                 count = count + 1;
%             end
%         end
```

```
%     end
% end
% Epolyfit0 = mean(PEs,2);
% EA = zeros(3,size(PEs,2));
% EA(1,:) = PEs(1,:)-Epolyfit0(1);
% EA(2,:) = PEs(2,:)-Epolyfit0(2);
% EA(3,:) = PEs(3,:)-Epolyfit0(3);
% [EU,ES,~] = svd(EA);
% d = EU(:,1);
% t = d'*EA;
% t1 = min(t);
% t2 = max(t);
% temp = ([t1,t2]'*d')';
% Epolyfitl(:,1) = Epolyfit0 + temp(:,1);
% Epolyfitl(:,2) = Epolyfit0 + temp(:,2);
Epolyfitl(:,1) = MaxRC;
Epolyfitl(:,2) = (C-MaxRC)+C;
plot3(Epolyfitl(1,:),Epolyfitl(2,:),Epolyfitl(3,:),'r');
% Epolyfitr = Epolyfitl(:,1)-Epolyfitl(:,2);
Epolyfitr = MaxRC-C;
Eangle =
acos(sum([0;1;0].*Epolyfitr)/sqrt(sumsqr(Epolyfitr)))/pi()*180;

KZ = (1-(sum(Ellipse3D(:))-
sum(sum(sum(Ellipse3D.*Ps3DKill))))/sum(Ellipse3D(:)))*100;
KV = sum(sum(sum(sum(Ps3DKill))))*pmm^3/1e3;

figure;
plot3(P(1,:),P(2,:),P(3,:),'.');
daspect([1 1 1]);

figure;
imagesc(PostProj);
daspect([1 1 1]);

% figure;
% plot3(PE(1,:),PE(2,:),PE(3,:),'.','color','r');
% daspect([1 1 1]);
% hold on
% plot3(PKill(1,:),PKill(2,:),PKill(3,:),'.','color','b');

Output(n).Name = folName;
Output(n).MVEE = MVEE;
Output(n).Angle = Eangle;
Output(n).PreProj = PreProj;
Output(n).PostProj = PostProj;
Output(n).Killzone = KZ;
Output(n).KillVolume = KV;
Output(n).PreVol = PreVol*pmm^3/1e3;
Output(n).PostVol = PostVol*pmm^3/1e3;
Output(n).MWidthPre = MWidthPre;
Output(n).MHeightPre = MHeightPre;
Output(n).MDepthPre = MDepthPre;
Output(n).MWidthPost = MWidthPost;
Output(n).MHeightPost = MHeightPost;
Output(n).MDepthPost = MDepthPost;

else

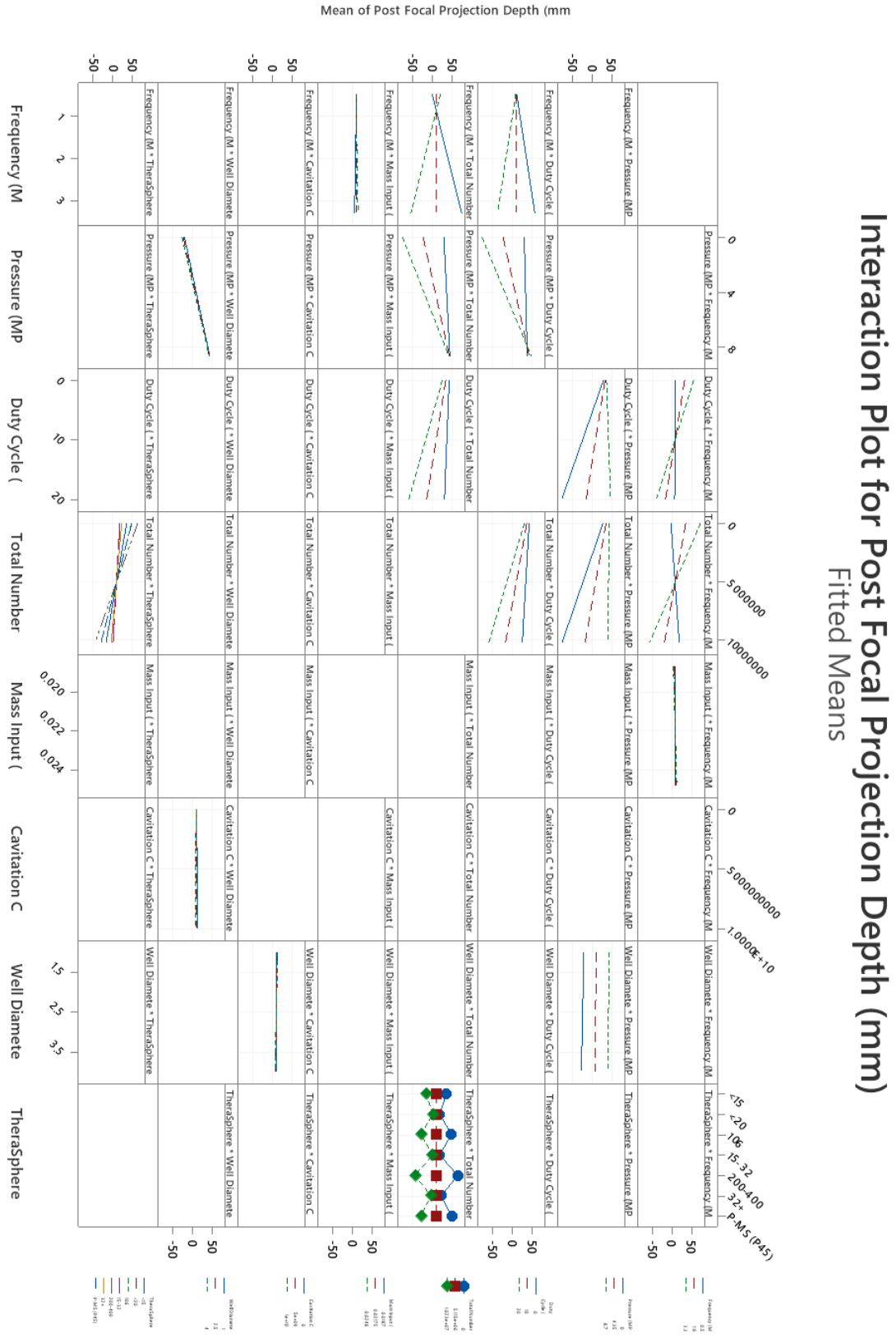
Output(n).Name = folName;
```

```
Output(n).MVEE = 0;
Output(n).Angle = 0;
Output(n).PreProj = zeros(size(thresholded,1),size(thresholded,2));
Output(n).PostProj = zeros(size(thresholded,1),size(thresholded,2));
Output(n).Killzone = 0;
Output(n).KillVolume = 0;
Output(n).PreVol = 0;
Output(n).PostVol = 0;
Output(n).MWidthPre = 0;
Output(n).MHeightPre = 0;
Output(n).MDepthPre = 0;
Output(n).MWidthPost = 0;
Output(n).MHeightPost = 0;
Output(n).MDepthPost = 0;

end
end
toc
end

save('Output.mat','Output');
disp('Code Finished');
```

3. Interaction Plot for Post Focal Projection Depth (mm)



4. HPV-X2 Image Calibration and Objective Limitations

As the HPV-X2 camera was initially designed for long distance high magnification observations of explosive materials at a resolution of 200x450 pixels, it does not have internal programmable scaling of the objectives in use. Manual calibration was therefore required for both objectives (4x and 10x). A 20x objective (CFI Plan Fluor, NIKON, Tokyo, Japan) was investigated initially, but the glass cover obscured the image quality to such a degree as to make individual beads indistinguishable from one another, only general positioning of bead clusters within the frame, making measurements using the haemocytometer and image calibration impossible (Figure lxx). Images captured at 20x were therefore not calibrated.

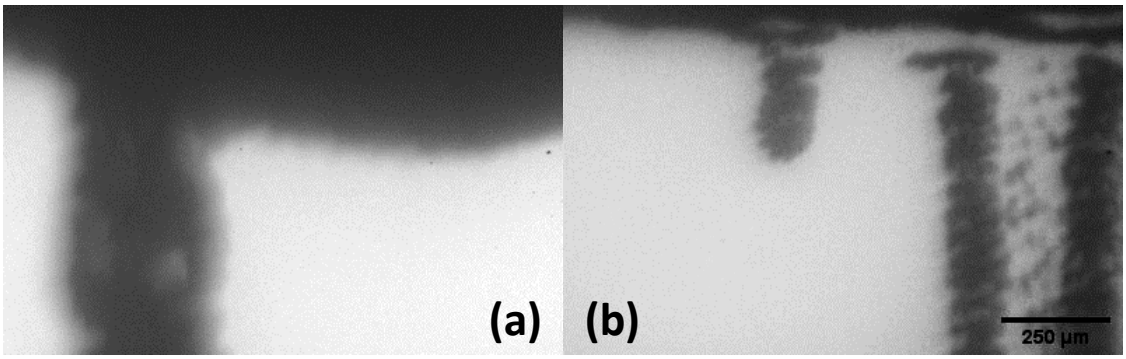


Figure lxx: 20x objective view of 15-32um black glass microspheres within a channel of a newly formed projection. Individual spheres are indiscernible (a) at 20x and discernible (b) at 10x magnification.

For the 4x objective, a clear transparent plastic ruler was used to capture the 1mm intervals for calculation of the image size at the focus. For the 10x objective a haemocytometer (Bright Line, Hausser Scientific, Horsham, PA) was used to measure a 200µm square etched at the centre of the glass slide. Measurements were taken with both objectives with and without the covering glass beaker to calculate the difference the change in the light path had on the accuracy of the images, particularly noticeable at 10x magnification.

Images were thresholded in black and white to produce contrasting images using ImageJ (NIH, Bethesda, MA). This provided clean cut edges from which to consistently take a series of 6 measurements using the gradations on either measuring apparatus (Figure ii).

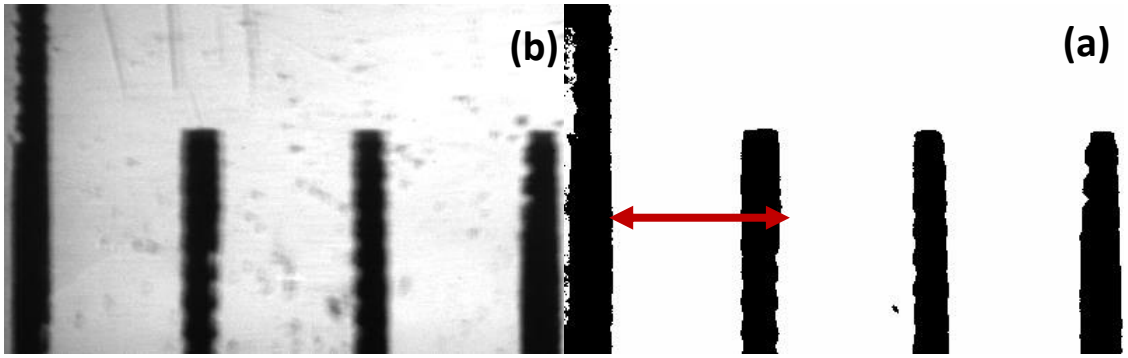


Figure lxxi: 4x calibration images original (left), thresholded (right). 1mm increments. Where the red arrow indicates the lengths measured.

For the 4x objective measurements were made of a 1mm increment from the furthest right to furthest right edge of the next gradation of the ruler, perpendicular to the gradations, with the height and increment selected chosen at random. The first measurement of the known distance was used to scale the image. A further 5 measurements of the known distance were taken (total n=6) and the mean distance divided by the number of pixels used in the first measurement. The scale value in pixelsmm^{-1} or pixelsμm^{-1} was used thereafter for all 4x images acquired.

The same procedure was used for the 10x objective but with the measurements using a calibrated haemocytometer with a known distance of 200µm, one large square or four smaller squares (See Figure iii). Measurements were consistently taken at -0.9 degrees to match the manual positioning error of the haemocytometer, to keep the measured distance parallel to the known distance in the image.

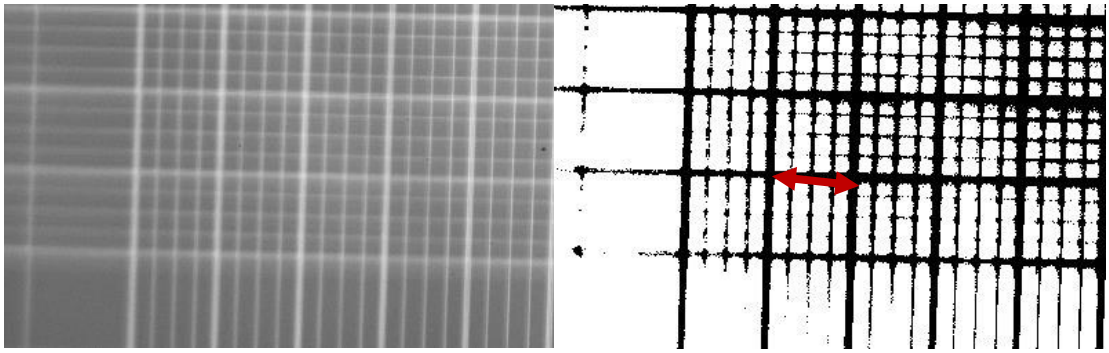


Figure lxxii: 10x calibration images, original (left) thresholded (right). Arrow depicting area of square which was measured.

Measurement	4x objective w/o cover Distance (mm)	4x objective with cover Distance (mm)	10x objective w/o cover Angle (degrees)	10x objective w/o cover Distance (µm)	10x objective with cover Angle (degrees)	10x objective with cover Distance (µm)
1	1.000	1.217	-0.955	200.000	-0.909	200.000
2	0.983	1.000	0.000	204.404	-0.909	198.347
3	1.036	1.002	-0.939	201.105	-0.924	196.722
4	0.992	1.027	-0.939	201.105	-0.924	196.722
5	1.008	0.962	-0.939	201.089	-0.924	196.713
6	1.008	1.053	-0.955	200.000	-0.939	194.275
Mean	1.005	1.043	-0.788	201.284	-0.922	197.130
SD	0.018	0.090	0.386	1.621	0.011	1.917
Min	0.983	0.962	-0.955	200.000	-0.939	194.275
Max	1.036	1.217	0.000	204.404	-0.909	200.000
Pixel Count	121.333	116.796	NA	60.342	NA	63.000
Mean Distance/Pixel (µm/pixel)	8.283	8.930		3.336		3.129
SD Distance/Pixel (µm/pixel)	0.148	0.771		0.0269		0.030

Table iii: Calibration measurements for NIKON objectives used with the HPV-X2 Hi-Speed camera

Therefore, each 400x250 pixel image (frame) captured whilst using the glass cover over the objective is 3572.04 x 2232.53 ± 308.24 x 192.65 µm for the 4x objective and 1251.6 x 782.25 ± 12.6 x 7.6 µm when using the 10x objective. Scale bars in each picture are either 1mm for the 4x images or 250 µm for the 10x images.

5. HPV-X2 External Trigger Methods

5.1. Manual Gated Timing

Increasing the contrast under illumination, projections containing the microsphere /microbubble mixture were significantly darker than that of the surrounding agarose gel and acrylic; which was largely optically transparent even at a thickness of 60mm (acrylic walls included). This contrast combined with a light detector produced a sufficient change in output voltage from the detector to enable time resolved monitoring of the projection events.

With the Solis LED at maximum light output for maximum image contrast at low exposure levels, the voltage output from the light detector was lower than expected due to the protective diffuser lens in the light path and the natural aperture of the lens. As a result the switchable gain was increased to 30dB for 10x objective use. This produced an output voltage of approximately 1.9V, but not so high as to exceed the recommended output voltage of the detector (5V) or the recommended channel input for either of the two oscilloscopes (2V). At a gain of 30dB (2.38 x 104 V/A ±2%, 260kHz Bandwidth[3], 211µV noise) each data point is produced at intervals of every 3.9µs a considerable drop off from the 12MHz bandwidth[3] at 0 gain, or a sampling every 83.3ns.

The two oscilloscopes available for use were the Le Croy (HDO4024, Teledyne, CA) and the WaveSurfer (2014z, Teledyne, CA). Both models have incredibly high sampling frequencies capable of detecting up to a maximum 10 and 4GS/s respectively however this is only at a relatively short time period, as irrespective of the time interval, both oscilloscopes can only record 10,001 data points to memory at any given time. A trade-off between total time captured and resolution of the data exported by the oscilloscope was therefore required, particularly given the .csv file export time being significantly longer than that of the trace time captured.

To ascertain the timescale of the delay between the exposure to ultrasound and the first projections being formed, a time trace of the detector output was produced using the manual time gated experimental setup (See section 4.2.4). Each experiment was run between 2-3 minutes of exposure, with 200us of time captured every second with a resolution of 2ns; our temporal resolution therefore was not that of the oscilloscope but the output from the light detector at 30dB gain. The mean of each output file (200us), was plotted against the indices file number in time producing a plot of mean voltage over the exposure time (below).

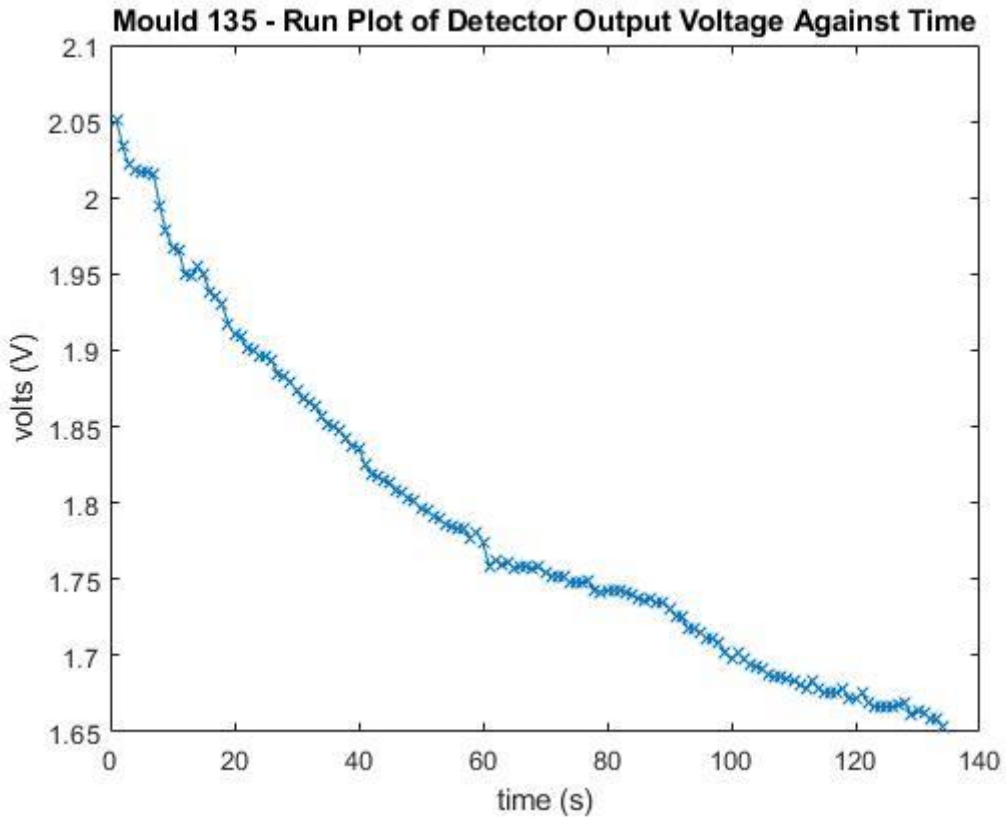


Figure lxxiii: Example of light detector output voltage trace against time for mould 135.

In figure iv there is an initial drop in light intensity in the first few seconds of time, as the dark contrast of the filled well is pressed forward by the acoustic radiation force, decreasing the output voltage. There appeared to be no immediate recovery of the output voltage once the ultrasound was turned off, thought to be as a result of the microspheres being compacted

against the well edge by the acoustic radiation force, decreasing the transmission of light at the top of the image frame (See Figure v).

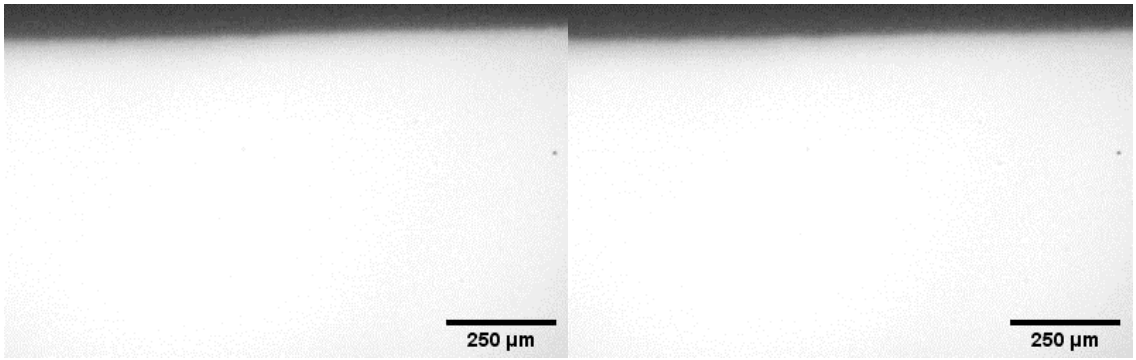


Figure lxxiv: 4x Objective. Slight compression of the gel well, at rest (left) under US exposure (right). The slight angle of the well in this image is caused by the variation in the gel fabrication process, only noticeable under increased magnification.

Within the first 10 seconds, a second far steeper decline in voltage is observed; this is the beginning of a successful projection event (confirmed via image capture) and cavitation. The voltage trace does not indicate, however, at the time at which the projection begins, only that under the applied ultrasound, black beads crossing the image frame provide a measurable decrease in transmitted light.

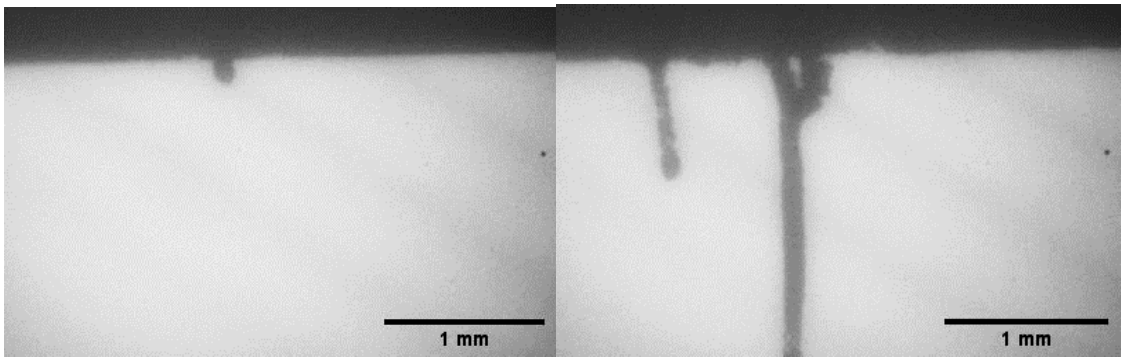


Figure lxxv: 4x objective. Beginning of a single microsphere projection (left), multiple projections (right). Diagonal lines across the image are a crinkling artefact of the mylar sheet on the surface of the mould.

To increase the temporal resolution of the detector trace during the first 10 seconds of exposure, a single 10,001 timepoint file output was recorded over the initial 10s period from the first Verasonics™ trigger. The corresponding voltage trace had a temporal resolution of 0.1ms. This trace showed that the output from the PDA36A2 Si Switchable gain detector oscillated frequently between two points even at 'steady' light levels and was associated with the noise of the detector (Figure vii).

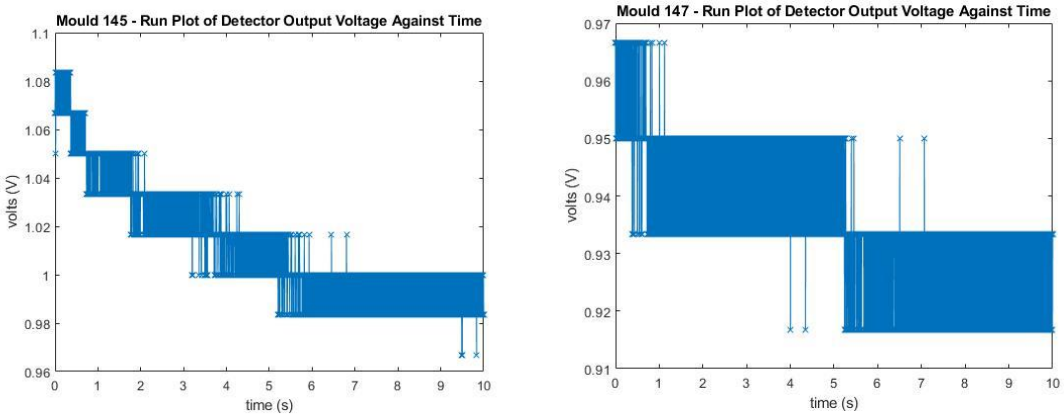


Figure lxxvi: Detector output voltage traces for the first 10s of ultrasound exposure. Single files 0.1ms resolution. 16.6mV noise band (left) and 33.3mV noise band (right).

Even at a 'steady' light input the noise band of the detector at 30dB gain can be seen oscillating over increments of 16.7mV or 33.3mV, despite the same gain level, light and exposure conditions on the same day. The reason for the change in noise band in each experiment is not precisely known but does not appear to correlate to any purposeful in change in experimental or parameter setup.

Despite the apparent step-wise decrease in voltage, there appears to be no consistent voltage drop consistent with the initiation of a projection event, most likely the result of improper and inconsistent focussing between each experimental run.

Reducing the time window for the manual delay therefore did not improve the likelihood of capturing the stochastic events concurrently. Visual confirmation from stationary images

between pulses, was the only evidence that the timing of the microsphere projections was loosely grouped, around 5.000 ± 0.250 seconds after initiation of ultrasound exposure.

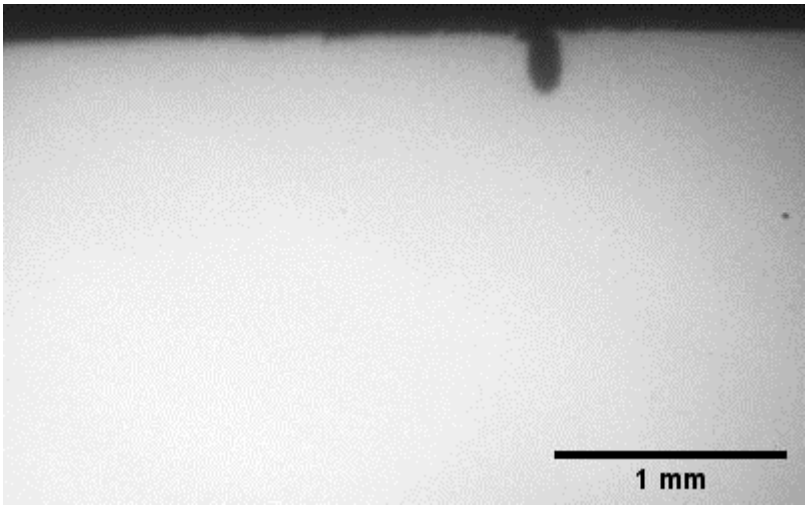


Figure lxxvii: Example image of an immature projection captured by manual delay. The capture event has taken place after the initial projection formation and between any subsequent elogation of the projection channel. The manual delay timing was therefore too long for this particular example.

5.2. Light Responsive Trigger Method

Whilst reducing the size of the delay window was beneficial for the manual input; it did not improve the chance of the cavitation events coinciding with the trigger of Hi-speed camera. For example; within a delay window of 500ms (5.000 +/- 0.250s) there is the potential for the camera to capture 19 distinct events at 10,000 fps (25.6ms per recording) or 195 distinct events at 100,000 fps (2.56 ms per recording) within the same time interval, with the chances of serendipitous overlap between the two being incredibly unlikely. In practise it was only possible to record a few videos recordings manually at 10,000 fps of a single mould over the entire ultrasound duration. Manually capturing any microsphere movements over a single run was incredibly difficult and sporadic.

As the save time of the HPV-X2 is of the order of seconds for a single capture, only one attempt per experimental mould could be performed using the manual delay electronic setup

(See Chapter 4, Figure 3) before resorting to manual triggering of the HPV-X2, it was decided that a light-responsive trigger was required to increase the chance of capturing cavitation events above that of 10,000 fps.

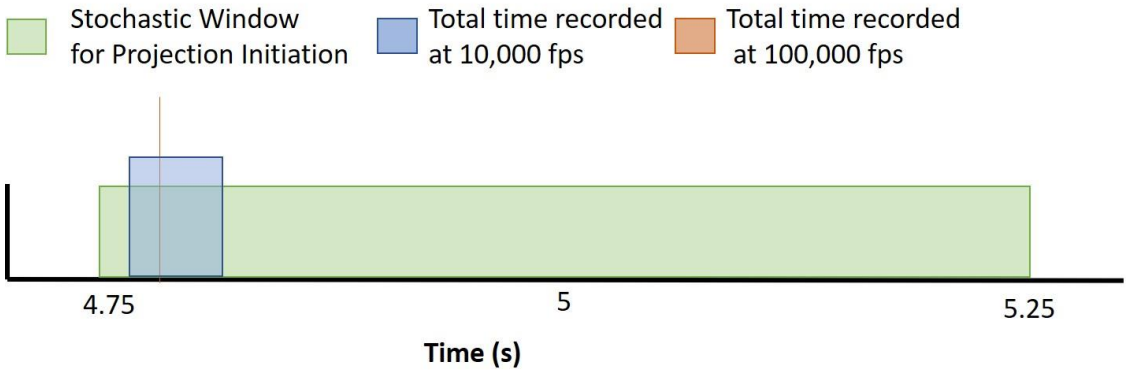


Figure lxxviii: Manually gated timing window for stochastic formation of ultrasound induced cavitation projections. Image is to scale.

The light responsive electronic setup (Chapter 4, Figure 4) was primarily used with the 10x objective and did eliminate the difficulty experienced with timing the capture of a stochastic event but it could not be effectively standardised due to the variable exposure of the gel mould. Voltage outputs at t0 were variable between moulds and objectives used, resulting in each mould requiring manual editing of the initial voltage, trigger method (window or negative edge) and trigger voltage for each hi speed recording.

Whilst the changes in ambient light surrounding the gel were not seen to impact the image quality, compared to the intensity of light transmitted by the H-LED; issues created by the glass beaker cover reduced the focus of the objective and image quality sufficiently for the blurring to affect the received light by the detector (See Appendix 4). Whilst the agar hydrogel protocol was standardised, the inherent variation in hydrogels did produce a variation in the optical clarity of the gels used, this in combination with suspended bodies in the water tank (from the laboratory ventilation and manual manipulation) also diminished the final image quality.

The variation in the image quality observed resulted in variable intensities of light transmitted and thus the output voltages associated with each mould had inconsistent maximum values. The noise band associated with the detector however remained relatively constant with the gain setting, with a maximum noise band of 33.3mV.

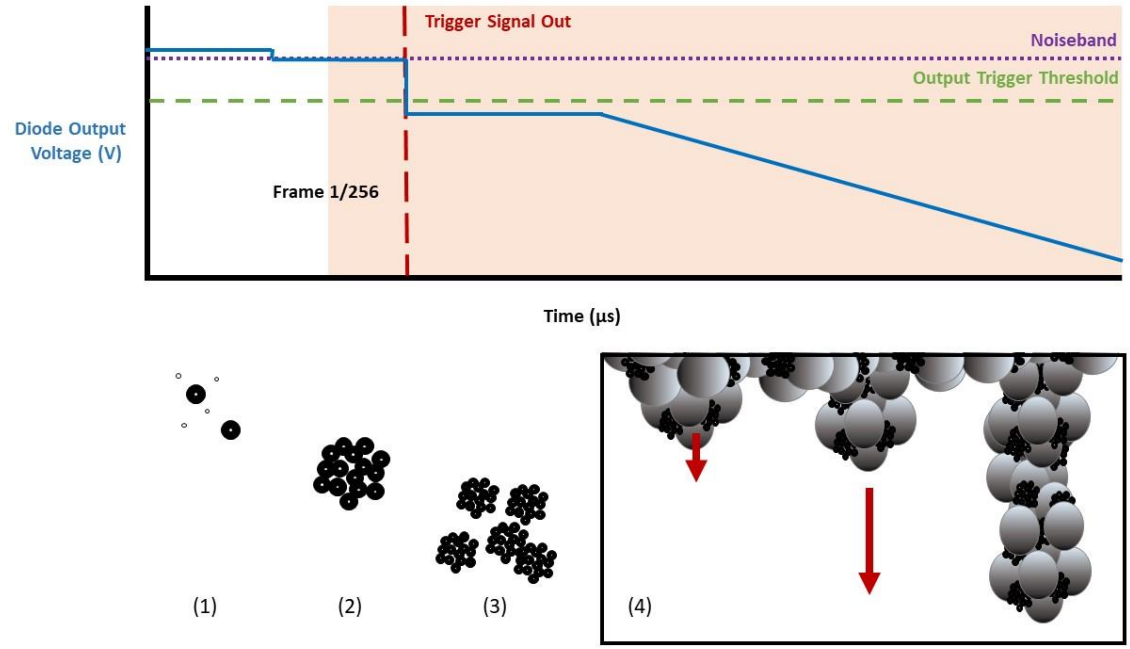


Figure lxxix: Cavitation activity corresponding to diode voltage changes and subsequent triggering of the HPV-X2 high speed camera. Voltage trace is indicative of the scale of cavitation activity below (1:4). Individual microbubble oscillations (1), microbubble cloud oscillations (2), numerous cloud activity (3) leading to extension of projection channels via microsphere extravasation (4).

Irrespective of the trigger method (falling edge vs window) it was found that even relatively small changes in voltage, below the noise band were sufficient to trigger the hi-speed recordings, independent of the mean voltage at t=0. As expected changing the delta value of the trigger setting was related to the size of the cavitation activity and the respective change in image contrast. Setting the delta trigger value, below that of 60ms resulted in immediate capture, due to the contrast produced by oscillating bubbles on mass in and out of focus (Figure x, 1). 80-100mV corresponded to the oscillations of a single microbubble cloud (Figure x, 2) with increasing levels of activity (Figure x, 3) as the delta value increased (100-200 mV).

Setting of the delta voltage value too high (>200mV) resulted in capturing only gross changes to the well in frame i.e formation of a new microsphere projection or drastic changes in size to an existing microsphere projection within the frame (Figure x, 4); trigger sensitivity ignored at this level ignored any microbubble cloud or projection bolus phenomena.

Images which were not in focus, where there was no clear edge to the microspheres in frame either due to shadowing or optical resolution of the setup, resulted in microsphere movements not being recorded due to a lack of camera triggering. The blurring and distortion of the image averaged the light intensity transmitted to such an extent that even multiple channel microsphere projections could not be detectable. In these instances, when using a voltage trigger window, only removing the mould or turning off the light source would cause a sufficient change in light intensity to trigger the camera capture.

For each mould in sufficient focus, the first capture was achieved using a negative falling edge rather than a voltage window. This was chosen because during the first few seconds of ultrasound exposure the gel channel could move in global position, assumed to be slight compression of the gel within the mould. This movement of the entire well could pull the contrasting edge of the well out of focus, causing the transmitted light to increase, exceeding the voltage window threshold and causing a false positive trigger for recording. This undesirable false-triggering resulted in recording only dead space of the undisturbed gel as white frames.

Thus, choosing a negative falling edge, whereby the light transmitted decreased due to the black microspheres increasing in number across the screen, minimised the occurrence of false positive triggers but did not eliminate them entirely. Multiple falling edge captures were therefore used until it was observed that a projection channel had been initiated; after which a voltage gated window trigger was found to be more consistent. Window voltages were double that of single negative edge triggers. The applied ultrasound was turned off after each trigger

event of the HPV-X2, to account for the save time of the video files. This start-stop approach whilst tedious, allowed for multiple sequential video captures of the same microsphere projection without a large expanse of time between each capture; critical to tracing the movements of microspheres and microbubble cloud within the projection channels.

Initially a larger voltage decrease was required to begin a projection, a decrease of 60-100mV was sufficient to capture initial movements of beads crossing the boundary edge. After which using a window of 60-100mV, resulted in far more consistent capture of channel progression after crossing the initial boundary edge. Once outside the initial gel well, bead and bubble movements were more identifiable due to the lack of overlapping layers of microspheres in and out of focus, contributing to the overall image.

6. Microsphere Banding within Projection Channels

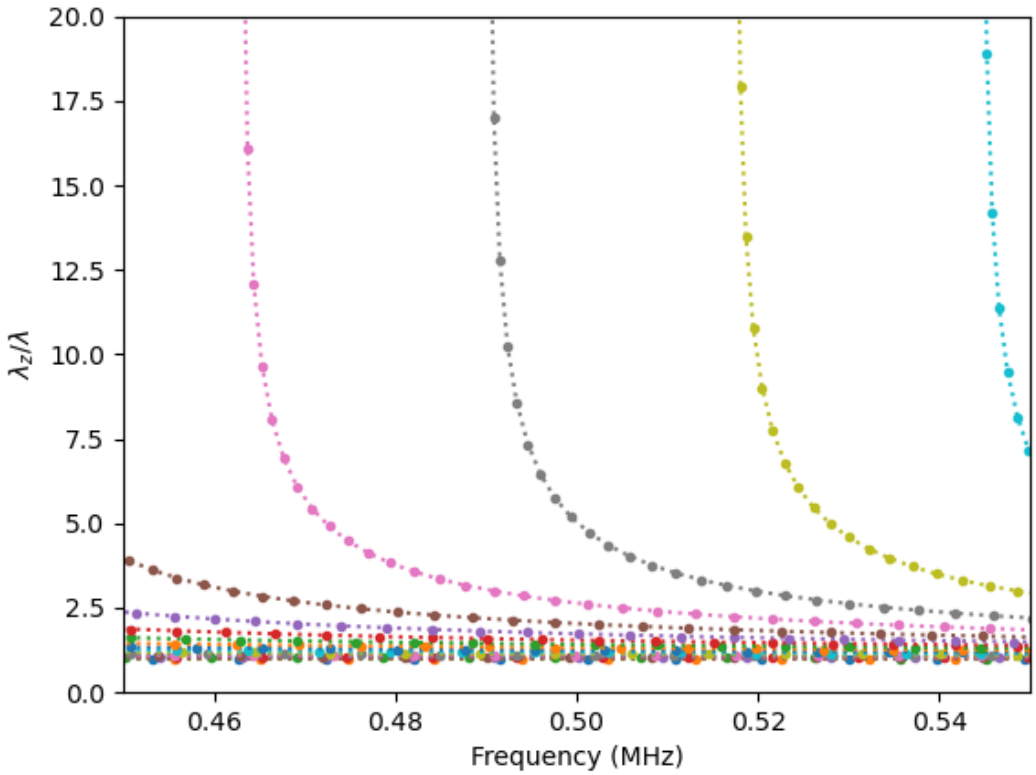


Figure lxxx: Simulation performed by Bernard Shieh (BUBBL, IBME, Oxford University) modelling the ratio of the longitudinal wavelength to the bulk wavelength, for modes of a rectangular cavity near the driving frequency. The longitudinal wavelength is always greater than the bulk wavelength.

Removal of the glass microspheres from the well cavity shows that a similar albeit fainter banding is observed within the bulk of the well cavity with Sonovue® microbubbles (Figure xii).

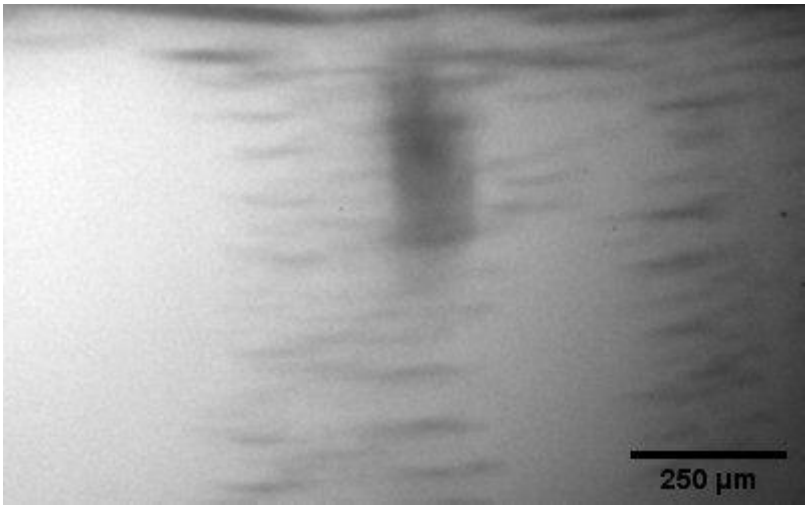


Figure lxxxi: Image banding from applied ultrasound on neat Sonovue®. Mould 184 using a 10x objective. Mean 46.510, SD 16.002, Min 22.222, max 95.244, n= 51. All values are in microns (µm).

After initially placing the mould within the experimental setup, a faint band of microbubbles and microbubble foam can be seen gathering at the highest point of the cylindrical well before ultrasound exposure. Once the ultrasound field is applied the microbubbles and foam can be seen cavitating producing the pronounced banding, which travels downwards, presumably due to the acoustic radiation force [26,28,50].

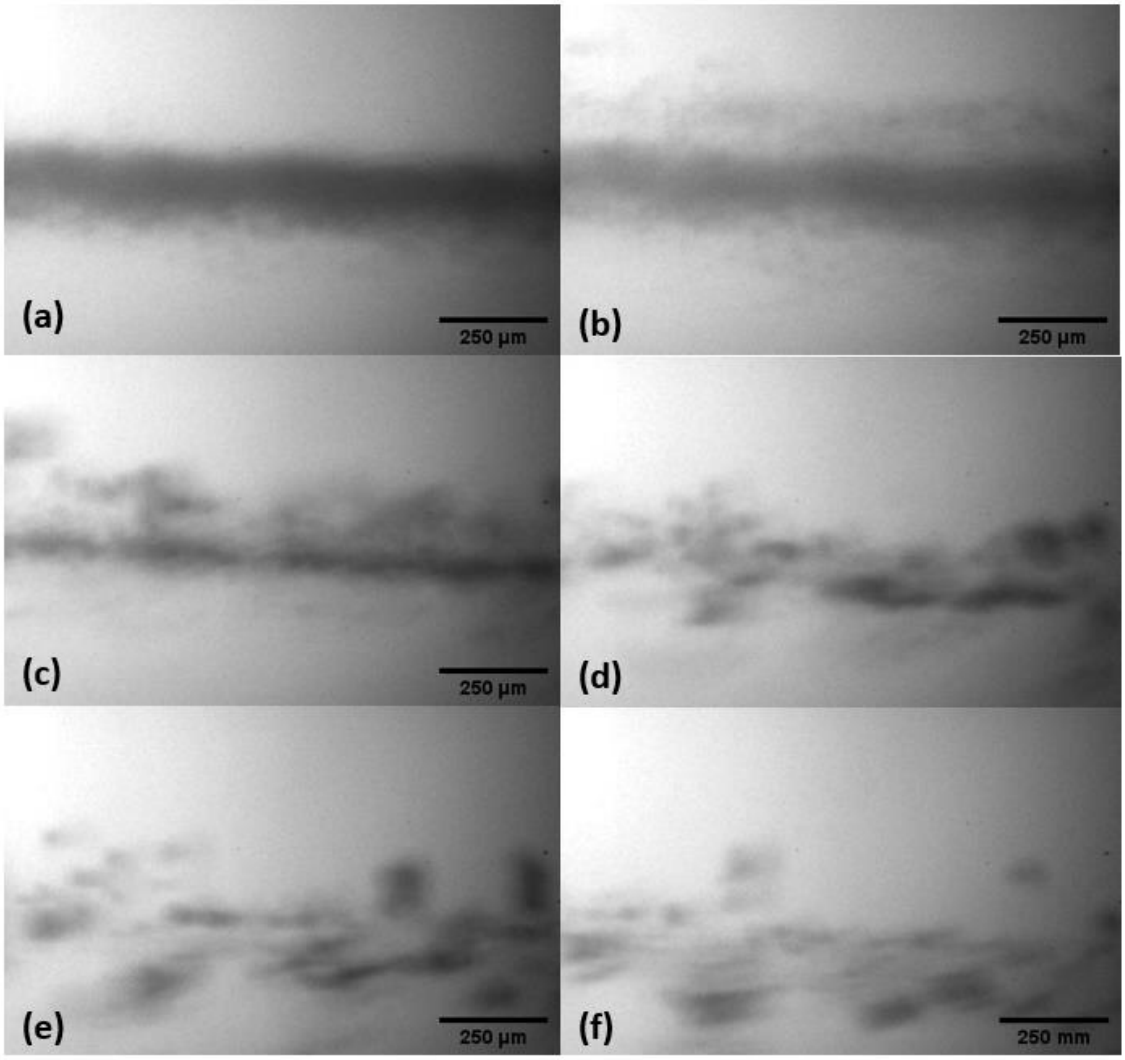


Figure lxxxii: Frames 001, 150, 175, 200, 225 and 250 of a 256 frame Sonovue® only using a 10x objective at 500,000 fps under 1.9Mpa of focal pressure, 0.50 MHz, 5% DC, 3.3Hz PRF (Section 4.2.5).

In Figure xiii the initial dispersion of the cloud foam and entrapped microbubbles which have floated to the surface of the well cavity can be seen (a). Coalescence of the microbubbles leads to larger macro-bubbles (c) and clouds which continue to cavitate, producing spherical blurred objects which have significant contrast (e), which slowly move forward and down in elevation as they traverse the boundary edge of the well cavity (f). These striations across the image (h) are similar to that of the banding observed. The number and size of the bubble clouds produced as well as the visible banding increases with increased focal pressure (2.8 MPa) as seen in Figure xiv; the explanation of which remains unclear.

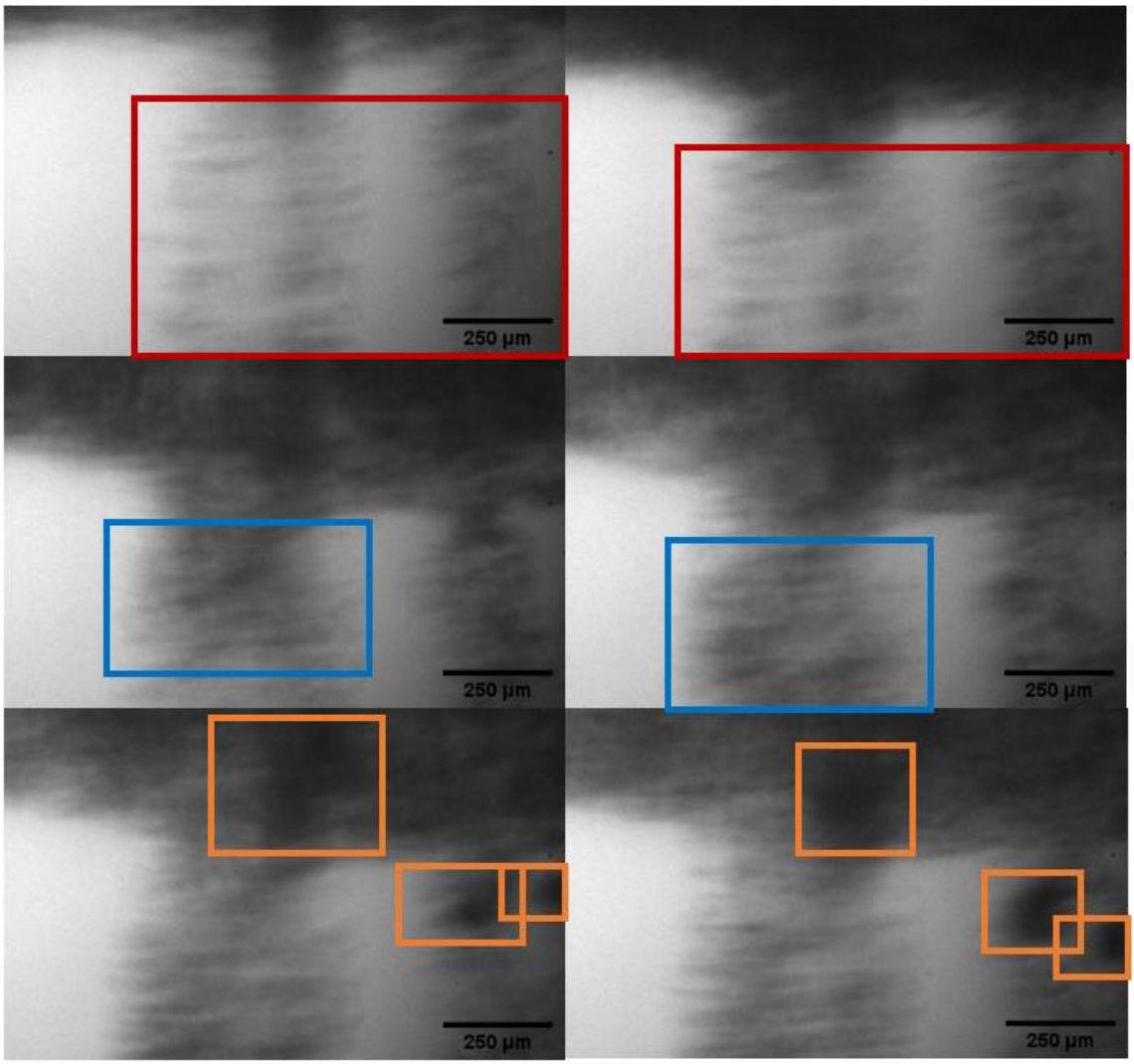


Figure lxxxiii: Frames 001, 125, 175, 200, 225 and 250 of a 256 frame sequence of ultrasound exposure to Sonovue® using a 10x objective at 500,000 fps. Ultrasound parameters are identical to that of Fig 28 (Section 4.2.5) except the focal pressure which is increased to 2.8 MPa. Microbubble foam edge is placed at the top of frame for allow for visualisation of movement. Visible pitched banding (red) increases in density (blue) with increased duration of applied ultrasound and finally to concentrated circular objects (orange). Banding (red) is restored after cessation of the applied ultrasound.

The cause of the microsphere banding which occurs in the channel lumen of some projections remains to be explained. The frequency spectra from individual experimental runs, show no components with sufficient magnitude which correlate to the pitch distance of the microsphere striations observed. Standing wave phenomena within the tank, was also not found to be responsible for the pitch distance measured from the images gathered.

Sonovue® only experiments indicated that the banding phenomena witnessed may be because of microbubble cloud activity emerging from the grouped microbubble foam and entrapped microbubbles prior to initial ultrasound exposure; suggesting a mechanical rather than an acoustic rationale for the banding formation. Further work is required to fully elucidate these findings.

It remains unclear as to the exact mechanism which causes the observed banding pitch distance of the black glass microspheres, it seems unlikely however to be related to a frequency component. Physical interactions and settling or separation of microspheres from microbubbles or bubble clouds have not been ruled out but further work into the area is required. The acoustic attenuation and scattering of the acoustic signal by the incompressible glass microspheres must predominate in this setup as there are no signs of a standing wave being present, unlike that of witnessed in highly compressible cellular cultures using continuous wave ultrasound at elevated frequencies[51–53]. Where cells will migrate in bands of $\lambda/2$, corresponding to the nodes of the wavelength acting upon them.

Which suggests that the foaming and redistribution of microbubbles within the concentrated bolus pockets causes the channel microsphere banding, as there is no frequency detected which the observed banding distance. Exactly what causes this phenomenon remains unknown, particularly as it is not observed in earlier work (See Chapter 2) which uses a vertical orientation of the well for the microbubble and microsphere slurry.

7. Design and Fabrication of a Novel Ultrasound Horn for Intraoperative adjuvant use in Glioblastoma Multiforme Resections

7.1. Proof of Principle

An unoptimized commercially available sonicator horn (Q125, QSonica, Connecticut, USA) normally used for cell disruption, DNA/RNA shearing and homogenisation was used for initial benchmark testing for proof of principle experimentation. The Q125 is a programmable ultrasonic processor which operates at a maximum of 125W @20 kHz and a 1/8 inch (3.175 mm) cylindrical tip (#4422) with a tip displacement of 30-180µm. The horn has limited cycle control and can only be run in continuous phase with the duration of each pulse controllable to a 1s resolution.

Each distribution of black glass microspheres, analogous to that of the commercially available TheraSphere™ (15-32µm, See Section 4.2.1), was tested in combination with 200 µL neat Sonovue (mean 2.5 µm, 1-5 x 10^8 bubbles mL^{-1}, Bracco Diagnostics, USA) using ~0.020g of microspheres. The slurry of microspheres and microbubbles were added to 4mm agar gel cavities (See Section 2.2.2) and the sonicator tip immersed in the liquid within the well until it approached the bottom (distance from the agar floor to the sonicator tip <5 mm, See Figure xv).

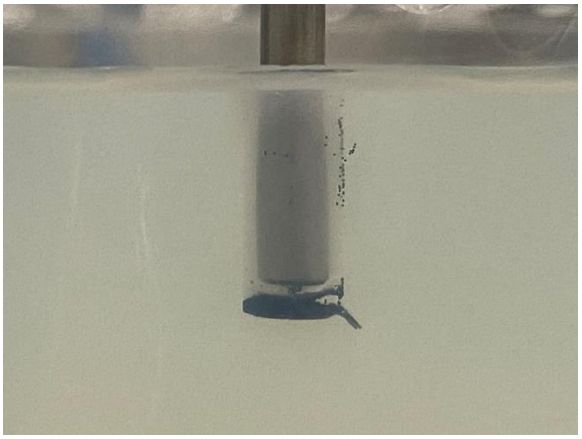


Figure lxxxiv: Placement of the sonicator tip within the 4mm agar wells filled with neat Sonovue and black glass microspheres analogous to TheraSphere™.

The sonicator was run at maximum output (125W) for 1s followed by 19s of rest for a total of 60s (3s total on time) to achieve a 5% duty cycle, for each microsphere distribution (see Figure xvi).

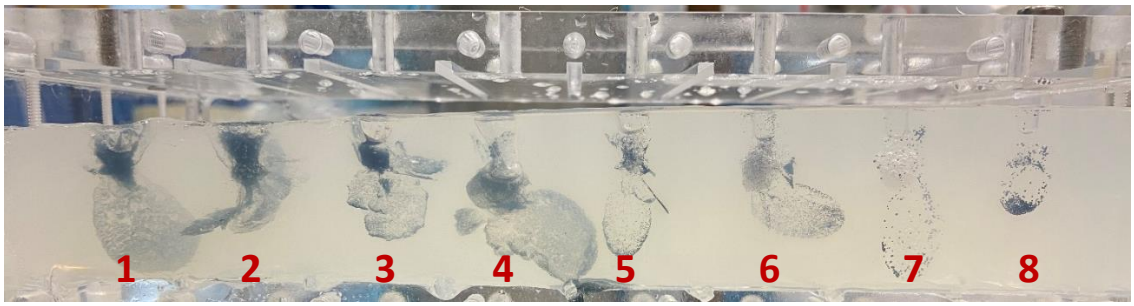


Figure lxxxv: Initial testing using the sonicator horn with neat Sonovue and black glass microspheres of various diameters. Microsphere sizes <15 µm (1&2), 15-32 µm (3&4), 106µm (5&6), 200-400 µm (7&8).

Initial results using the unoptimized sonicator are shown in Figure xvi. No two projections formed by the sonicator were identical, the majority of the projections produced by the sonicator occupied a single 2D plane of microspheres fixed within the agar gel with microspheres of larger distributions travelling shorter distances (Figure xvi, 7&8) compared to the smaller microspheres (Figure xvi, 1 & 2). None the less the concept of using an unfocussed ultrasonic horn, rather than a focussed transducer appeared promising and feasible.

7.2. Methods

The parameter findings from Chapters 3 in addition to the observations of microbubble cloud activity in Chapter 4 were used to design an ultrasonic horn device that would be suitable for use intraoperative within the skull. With help from Dr. Bernard Shieh, two prototype horns were designed and constructed from 304 grade stainless steel using the Engineering Workshop within the Institute of Biomedical Engineering (IBME) and attached to a commercially bought driver. The fields produced by both devices were mapped and their pressure outputs recorded, albeit to a limited degree. Both prototypes suffered from variable impedance issues, the root cause of which is still unknown but is believed to be related to the clamping force exerted onto the driver and between the driver and the metal horn. Despite the limited PNP outputs of the two prototypes it was possible to embed 15-32 µm microspheres within the agar cavity, simulating the resection cavity however significant improvement on the depth of penetration is needed if the prototype devices are to be eligible for further translation towards a surgical application.

7.2.1.Design Parameters

The findings in Chapter 3 demonstrated that producing post-focal microsphere projections of increasing length was dependent upon two key acoustic attributes: frequency and pressure for applications using a focussed transducer. 0.5 MHz proved to be the most useful and versatile frequency tested, but the H107 series transducers (64mm, Section 2.2.4) used for the parameter screening are far too large to be inserted with the skull cavity within a typical procedure[41,42,44,46] even if sufficient coupling was available. Using an unfocussed acoustic horn, whilst less efficient at producing large peak negative pressures, would be more suitable for a therapeutic device than a large focussed decoupled transducer. In order to be usable within the skull, the prototype device would ideally be handheld and similar in dimensions to the

Sonopet device. Using an unfocussed horn with a terminal tip diameter of 3-4mm would provide the operator with the required fidelity and dexterity to carry out the procedure, successfully delivering the radioactive material to the desired location(s) for treatment.

A trade-off between driver size, weight, power and frequency would also be required in order to make the device portable to use, whilst being powerful enough to generate the cloud cavitation observed to be the main vehicle for driving the post focal projection depth in Chapter 4.

7.2.2.Horn Prototypes x1c & x3c

A commercially available unfocussed ultrasonic driver operating at 0.5 MHz could not be sourced. An aluminium bolt-clamped transducer (Langevin, Part# SMBLTF120W60) using a SM111 piezo electric material, was chosen based on availability, price and compromise between the desired attributes. The driver was capable of maximum output power of 60 W, at a 122 ±2.5 kHz resonant frequency, 800 ±25% Mechanical Q, <25 Ω resonant impedance to a 40mm contact surface tapped with a M10 x 1.0mm thread, for attachment of the bespoke horn designs: the x1c (Figure xvii) and the x3c (Figure xviii).

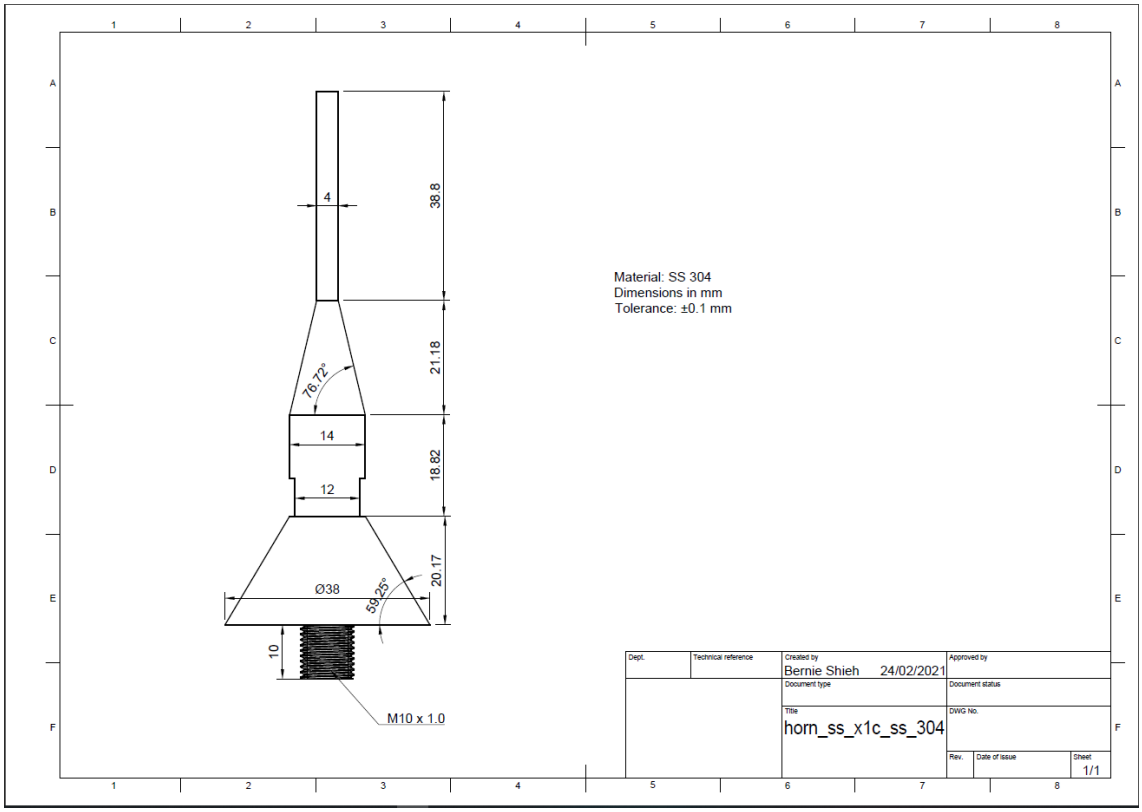


Figure lxxxvi: x1c final design iteration drawing for production.

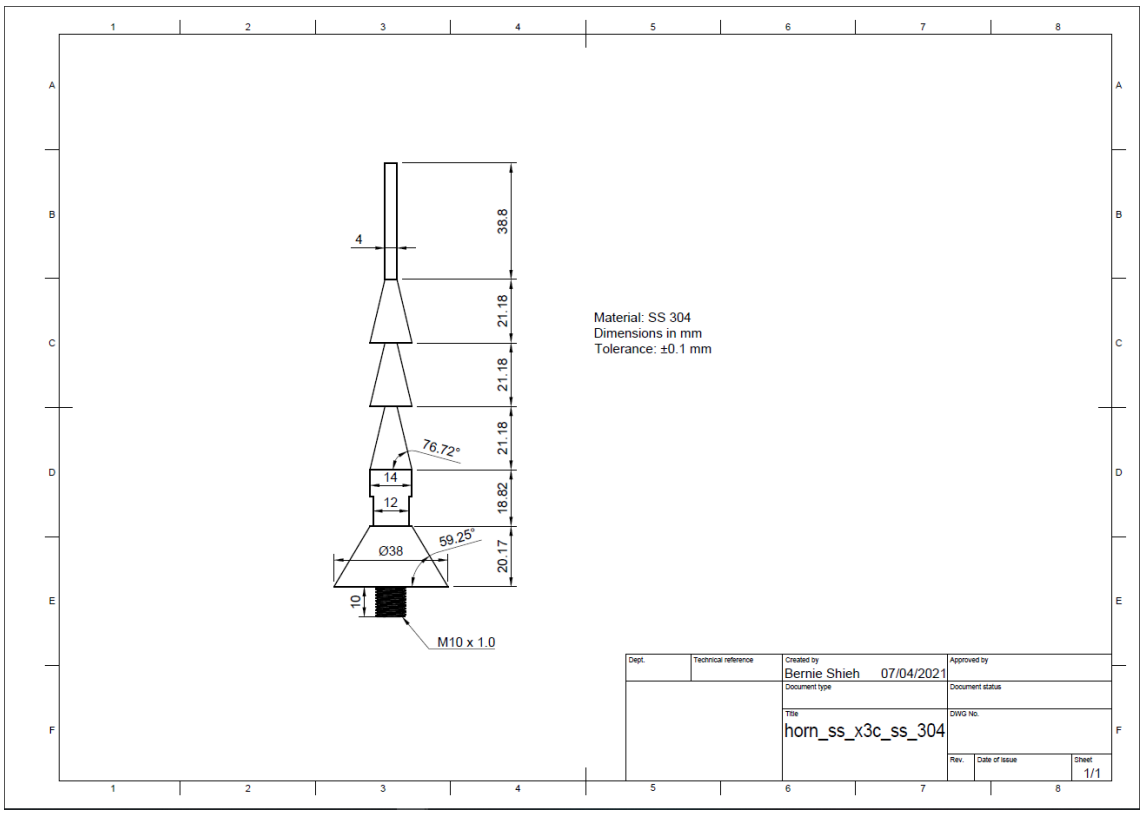


Figure lxxxvii: x3c final design iteration drawing for production.

Each horn was manually screwed into the driver using the 12mm relief cut out until the end range of motion, careful not to overtighten and damage the aluminium threads on the Langevin driver. Both horn designs take advantage of acoustic focussing using a 76.72^{o} cone element; once in the x1c and three times in the x3c design. The acoustic focussing was simulated to provide a PNP of 0.41 MPa at 5mm and 0.21 MPa at 10mm for the x1c horn. With the x3c horn PNP was simulated to be 1.3 MPa at 5mm and 0.7 MPa at 10mm distance from the horn tip. A 38mm 59.25^{o} cone was added to each horn design after initial versions demonstrated a reduction in acoustic output when using a small contact surface with the driver.

The electrical impedance of each horn was measured using a vector network analyser (SDR-Kits, DG8SAQ) sweeping from 110-140 kHz. Individual matching networks were also fabricated by Bernard Shieh from L-networks made from passive components (inductor in series and parallel) where the inductance and capacitance were selected based on the measured impedance. The final operating frequencies of the horns with appropriate matching networks was 103.10 and 129.49 kHz for the x1c and x3c horns respectively. Each horn weighed <390g with the driver attached.

7.3. Results

7.3.1. Acoustic Field (x1c)

The two horns were pressure calibrated using a 10 – 800 kHz needle hydrophone (Reason, TC4038, Teledyne) in an analogous manner to that previously (Section 2.2.4) using a waveform generator to control the ultrasound parameters of the horns. Each horn was tested using a 8000 cycle burst with a 100ms PRF (10Hz), this was because the maximum input of each horn took several thousand cycles to meet maximum output and displacement at their respective operating frequencies. The horn was mounted in place using a 3 prong rubber insulated clamp

attached to a 3-axi movement stage. Field scans were performed in the XY, YZ and XZ planes to establish the acoustic field emitted from the 4mm stainless steel cylindrical tips, at a depth of <1 mm from the tip surface.

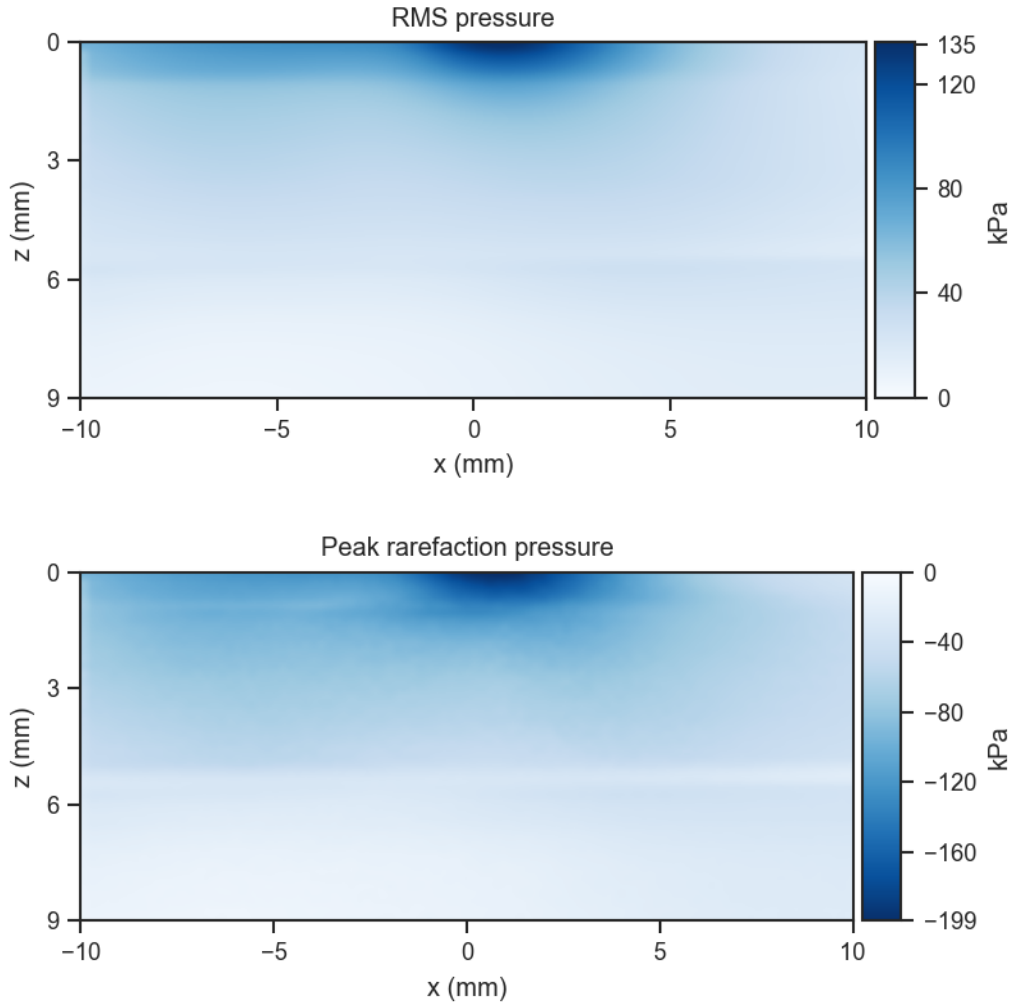


Figure lxxxviii: Root mean squared (RMS) and peak rarefactional pressure of the XY field of the x1c horn, 0.2mm resolution. Using the Reson TC4038 needle hydrophone.

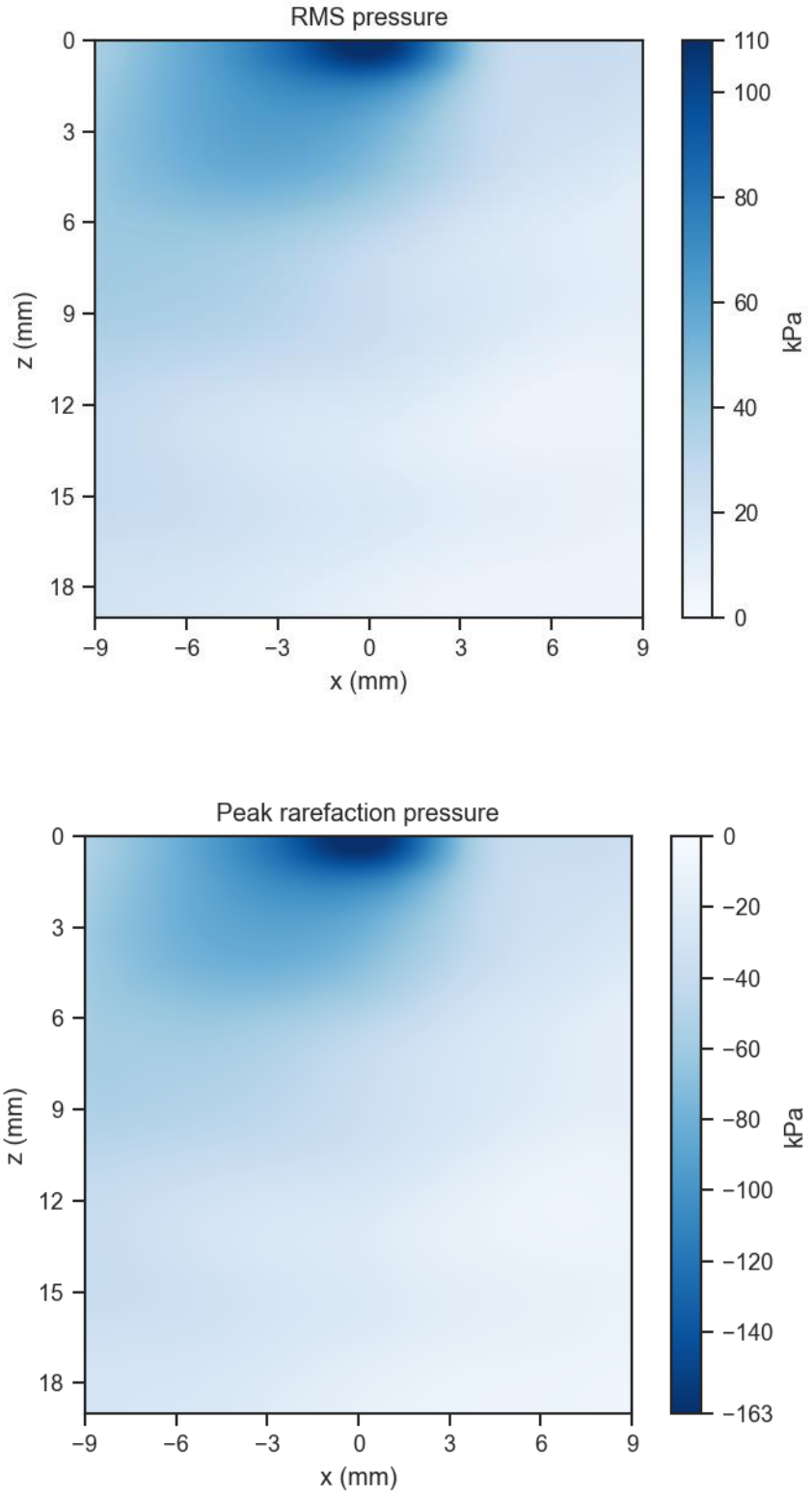


Figure lxxxix: RMS and peak rarefaction pressures for YZ field of the x1c horn, 0.2mm resolution. Using the Reson TC4038 needle hydrophone

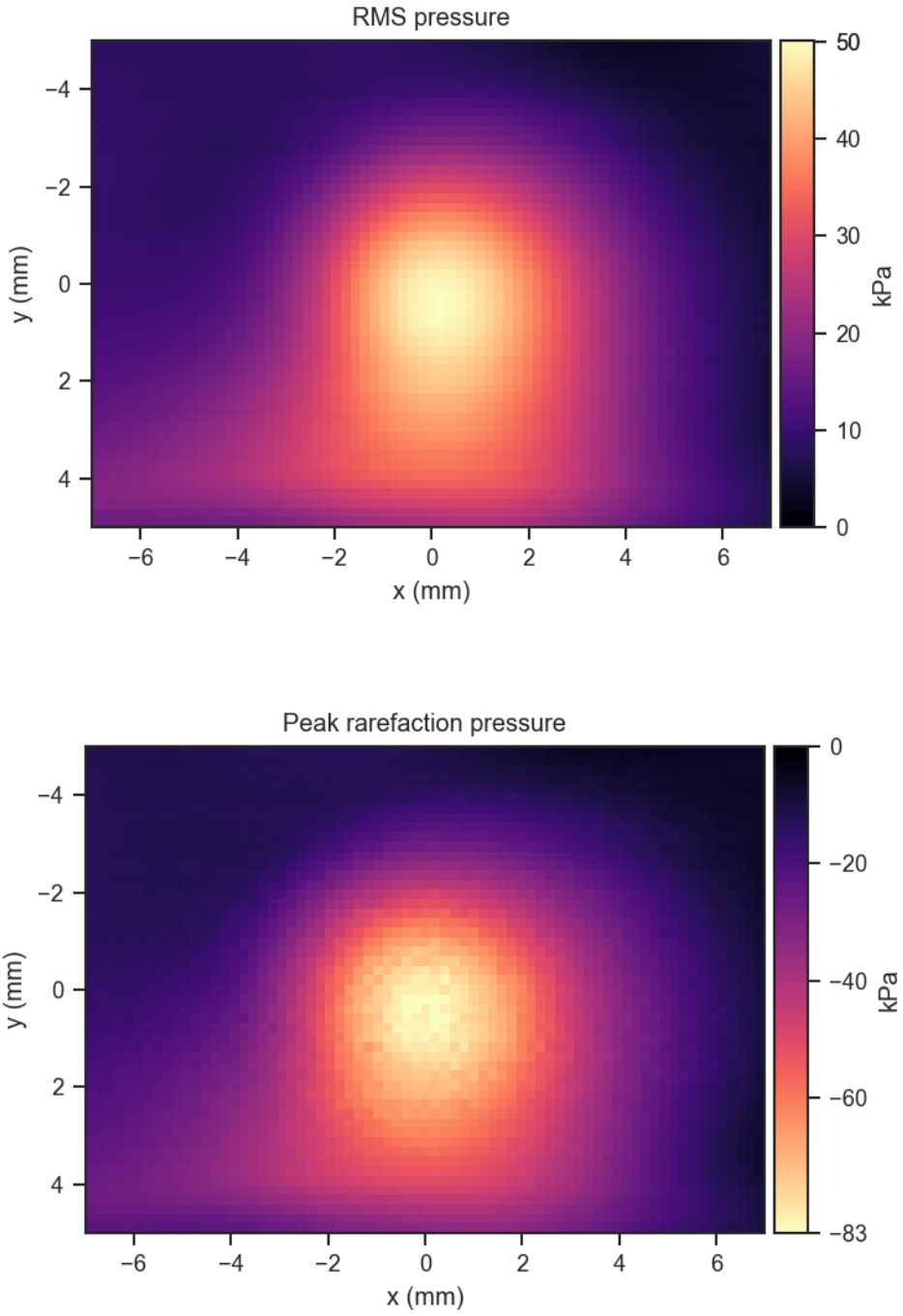


Figure xc: RMS and peak rarefaction pressure XZ acoustic field for the x1c horn, slight asymmetry in the lower left corner of the field. 0.2mm resolution. Using the Reson TC4038 needle hydrophone

7.3.2.Pressure Output (x1c)

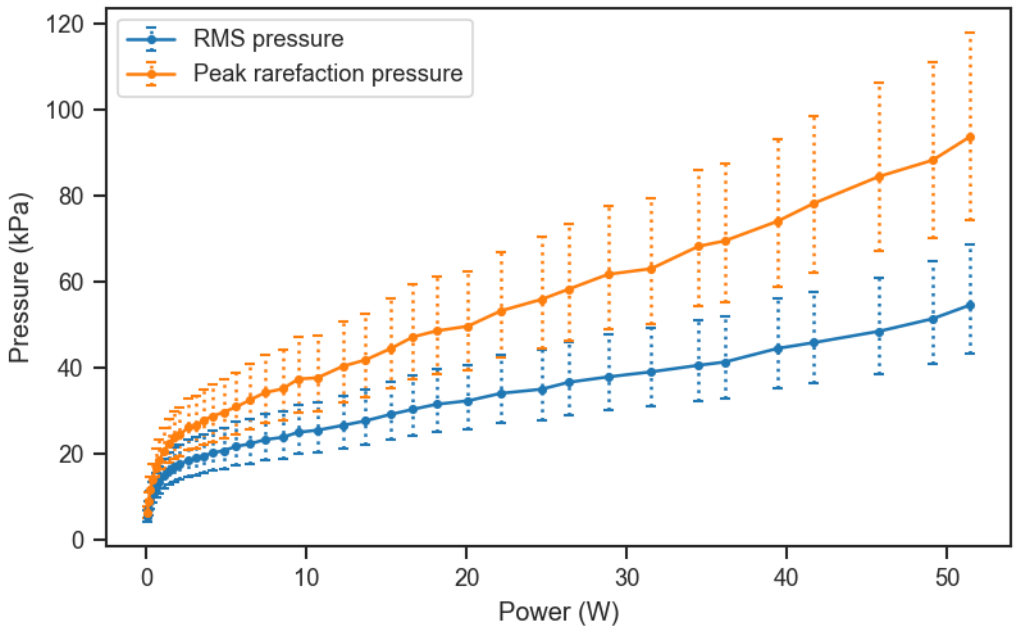


Figure xci: x1c with matching network, peak rarefaction pressure (kPa) to power input (W) measured using the Reson TC4038 needle hydrophone.

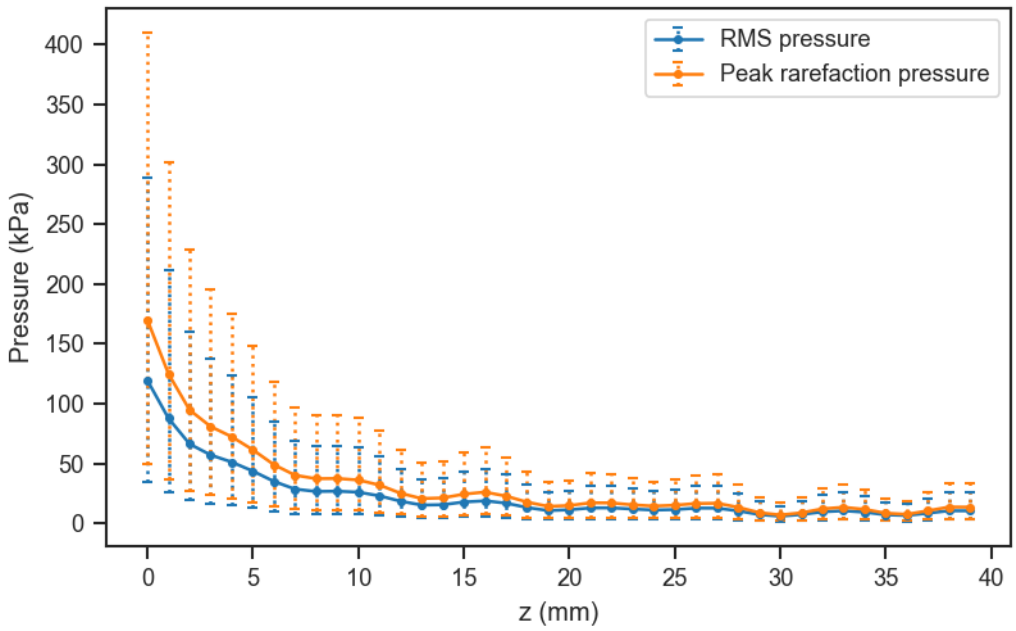


Figure xcii: x1c pressure (kPa) loss over distance (mm) calibration using the Reson TC4038 needle hydrophone.

7.3.3.Acoustic Field (x3c)

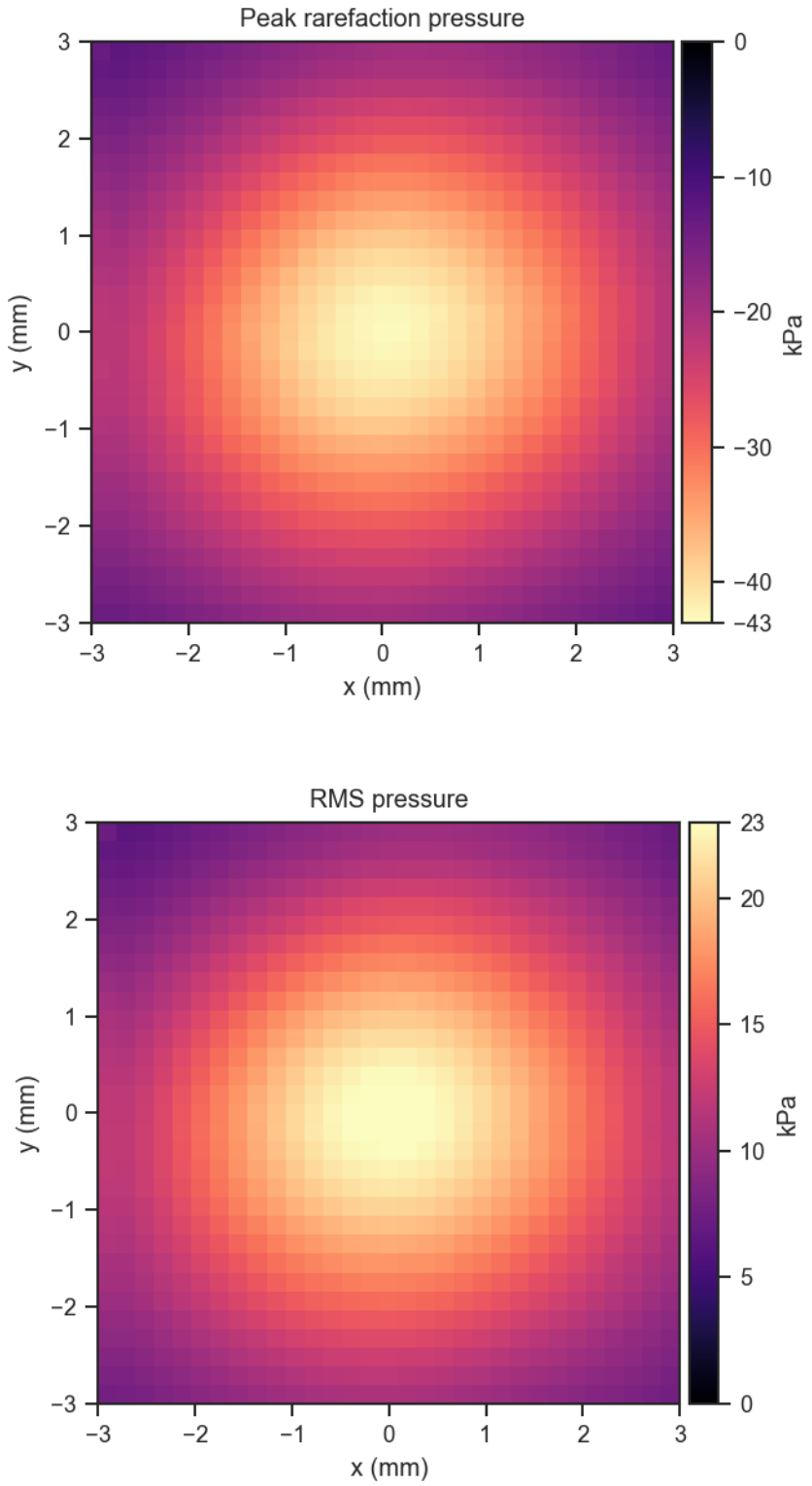


Figure xciii: RMS and peak rarefaction *pressure XZ acoustic field for the x3c horn, 0.2mm resolution. Using the Reson TC4038 needle hydrophone. 0.2mm Resolution.*

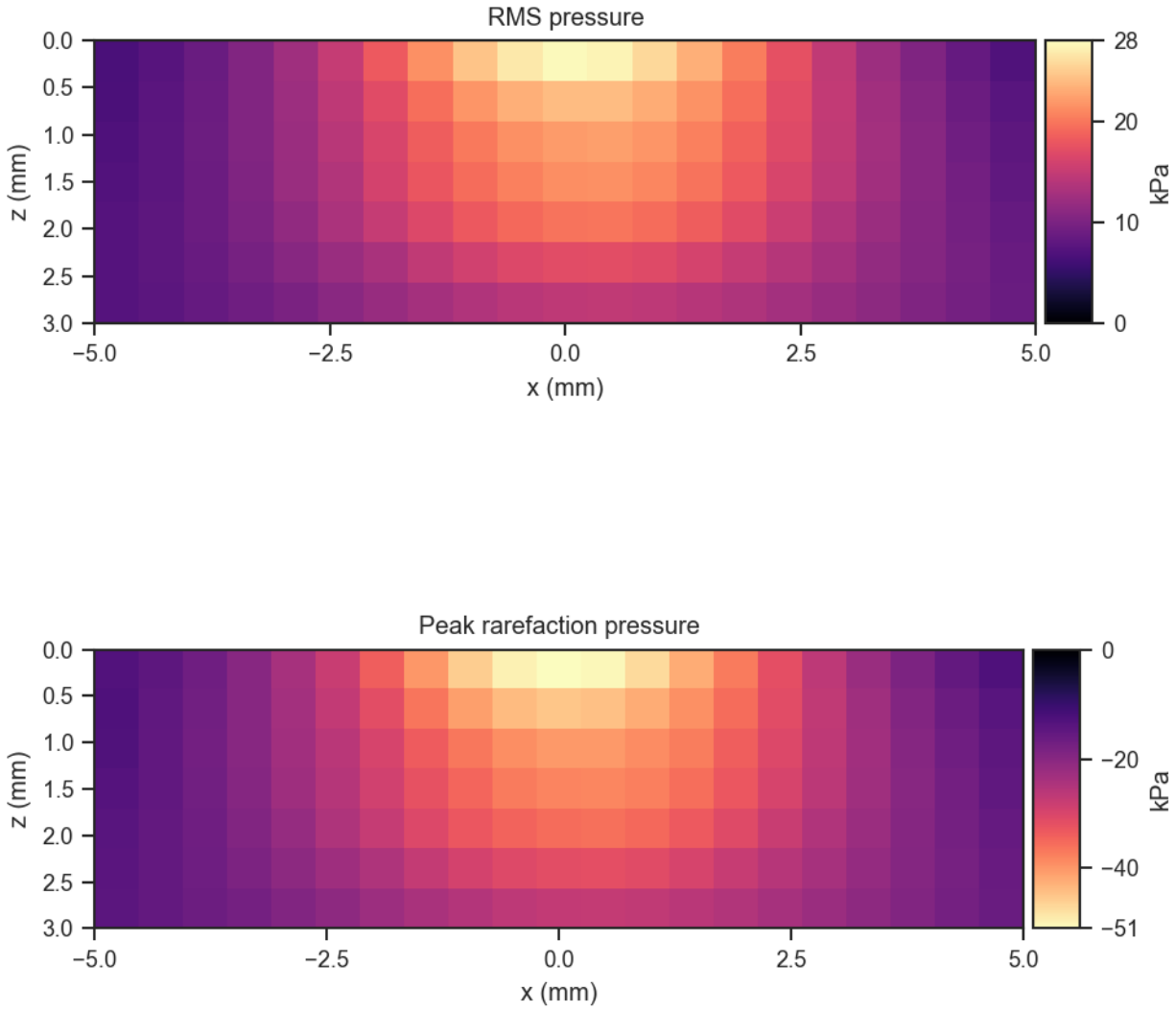


Figure xciv: RMS and peak rarefaction pressure XY acoustic field for the x3c horn. 0.5mm resolution. Using the Reson TC4038 needle hydrophone. 0.5mm Resolution.

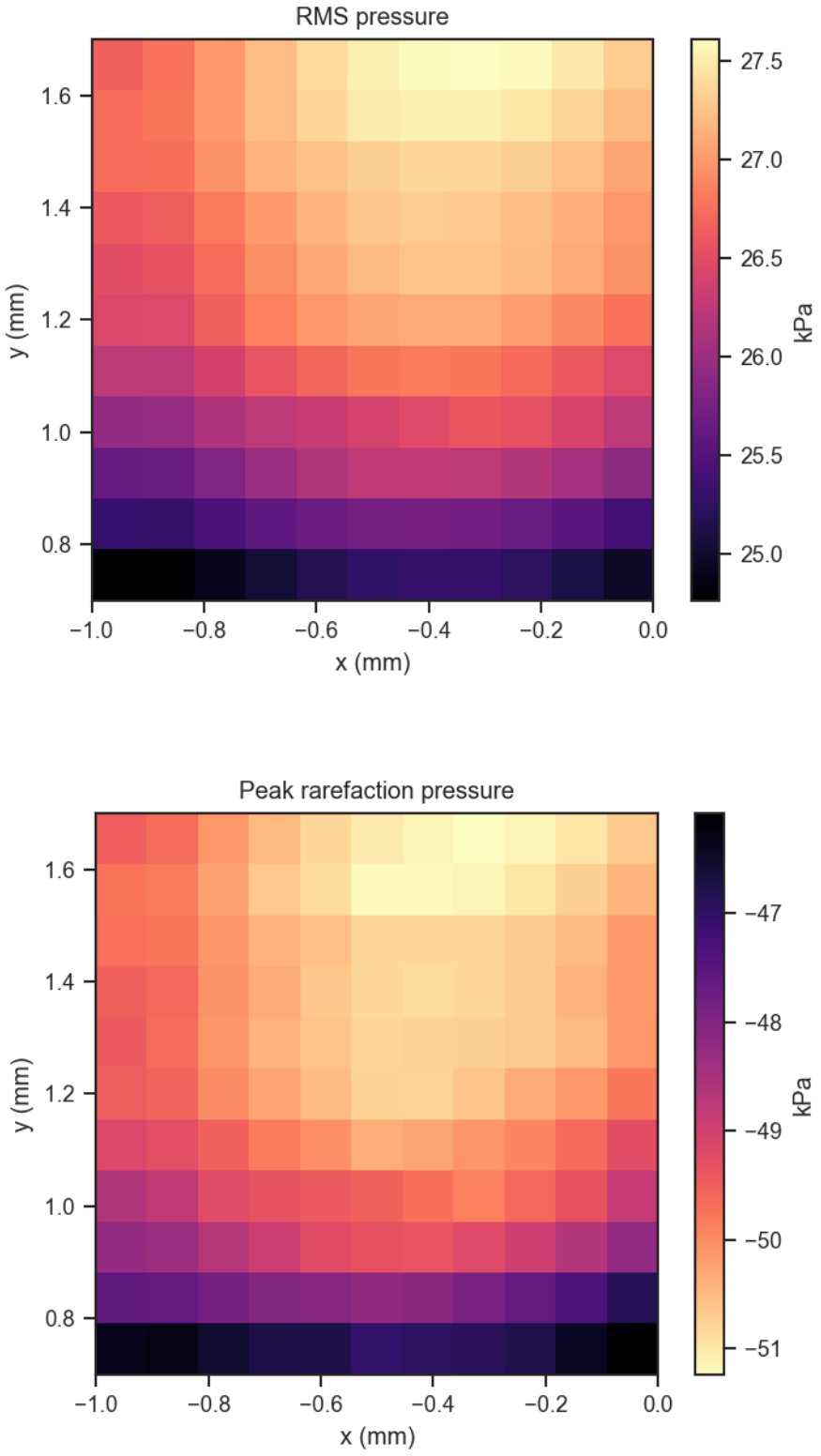


Figure xcv: RMS and peak rarefaction pressure YZ acoustic field for the x3c horn.0.5mm resolution. Using the Reson TC4038 needle hydrophone. 0.2mm Resolution.

7.3.4.Pressure Output (x3c)

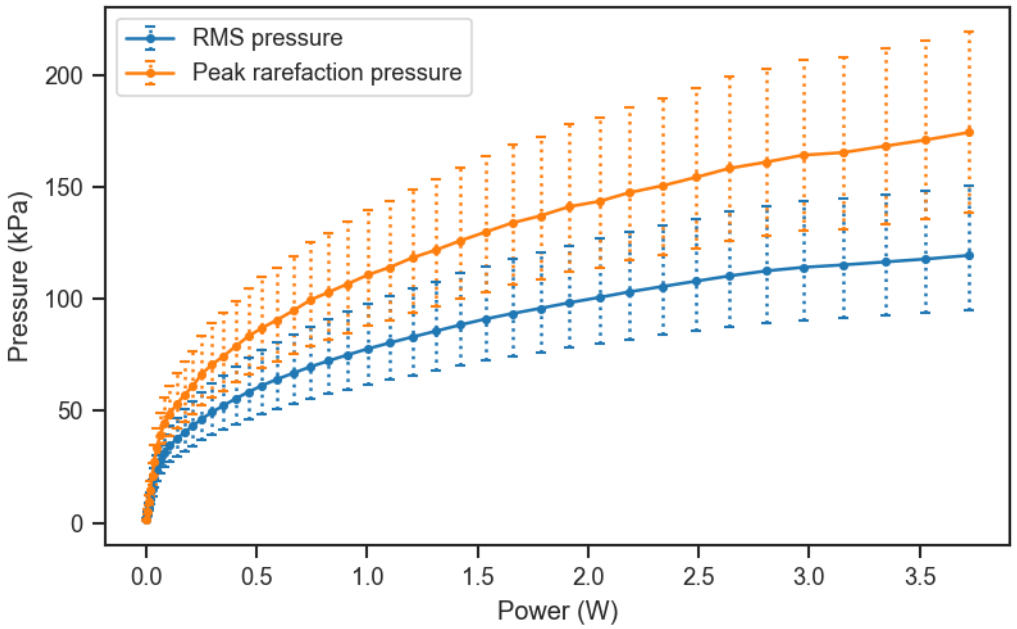


Figure xcvi: Pressure ramp for x3c horn without a matching network, using the Reson TC4038 hydrophone. Maximum power rating of the driver is 60W.

7.3.5.LDV Measurements x3c

As the TC4038 hydrophone was only capable of operating under pressures equivalent to ~3.5W of power using the x3c, from a potential maximum 60W of power input from the driver (5.8%), another method was required to calibrate the maximum output pressures from the x3c. Using either a fibre optic hydrophone or a TC4013 needle hydrophone (Reson, Teledyne) it was not possible to accurately measure the x3c pressure output. The fibre optic system (See section 2.2.4) did not have the frequency bandwidth required to measure the horns in the 129-130 kHz range. Whilst the TC4013 was sensitive down to 10 kHz, it was not suitable for operation under sufficient pressures to calibrate the maximum input of the 60W driver.

Laser doppler velocimetry (Polytec, NLV-2500), was employed to accurate measure the tip displacement of the x3c horn and theoretically calculate the RMS and PNP pressures achievable by the prototype device running at maximum power (60W). The NLV-2500 is a class

2, <1 mW, Helium Neon (HeNe) laser operating at 633 nm wavelength (visible red). With a variable working distance and a frequency bandwidth from 100 – 3000 kHz[47].

The LDV was mounted to a 3-axis movement stage pointing upwards, similar to that used previously (Section 2.2.2) and the horn placed in a vertical orientation above the LDV, pointing down attached to a second 3-axis movement stage using a clamp stand. Measurements were obtained in air. The variable impedance of the horn and poor network matching resulted in the maximum input voltage to the amplifier being reached before the maximum 60W power rating of the driver.

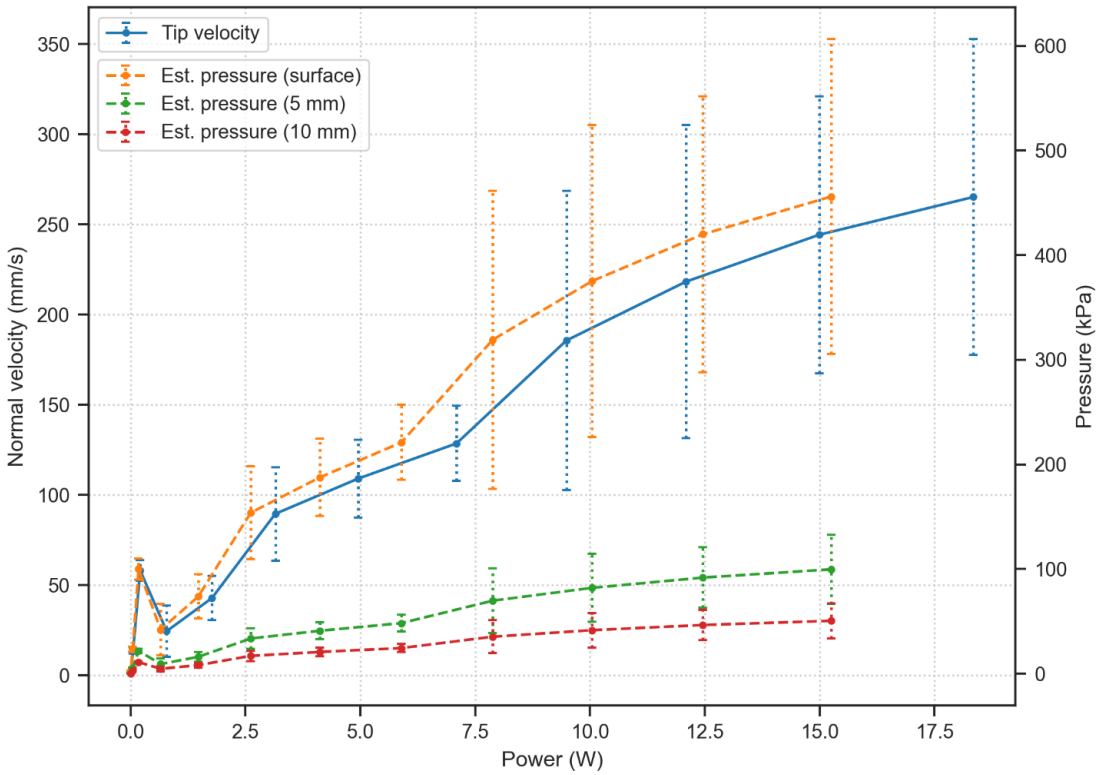


Figure xcvii: Measurements of the x3c tip velocity at the surface, 5mm and 10mm of depth.

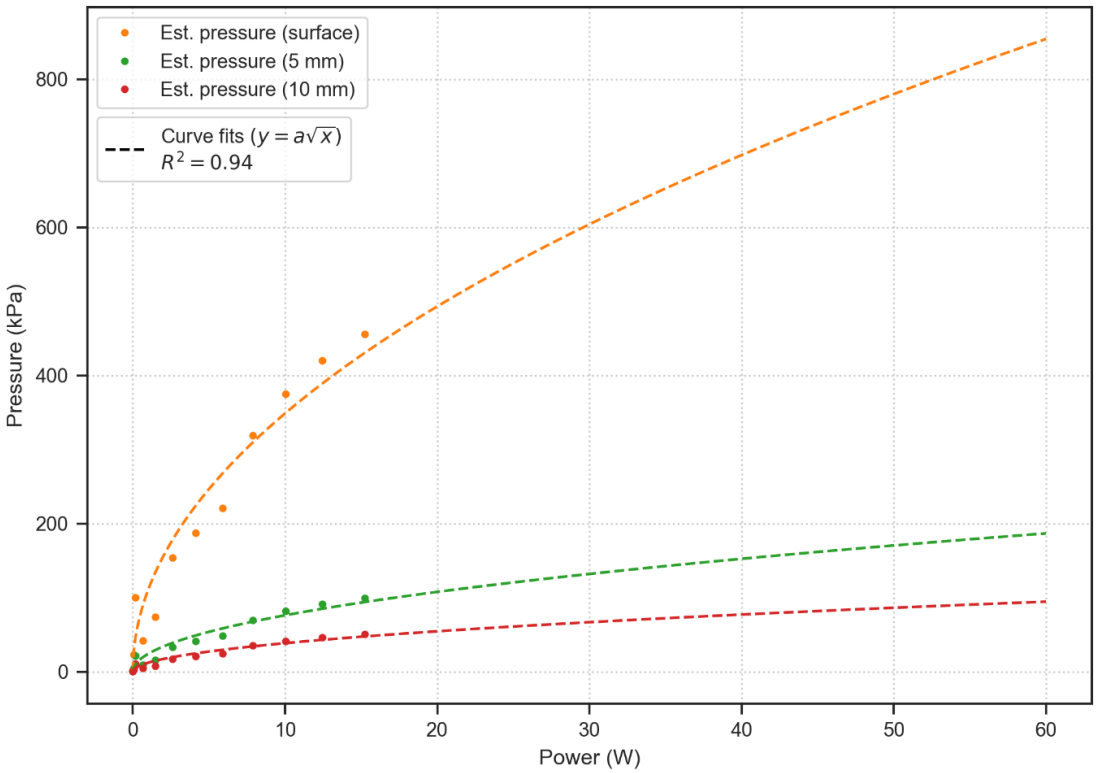


Figure xcviii: Estimated pressure outputs from the x3c in air at the tip surface, 5mm and 10mm of depth. Second order polynomial used to estimate pressures above 15W power.

7.3.6.Initial In Vitro Phantom Testing

Repeating the initial experiments with either the x1c or the x3c did not produce any sufficeint formation of projections or extravasation of the microspheres into the agar gel; even when running in continuous mode at maximum output. The horns were also tested in a more case representative fashion, using a crude hemi-sphere void carved out of a solid agar block by hand and filled with the slurry of micropsheres and Sonovue®. Repeating the testing at maximum output and in coninous wave did sufficeintly cavitate the microbubbles within the liquid, seen as an improvement in clarity of the liquid within the cavity. Turbulance of the desposited slurry was also evident within the cavity, as initially sedimented microspheres were aggitated and suspended within the saline from the Sonovue® addition. After the inertial cavitation of the microbubbles a focussing and pusling of microspheres could be seen infront

of the horn tip. No apparent projections were seen during the ultrasound exposure however upon flushing the cavity with deionised water, to remove any free microspheres and phospholipid foam, microspheres could be seen to be embedded within the boundary edges (Figure xxx),demonstrating projection of the microspheres in a limited capacity.



Figure xcix: Hemi-sphere agar voids with 15-32 µm black glass microspheres embedded in the boundary surface.

7.4. Discussion

7.4.1. Variable Impedance of the x1c and x3c Horn Prototypes

The most significant problem with the current prototype designs is the variance of the impedance when in use. The impedance varied to such a degree for the x3c that a standard 'fixed' matching network was not suitable and a variable matching network (T1K-7A, T&C Power Conversion Inc.) had to be used to increase the 50 Ω impedance of the amplifier (Setting 6 1:4.2, Setting 7 1:2.5) to an impedance more closely matching the x3c prototype. The variable matching network was therefore used for the LDV measurements and initial testing. Impedance measurements for the x3c were 55.41 Ω (54.53 + 9.86i) prior to use and 62.43 Ω (25.24 +57.10i) afterwards. This continually mismatched impedance meant that the driver was reflecting a large proportion of the voltage supplied back towards the amplifier,

resulting in a significantly reduced pressure output. We could not find a matching network that would adapt to changes of impedance during use.

The underlying reason as to why the x3c experienced a change in impedance during use is unknown. It is thought to stem from the unequal manual clamping of the driver via the 3 prong clamp, which slowly loosens over the number of cycles the driver experiences. The clamping force is known[48,49] to alter the power output of other ultrasound devices.

7.4.2.Design Improvements

Whilst the Langevin 60W driver appeared to be suitable for our needs, our choice of driver may have been the limiting factor in the success of this application. Although we don't have accurate maximum pressure outputs for either the sonicator or the x3c prototype, the sonicator does user a driver with twice the power maximum power rating compared to the x3c. Particularly given the conclusions from Chapter 3, that PNP is the largest most significant factor contributing to post focal microsphere projection depth, it seems unlikely that the estimated PNP of ~840 kPa would be sufficient to reproduce the chaotic projections observed with the sonicator horn (Figure xvi). Using a driver with double the power (120W) however should be capable to produce a PNP of 1.5 MPa, assuming some loss due to non-linearity (See Section 2.2.4). Values of which more closely match the initial estimates (1.3 MPa at 5mm and 0.7 MPa at 10mm distance) produced from the horn simulations by Bernard Shieh (Section 5.2.3).

Commercially available ultrasonic transducer (drivers) for non-HIFU applications, such as the one purchased for the prototype designs, are orientated towards biodiesel mixing[50,51], plastic welding[52,53], ground sonar[54,55], ultrasonic cleaning and biofouling applications[56,57]; none of which require power inputs to illicit inertial cavitation and microbubble clouds. These designs utilise very few layers of piezo-electric material to minimise complexity and production costs,

which can be drastically improved on given sufficient time, funding and expertise. This also extends to the power supply used in the case of the sonicator and Sonopet, a small power unit (combination of waveform generator and amplifier) is provided to allow control over the device output, amplify the voltage for the ultrasonic driver and potentially regulate the devices impedance during use.

Whilst the crude use of a sonicator demonstrated that very low frequency unfocussed horns are capable of producing large chaotic projections; the optimised surgical device needs to form predictable, repeatable projections which are dimensionally similar to one another in order for it to be useful in pre-operative planning. Despite the reduction in power experienced with both prototypes, the acoustic fields generated by both prototypes look suitable for the intended microsphere deposition. The microsphere projections formed using the sonicator, with an analogous unfocussed acoustic field, demonstrate an even distribution of microspheres (and therefore uniform radiation dose) within the projection produced; particularly with microspheres of smaller distributions (<15 and 15-32 μm).

7.5. Conclusion

Using the unoptimised Q125 ultrasonic horn demonstrated proof of principle for the use of an unfocussed horn for intraoperative use. The current x1c and x3c prototypes however are not capable of producing microsphere projection of the desired depth to be suitable for intraoperative adjuvant use for glioblastoma resections. This is expected to be due to insufficient peak negative pressure being generated via the mismatched electrical components. Improvements in the matching network and an increase in the driver power rating will drastically improve the performance and utility of both prototypes. Significant further work is required for translation of the x1c and x3c prototypes into a surgical setting.